

Dynamical Systems in Neuroscience: the Hindmarsh-Rose model

Sistemas Dinámicos en Neurociencia:
el modelo de Hindmarsh-Rose

Lucía Pérez Pérez

Programa de Doctorado en Matemáticas y Estadística



Universidad de Oviedo

Universidá d'Uviéu

University of Oviedo



RESUMEN DEL CONTENIDO DE TESIS DOCTORAL

1.- Título de la Tesis	
Español/Otro Idioma: Sistemas Dinámicos en Neurociencia: el modelo de Hindmarsh-Rose.	Inglés: Dynamical Systems in Neuroscience: the Hindmarsh-Rose model.
2.- Autor	
Nombre: Lucía Pérez Pérez.	DNI/Pasaporte/NIE. 7
Programa de Doctorado: Programa de Doctorado en Matemáticas y Estadística.	
Órgano responsable: Centro Internacional de Postgrado.	

RESUMEN (en español)

Comprender el funcionamiento del cerebro es uno de los grandes retos para la ciencia, y diferentes disciplinas participan en esta formidable tarea. En este escenario, las interacciones entre Matemáticas y Neurociencia son abundantes y fructíferas.

En esta tesis estamos interesados en el estudio del comportamiento de neuronas aisladas entendidas como sistemas dinámicos. Nuestros modelos neuronales se establecerán en términos de ecuaciones diferenciales ordinarias, y la Teoría de Bifurcaciones jugará un papel fundamental.

A mediados del siglo pasado, Hodgkin y Huxley propusieron un modelo para explicar y reproducir el comportamiento neuronal. Sus estudios les hicieron merecedores del Premio Nobel de Fisiología y Medicina en 1963. El modelo de Hodgkin y Huxley es extremadamente realista, pero su estudio presenta complicaciones. Por ello, aparecieron diversos modelos simplificados. Uno de ellos fue el modelo de Hindmarsh-Rose, que desempeña el papel protagonista en este trabajo.

El modelo de Hindmarsh-Rose es un sistema tridimensional de tipo fast-slow, es decir, presenta diferentes escalas temporales; en particular, dos variables rápidas y una lenta. La evolución de la variable lenta está controlada por un pequeño parámetro de manera que, cuando se anula, la variable se detiene. Los sistemas fast-slow son habituales en muchos campos y en contextos muy diferentes. La teoría de Fenichel permite obtener información relevante, aunque parcial, sobre las órbitas, aproximando la dinámica del sistema global por la del subsistema rápido, esto es, el sistema resultante de anular el pequeño parámetro.

Una de las características más notables del modelo de Hindmarsh-Rose es su realismo. Entre otros comportamientos, es capaz de reproducir el fenómeno del bursting, una señal neuronal en la que se alternan ráfagas de potenciales de acción o spikes y períodos de reposo. El bursting es un comportamiento habitual en las neuronas, de gran importancia en la codificación de la información. Uno de los mecanismos más relevantes en relación con el bursting es la ganancia de spikes (spike-adding).

Existen diferentes tipos de spike-adding. En 1991, Terman describió dos procesos, uno de ellos continuo, que más tarde se relacionó con las soluciones de tipo canard, y



otro caótico, relacionado con una transición de patrones irregulares antes de obtener el nuevo spike. Diferentes estudios han identificado los elementos relevantes en estos procesos, incluyendo curvas de bifurcación de period-doubling y fold de ciclos límite. Eligiendo un plano paramétrico adecuado, puede observarse cómo estas curvas de bifurcación nacen de degeneraciones homoclínicas de codimensión dos: orbit flips, inclination flips y puntos de Belyakov. Por ello, la estructura de bifurcación homoclínica se considera el centro organizador de los fenómenos de bursting.

En los artículos que constituyen el corazón de esta tesis, se abordan diferentes aspectos de la dinámica del modelo de Hindmarsh-Rose. Con anterioridad, el modelo había sido estudiado en un escenario biparamétrico, pero fijando el valor del pequeño parámetro. Nosotros analizamos diagramas de bifurcación tridimensionales que revelan un intrincado esqueleto homoclínico que explica las características clave de los fenómenos de bursting. Estas características incluyen la simplificación de los mapas de bursting cuando el pequeño parámetro crece, y también buena parte de los mecanismos de spike-adding. También se incluye un trabajo adicional sobre un modelo de un cardiomiocito.

Nuestras contribuciones originales están incluidas en el Capítulo 4. El Capítulo 1 está dedicado a los modelos neuronales y el Capítulo 2 presenta los resultados de sistemas dinámicos que son esenciales para la discusión posterior. En el Capítulo 3 se discuten los antecedentes de nuestra investigación. El Capítulo 5 consiste en las conclusiones y una breve propuesta de futuras líneas de investigación.

RESUMEN (en Inglés)

Understanding the functioning of the brain is one of the great challenges in science and there are many different fields involved in that enormous task. In this scenario, interactions between Mathematics and Neuroscience are abundant and fruitful.

In this Thesis we are interested in the study of the behaviour of isolated neurons as dynamical systems. Our neuron models will be established in terms of ordinary differential equations, and Bifurcation Theory will play a fundamental role.

In the middle of the last century, Hodgkin and Huxley proposed a model to explain and reproduce neural behaviour. Their studies earned them the Nobel Prize in Physiology and Medicine in 1963. The Hodgkin and Huxley model is highly realistic, but its study presents complications. Due to this, different simplifications appeared. One of them was the Hindmarsh-Rose model, which plays the starring role in this work.



The Hindmarsh-Rose model is a three-dimensional system of fast-slow type, that is, it presents different time-scales; in particular, two fast variables and one slow variable. The evolution of the slow variable is controlled by a small parameter in such a way that, when it vanishes, this variable stops. Fast-slow systems are common in many fields and in very diverse contexts. Fenichel Theory allows the obtaining of relevant, albeit partial, information about the orbits, approximating the dynamics of the global system by that of the fast subsystem, that is, the system resulting from canceling the small parameter.

One of the most notable characteristics of the Hindmarsh-Rose model is its realism. Among other behaviours, it is capable of reproducing bursting phenomenon, a neural signal in which bursts of action potentials or spikes and resting periods alternate. Bursting is a typical behaviour of neurons, of great importance in the coding of information. One of the most relevant mechanisms in relation to bursting is the gaining of spikes (spike-adding).

There are different types of spike-adding. In 1991, Terman described two processes, one of them continuous, which was later related to canard solutions, and the other chaotic, related to a transition of irregular patterns before obtaining the extra spike. Different studies have identified relevant elements in these processes, including period-doubling and fold bifurcations of limit cycles. Considering a suitable parametric plane, it can be observed how these bifurcation curves arise from homoclinic degeneracies of codimension two: orbit flips, inclination flips and Belyakov points. Because of this, the homoclinic bifurcation structure is understood as the organizing center of bursting phenomena.

In the papers that constitute the heart of this Thesis, different aspects of the dynamics of the Hindmarsh-Rose model are addressed. Previously, the model had been studied by moving two of its parameters, but fixing the value of the small one. We analyse three-dimensional bifurcation diagrams that reveal an intricate homoclinic skeleton that explains the key characteristics of bursting phenomena. These features include the simplification of the bursting map as the small parameter increases, and also a good deal of the spike-adding mechanisms. Additional work includes a study on a cardiac myocyte cell model.

Our original contributions are included in Chapter 4. Chapter 1 presents the neuron models and Chapter 2 compiles the results of dynamical systems that are essential for further discussion. In Chapter 3 the background to our research is discussed. Chapter 5 consists of the conclusions and a brief proposal for future research.

Acknowledgements

I thank my PhD advisors, professors Roberto Barrio Gil and Santiago Ibáñez Mesa, for their help and support during these years. It has been my distinct privilege to have Santi as my instructor of several courses during my undergraduate studies. His impressive teaching and willingness to help his students lead me to pursue my doctoral studies under his supervision. I am especially thankful to him for letting me choose the topic of my final degree project, which was my introduction in the study of neuron models in the context of dynamical systems. I am also very thankful to him for having sought the support of Roberto Barrio, from the University of Zaragoza. Thanks to the guidance of Roberto I started my PhD studies in a promising subject. Roberto has always been warm and helpful, and I only have fond memories of my stays in Zaragoza. Working with both of them has been a pleasure and a fruitful experience.

To my parents, for supporting me not only through this thesis but my whole life.

Thanks to all my friends for creating a warm, math-free environment. Special mention to Carlos, who proof-read a great deal of my texts throughout these years, including this very section.

Financial support from Principado de Asturias through a Severo Ochoa research contract (Grant PA-18-PF-BP17-072) is gratefully acknowledged.

Contents

Introduction	15
1 Mathematical models in Neuroscience	17
1.1 Biological foundations	17
1.2 Hodgkin-Huxley model	23
1.3 Hindmarsh-Rose model	25
2 Essentials from dynamical systems	33
2.1 Homoclinic bifurcations	33
2.2 Classification of bursting patterns	42
3 A brief review of prior research	49
4 Contributions	61
4.1 Paper I	61
4.2 Paper II	71
4.3 Paper III	95
4.4 Paper IV (submitted)	113
4.5 Paper V	129
4.6 Poster	149
4.7 Publications' report	152
5 Conclusions and future research	153

Introduction

Understanding the functioning of the brain is one of the great challenges in science and there are many different fields involved in that enormous task. In this scenario, interactions between Mathematics and Neuroscience are abundant and fruitful.

In this Thesis we are interested in the study of the behaviour of isolated neurons as dynamical systems. Our neuron models will be established in terms of ordinary differential equations, and Bifurcation Theory will play a fundamental role.

In the middle of the last century, Hodgkin and Huxley proposed a model to explain and reproduce neural behaviour. Their studies earned them the Nobel Prize in Physiology and Medicine in 1963. The Hodgkin and Huxley model is highly realistic, but its study presents complications. Due to this, different simplifications appeared. One of them was the Hindmarsh-Rose model, which plays the starring role in this work.

The Hindmarsh-Rose model is a three-dimensional system of fast-slow type, that is, it presents different time-scales; in particular, two fast variables and one slow variable. The evolution of the slow variable is controlled by a small parameter in such a way that, when it vanishes, this variable stops. Fast-slow systems are common in many fields and in very diverse contexts. Fenichel Theory allows the obtaining of relevant, albeit partial, information about the orbits, approximating the dynamics of the global system by that of the fast subsystem, that is, the system resulting from canceling the small parameter.

One of the most notable characteristics of the Hindmarsh-Rose model is its realism. Among other behaviours, it is capable of reproducing bursting phenomenon, a neural signal in which bursts of action potentials or spikes and resting periods alternate. Bursting is a typical behaviour of neurons, of great importance in the coding of information. One of the most relevant mechanisms in relation to bursting is the gaining of spikes (spike-adding).

There are different types of spike-adding. In 1991, Terman described two processes, one of them continuous, which was later related to canard solutions, and the other chaotic, related to a transition of irregular patterns before obtaining the extra spike. Different studies have identified relevant elements in these processes, including period-doubling and fold bifurcations of limit cycles. Considering a suitable parametric plane, it can be observed how these bifurcation curves arise from homoclinic degeneracies of codimension two: orbit flips, inclination flips and Belyakov points. Because of this, the homoclinic

bifurcation structure is understood as the organizing center of bursting phenomena.

In the papers that constitute the heart of this Thesis, different aspects of the dynamics of the Hindmarsh-Rose model are addressed. Previously, the model had been studied by moving two of its parameters, but fixing the value of the small one. We analyse three-dimensional bifurcation diagrams that reveal an intricate homoclinic skeleton that explains the key characteristics of bursting phenomena. These features include the simplification of the bursting map as the small parameter increases, and also a good deal of the spike-adding mechanisms. Additional work includes a study on a cardiac myocyte cell model. Our original contributions are included in Chapter 4. Chapter 1 presents the neuron models and Chapter 2 compiles the results of dynamical systems that are essential for further discussion. In Chapter 3 the background to our research is discussed. Chapter 5 consists of the conclusions and a brief proposal for future research.

Chapter 1

Mathematical models in Neuroscience

1.1 Biological foundations

The transmission of information in the brain is possible due to the activity of neurons, their basic functional units. Understanding the biological basis of their activity permits to abstract their fundamental properties and obtain dynamical models. The development of models allows Neuroscience to have a broader perspective, considering neurons not only from a biological perspective, but also from a mathematical point of view.

We will begin by reviewing the neuronal morphology and the physiology of action potential, its basic unit of communication. This biology background can be found in [20] and [27], among many others. Next we will see how the Hodgkin-Huxley model can be derived from the previous information. The Hodgkin-Huxley model [23] is an example of a complex system with a direct biophysical interpretation which reproduces biological phenomena in a very realistic way. Lastly, we will present the derivation of the Hindmarsh-Rose model [21], [22]. The Hindmarsh-Rose model is an example of a fairly simple model that allows isolating the mathematical mechanisms responsible of certain biological behaviours. It also permits to perform a detailed analysis.

A neuron is an electrically excitable cell that can transmit signals over long distances. The human brain has approximately 100 billion neurons and a significantly bigger amount of neuroglia, the cells that support and protect the neurons.

Morphology

The anatomy of neurons changes depending on the type they belong to, but typically they have three parts: the body or soma, the dendrites and the axon. The soma is the metabolic center of the neuron and contains its genetic material. It also synthesises the

majority of the proteins that the neurons need to produce. Different protusions extend from the soma: the axon and the dendrites. The axon is a long, thin prolongation that propagates electric signals (known as action potentials or spikes) towards other neurons. The dendrites are shorter, branching extensions that receive signals from other neurons. In Figure 1.1 the basic scheme of a neuron is shown.

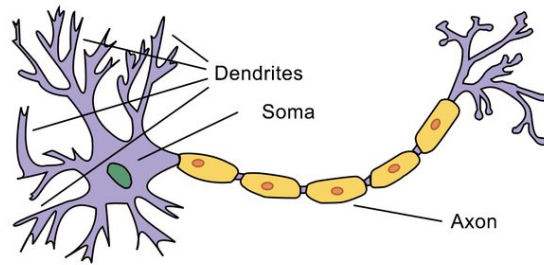


Figure 1.1: Schematic view of a neuron. Reproduced from [35].

Brief review of electricity

Due to the importance of electrical activity in neuronal communications, we must review some basic concepts related to electrical phenomena. Electrical phenomena occur when charges of opposite signs separate or can move independently. Electric *charge* is defined as the property of matter that causes it to experiment a force when kept in an electromagnetic field. It is measured in coulombs and represented by q . Any net flow of charges is a *current*. It is measured in amperes and represented by I . The amount of the flow of charges between two points is determined by the potential difference between the points and the conductance of the environment. The *potential difference* is represented by V and is measured in volts, being one volt the work required to move a charge of one coulomb without resistance from one point to other. *Conductance*, represented by G , is measured in siemens and measures the ease with which the electric current moves from one point to another in a certain medium. The reciprocal of the conductance is the *resistance*, which is measured in ohms and represented by R . *Capacitance*, represented by C , is the ratio of electric charge accumulated on a conductor to a difference in electric potential ($C = q/V$) and it is measured in farads. Later we will use these concepts to describe changes in the neuronal membrane and for the formulation of models.

Neural membrane and ion channels

Membranes enclose the body of neurons and consist of a bilayer of lipid molecules (which is an electrical insulator) with different types of protein structures embedded in it, including

ion channels. Figure 1.2 provides a schematic representation. Ion channels are proteins that allow the flow of specific ions across the membrane. Ion channels are often regulated, that is, whether they are open or closed depends on the stimuli they receive. They can have activation and inactivation gates or only the first type. Activation gates open the channels, and inactivation gates block them. There are also non-regulated channels, which are continuously open, like the *leak* channels, which are crossed mainly by chloride ions, Cl^- . Membrane is permeable to a great variety of ions, sodium ion (Na^+) and potassium ion (K^+) being the most relevant. Both sodium and potassium channels are voltage-dependent.

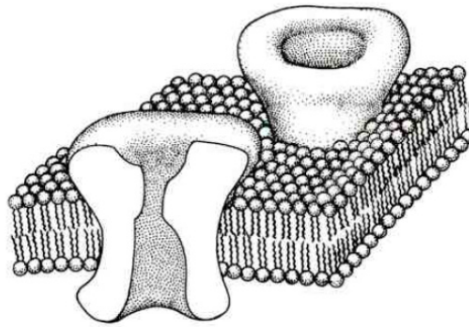


Figure 1.2: Schematic view of the membrane on a neuron. Obtained from [20]

Membrane potential

In resting state, neurons have a relative excess of positive charges in the outside (thus a relative excess of negative charge in the inside). This situation gives rise to an electrical potential difference, known as membrane potential. Specifically, the membrane potential V_m is defined as

$$V_m = V_{int} - V_{ext}$$

V_{int} being the potential inside the cell and V_{ext} the potential outside. The potential across the membrane when the neuron is in resting state (not producing signals) is known as the resting potential. By convention the potential outside the neuron is defined as 0. As a result, the resting potential takes negative values, ranging from -70 to -60 mV. The charge separation across the membrane is maintained due to passive transport and active transport. Passive transport does not require energy, and it takes place as a result of concentration gradients. Active transport requires the cell to expend energy to move a substance against its concentration gradient. An example of active transport is the

sodium–potassium pump, which uses energy to move sodium and potassium ions against their gradient.

Nernst potential

There are two forces that drive each diffusible ionic species through the membrane: concentration (chemical) gradient and electric potential gradient. Concentration of ionic species tends to balance, thus ions of a certain type leave the cell if their outer concentration is less than the inner concentration. When ions leave the cell, they carry their charge to the outside. The positive and negative charges accumulate outside and inside the membrane, respectively. This creates an electric potential gradient across the cell membrane, which reduces the flow of the ionic species. Eventually, there is a balance of the two forces (chemical and electrical) and the net cross-membrane current is null. The value of the potential for which this equilibrium is reached is known as Nernst potential, and is given by the Nernst equation:

$$E_{ion} = \frac{RT}{zF} \ln \frac{[Ion]_{ext}}{[Ion]_{int}} \quad (\text{volts})$$

where $[Ion]_{int}$ is the concentration of the ionic species inside the cell and $[Ion]_{ext}$ is the ionic concentration outside the cell; R is the universal gas constant ($8315 \text{ mJ}/(K \cdot \text{Mol})$); T is the temperature measured in Kelvin; F is the Faraday constant ($96480 \text{ coulombs}/\text{Mol}$); z is the charge of the ion (for example, $z = -1$ for Cl^- and $z = 2$ for Ca^{2+}).

Action potential

Every time there is a net flow of ions through the cell membrane the polarization changes. An increase of the polarization is known as hyperpolarization, while a reduction is known as depolarization. Typically, hyperpolarization does not cause voltage-dependent ion channels to open. On the other hand, depolarization may lead to their opening if the intensity is appropriate, inducing an abrupt change in the membrane voltage. Namely, there is a rapid rise and fall of the membrane potential. This phenomenon is known as action potential or spike and is represented in Figure 1.3. Spikes are often referred to all-or-none responses: either there is a full response or there is no response at all.

Spikes are the basic units in neural communication, since more complex behaviours can be explained from them. There is a plethora of electrical phenomena regarding neural communication, but the following behaviours are specially relevant:

- Quiescence: where the neuron does not produce a response and the membrane potential remains constant.
- Spiking: continuous repetition of spikes.

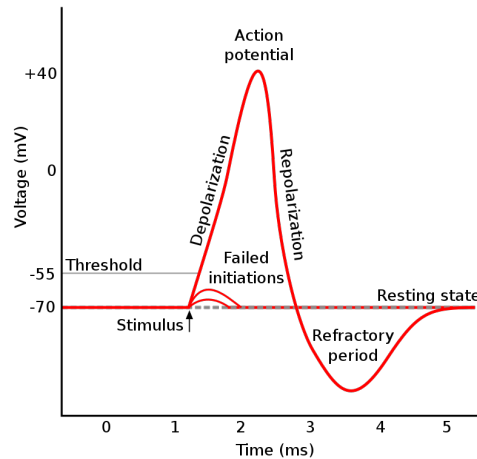


Figure 1.3: Representation of the action potential and its phases. Reproduced from [29].

- **Bursting:** alternation between a silent phase (quiescence) and an active phase (spiking). Bursting can be regular or irregular (chaotic). It is possible for a neuron to respond to a certain stimulus with a single train of spikes. This train of spikes is called a burst.

Sodium and potassium voltage-dependent channels

Sodium and potassium voltage-dependent channels present similarities and differences. A greater depolarization increases their probability of opening, as well as the speed with which they open. On the other hand, they differ in their velocity and in their response to a long-lasting depolarization. When there is a depolarization, sodium channels open faster than potassium channels. Sodium channels present activation and inactivation gates, while potassium channels only have activation gates. When a prolonged depolarization occurs, the inactivation gates of sodium channels cause the flow of sodium ions through the channel to stop. This is not the case for potassium channels, which continue to allow ionic flow when the depolarization is prolonged. Inactivation is only reversed with hyperpolarization, and requires a certain amount of time to take place.

Phases of the action potential

When the neuron receives an appropriate stimulus, the sodium channels of the cell membrane open first, causing an increase in sodium intracellular concentration. The membrane potential grows, reaching high, positive values (close to E_{Na}). After that, potassium channels open (they respond slower than their sodium counterparts) and, at a certain point,

sodium channels inactivate (making the occurrence of another action potential impossible for a period of time, known as absolute refractory period). Potassium channels stay open, so, consequently, the permeability of the membrane to potassium is much higher than to sodium. The membrane potential decreases, reaching negative values close to E_K . Sodium channels go from inactivated to closed, while potassium channels stay open. Membrane potential is still hyperpolarized. Lastly, membrane potential takes resting values and potassium channels close. At this point a new spike may occur, but ion channels would need a bigger stimulus to open. This period of time is known as relative refractory period.

Equivalent circuit

An useful and common way to describe the activity of the membrane potential is with an electrical analogue, considering an equivalent circuit that models the main features of the membrane behaviour.

As already mentioned, the cell membrane consist of a phospholipid bilayer with certain proteins (ion channels) that may let different ionic species to cross the membrane. The phospholipid bilayer does not allow the pass of ionic currents, and, thus, we have a thin conductor (the membrane) separating two electrolytic media (the cytoplasm and the exterior space). Therefore, the cell membrane acts like a capacitor in an electric circuit. When a generator is connected to a battery in an electrical circuit, a movement of charges from the positive end of the battery to one of the capacitor plates appears, causing positive charges to shift from the other side by magnetism. This movement of charges is known as capacitive current I_c associated with the capacitor.

The membrane permeability depends on the number of open channels. Therefore, ion channels act like conductors in an electrical circuit. There exist concentration gradients across the membrane, maintained by biological mechanisms like the sodium-potassium pump. The fact that ion channels are embedded in concentration gradients makes them act like conductors connected in series with a battery of voltage equal to the Nernst potential of the corresponding ion. Figure 1.4 shows the equivalent circuit of the neuron considering chloride, sodium and potassium ion channels. The current associated to each ion channel is represented by I_{ion} . Chloride channels were included since they were considered in the Hodgkin and Huxley model, which we will present in the next section. An external injected I_{ext} current is also considered. This external current can represent a current artificially injected in an *in vitro* experiment, or it could be a current received from other neuron.

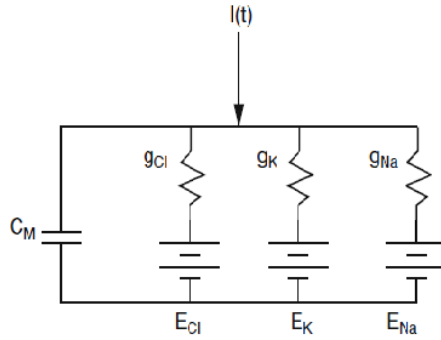


Figure 1.4: Equivalent circuit of the activity of the membrane potential. Obtained from [23].

1.2 Hodgkin-Huxley model

Neuroscience is heavily influenced by the Hodgkin and Huxley model, one of the most successful models regarding complex biological phenomena. In the mid twentieth century, Hodgkin and Huxley investigated the functioning of ionic currents during the generation of action potentials. They used the voltage-clamp technique for studying the spike-generation mechanisms in the squid *Loligo*, which has axons of giant size (1mm) compared to other species. They published their results in a series of five papers, the latter one presenting the model named after them [23]. In 1963, Hodgkin and Huxley received the Nobel prize because of their investigation in the subject.

Modeling activity of the neuron membrane as the equivalent electric circuit shown in the previous section allows the application of different physics laws to provide a mathematical description.

According to Kirchoff's first law, the sum of currents in a network of conductors meeting at a point is equal to zero. Equivalently,

$$I_c + \sum I_{ion} = I_{ext}.$$

Hodgkin and Huxley considered potassium (K^+) and sodium (Na^+) ion channels, as well as *leak* channels, which are permanently open and allow mainly chloride ions to pass through the membrane. We refer to the current passing through leak channels as I_L . Hence, we have

$$I_c + I_K + I_{Na} + I_L = I_{ext}.$$

Recall that $V = \frac{q}{C}$, C being the capacitance (in our case, the membrane capacitance). On the other hand, the current is the rate at which electric charge flows through a point on the electric circuit, thus $\dot{q} = I_c$. This allow us to write the capacitive current I_c as $C\dot{V}$.

Regarding ionic currents, we have the relationship $I_{ion} = g_{ion} \cdot (V - E_{ion})$, being g_{ion} the conductance for the corresponding ion channel. The term $V - E_{ion}$ is known as *driving force*. It is important to recall that, while leak channels are not voltage-dependent, both sodium and potassium channels are, so their conductances are not constant but functions of V . The approximation of these functions is necessary in order to develop the model. Some relevant considerations regarding the conductances $g_{ion}(V)$ are the following. First, it is possible to measure the maximum conductance \hat{g}_{ion} for a given ionic species. Moreover, we have that $0 \leq g_{ion} \leq \hat{g}_{ion}$, so we can think of g_{ion} as the product $\hat{g}_{ion}p_{ion}$, being $p_{ion} = p_{ion}(V)$ the probability of the corresponding channel being open. Lastly, we should recall that potassium channels have activation gates, that determine whether potassium ion can cross the membrane or not; sodium channels have activation and inactivation gates, and both of them must be in permissive position to let sodium ions cross the membrane. Hence, $p_K = n^a$, where n is the probability of potassium activation gates being open at a certain membrane voltage and a the number of activation gates per channel; $p_{Na} = m^b \cdot h^c$, where m is the probability of sodium activation gates being open at a certain voltage value, b the number of activation gates per channel, h the probability of sodium inactivation gates being in permissive position at a certain membrane voltage value and c the number of inactivation gates per channel. Hodgkin and Huxley experiments conclude that $a = 4, b = 3$ and $c = 1$. Thus, we have

$$\begin{aligned} I_K &= \hat{g}_K n^4 (V - E_K) \\ I_{Na} &= \hat{g}_{Na} m^3 h (V - E_{Na}) \end{aligned}$$

and we can write the equation corresponding to the evolution of membrane voltage as

$$C\dot{V} = I_{ext} - \underbrace{\hat{g}_K n^4 (V - E_K)}_{I_K} - \underbrace{\hat{g}_{Na} m^3 h (V - E_{Na})}_{I_{Na}} - \underbrace{g_L (V - E_L)}_{I_L}$$

The dynamics of the different activation and inactivation gates can be described in the following way. Consider the proportion m of open activation gates for sodium. Thus, $1 - m$ is the proportion of closed gates. Let $\alpha_m(V)$ and $\beta_m(V)$ be the voltage-dependent rate constants at which sodium activation gates go from closed state to open state and vice versa. Then,

$$\dot{m} = \alpha_m(V)(1 - m) - \beta_m(V)m$$

Following the same reasoning,

$$\begin{aligned} \dot{n} &= \alpha_n(V)(1 - n) - \beta_n(V)n \\ \dot{h} &= \alpha_h(V)(1 - h) - \beta_h(V)h \end{aligned}$$

The functions $\alpha_*(V)$ and $\beta_*(V)$, where $*$ $\in \{n, m, h\}$, have been obtained experimentally and are related to equations that describe the movement of a charged particle in an electric

field. The interested reader can find them in [23]. It is common to define

$$*_{\infty}(V) = \frac{\alpha_*(V)}{\alpha_*(V) + \beta_*(V)}, \quad \tau_*(V) = \frac{1}{\alpha_*(V) + \beta_*(V)}$$

The functions $*_{\infty}, \tau_*$ (with $* \in \{n, m, h\}$) can be approximated by Boltzmann and Gaussian functions. They are depicted in Figure 1.5.

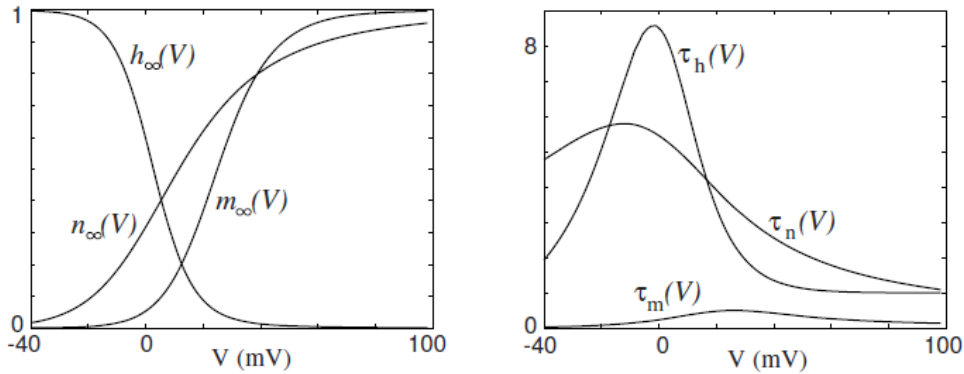


Figure 1.5: Auxiliary functions of the Hodgkin-Huxley model. Reproduced from [27].

Finally, we obtain the Hodgkin-Huxley model:

$$\begin{cases} C\dot{V} &= I_{ext} - \hat{g}_K n^4 (V - E_K) - \hat{g}_{Na} m^3 h (V - E_{Na}) - g_L (V - E_L) \\ \dot{n} &= (n_{\infty}(V) - n) / \tau_n(V) \\ \dot{m} &= (m_{\infty}(V) - m) / \tau_m(V) \\ \dot{h} &= (h_{\infty}(V) - h) / \tau_h(V) \end{cases}$$

1.3 Hindmarsh-Rose model

1.3.1 The Hindmarsh-Rose model of 1982

In 1979 Hindmarsh and Rose began a collaboration with the goal of finding a model for the study of the synchronization between the activity of two snail neurons, leading to their 1982 model [21]. When dealing with couplings, one tries to consider equations for single neurons as simple as possible to make numerical simulations more efficient. Therefore the Hodgkin-Huxley model was not a nice option. However, this is not the only advantage of simple models, since they allow to discover the minimal dynamical ingredients which

are required to reproduce a given phenomenon. Their choice was to consider a system of equations of the form

$$\begin{cases} \dot{x} = a(y - f(x) + I(t)) \\ \dot{y} = b(g(x) - y) \end{cases} \quad (1.1)$$

where x represents the membrane potential, y represents a recovery variable, $I(t)$ is the applied current at time t , either external or coupling, and the constants a and b are time rates.

This formalism had been previously used by FitzHugh, who studied the Hodgkin and Huxley model and proposed a simplification known as FitzHugh-Nagumo model [17] (Nagumo independently proposed an electric circuit model [38], whose dynamics is equivalent to that of the FitzHugh's equations). In the FitzHugh-Nagumo model the function f is cubic and the function g is linear, but the model does not achieve a very realistic description of the action potential. Namely, the model does not predict the relative long interval of quiescence compared with the firing duration and the frequency-current relationship is not adequate.

To avoid this shortcoming, Hindmarsh and Rose used the voltage clamp technique to determine the appropriate form of the functions f and g . The voltage clamp is a classic method developed in the middle of the last century to measure ion currents across the membrane of nerve cells, fixing the value of the membrane potential.

The process employed to deduce the model was the following. It was assumed that the model was governed by equations (1.1). The voltage was clamped to an initial potential x_i , thus $y(t)$ shifts to $g(x_i)$, its equilibrium value. After that, the cell was clamped to a new potential x_c . The time at which this new clamp occurs will be considered time $t = 0$ in the sequel. The applied current $I(t)$ with $t \geq 0$ is given by

$$I_{x_c}(t) = f(x_c) - y(t)$$

from equations (1.1) with $\dot{x} = 0$ (since the voltage is clamped). The function $y(t)$ satisfies the differential equation

$$\begin{cases} \dot{y} = b(g(x_c) - y) \\ y(0) = g(x_i). \end{cases}$$

It is easy to check that

$$y(t) = g(x_c) - (g(x_c) - g(x_i))e^{-bt}$$

and thus

$$I_{x_c}(t) = f(x_c) - g(x_c) + (g(x_c) - g(x_i))e^{-bt}.$$

A rescaling was done so $x_i = 0$ and it was assumed that the origin $(0, 0)$ is an equilibrium point of the system when $I = 0$. In particular, $f(0) = 0, g(0) = 0$. With these considerations

$$y(t) = g(x_c)(1 - e^{-bt})$$

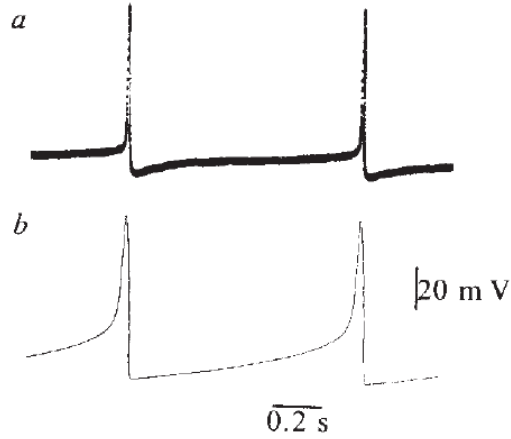


Figure 1.6: Activity produced by a biological neuron (a) and the Hindmarsh-Rose model of 1982 with parameters $a = 5.4$, $b = 30$, $c = 0.00017$, $d = 0.001$, $e = 0.01$, $h = 0.1$, $q = 0.024$, $r = 0.088$, $s = 0.046$. The applied current is set as a constant $I = 0.008$. Extracted from [21].

and

$$I_{x_c}(t) = f(x_c) - g(x_c)(1 - e^{-bt})$$

In particular, the initial and steady-state values of the clamping current are

$$I_{x_c}(0) = f(x_c), \quad I_{x_c}(\infty) = f(x_c) - g(x_c).$$

For each value of x_c a value of $I_{x_c}(0)$ and a value of $I_{x_c}(\infty)$ are obtained. The pairs $(x_c, I_{x_c}(0))$ give rise to a curve that can be approximated by a cubic function. On the other hand, the curve formed by the pairs $(x_c, I_{x_c}(\infty))$ can be approximated by an exponential function. With this substitutions, the model became

$$\begin{cases} \dot{x} = -a(cx^3 + dx^2 + ex + h - y - I) \\ \dot{y} = b(cx^3 + dx^2 + ex + h - qe^{rx} - y). \end{cases} \quad (1.2)$$

Figure 1.6 shows a comparison between an actual action potential and an action potential predicted with the model with the following parameters values: $a = 5.4$, $b = 30$, $c = 0.00017$, $d = 0.001$, $e = 0.01$, $h = 0.1$, $q = 0.024$, $r = 0.088$, $s = 0.046$. The applied current is set as a constant $I = 0.008$. It is apparent that the model gives a realistic relationship between the duration of the spike and the duration of the quiescence period.

The phase portrait provides a mathematical explanation of this phenomenon. In Figure 1.7 we can see the nullclines of the system ($\dot{x} = 0$, $\dot{y} = 0$), as well as a limit cycle corresponding to periodic spiking. Three points of the limit cycle are marked: A , B , and

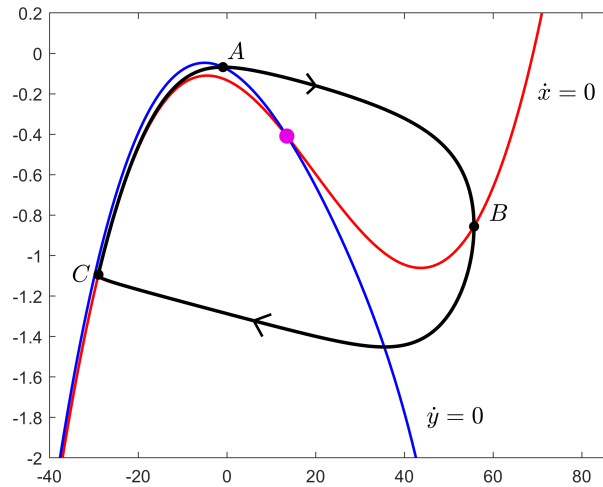


Figure 1.7: Limit cycle of the Hindmarsh-Rose of 1982 superimposed with the nullclines of the system. The values of the parameters are the same as in Figure 1.6 except I , which is set at 0.033. The nullcline $\dot{x} = 0$ ($\dot{y} = 0$) is represented in red (blue). The limit cycle is depicted in black, and the equilibrium of the system is shown in purple. Point B (C) is the point at which the variable x has the highest (lowest) value. Point A has been selected so the fragment of the limit cycle going from C to A is constrained in the narrow channel formed by the nullclines.

C . Point B (C) is the point at which the variable x has the highest (lowest) value. Point A has been selected so the fragment of the limit cycle going from C to A is constrained in the narrow channel formed by the nullclines.

Because of the values of variable x , the limit cycle is split between an action potential phase (when it travels from point A to C , passing through B) and a resting phase (when it travels from C to A). Because the closeness to both nullclines, the orbit moves slowly during the resting phase, giving rise to the long interval of quiescence (see Figure 1.6). This phenomenon is known as *narrow channel property*. In Figure 1.8, the solution corresponding to the limit cycle of Figure 1.7 is represented in (t, x) . The points corresponding to A , B and C in the limit cycle are labeled, to make the relationship between the different phases of the action potential and the phase portrait of the orbit more clear.

1.3.2 Hindmarsh-Rose model of 1984

Shortly after the publication of their 1982 model, Hindmarsh and Rose proposed a modification to mimic and explain certain physiological behaviours [22]. Namely, it was discovered that a cell in the brain of the pond snail *Lymnaea* jumped from silent to bursting

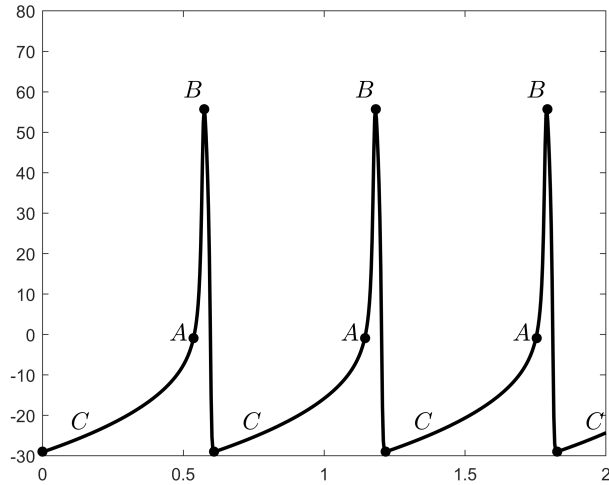


Figure 1.8: Representation in (t, x) of the solution corresponding to the limit cycle of Figure 1.7. The points (t, x) corresponding to the points A , B and C of the limit cycle are indicated.

when it received a short depolarizing stimulus. Similar responses had been observed in other molluscan burst cells. The transition from a silent state to a repetitive firing corresponds dynamically to a phase point traveling from an stable equilibrium point to a stable limit cycle. From Poincaré-Bendixson Theorem it is known that at least an additional equilibrium point must exist inside the stable limit cycle. In the simplest case (only one equilibrium point surrounded by the stable limit cycle), this equilibrium should be an unstable spiral. In addition, a third equilibrium point is required to provide a stable manifold separating the basins of attraction.

Hindmarsh and Rose observed that a small change in the nullclines could create the required additional equilibrium points, since they were already very close to each other in the recovery side of the phase plane. It is easy to observe that choosing one nullcline to be cubic and the other one to be parabolic could lead to an appropriate deformation, so Hindmarsh and Rose proposed the following equations.:

$$\begin{cases} \dot{x} = y - ax^3 - bx^2 + I \\ \dot{y} = c - dx^2 - y \end{cases} \quad (1.3)$$

A typical choice of the parameters to get three equilibrium points is $a = 1, b = 3, c = 1, d = 5$. Figure 1.9 shows a limit cycle and the nullclines of the system 1.3 for $I = 0$. The nullcline $\dot{x} = 0$ ($\dot{y} = 0$) is depicted in red (blue). The limit cycle is represented in black, and the three equilibria are marked in purple. Point B (C) is the point at which the variable x has the highest (lowest) value. Point A has been selected so the fragment of

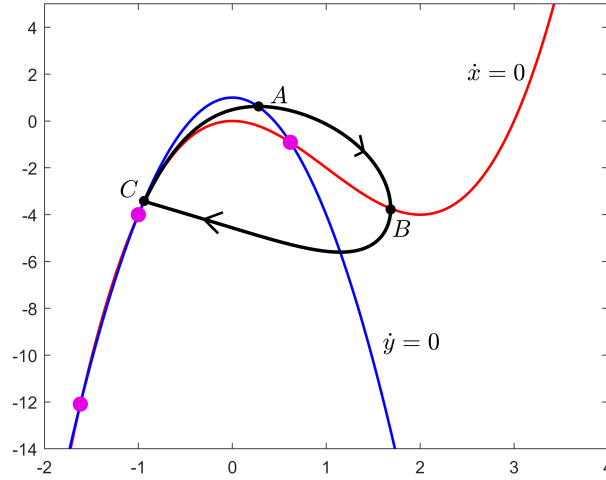


Figure 1.9: Nullclines of the system 1.3 superimposed with a limit cycle. The nullcline $\dot{x} = 0$ ($\dot{y} = 0$) is represented in red (blue). The limit cycle is depicted in black, and the equilibria are shown in purple. Point B (C) is the point at which the variable x has the highest (lowest) value. Point A has been selected so the fragment of the limit cycle going from C to A is constrained between both nullclines.

the limit cycle going from C to A is constrained between the nullclines. As in the model of 1982, when the limit cycle travels from A to C , the system mimics the active phase of the action potential, and when it travels from C to A , the system exhibits a resting period. In Figure 1.10 we show the corresponding solution in (t, x) coordinates, labeling the points A , B and C associated with their analogues in the limit cycle.

This new system allows the coexistence of an attracting equilibrium point and an attracting limit cycle, but in order to terminate the firing phase (corresponding to the phase point moving along the stable limit cycle) a third variable is required. This new variable, z , mimics the effect of a slow current that adjusts the applied current I to a factual applied current $I - z$. The parameter ε takes positive values very close to 0. As the variable z increases, the effective applied current $I - z$ lowers its value, forcing the system to terminate the firing. The equation for z was chosen to be:

$$\dot{z} = \varepsilon(s(x - x_1) - z)$$

where x_1 is the x -coordinate of the attractor equilibrium point for the planar system 1.3. In conclusion, the model became

$$\begin{cases} \dot{x} = y - ax^3 - bx^2 + I - z \\ \dot{y} = c - dx^2 - y \\ \dot{z} = \varepsilon(s(x - x_1) - z) \end{cases} \quad (1.4)$$

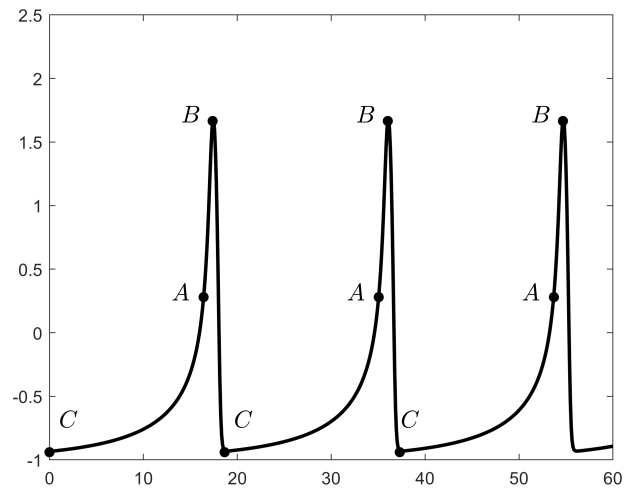


Figure 1.10: Representation in (t, x) of the solution corresponding to the limit cycle of Figure 1.9. The points (t, x) associated with A , B and C are labeled.

The different time scales of the variables play an important role in the behaviour of the system. Loosely speaking, as long as ε is small enough we can think the slow variable z as a parameter of the planar system 1.3; in other words, the dynamics of the full system can be partially understood by looking the dynamics of the *frozen* system with $\varepsilon = 0$. A formalization of this idea will be given in Section 2.2.

Chapter 2

Essentials from dynamical systems

Bifurcation theory plays a key role when studying how a model behaves when parameters change. We will assume the reader is familiar with the basics of this topic, such as the concepts of topological equivalence or codimension, and also that saddle-node, period-doubling and Hopf bifurcations are known. This material is covered in [31], among many others.

Our investigation is strongly related to homoclinic bifurcations and some of their degeneracies (orbit flips, inclination flips and Belyakov points). In Section 2.1 we review the aspects of the topic that are relevant to our work. Our main references are [25] and [31].

In Section 2.2 we present the classification of bursting patterns proposed by Izhikevich [27], which relies heavily on Bifurcation theory and Fenichel theory [15]. We review the patterns that can be found in the Hindmarsh-Rose model, namely fold/homoclinic and fold/Hopf bursting.

2.1 Homoclinic bifurcations

We will consider a smooth family of vector fields

$$x' = f_\mu(x) \tag{2.1}$$

with $x \in \mathbb{R}^n$ and $\mu \in \mathbb{R}^k$. Denote by φ^t the corresponding flow and assume x_0 is an equilibrium of the system. We recall the following

Definition 2.1.1. *An orbit Γ_0 starting at a point $x \in \mathbb{R}^n$ is said to be homoclinic to x_0 if $\varphi^t x \rightarrow x_0$ as $t \rightarrow \pm\infty$.*

In Figure 2.1 (2.2) a homoclinic orbit in a two-dimensional (three-dimensional) system is shown.

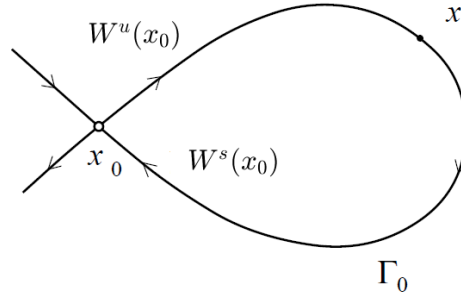


Figure 2.1: An example of a homoclinic orbit in the plane. Modified from [31].

Remark. *It is clear that $\Gamma_0 \subset W^s(x_0) \cap W^u(x_0)$, where $W^s(x_0)$ and $W^u(x_0)$ denote the stable and unstable manifolds at x_0 , respectively.*

Homoclinic orbits are not structurally stable. Generically, the existence of a homoclinic orbit is a codimension-one phenomenon, that is, generic for one-parameter families. In the sequel, we will consider a smooth family of vector fields f_μ on \mathbb{R}^n with $\mu \in \mathbb{R}^k$ and assume that there exist $\mu_0 \in \mathbb{R}^k$ and $p_0 \in \mathbb{R}^n$ such that p_0 is a hyperbolic equilibrium point of saddle type of f_{μ_0} . Without loss of generality we can assume that $\mu_0 = 0$ and $p_0 = 0$. We will denote by p_μ the saddle hyperbolic equilibrium that persists close to 0 for μ small enough. Let ν_1, \dots, ν_n be the eigenvalues of $Df_0(0)$ ordered by increasing real part:

$$\operatorname{Re}(\nu_1) \leq \operatorname{Re}(\nu_2) \leq \dots \operatorname{Re}(\nu_k) < 0 < \operatorname{Re}(\nu_{k+1}) \leq \dots \operatorname{Re}(\nu_n)$$

Following [25], we introduce the following notions:

Definition 2.1.2. *The eigenvalues with positive (resp. negative) real part that are closest to the imaginary axis are called the unstable (resp. stable) leading eigenvalues, and their corresponding eigenspaces are called the unstable (resp. stable) leading eigenspaces.*

Definition 2.1.3. *The saddle quantity σ of a hyperbolic equilibrium is the sum of the real parts of its leading stable and unstable eigenvalues:*

$$\sigma = \operatorname{Re}(\nu_k) + \operatorname{Re}(\nu_{k+1})$$

As we will see, the saddle quantity plays an important role regarding the dynamics that can appear when perturbing a system with a homoclinic orbit. We will present first the Andronov-Leontovich theorem, which addresses the planar case. Next we will review the three-dimensional case.

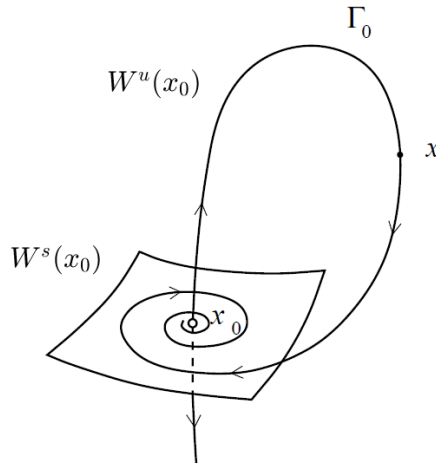


Figure 2.2: An example of a homoclinic orbit in the three-dimensional space. Modified from [31].

2.1.1 Planar case: Andronov-Leontovich theorem

Assume $n = 2$ and $k = 1$ for the smooth family of vector fields f_μ on \mathbb{R}^n with $\mu \in \mathbb{R}^k$ we are considering. For $\mu = 0$ there is a hyperbolic saddle at 0 with associated eigenvalues λ_s and λ_u with $\lambda_s < 0 < \lambda_u$, and Γ_0 is a homoclinic orbit to 0. The so-called saddle quantity is given by $\sigma = \lambda_u + \lambda_s$. For $|\mu|$ small enough, we can consider a cross section Σ at a point in Γ_0 and define the signed distance $\Delta(\mu)$ between the points $W^s(p_\mu) \cap \Sigma$ and $W^u(p_\mu) \cap \Sigma$. The following theorem describes the possible generic dynamics that can be found near a homoclinic orbit.

Theorem 1. *Suppose $\sigma \neq 0$ and $\Delta'(0) \neq 0$. Then, all systems with $\sigma < 0$ (resp. $\sigma > 0$) have topologically equivalent bifurcation diagrams in a neighborhood U_0 of $\Gamma_0 \cup 0$ for $|\mu|$ small enough as presented in Figure 2.3 (resp. Figure 2.4).*

When $\mu = 0$ the system possesses a homoclinic orbit connecting the equilibrium at the origin to itself. For $|\mu|$ small enough, a saddle equilibrium point exists close to the origin for the system $x' = f_\mu(x)$, while the homoclinic orbit no longer exists, since it splits up or down. Since we have assumed $\Delta'(\mu) \neq 0$, the distance function $\Delta(\mu)$ can be seen as a parameter. If the saddle quantity is negative ($\sigma_0 < 0$), then the homoclinic orbit that exists for $\mu = 0$ is *attracting from the inside*, and a unique and stable limit cycle $L_\mu \subset U_0$ exists for $\mu > 0$. For $\mu < 0$ there are no periodic orbits in U_0 . If the saddle quantity is positive ($\sigma > 0$), then the homoclinic orbit Γ_0 that the system possesses for $\mu = 0$ is *repelling from the inside*, and a unique and repelling limit cycle $L_\mu \subset U_0$ exists for $\mu < 0$. For $\mu > 0$ there are no periodic orbits in U_0 .

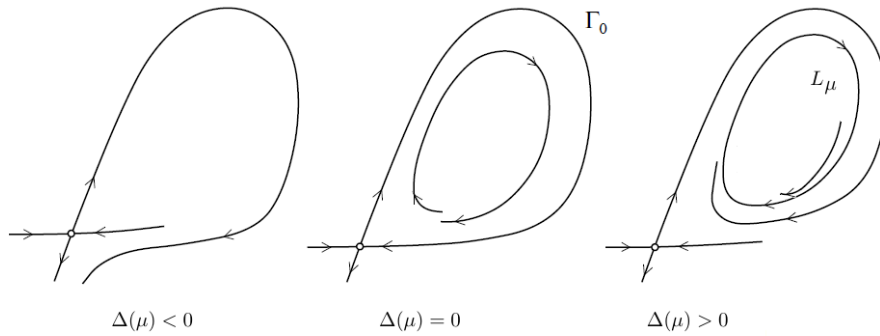


Figure 2.3: Homoclinic bifurcation in the planar case with $\sigma < 0$. Modified from [31].

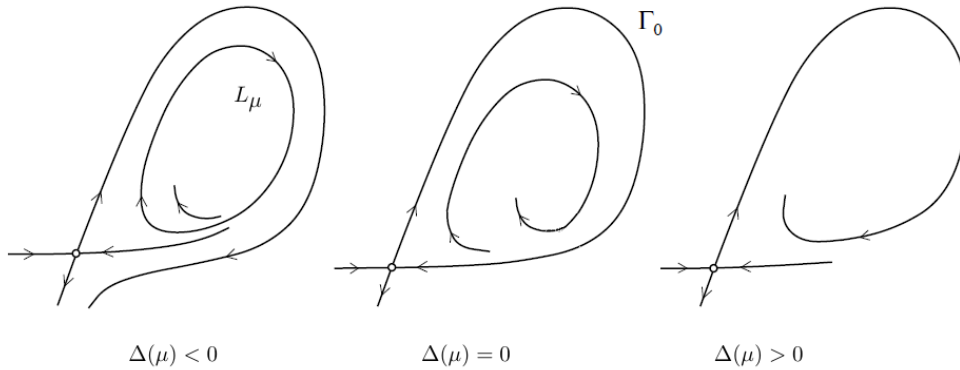


Figure 2.4: Homoclinic bifurcation in the planar case with $\sigma > 0$. Modified from [31].

2.1.2 Three-dimensional case

We assume that $x \in \mathbb{R}^3$ and $\mu \in \mathbb{R}$ in (2.1). Again, without loss of generality we can assume that $\mu_0 = 0$ and $p_0 = 0$. Up to time reversal, we suppose that $\dim(W^s(0)) = 1$ (and thus $\dim(W^u(0)) = 2$), since it is the case found in the Hindmarsh-Rose model.

As in the planar case, we can consider a cross section Σ at a point in Γ_0 and define the signed distance $\Delta(\mu)$ between the point $W^s(p_\mu) \cap \Sigma$ and the curve $W^u(p_\mu) \cap \Sigma$. We assume that $\Delta'(\mu) \neq 0$.

Before presenting the possible codimension-one homoclinic orbits, we must introduce the notions of strong unstable manifold and center stable manifold for the case of real eigenvalues. Assume that $Df_0(0)$ has real eigenvalues λ_s , λ_u and λ_{uu} with $\lambda_s < 0 < \lambda_u <$

λ_{uu} . The strong unstable manifold $W^{uu}(0)$ is a one-dimensional invariant manifold whose tangent space at 0 is given by the eigenspace corresponding to the eigenvalue λ_{uu} (the so called strong unstable direction). It is common to use a double arrow to represent it. On the other hand, the center stable manifold $W^{cs}(0)$ is a two-dimensional invariant manifold whose tangent space at 0 is given by the eigenspace corresponding to the eigenvalues λ_u and λ_s .

There exist four classes of codimension-one homoclinic orbits.

Case 1 Eigenvalues of $Df_0(0)$ are λ_s , λ_u and λ_{uu} , with $\lambda_s < 0 < \lambda_u < \lambda_{uu}$ and $\sigma_0 = \lambda_s + \lambda_u > 0$.

Case 2 Eigenvalues of $Df_0(0)$ are λ_s , λ_u and λ_{uu} , with $\lambda_s < 0 < \lambda_u < \lambda_{uu}$ and $\sigma_0 = \lambda_s + \lambda_u < 0$. Moreover,

(H1) $\Gamma_0 \not\subset W^{uu}(0)$.

(H2) $W^{cs}(0)$ intersects $W^u(0)$ transversally along Γ_0 .

Case 3 Eigenvalues of $Df_0(0)$ are $\lambda_s < 0$ and $\rho_u \pm \omega_u i$, with $\rho_u > 0$, $\omega_u \neq 0$ and $\sigma_0 = \lambda_s + \rho_u > 0$.

Case 4 Eigenvalues of $Df_0(0)$ are $\lambda_s < 0$ and $\rho_u \pm \omega_u i$, with $\rho_u > 0$, $\omega_u \neq 0$ and $\sigma_0 = \lambda_s + \rho_u < 0$.

Conditions $\lambda_s + \lambda_u \neq 0$ and $\lambda_s + \rho_u \neq 0$ are non-resonance hypotheses. Condition (H1) implies that Γ_0 is tangent to the weak unstable direction, that is, the direction given by the eigenspace associated with the leading unstable eigenvalue λ_u . Condition (H2) is a “non-inclination” property.

In **Case 1** and **Case 3**, a single unstable (repelling) periodic orbit is born from the homoclinic connection for parameter values on one side of the $\mu = 0$. In **Case 2**, a saddle periodic orbit emerges from the homoclinic orbit. Its stable manifold is orientable or not, depending on the orientability of $W^u(0)$. In **Case 4**, there exist infinitely many saddle type periodic orbits in any neighbourhood of the homoclinic orbit. In fact, as argued in Ref. [45], there exist infinitely many horseshoes in any neighbourhood of the homoclinic orbit Γ_0 . When the connection is destroyed, finitely many of the horseshoes persist and an infinite number of periodic solutions exist. The appearance or disappearance of horseshoes is accompanied by unfoldings of homoclinic tangencies of saddle type periodic orbits and hence, strange repellers should emerge [13], [14], [34]. More comprehensive explanations about these bifurcation results can be found in Refs [25] and [42].

The bifurcations described in the previous paragraph are all of codimension one. Besides this, because they play a key role in the study of the Hindmarsh-Rose model, we are interested in some codimension two homoclinic bifurcations. In the sequel, we consider a parameter space of dimension k : $\mu \in \mathbb{R}^k$, with $k > 1$ and we assume that the family

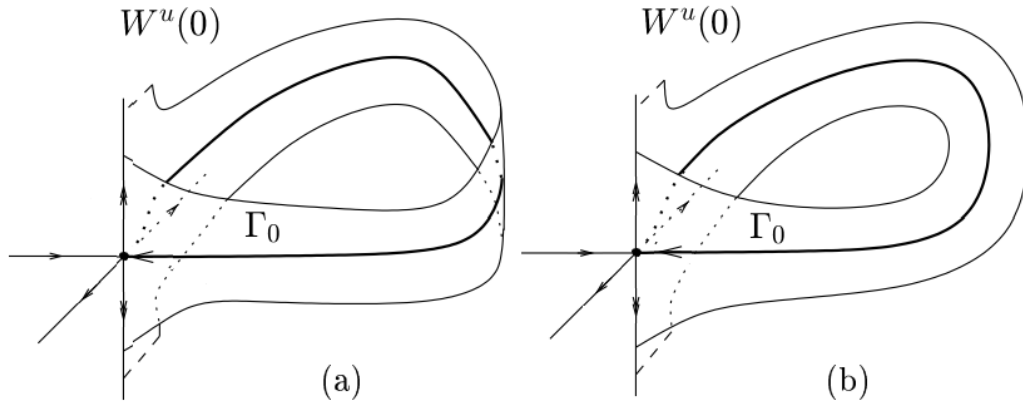


Figure 2.5: In a codimension-one homoclinic orbit, $W^u(0)$ can be orientable (a) or twisted (b). Moreover, $W^{cs}(0)$ is transverse to $W^u(0)$ along Γ_0 and the homoclinic orbit does not leave the origin along the strong direction $W^{uu}(0)$, depicted with a double arrow. The violation of one of these two conditions lead to an inclination flip or orbit flip configuration. Modified from [37].

f_μ unfolds Γ_0 generically. We say that Γ_0 is generically unfolded with respect to μ if $D_\mu \Delta(0) \neq 0$. Under this generic assumption, there always exists a hypersurface H in the parameter space such that $0 \in H$ and f_μ has a homoclinic orbit asymptotic to p_μ for all $\mu \in H$. There are three codimension-two homoclinic bifurcations we are interested in: inclination flip, orbit flip and Belyakov bifurcations. We describe the cases below.

Inclination Flip (IF) Eigenvalues are real with $\lambda_s < \lambda_u < \lambda_{uu}$ and (H1) is satisfied, but not (H2), that is, we assume that the intersection between $W^{cs}(0)$ and $W^u(0)$ is non-transversal along Γ_0 .

Orbit Flip (OF) Eigenvalues are real with $\lambda_s < \lambda_u < \lambda_{uu}$ and (H2) is satisfied, but not (H1), that is, we assume that $\Gamma_0 \subset W^{uu}(0)$.

Belyakov Point Assume that the equilibrium point is a saddle-node with eigenvalues λ_s and λ_u with $\lambda_s < 0 < \lambda_u$. The eigenvalue λ_u has geometric multiplicity one and algebraic multiplicity two.

Figure 2.6 illustrated the possible configurations of an inclination flip and Figure 2.7 shows the configuration of an orbit flip. Compare with the configuration of a codimension-one homoclinic orbit depicted in Figure 2.5.

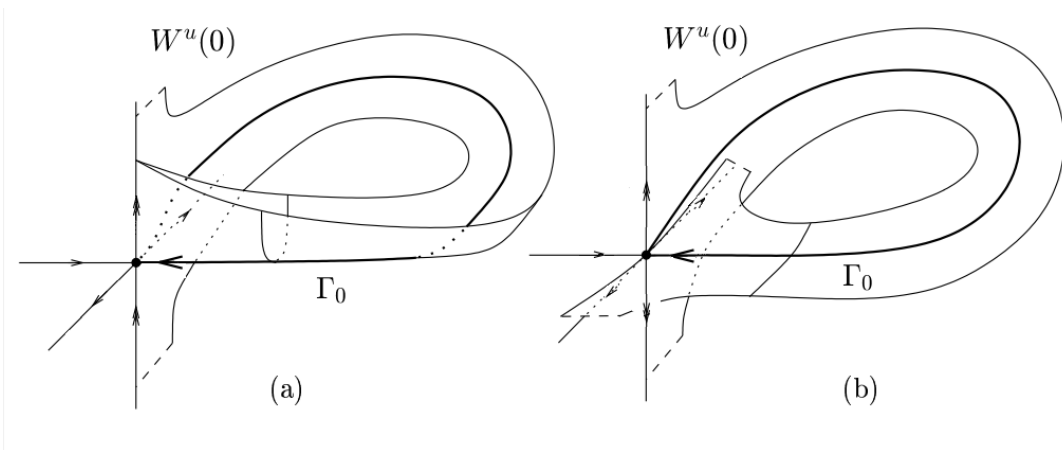


Figure 2.6: In an inclination flip configuration there is a loss of the transversality of the intersection of $W^{cs}(0)$ and $W^u(0)$. The inclination flip represented in (a) corresponds to the case $\lambda_{uu} < 2\lambda_u$ (see condition (I2)), and (b) corresponds to the case $\lambda_{uu} > 2\lambda_u$ (see condition (I3)). Modified from [37].

To characterize the different types of inclination and orbit flip bifurcations we need to introduce the following ratios between eigenvalues

$$\alpha = -\frac{\lambda_{uu}}{\lambda_s}, \quad \beta = -\frac{\lambda_u}{\lambda_s} \quad (2.2)$$

Note that $\alpha > \beta$.

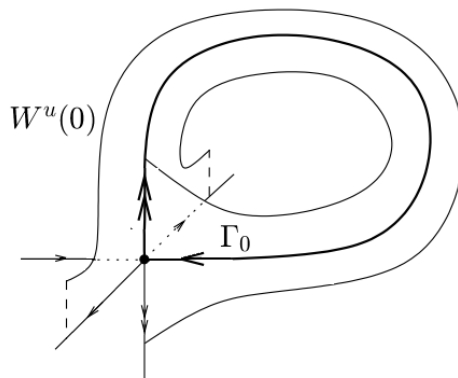


Figure 2.7: In an orbit flip configuration the homoclinic orbit leaves the origin along the non-dominant (strong) direction, denoted by a double arrow. Modified from [37].

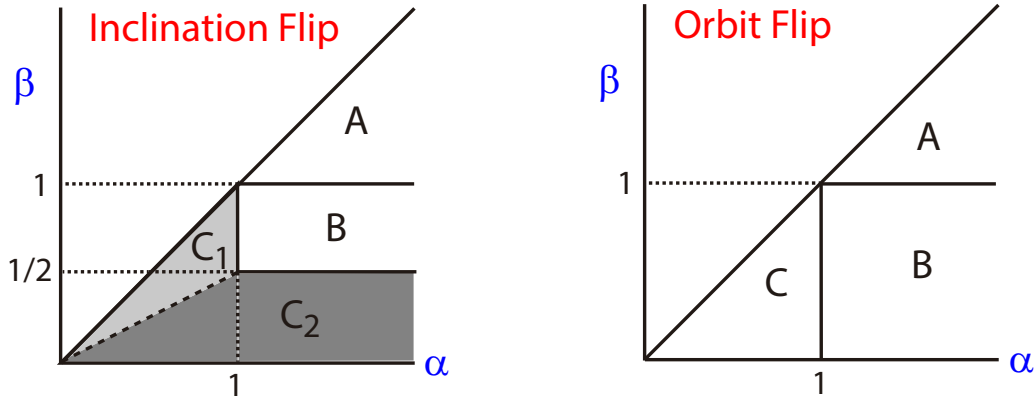


Figure 2.8: Types of inclination and orbit flips. Values of the ratios α and β are given in (2.2).

Bifurcation diagrams corresponding to IF and OF bifurcation points are quite similar and they can be described simultaneously. First, we observe that the hypersurface H of homoclinic bifurcation splits in two regions separated by a manifold of codimension-two homoclinic bifurcations. The orientation of the unstable invariant manifold at the equilibrium point reverses when such manifold is crossed.

For either IF or OF bifurcations there are three cases (see Fig. 2.8):

	Inclination Flip	Orbit Flip
Case A	$\beta > 1$	$\beta > 1$
Case B	$\alpha > 1$ and $\frac{1}{2} < \beta < 1$	$\beta < 1$ and $\alpha > 1$
Case C	$\alpha < 1$ or $\beta < \frac{1}{2}$	$\alpha < 1$

In **Case A** no extra bifurcations occur. **Case B** leads to homoclinic-doubling, involving the following one-side curves emanating from the origin: a period-doubling bifurcation and a 2-homoclinic bifurcation on the twisted side and a saddle-node bifurcation on the orientable side. A 2-homoclinic orbit is a homoclinic orbit that follows twice the primary homoclinic orbit before closing up. **Case C** is the only case detected in our exploration of the HR model. Homoclinic flip bifurcations in **Case C** require additional generic assumptions. Namely, for inclination flips we assume:

- (I1) $\beta \neq \frac{1}{2}\alpha$.
- (I2) If $\beta > \frac{1}{2}\alpha$ (region C_1 in the left panel of Fig. 2.8), the homoclinic orbit does not lie in the unique smooth leading unstable manifold.
- (I3) If $\beta < \frac{1}{2}\alpha$ (region C_2 in the left panel of Fig. 2.8), there is a quadratic tangency between $W^{cs}(0)$ and $W^u(0)$ along the homoclinic orbit.

On the other hand, for orbit flips in **Case C** we assume:

(O1) $W^{cs}(0)$ intersects $W^u(0)$ transversally along Γ_0 .

Hypothesis **(I2)** (resp. **(I3)**) makes sense in the region C_1 (resp. C_2) depicted in Fig. 2.8. Since these two cases make no difference in the unfoldings we will not devote any further attention to them. The essential distinction has to do with the way in which the unstable manifold approach the origin when it is followed along the homoclinic orbit by the forward flow (see Figure 2.6).

There are two possible bifurcation diagrams in case C. In both cases, horseshoes exist in a region of the parameter space. Depending on how they are formed, cases **C (in)** and **C (out)** are distinguished (see Fig. 2.9). In both, infinitely many one-sided curves of N -homoclinic orbits emerge for each $N \geq 2$ from the flip point on the branch of primary homoclinic orbits (labelled **hom** in Fig. 2.9). These are homoclinic orbits which follow N times the primary one before closing up. Also in both cases, the bifurcation diagram exhibits an infinite fan of bifurcation curves corresponding to period doublings and folds of periodic orbits. The horseshoe dynamics appear in between that cascade and the infinite fans of N -homoclinic orbits. In case **C (in)**, shift dynamics and the homoclinic cascade are separated by the curve **hom**, whereas, in case **C (out)**, the homoclinic cascade, the shift dynamics and the fan of bifurcations of periodic orbits are located on the same side of the curve **hom** (see Fig. 2.9). A complete description of the bifurcation diagrams can be found in Refs. [37], [24] and [25].

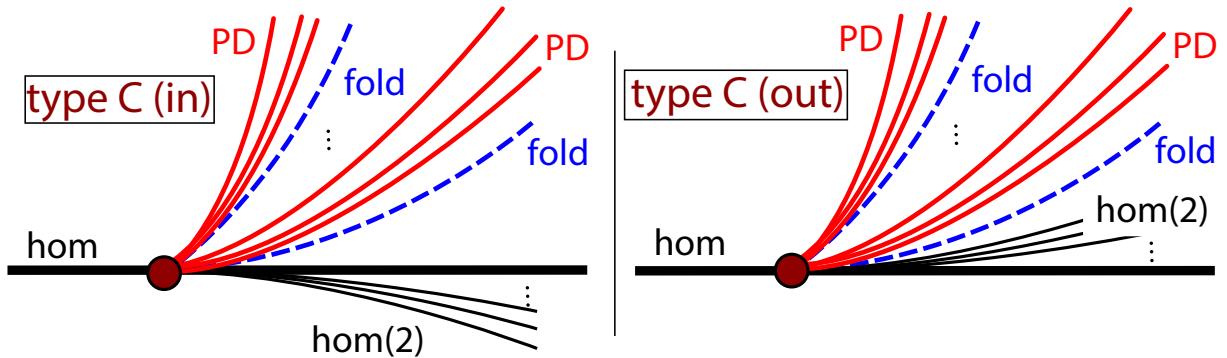


Figure 2.9: Theoretical two-parameter unfolding of the codimension-two OF and IF homoclinic bifurcations of type **C (in)** and **C (out)** describing the fans of period doubling and fold bifurcations of periodic orbits. Bifurcation diagrams for Belyakov bifurcations are similar, but folds and period doublings accumulate from both sides of the primary homoclinic bifurcation (see details in Ref. [32]). A fan of 2-homoclinic orbits (labelled **hom(2)**) is also depicted.

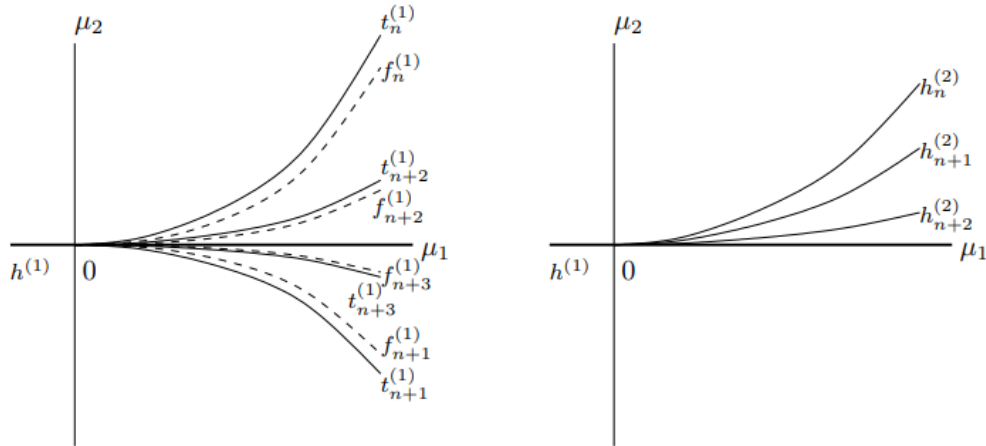


Figure 2.10: Theoretical two-parameter unfolding of the codimension-two Belyakov bifurcation. The bifurcation curves rooted at the Belakov point are fold (labeled as $t_n^{(1)}$), period-doubling (labeled as $f_n^{(1)}$) and homoclinic bifurcations curves (labeled $h^{(1)}$ in the case of the primary homoclinic bifurcation curve and $h_n^{(2)}$ in the case of secondary (double) homoclinic bifurcation curves. Obtained from [32].

Regarding Belyakov bifurcations we remark that the hypersurface H of homoclinic bifurcation splits in two regions separated by a manifold of codimension-two homoclinic bifurcations. Saddles change from saddle-node type to saddle-focus type when such manifold is crossed. Additional generic conditions include global assumptions on the behaviour of the invariant manifolds (see Refs. [25] and [32] for a complete description).

If $\lambda_s + \rho_u < 0$, a unique unstable limit cycle bifurcates from the homoclinic orbit (see Ref.[32]). Otherwise, the two-parameter bifurcation diagram is quite similar to those in Fig. 2.9. Infinitely many one-sided curves of N -homoclinic orbits emerge for each $N \geq 2$ from the Belyakov point and they are tangent at the flip point to the branch of primary homoclinic orbits corresponding to saddle-focus. The bifurcation diagram also exhibits infinite fans of bifurcation curves corresponding to period doublings and folds of periodic orbits, but, on the contrary to what is shown in Fig. 2.9, they accumulate on the branch of saddle-focus homoclinic orbits from both sides (see Figure 2.10).

2.2 Classification of bursting patterns

As already explained in Chapter 1, bursting is one of the typical behaviors exhibited by biological neurons and it is believed to play a fundamental role in the transmission of messages along the neural network. A bursting orbit switches between active and

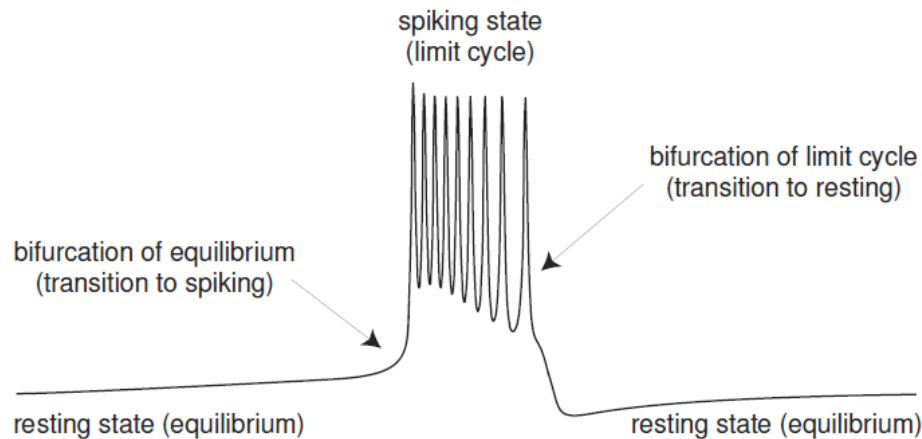


Figure 2.11: There are two key bifurcations in the fast subsystem of a bursting model. Extracted from [27].

resting states. When active, neuron produces trains of spikes. On the contrary, when resting, it does not fire, but stays stationary. Usually, this phenomenon appears because of successive changes where control of the dynamics is taken, alternatively, by fast and slow ionic currents. The former ones are responsible of the firing phase whereas slow ionic currents modulate the neuron activity. In a parallel manner, there are many dynamical systems which are able to display bursting behaviors because equations themselves include two different time scales, one fast and the other slow. Usually, trains of spikes emerge when system is running rapidly, but the passage through quiescence evolves slowly. Just now, we need to understand how an orbit switches from a spiking phase to an stationary one and vice versa, see Figure 2.11.

We consider systems where variables are grouped into slow and fast, and equations can be written as

$$\begin{cases} \dot{x} = f(x, y) & \text{fast subsystem} \\ \dot{y} = \varepsilon g(x, y) & \text{slow subsystem} \end{cases} \quad (2.3)$$

with $x \in \mathbb{R}^m$, $y \in \mathbb{R}^n$ and $0 \leq \varepsilon \ll 1$. Roughly speaking, bursting can be explained based on the coexistence of two attracting invariant manifolds and orbits making alternate passages near one or another. These manifolds arise as perturbations of families consisting of either attracting equilibria or attracting periodic orbits in the fast subsystem given by $\varepsilon = 0$, where variable y acts as a parameter. At this stage, Fenichel Theory regarding the persistence of normally hyperbolic invariant manifolds plays an essential role (see [15]).

As a preliminary classification, we can refer to point-cycle and cycle-cycle bursters. We say point-cycle when the the quiescent state is an equilibrium point and the spiking state is a limit cycle. When the quiescent state is a small amplitude (subthreshold) oscillation,

then the burster is said to be cycle–cycle.

When $n = 1$ we expect to find jumping mechanisms linked to codimension-one bifurcations that cause the loss of stability in a certain family of attractors. Hence dynamics is forced to travel to another area of the phase space as one basin of attraction is replaced by another one. After that switching, parameter is followed in the reverse direction along the new family of attractors until another loss of stability arises that allows the cycle to be restarted once more again. In [27], Izhikevich proposes a classification of bursters for the case in which the fast subsystem is planar. Namely, he distinguishes 16 different classes of point-cycle planar bursters (see Figure 2.12) and 8 cycle-cycle planar bursters. For our later interests we only need to understand 2 of the 16 types of point-cycle bursters: the cases fold/hom and fold/Hopf, since they are the ones that can be found in the Hindmarsh-Rose model.

2.2.1 Fold/homoclinic bursting

When the resting state along a bursting orbit is terminated due to a saddle-node bifurcation of equilibria and the active phase is terminated due to a homoclinic bifurcation, the bursting is said fold/homoclinic (or fold/hom) bursting. Figure 2.13 shows a typical configuration of a fold/hom burster. The upper part shows an orbit of the full system (in blue) moving near the manifolds of equilibria (M_{eq}) and limit cycles (M_{lc}) of the fast subsystem.

As already mentioned, this phenomenon occurs because up to bifurcations, M_{eq} and M_{lc} are normally hyperbolic invariant manifolds. Thus, as follows from Fenichel theory, as long as they are normally hyperbolic, they are persistent. In fact, the perturbed manifolds M_{eq}^ε and M_{lc}^ε are the ones that the bursting orbit of the full system follows. However, to keep the visualization clear, only the manifolds of the fast subsystem are represented. The key bifurcations of the fast subsystem with respect to the slow variable are marked. In the bottom part of the figure we can see the different phase portraits that the fast system presents along different bursting phases.

The typical configuration of a fold/hom bursting system can be summarized as follows. Prior to the active phase, the fast subsystem possesses two attractors: the left, stable equilibrium point and the limit cycle on the right. Besides the stable equilibrium point, there are two additional equilibria: one unstable equilibrium inside the stable limit cycle (that must exist since the fast subsystem has dimension two and Poincaré-Bendixson theorem holds) and a saddle equilibrium point whose unstable manifold separates both attraction basins.

As the slow variable takes different values, the nullcline of the fast subsystem corresponding to the membrane potential moves upwards, and thus the distance between the stable equilibrium and the saddle point becomes smaller. At a certain point they collide and disappear through a saddle-node bifurcation. When this bifurcation occurs, the orbit

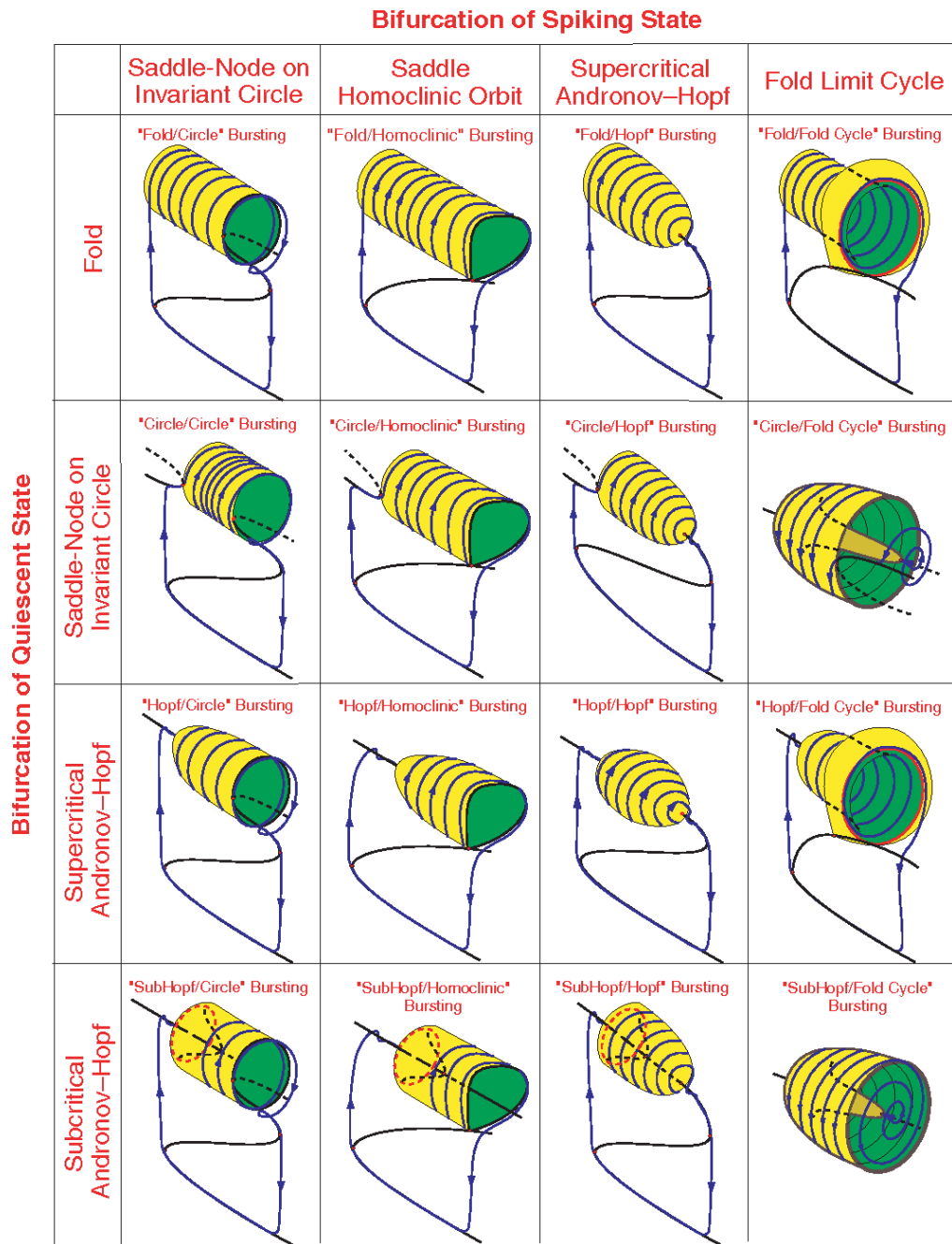


Figure 2.12: Classification of point-cycle bursting patterns. Extracted from [28].

of the full system jumps to the spiking manifold M_{lc}^ε that is close to the manifold of limit cycles M_{lc} depicted in Figure 2.13. The orbit of the full system turns around the spiking manifold, and each turn corresponds to one spike of the burst. Due to the variation of the slow variable, the nullclines of the system go back to their original position, making the stable and saddle equilibria to appear again. In other words, the fast subsystem undergoes the saddle-node bifurcation in the reverse direction. The slow variable also makes the distance between the saddle point and the limit cycle to become smaller, until they collide in a homoclinic bifurcation, causing the limit cycle to disappear. When this happens the active phase of bursting ends, and the dynamics of the fast subsystem goes back to M_{eq} .

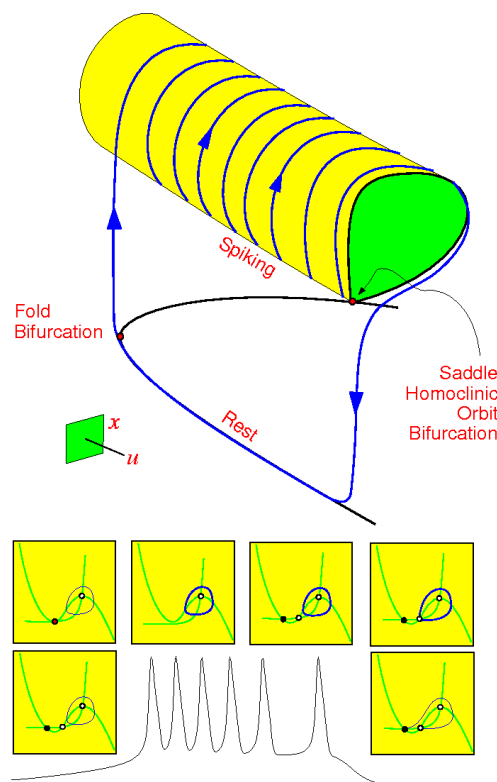


Figure 2.13: Fold/homoclinic bursting. In the upper part, an orbit of the global system follows the manifolds of equilibria and limit cycles, M_{eq} and M_{lc} . The lower part shows different phase portraits of the fast subsystem, corresponding to different values of the slow variable, which acts as a parameter of the fast subsystem. Reproduced from [28].

Fold/homoclinic bursting can be found in many neuron models, such as the Hindmarsh-Rose or the Sherman model of pancreatic β -cells [40]. Figure 2.14 shows a recording of a pancreatic β -cell producing bursting patterns that can be considered of fold/homoclinic



Figure 2.14: Putative fold/hom bursting in a pancreatic β -cell. Reproduced from [30].

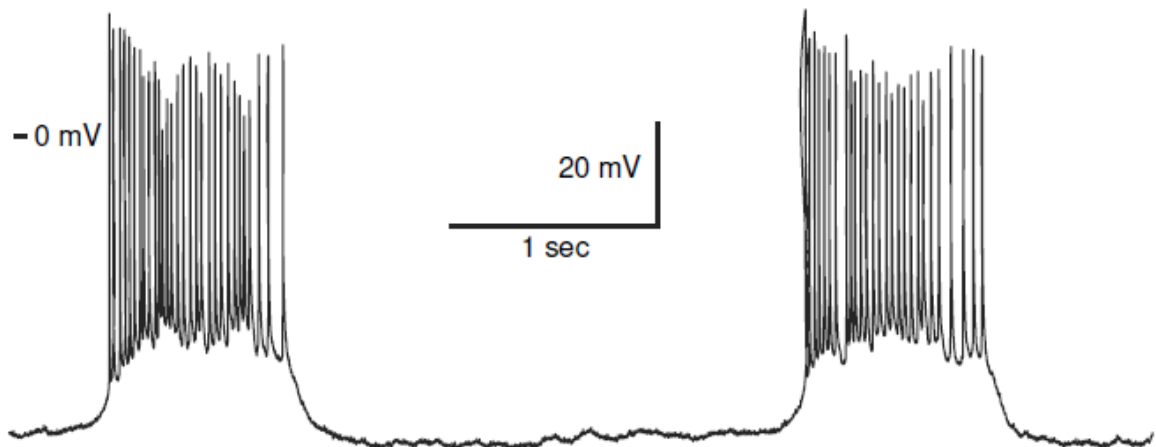


Figure 2.15: Putative fold/hom bursting in a cell located in the pre-Botzinger complex of rat brain stem. Reproduced from [27].

type, as the bursting activity shown in Figure 2.15, which corresponds to a cell located in the pre-Botzinger complex of the rat brain stem. This bursting pattern is said square/wave bursting due to the shape of the oscillations.

2.2.2 Fold/Hopf bursting

When the resting phase of the bursting terminates due to a saddle-node bifurcation and the active phase ends due to a Hopf bifurcation, the bursting is said of fold/Hopf type. The beginning of the bursting is similar to the already explained fold/homoclinic bursting. The system has three equilibria: a stable one, a saddle and a repeller (which is surrounded by a stable limit cycle). The global system initially follows the stable equilibria manifold. The active phase begins after a saddle-node bifurcation in the fast subsystem makes the stable equilibrium point to disappear. Then the system starts following the spiking manifold. What terminates the active phase is however different: as the slow variable moves, the

fast system undergoes a Hopf bifurcation. That is, the limit cycle becomes smaller and smaller until it shrinks into the equilibrium inside it. This equilibrium inherits its stability. The full system follows this branch of stable equilibria a small amount of time, since it quickly disappears due to an additional saddle-node bifurcation. After that, the system goes back to the original stable equilibrium of the left. The slow variable variation causes these bifurcations to reverse, taking the system to its original configuration. Figure 2.16 shows the typical configuration of a fold/Hopf burster.

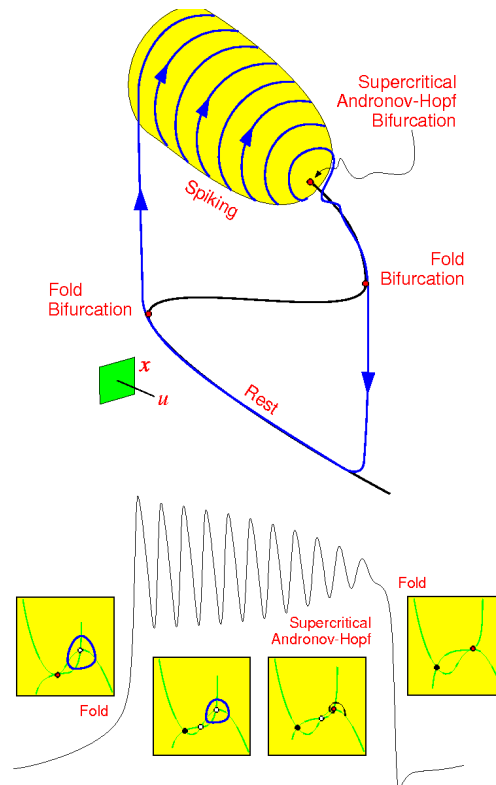


Figure 2.16: Fold/Hopf bursting configuration. In the upper part, an orbit of the global system follows the manifolds of equilibria, M_{eq} , and limit cycles, M_{lc} . The lower part shows the different phase portraits of the fast subsystem. Reproduced from [28].

Chapter 3

A brief review of prior research

Literature regarding bursting phenomena in the Hindmarsh-Rose model (and other neuron models) is plentiful. In this chapter we will review the main works studying the organizing centers of bursting behaviour, in particular those discussing the relationship between the bifurcation diagram of the system with the spike-adding process. Our main references are [6], [8], [18], [19], [33], [43] and [44]. We must also cite [41], which presents a comprehensive study of the dynamics of the Hindmarsh-Rose model.

We will fix the following parameter values in the Hindmarsh-Rose model (1.4):

$$a = 1, \quad c = 1, \quad d = 5, \quad s = 4, \quad x_0 = -1.6, \quad \varepsilon = 0.01$$

leaving b and I as bifurcation parameters.

As already explained, from a mathematical perspective, we say that a fast-slow system exhibits regular bursting when there exist a stable periodic orbit of the full system which, in the resting phase, passes close to one of the branches of stable equilibrium points of the fast subsystem, and, in the active phase, passes close to the family of stable periodic orbits of the fast subsystem. Each turn around the manifold of periodic orbits corresponds to a spike. If it happens that, after moving parameters, a burst gains an extra spike, it is said that the full system has undergone through a process of spike-adding. Since the number of spikes and their timing are key pieces for neural communication, the understanding of the underlying mechanisms in the spike-adding processes becomes crucial.

Particular attention has been paid to the spike-adding processes of fold/homoclinic bursting, because it is exhibited by many biological neurons, like, for instance, the pancreatic beta cells.

In [44], Terman studied a class of ODE's that models the electrical activity of pancreatic beta cells. The systems were assumed to be of fast-slow type, and their fast subsystem to be similar to the fast subsystem of fold/homoclinic bursters later described by Izhikevich. It is shown that these systems give rise to both bursting and continuous spiking solutions, for different values of the parameters. A dynamical analysis of the

spike-adding processes is also presented. Two types were distinguished: continuous and chaotic spike-adding. Figures 3.1 and 3.2 provide illustrations of these two cases in the Hindmarsh-Rose model. The continuous spike-adding process is shown in Figure 3.1. Different bursting solutions are represented in (t, x) coordinates, corresponding to different values of the parameter b and $I = 2.25$. In panel A, the bursting solution has clearly 2 spikes. In panel B, we can see that after the second spike, the membrane potential does not immediately decay to resting values, like in the previous case; instead, it stays close to stationary at intermediate values before going back to resting values. In panel C, the plateau region after the first two spikes still exists, but it is continued by a third, extra spike. After this extra spike, the membrane potential quickly returns to the resting value. Finally, panel D shows bursting of three spikes. We can see that the second and third spikes are slightly more distant than the first and second ones. The plateau region has notably shrunk. Terman [44] noted that this plateau phase corresponds to the orbit following the unstable branch of equilibria of the fast subsystem. An important feature of this transition is that the period of the orbit increases notably when the spike-adding starts (panels B and C), and it decreases to approximately their original values when is complete.

On the other hand, chaotic spike-adding is related to the existence of a Smale horseshoe, and it is characterized by the appearance of irregular bursting patterns like those shown in Figure 3.2. The plotted orbits correspond to $I = 2.7$ and different values of b . When moving b , the orbit increases its number of spikes from 2 (panel A) to 3 (panel C). However, for intermediate values of b the system exhibits irregular patterns (panel B).

Both spike-adding processes are part of the phenomena studied in several works focusing in the Hindmarsh-Rose model. In [18], the author studies the different dynamical behaviours exhibited by the model moving I and ε (varying one parameter each time). Complex structures arise, including chaotic behaviour and the so-called block-structured dynamics. Bifurcation diagrams and Lyapunov spectra are employed to perform the analysis. The bifurcation diagrams are constructed using inter-spike intervals (the time intervals between consecutive spikes). For each value of the parameter, the equations of the model are numerically integrated and a time series solution is obtained. The bifurcation diagram is the result of plotting the different values of the inter-spike intervals as dots for each value of the parameter. It is widely accepted that it is in the structure of the inter-spike intervals where neurons encode the information, so IBDs are a standard visualization of neuron models in the literature. Figure 3.3 shows an inter-spike bifurcation diagram (IBD). We take $b = 2.7$ and for this particular example, $x_0 = -1$. We leave I as the bifurcation parameter. The values of the parameters has been selected so both continuous and chaotic spike-adding processes are shown. Continuous spike-adding corresponds to the transition between blocks of consecutive number of spikes, while chaotic spike-adding occurs within the chaotic windows (in which the maximal Lyapunov exponent of the system is positive). Similar structures as the one shown in Figure 3.3 have

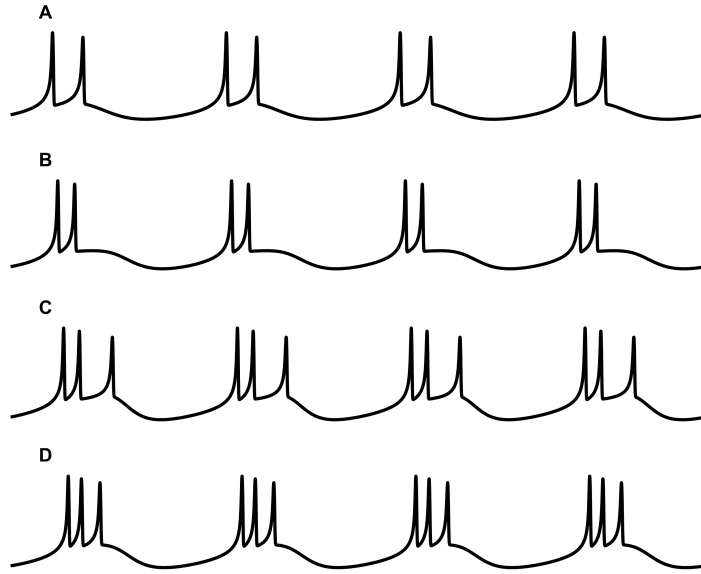


Figure 3.1: Continuous spike-adding process in the Hindmarsh-Rose model with $I = 2.25$. Panels A,B,C and D correspond to $b = 3, 2.91581, 2.915, 2.84106$, respectively. A comparison between panels B and C shows that a small change in the parameters may cause visible changes in the solutions (a new spike appears), since the transition occurs in a narrow interval of b . Note the plateau phase in panel B after the second spike. The solutions have been obtained by simulation using Matlab.

been observed in other models, namely, the Chay model for a nerve cell [11], analysed in [18], the modified Hodgkin-Huxley model of thermally sensitive neurons [10], studied in [16], and the Sherman model for a pancreatic cell [39], investigated in [36].

For high values of I (right hand side of the diagram) there is only one inter-spike interval, since the system exhibits spiking behaviour. As I decreases, a cascade of period-doubling bifurcation takes place, leading to the appearance of orbits with a high number of spikes after the system undergoes through a chaotic window. The periodic orbit with 12 spikes emerges abruptly after a fold bifurcation of periodic orbits that ends the chaotic window. As I takes lower values, another cascade of period-doubling bifurcation is encountered, giving rise to another chaotic region, narrower than the previous one. Again, this second chaotic region ends with a fold bifurcation and an orbit with 11 spikes emerges. For low values of the parameter I (left hand side of the diagram) the bursting regime is block-structured: each block corresponds to an interval of values of I that are associated to bursting with a certain number of spikes.

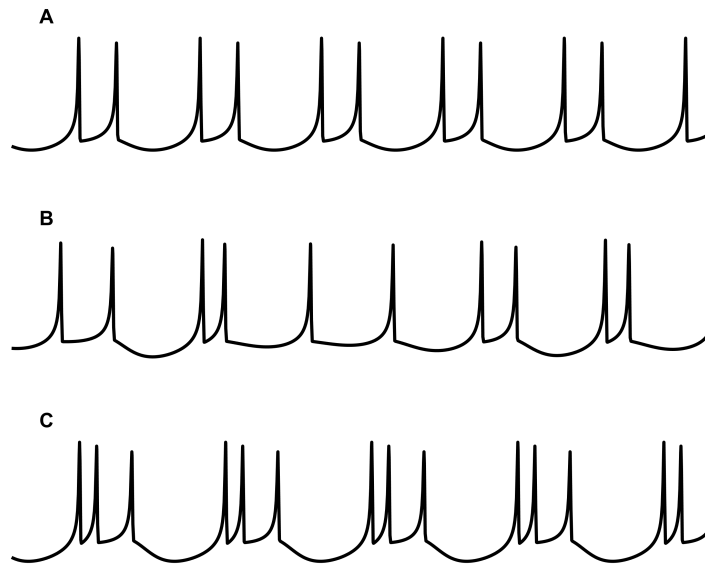


Figure 3.2: Chaotic spike-adding process in the Hindmarsh-Rose model with $I = 2.7$. Panels A, B and C correspond to $b = 3.12, 3$ and 3.056 , respectively. Panel B shows irregular bursting patterns associated with chaotic behaviour.

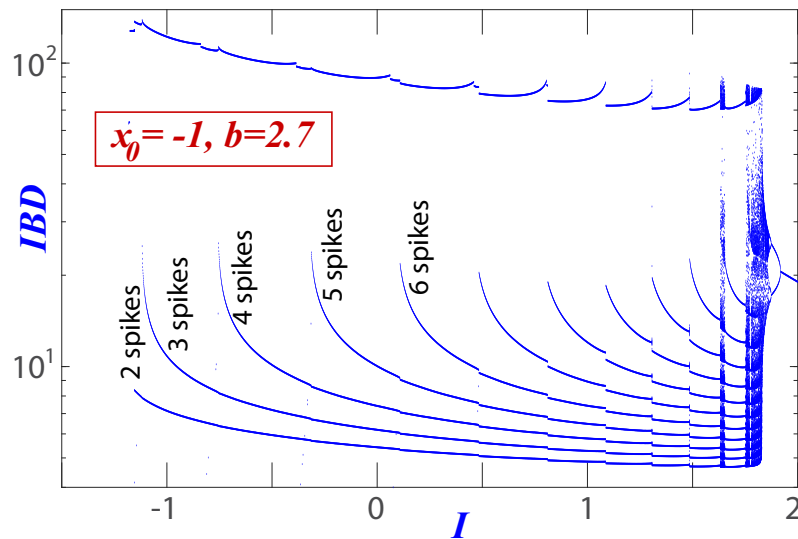


Figure 3.3: Inter-spike bifurcation diagram.

Different dynamical behaviours of the Hindmarsh-Rose model, and their transitions, were also studied in [26] by varying the parameter I and fixing $b = 3$ and $\varepsilon = 0.0021$. We will focus in their analysis of the continuous spike-adding, since their results are specially related with our own work. They employed continuation methods, which transform the task of performing a bifurcation analysis into the problem of finding roots of certain functions, a problem that can be solved systematically. A continuation of periodic orbits with respect to the parameter I was provided and a selection of them was shown in different states of the process of gaining an extra spike, superimposing these orbits over their corresponding fast-slow skeleton (equilibrium points and limit cycles). The fast system not only possesses the Z-shaped curve of equilibria and the manifold of limit cycles that are mentioned in Izhikevich's classification: it also presents a secondary manifold of limit cycles near the right knee of the equilibria curve. This secondary manifold has a relevant role in the spike-adding process.

According to their analysis, the birth of bursting orbits and the continuous spike-adding process occurs in the following way (see Figure 3.4). The system admits a unique equilibrium point, which is stable for $I = 0$. Increasing I causes the equilibrium to lose its stability at $I = 1.2895$, due to a subcritical Hopf bifurcation. An unstable limit cycle emerges from the Hopf bifurcation point and turns stable due to a fold bifurcation SN_{1a} . This stable limit cycle is a bursting orbit of one spike. The bursting orbit then undergoes two folds bifurcations, SN_{1b} and SN_{2a} which are very close to each other and give rise to a hysteresis phenomenon (the continuation curve is Z-shaped). In this process, the orbit develops an extra spike, evolving into a bursting orbit of two spikes. The birth of the new spike is a continuous process (including in the picture the unstable orbits) related to canard phenomena [9] [12] [46] (see Figure 3.5). As the orbit undergoes the fold bifurcation SN_{1b} , it starts following the middle branch of unstable equilibrium points of the fast subsystem (headless canard in the literature), which causes an increase in the period (see panel B in Figure 3.1). The time spent following the unstable branch corresponds to the plateau phase of the solution. The orbit, now unstable, extends more and more along the unstable branch of equilibria until it reaches the secondary limit cycle manifold and makes a turn around it (the orbit is now a canard with head, the head corresponding to the extra spike). This happens when the orbit undergoes the fold bifurcation SN_{2a} . After that, the orbit spends less time following the unstable branch of equilibria of the fast subsystem while keeping the extra spike, until it becomes a bursting orbit with two spikes. As I increases, a sequence of pairs of fold bifurcations takes place, leading to more hysteresis phenomena in which the orbit gains more spikes. In particular, the evolution from n to $n + 1$ spikes occurs during the hysteresis delimited by two fold bifurcations, SN_{nb} and $SN_{n+1,a}$. Due to the hysteresis phenomena, there is a coexistence of bursting orbits of n and $n + 1$ spikes in a small current interval for each n . These results are summarized in Figure 3.4, where the continuation of equilibria and periodic orbits is represented, and in Figure 3.5, where different orbits in the process of going from 4 to 5

spikes are shown.

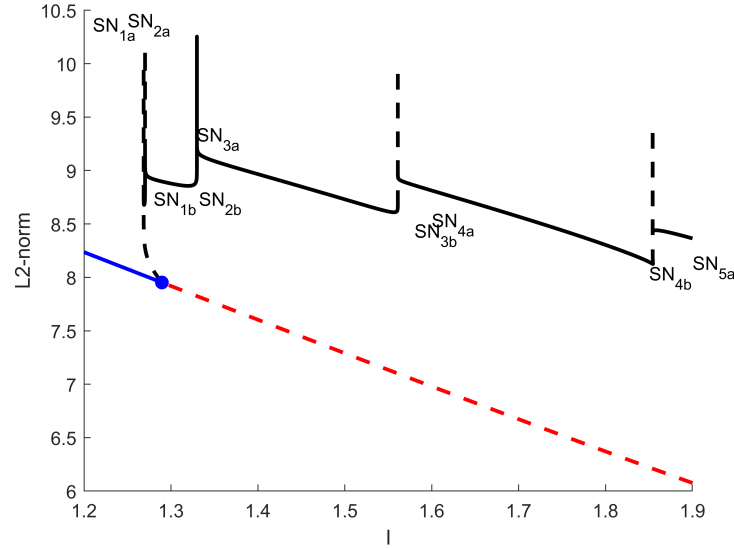


Figure 3.4: Continuation of a periodic bursting orbit undergoing continuous spike-adding. Continuous blue line indicates stable equilibrium points and dashed red line indicates unstable equilibrium points. Continuous black line stands for stable limit cycle and dashed black line is for unstable limit cycles. The blue point is a subcritical Hopf bifurcation.

The mechanism underlying the continuous spike-adding (through canard transitions [9] [12] [46]) was already predicted by Terman [44], but an important difference is that in [44] it was suggested that the solution remains stable during the whole process, while in the Hindmarsh-Rose model this is not always the case.

The results regarding the continuous spike-adding process were extended in [33], where the authors consider b as the bifurcation parameter. The spike-adding process is the same as described in [26], with the difference that they also identify period-doubling bifurcations during the continuation of periodic bursting orbits gaining an extra spike. In Figure 3.6 we show a continuation of periodic orbits with respect to b . We chose an interval of b corresponding to the evolution from 2 to 3 spikes. Continuous line denotes stable solutions and dashed line denotes unstable solutions. Blue points are fold bifurcation of limit cycles, while red points stand for period-doubling bifurcation. The presence of period-doubling bifurcations creates two bistability regions, although one of them is indistinguishable, since the right fold and the right period-doubling are very close to each other. The other bistability region is visible and is delimited by the left fold and the left period-doubling, and its width is less than if there were no period-doubling points.

The dynamics of the Hindmarsh-Rose model have been also investigated considering two parameters of bifurcation. This allows a better understanding of the phenomena

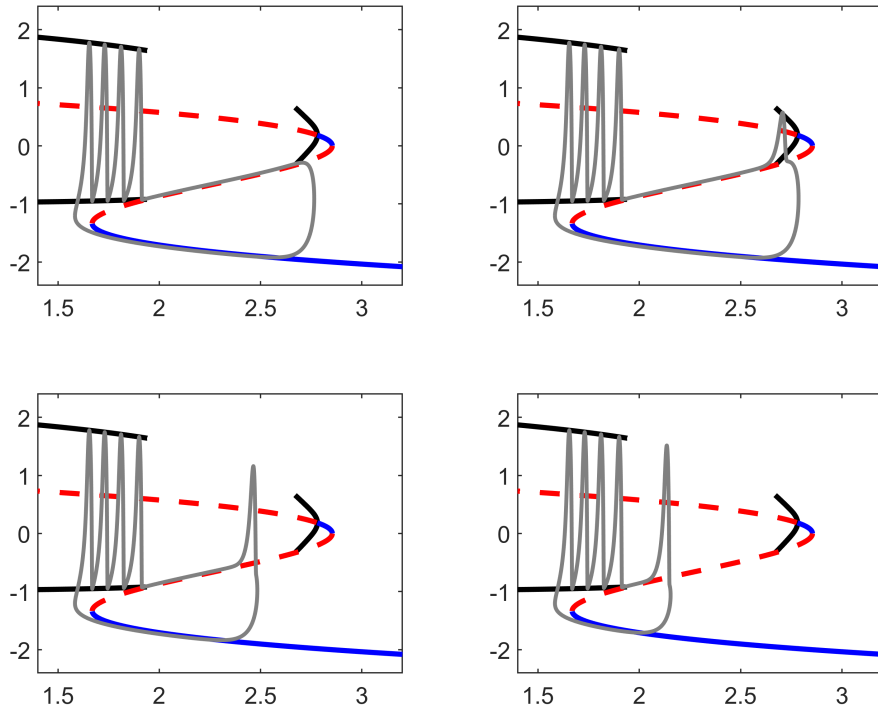


Figure 3.5: Different orbits undergoing the continuous spike-adding process from 4 to 5 spikes, which occurs at $I = 1.85414$, where the continuation curve suffers a very sharp hysteresis. The corresponding fast-slow skeleton is also represented. Continuous blue line denotes stable equilibria, dashed red line denotes unstable equilibria and continuous black line is for the maxima and minima x -values of limit cycles.

founded in previous studies where only one parameter of bifurcation was considered. Only in relation with our interest, we can cite [6], [8],[19], [33] and [43].

In [19] the author analysed the model in the parametric plane (I, ε) . Combining a linear stability analysis (screening the eigenvalues of the jacobian of the system at the unique equilibrium point) and a nonlinear analysis (calculating the Lyapunov spectrum), they determined the different behaviours available. There are regions where the dynamics falls to an equilibrium point (quiescence), regions where there exist simple limit cycles (spiking), and regions characterised by bistability. Moreover, areas displaying complex phenomena (periodic bursting and chaotic firing of spikes) are delimited. Inter-spike intervals are used to define different measures that allow screening the plane (I, ε) and building color maps that make the different behaviours distinguishable. This information, combined with the information of the Lyapunov spectrum, permits identifying chaotic

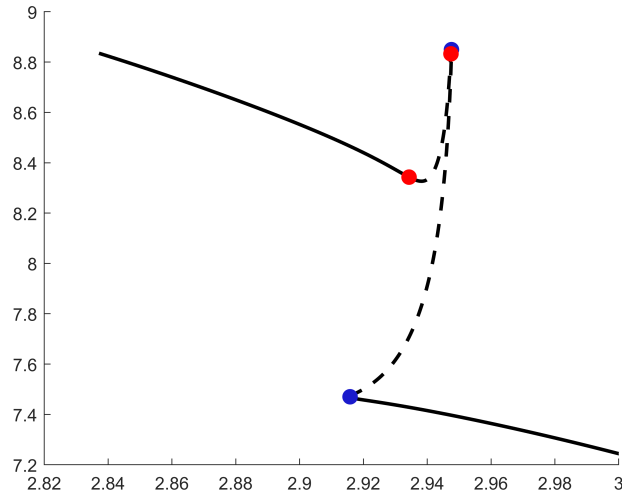


Figure 3.6: Continuation of a periodic bursting orbit undergoing continuous spike-adding. Continuous line corresponds to stable solutions and dashed line refer to unstable solutions. Blue points indicate a fold bifurcation of limit cycles, while red points stands for period-doubling bifurcation.

lobes in the system, and a band structure formed by strips of similar periodicity. Straight cuts of this structure would yield inter-spike bifurcation diagrams similar to the one shown in 3.3 (the chaotic regions in the IBD corresponding to the chaotic lobes and the blocks of the same number of spikes corresponding to the bands).

Regarding parameter-sweeping techniques, we must cite [8], where the authors perform different screenings in the (b, I) plane employing the software TIDES, a numerical integrator based in the Taylor method (see [1] and [2]). They use common indicators in neuroscience-related works, such as the duty cycle and the spike-counting, and the calculation of the Lyapunov spectrum, standard in the nonlinear-related studies. Both approaches yield coherent results, and the method used allows a great accuracy. The plane (x_0, I) was also studied, revealing a structure characterised by diagonal bands of the same periodicity, surrounded by a region characterised by quiescence.

In [43] authors analysed the dynamics of the model in the (b, I) plane, fixing $\varepsilon = 0.01$. They complement brute-force methods (performing extensive simulations) with continuation techniques. The use of extensive simulations allow to identify the typical dynamical behaviours for each value of (b, I) . More than that, when periodic bursting is founded, the number of spikes per burst is identified. A color code is used so different number of spikes are represented in different colors (see Figure 3.7). We will refer to these color maps as spike-counting maps. Continuation methods allow to follow the

different codimension-one bifurcation curves and to locate codimension-two bifurcation points in the (b, I) -plane. Combining the results, it is possible to see how bifurcations are related with the spike-adding phenomenon. In a similar way to the case of the parametric plane (I, ε) studied in [19], the bursting region is divided in bands of different number of spikes, with consecutive bands differing in 1 spike. Chaotic bulbs also exist in this region, as in the case of [19]. Figure 3.7 shows a spike-counting map superimposed with the corresponding bifurcation diagram. Yellow curves are fold bifurcations of periodic orbits and red curves represent period-doubling bifurcations. The black, C-shaped curve is a homoclinic bifurcation curve. Green is used for orbit flips and magenta for inclination flips.

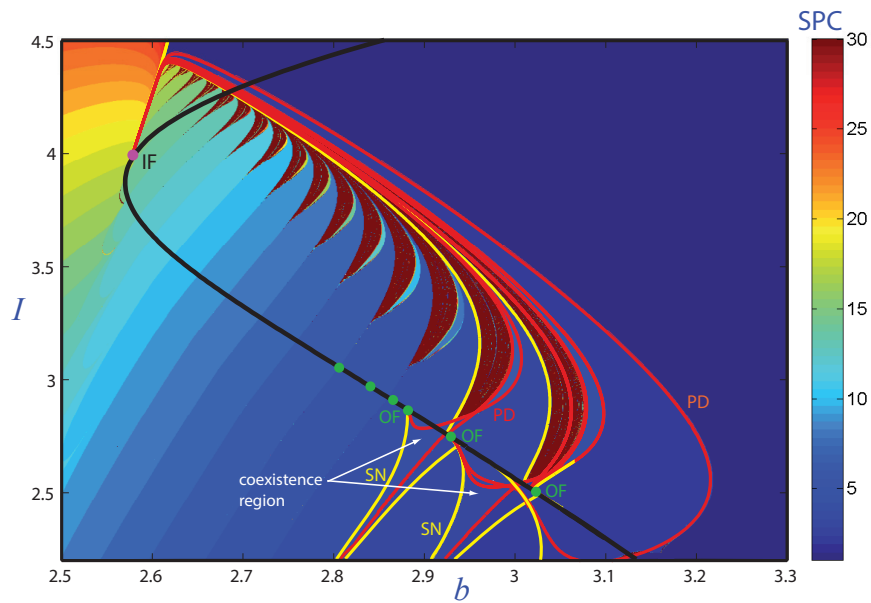


Figure 3.7: Spike-counting map for $\varepsilon = 0.01$ superimposed with the bifurcation diagram. Modified from [6].

The bursting structure is induced by fold and period-doubling bifurcation curves. Namely, the chaotic bulbs are delimited by fold and period-doubling bifurcation curves, and the bursting bands are bordered by fold bifurcation curves. There exist cascades of period-doubling curves inside the chaotic bulbs, causing the high number of spikes and the chaotic behaviour. Period-doubling curves also appear inside the periodic bursting bands, delimiting bistability regions that the spike-counting map does not show. Recall that an horizontal cut of a bursting map would correspond to the situation illustrated in Figure 3.6, where a visible bistability region is located between the left fold and the left period-doubling.

The existence of the fold and period-doubling bifurcation curves is explained by the

presence of homoclinic degeneracies that act as organizing centers of the bursting structure. In Figure 3.7, we see how the fold and period-doubling curves are born from the codimension-two homoclinic points: orbit flips, inclination flips and Belyakov points (the last ones are located near the apparent ends of the curve, not visible in the figure due to the diagram limits). According to our numerical studies, orbit and inclination flips are of type C, thus their existence ensures the presence of an infinite number of period-doubling and fold bifurcation curves. The role of the codimension-two homoclinic degeneracies as organizing centers has been studied in [6], where the authors analyze how the fold and period-doubling curves emanating from them form chaotic regions, both macroscopic (the dark brown bulbs in Figure 3.7) and microscopic, where stable periodic bursting solutions coexist with chaotic ones. Reference [33] provides a detailed analysis of the situation of the different homoclinic curves and their degeneracies in the (b, I) plane, with $\varepsilon = 0.01$ fixed.

It is compulsory to make some remarks regarding the situation of the homoclinic curve that cannot be inferred from the bifurcation diagram shown in Figure 3.7. The main one is that actually there exist one homoclinic bifurcation curve for each spike-adding transition (there is one curve for the transition from 1 to 2 spikes, another curve for the transition from 2 to 3 spikes, and so on). The apparent ends of each homoclinic bifurcation curve are actually very sharp turns. References [33] and [43] show how the homoclinic orbits gain an extra spike after the lower turn. The gaining of the spike is due to canard phenomena, as in the case of stable orbits of small period, already studied. Thus, part of each homoclinic curve corresponds to solutions of n spikes, and other part corresponds to solutions of $n + 1$ spikes. We refer to them as $hom(n, n + 1)$ curves. We must remark that the results regarding the structure of the homoclinic bifurcation curves shown in [43] and [33] are partial. Namely, the numerical continuations in these previous works do not show what happens to the curve after the sharp turns. In fact, only the lower turn was investigated. Our numerical findings allow to give a more complete picture, as we will see in the next chapter.

Another relevant fact about the homoclinic bifurcation curves is that they are very close in the parameter space, so it is not possible to distinguish them if represented in the same plot. In Figure 3.7 the homoclinic bifurcation curve corresponding to the transition from 1 to 2 spikes is represented. It is the bigger one, since, as [33] shows, the size of each $hom(n, n + 1)$ curve decreases as n increases. Different codimension-two homoclinic points exist in each homoclinic bifurcation curve. Consequently, fold and period-doubling curves corresponding to different transitions emanate from different homoclinic bifurcation curves.

There exist Belyakov points in the homoclinic bifurcation curves for the first two transitions, and they lie very close to each other in the parameter space. However, homoclinic bifurcation curves $hom(n, n + 1)$ with $n \geq 3$ do not present Belyakov points (for $\varepsilon = 0.01$). In particular, this implies that the homoclinic bifurcation curves associated with these

transitions only correspond to the case of real eigenvalues, thus their solutions do not present the oscillations related with the imaginary eigenvalues case.

All the bifurcation curves (as far as they have been studied) present an inclination flip point close to $I = 3.9$. Different inclination flips corresponding to different homoclinic bifurcation curves lie very close to each other. Thus, as it happens with Belyakov points, inclination flips corresponding to different homoclinic curves are not distinguishable in the parameter space. However, the orbit flips that exist for each transition are clearly separated from each other, as Figure 3.7 shows.

Each fold bifurcation curve separating a pair of bands of n and $n + 1$ spikes is born from a different homoclinic bifurcation curve $hom(n, n + 1)$. In particular, they are born from the very sharp turn in the lower part. While it has not been possible to detect a codimension-two point in this position, in [33] it is conjectured that there exist an inclination flip located there, and the authors give geometrical arguments supporting the conjecture.

In [6], [8] [43] and other spike-counting maps, corresponding to different values of ε , have been obtained. For instance, in [6] the case $\varepsilon = 0.001$ is shown. In [43] different diagrams are presented, with ε ranging from 0.001 to 0.28. The band structure of the spike-counting maps, as well as the presence of chaotic bulbs, persists when ε changes. However, the structure undergoes noticeable changes. First, as ε decreases, there is an increase in the number of spikes per burst that is exhibited by periodic bursting solutions. Second, smaller values of ε correspond to a higher number of chaotic bulbs. Lastly, the band-structured region corresponding to bursting behaviour gets smaller as ε increases. We must remark that case $\varepsilon = 0.01$ is the only one that have been studied in regards to the bifurcation diagram. Therefore, the changes that the spike-counting maps suffer when ε varies have not been explained previously to our work. It should be pointed out that the parameter ε has a special relevance, since it is the parameter responsible to the fast-slow dynamics, and thus, is the one that places the system close or far to the singular limit.

For that reason, the analysis of the evolution of the dynamics when ε varies was the first goal of this thesis. In particular, we were interested in the evolution of the bifurcation diagram when ε brings the system far from the singular limit, and to explain the changes in the spike-counting maps in the context of the bifurcations of the system. Our second goal was to deepen into the relationship between the bifurcation diagram and the spike-adding processes in the case $0 < \varepsilon \ll 1$. While many works have approached this subject, a global scheme putting together the different findings was missing. For instance, we were interested in determining in which parametric regions the different spike-adding processes take place, and how the distance to the homoclinic influences them. Our work in these matters resulted in the papers presented in the next chapter.

Chapter 4

Contributions

4.1 Paper I

This paper [4] investigates the Hindmarsh-Rose model from a novel perspective, taking a first step in the analysis of the bifurcation diagram as the small parameter ε takes different values and moves far from the singular limit. We have considered b, I and ε as parameters and have studied the dynamics of the system. Our main interest is the evolution of the homoclinic bifurcation curves corresponding to bursting of 1 and 2 spikes in the plane (b, I) as ε takes different values. Different homoclinic bifurcation curves in the (b, I) plane were computed, corresponding to values of ε ranging from 0.005 to 0.08. The results show evident changes in the shape of the homoclinic bifurcation curves as ε increases. We have also computed a three-parameter continuation curve of inclination flips, which disappears at $\varepsilon = 0.0197$ due to a folding mechanism. We provided two-parameter sweepings in the (b, I) plane for different values of ε using the spike-adding technique, and observed a correlation between the changes of the homoclinic bifurcation curves and the deformation of the spike-counting map. Orbits of the system for different values of ε (0.01, 0.03, 0.05, 0.3) were shown, which allows to illustrate how the border between the two different bursting regimes exhibited by the Hindmarsh-Rose model (fold/homoclinic and fold/Hopf) blurs when ε grows. In the case $\varepsilon = 0.3$ the system keeps some features of the slow-fast dynamics but the spiking process becomes akin to the funnel structures around focus equilibria in Rössler-like systems.



Hindmarsh–Rose model: Close and far to the singular limit



Roberto Barrio^{a,b,*}, Santiago Ibáñez^c, Lucía Pérez^c

^a Departamento de Matemática Aplicada and IUMA, University of Zaragoza, E-50009 Zaragoza, Spain

^b Computational Dynamics group, University of Zaragoza, E-50009 Zaragoza, Spain

^c Departamento de Matemáticas, University of Oviedo, E-33007 Oviedo, Spain

ARTICLE INFO

Article history:

Received 12 August 2016

Received in revised form 9 December 2016

Accepted 10 December 2016

Available online 15 December 2016

Communicated by C.R. Doering

Keywords:

Hindmarsh–Rose model

Singular limit

Slow-fast dynamics

Spike-adding

ABSTRACT

Dynamics arising in the Hindmarsh–Rose model are considered from a novel perspective. We study qualitative changes that occur as the time scale of the slow variable increases taking the system far from the slow-fast scenario. We see how the structure of spike-adding still persists far from the singular case but the geometry of the bifurcations changes notably. Particular attention is paid to changes in the shape of the homoclinic bifurcation curves and the disappearance of Inclination-Flip codimension-two points. These transformations seem to be linked to the way in which the spike-adding takes place, the changing from fold/hom to fold/Hopf bursting behavior and also with the way in which the chaotic regions evolve as the time scale of the slow variable increases.

© 2016 Elsevier B.V. All rights reserved.

1. Introduction

It is out of discussion that to understand such a complex mechanism as the brain, and in general any living neural network, it is compulsory to know first the working of its basic building blocks: the neurons. Since the seminal contribution of Hodgkin and Huxley [1], neurons are commonly viewed as dynamical systems. Elements of bifurcation theory play an essential role in this context and help to understand neuronal activity.

The range of activity types that a neuron can exhibit is quite broad and includes quiescence (the state of not firing), tonic spiking, bursting and irregular (or chaotic) spiking. Each of these behaviors has its counterpart in the language of dynamical systems, either as stable periodic or chaotic orbits. Even the process of spike-adding can be linked to specific codimension-two homoclinic bifurcations (Orbit-Flip and Inclination-Flip points) and also to the so called canard explosions [2,3].

Hindmarsh–Rose (HR in the sequel) equations

$$\begin{cases} x' = y - ax^3 + bx^2 + I - z, \\ y' = c - dx^2 - y, \\ z' = \varepsilon(s(x - x_0) - z) \end{cases} \quad (1)$$

were introduced in [4] as a reduction of the Hodgkin–Huxley model. The HR model is simpler but it captures the main dynam-

ical behaviors which are displayed by real neurons: quiescence, tonic spiking, bursting and irregular spiking (see [5–13]). The system possesses two time scales: x and y evolve as fast variables while z does it as a slow variable (so, it is a slow-fast dynamical system). The x variable should be treated as the voltage across the cell membrane, while the y and z variables would describe kinetics of some ionic currents. The *small* parameter ε controls the time scale of z and x_0 controls the rest potential of the system.

Different choices of the parameters have been considered in the literature (see [11] for an excellent review of the dynamics of the model). Following [2,11,12] we assume that

$$a = 1, \quad c = 1, \quad d = 5, \quad s = 4, \quad \text{and} \quad x_0 = -1.6. \quad (2)$$

With this choice, (1) becomes a family dependent only on parameters (b, I, ε) . These parameters will be our primary bifurcation parameters.

In this paper we pay attention to the changes in the global picture as ε varies. From a realistic point of view it is clear that only small values of ε are of interest: typically $\varepsilon \ll 1$. We include a preliminary study about the singular limit of some relevant bifurcations. Nevertheless, in contrast with other approaches, we want to emphasize that the understanding of the bifurcation diagram for higher values of the slow time scale should be a crucial ingredient to get a whole picture of the dynamics and also it helps to understand what happens for $\varepsilon < 1$ (and not only $\varepsilon \ll 1$).

The article is arranged as follows: In Section 2 we compute the singular limit of the Hopf bifurcations as $\varepsilon \searrow 0$. Moreover, we show with numerical evidences that a singular limit also exists for the homoclinic bifurcation curves. We compare our results with

* Corresponding author at: Departamento de Matemática Aplicada and IUMA, University of Zaragoza, E-50009 Zaragoza, Spain.

E-mail addresses: rbarrio@unizar.es (R. Barrio), mesa@uniovi.es (S. Ibáñez), lpcuadrado@gmail.com (L. Pérez).

those in [14–16] where similar singular limits were studied in a different model. In section 3 we investigate how the homoclinic bifurcation curves change as ε increases from small (slow-fast dynamics) to large values. We will see that, although the geometry of the bifurcation curves changes rapidly, many common features seem to persist. Section 4 is devoted to show how the global picture of spike-adding, bursting and chaotic behavior, bounded inside a loop formed by the Hopf bifurcation curves, evolves with ε . We will describe how this evolution seems to be linked to the changes along the homoclinic bifurcation curves. A summary is presented in Section 5. All continuations of bifurcation curves have been done with the free software AUTO [17,18].

2. Singular limits: Hopf bifurcation and homoclinic bifurcation

It easily follows (fixing all parameters but (b, I, ε)) that the equilibrium points of (1) are given by

$$y = 1 - 5x^2, \quad z = 4(x + 1.6), \tag{3}$$

with x any real root of

$$P(x) = I - 5.4 - 4x + (b - 5)x^2 - x^3. \tag{4}$$

The Jacobian at a given equilibrium point is given by

$$\begin{pmatrix} -3x^2 + 2bx & 1 & -1 \\ -10x & -1 & 0 \\ 4\varepsilon & 0 & -\varepsilon \end{pmatrix}, \tag{5}$$

with characteristic polynomial

$$Q(\lambda) = \lambda^3 + q_2(x, b, \varepsilon)\lambda^2 + q_1(x, b, \varepsilon)\lambda + q_0(x, b, \varepsilon),$$

where

$$\begin{aligned} q_2(x, b, \varepsilon) &= 3x^2 - 2bx + 1 + \varepsilon, \\ q_1(x, b, \varepsilon) &= 3x^2 + (10 - 2b)x + \varepsilon(3x^2 - 2bx + 5), \\ q_0(x, b, \varepsilon) &= \varepsilon(3x^2 + (10 - 2b)x + 4). \end{aligned}$$

Necessary conditions for an Andronov–Hopf (AH) bifurcation are

$$\begin{aligned} P(x) &= 0 \\ C(x, b, \varepsilon) &= q_2(x, b, \varepsilon)q_1(x, b, \varepsilon) - q_0(x, b, \varepsilon) = 0 \\ q_1(x, b, \varepsilon) &> 0. \end{aligned}$$

The above conditions characterize a collection of surfaces on the space of parameters whose limit when $\varepsilon \searrow 0$ is given by

$$I - 5.4 - 4x + (b - 5)x^2 - x^3 = 0, \tag{6}$$

$$(3x^2 - 2bx + 1)(3x^2 + (10 - 2b)x) = 0, \tag{7}$$

$$3x^2 + (10 - 2b)x \geq 0. \tag{8}$$

Although the condition $q_1(x, b, \varepsilon) > 0$ is stated in terms of a strict inequality, we must consider the possibility of a non strict inequality at the limit when $\varepsilon \searrow 0$. The set S of points satisfying the above conditions consists of three curves as depicted (dashed blue) in Fig. 1. AH bifurcations curves for $\varepsilon = 0.005$ are also shown. Note that not the whole set S becomes the singular limit for AH bifurcations curves. When $x = 2(b - 5)/3$, (7) is satisfied and substituting in (6) we get the equation for the graph G of a polynomial $I(b)$ of degree 3. On the other hand, (8) is also satisfied because $3x^2 + (10 - 2b)x = 0$. It follows that G is the singular limit for a surface in the 3-parameter space satisfying $P(x) = 0$ and $C(x, b, \varepsilon) = 0$, but only a part of it satisfies $q_1(x, b, \varepsilon) > 0$. We note that the bifurcation diagram of the HR-model does not display a U-shaped Hopf bifurcation curve as that observed for other excitable systems (see [14–16,19]).

Fig. 1 also shows four homoclinic bifurcation curves (green and black) for different values of ε . The lowest value (black) is for

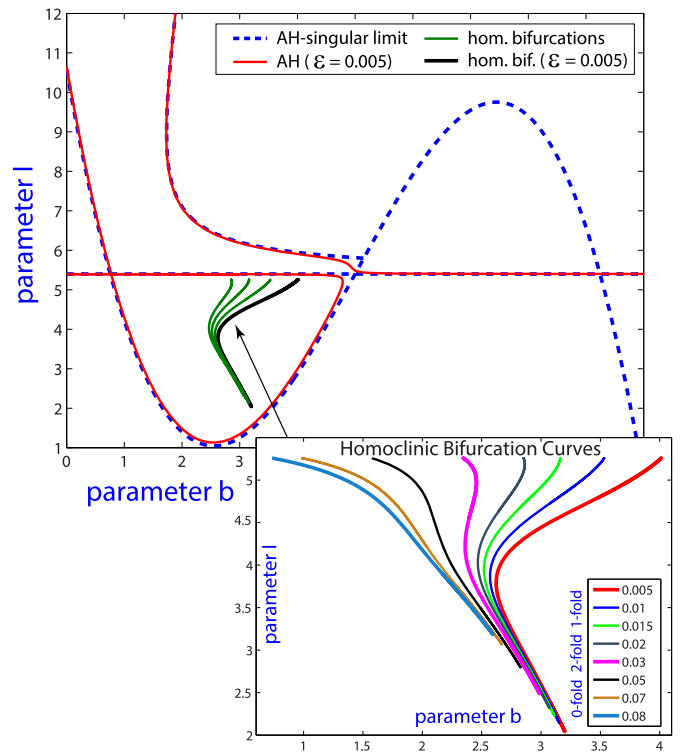


Fig. 1. Some features of the bifurcation diagram for the Hindmarsh–Rose model. Dashed blue curves show the set S of curves satisfying (6), (7) and (8), which contains the singular limit ($\varepsilon = 0$) of AH bifurcations in the full system. AH bifurcations (solid red) are shown for $\varepsilon = 0.005$. Note that not the whole set S is part of the singular limit. Homoclinic bifurcations (solid green and black) are shown for different values of ε (the lowest value (black) corresponds to $\varepsilon = 0.005$). In the magnification the first primary homoclinic bifurcations curves are shown for different values of ε . As the small parameter ε increases, the number of “visible” foldings (with respect to b) of the homoclinic curve changes. (For interpretation of the colors in this figure, the reader is referred to the web version of this article.)

$\varepsilon = 0.005$. In this case (for small values of ε), as for the systems considered in [14–16,19], homoclinic bifurcation curves are C-shaped. Numerical simulations show that there is a singular limit for the homoclinic bifurcations. Nevertheless, unlike the model studied in [15], a characterization of such singular limit involves extra difficulties and we pose this question as an open question for the next future. Anyway, it must be noticed that, as in [2,15], according to the numerical simulations, the homoclinic bifurcations curves do not terminate at a point approaching the set S . On the contrary, at both “ends” there is a sharp turning of the curve. However, this will make clear in the next section.

3. Homoclinic bifurcations

Of course, as already argued, an essential piece to get the whole picture of the dynamics emerging in the HR-model is to understand the role of the singular limit as the source of a puzzling bifurcation diagram. Nevertheless, to have a deeper knowledge of the model, it is also crucial to study a wider range of time scales of the slow variable z . In this approach, the latest goal should be to find organizing centers located not necessarily close to the singular limit and to understand how the bifurcations evolve as ε decreases. Hence, from a different perspective, this approach could be helpful to give some insight into the global picture that we already know to be very entangled for $\varepsilon \ll 1$.

Since this paper focuses mainly on the role played by the homoclinic bifurcation, we study how they evolve as ε varies (in this paper we just show the first primary homoclinic orbits, related with the first spike-adding process [2]). The numerical results dis-

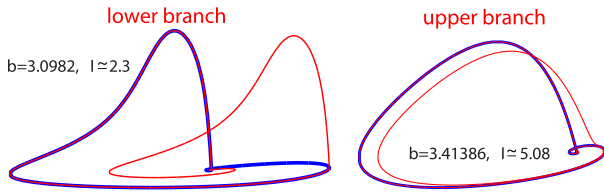


Fig. 2. Homoclinic orbits for parameter values in each of the two branches arising close to the lower and upper “endings or turning-points” of the homoclinic bifurcation curve for $\varepsilon = 0.01$. The selected value of b is the same in both cases of each branch, but the values of l corresponding to each homoclinic orbit (red and blue in each case) are slightly different as they correspond to different orbits of the double-cover homoclinic. (For interpretation of the colors in this figure, the reader is referred to the web version of this article.)

played in Fig. 1 show that the shape of the homoclinic bifurcations curves changes as ε increases. At this scale we clearly see three different shapes that we classify according to the number of “visible” folds in parameter b (the reason to say “visible” will be clear later). For ε small enough there is only one visible folding; these are the C-shaped curves already mentioned in Section 2 (the “standard” shape for slow-fast-systems [14–16,19]). For intermediate values there are two visible folding points in b , and as ε increases both visible foldings disappear. Moreover, an extra (and different) folding occurs at each “end” of the different branches of the homoclinic curves, giving a very sharp turn and so the curve doubles back on itself giving rise to a double-cover homoclinic curve (as shown in [2] for one value of ε). Fig. 2 shows two different homoclinic orbits obtained for parameter values at different branches at the lower and upper sharp folds (the value b is the same in both cases but the values of l are slightly different). The shape and relative position of the lower fold seems to be similar in all cases we have explored. On the contrary, the upper fold moves significantly in the biparametric plot as ε increases, as Fig. 1 shows.

4. Spike-adding and homoclinic bifurcations

From the observations of the previous section a clear question is: which consequences (if any) have the change of shape of the first primary homoclinic bifurcations curves?

First we remark that several recent works [2,5,6,11,12] were specifically focused on detailed studies of global bifurcations of tonic spiking and bursting orbits giving rise to chaotic dynamics in the HR model. In [2,6], the appearance of Orbit-Flip (OF) and Inclination-Flip (IF) codimension-two points in the primary homoclinic bifurcation curve was linked to the spike-adding process for square-wave (or fold/hom) bursting. Also, in [6] it was shown how these points give rise to the different macro-chaotic regions and a global scheme was proposed.

In order to observe in more detail the changes depending on the small parameter we show in Fig. 3 a three-parametric plot (ε on the vertical axis) with the first primary homoclinic bifurcation curves (blue lines) at different values of ε and a three-parameter continuation of the curve (green line) of the codimension-two Inclination-Flip points. The IF points play a relevant role for small values of ε , as shown in [2,6], because they are organizing centers of the pencils of period-doubling and fold bifurcations emanating from the OF points. All these points provide a complete picture of the spike-adding process, but when ε grows the IF points disappear, and so now the global structure has changed. It is interesting to remark that the disappearance of the IF points seems to take place in a codimension-three “fold” of IF points close to the parameter values $b = 2.525$, $l = 4.348$ and $\varepsilon = 0.0197$. The curve of codimension-two IF points also disappears when ε decreases in one side of the curve, but this fact may be related with numerical precision problems (in Fig. 4 we present

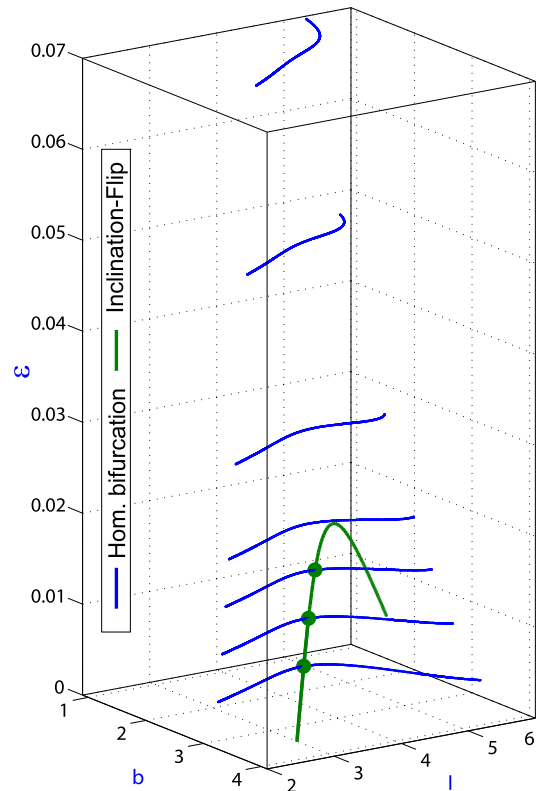


Fig. 3. A three-parametric plot (ε on the vertical axis) with the first primary homoclinic bifurcation curves (blue lines) at different values of ε and a three-parameter continuation of the curve (green line) of the codimension-two Inclination-Flip points. (For interpretation of the colors in this figure, the reader is referred to the web version of this article.)

all the IF points detected by AUTO for the corresponding ε values). All these facts are part of the current research of the authors.

In order to observe the changes originated from the disappearance of the IF points we use another very interesting approach, the spike-counting (SC) method, that works well for a neuron model when a bursting solution follows closely the slow motion manifolds of the fast subsystem and makes pronounced rapid jumps between them, thus defining the number of spikes per bursts in the voltage traces. Indeed, the spike number within a burst is that of the complete revolutions of the bursting orbit around the spiking manifold M_{IC} . In the spike-counting technique [5,12], a fixed number of spikes per burst is an indication of regular bursting, while unpredictably varying numbers are associated with chaotic bursting. Fig. 4 represents bi-parameter sweeps of the HR model in the (b, l) -plane for $\varepsilon = 0.01, 0.03$ and 0.05 , that are done with the spike-counting approach. The parameter plane is clearly demarcated into regions corresponding to quiescence (convergence to an equilibrium point), periodic tonic spiking, chaotic and regular bursting. The obtained maps are color-coded, so, the spike numbers are associated with specific colors. The resulting diagram can be easily read and interpreted: the region shown in a dark blue color is for stable spiking activity which can be treated as bursting with a single spike. The diagram reveals a global organization of spike-adding bifurcations occurring on borderlines between the corresponding stripes in the blue hue, which all correspond to square-wave bursting on the model. Stripes of gradually changing colors correspond to bursting with incrementally varying numbers of spikes due to a spike-adding cascade. Bursting becomes chaotic near the transitions to tonic spiking in a chain of “onion bulb scales”- shaped regions [6]. Decreasing the value of ε , which determines the dynamics of the slow z -variable, does not change

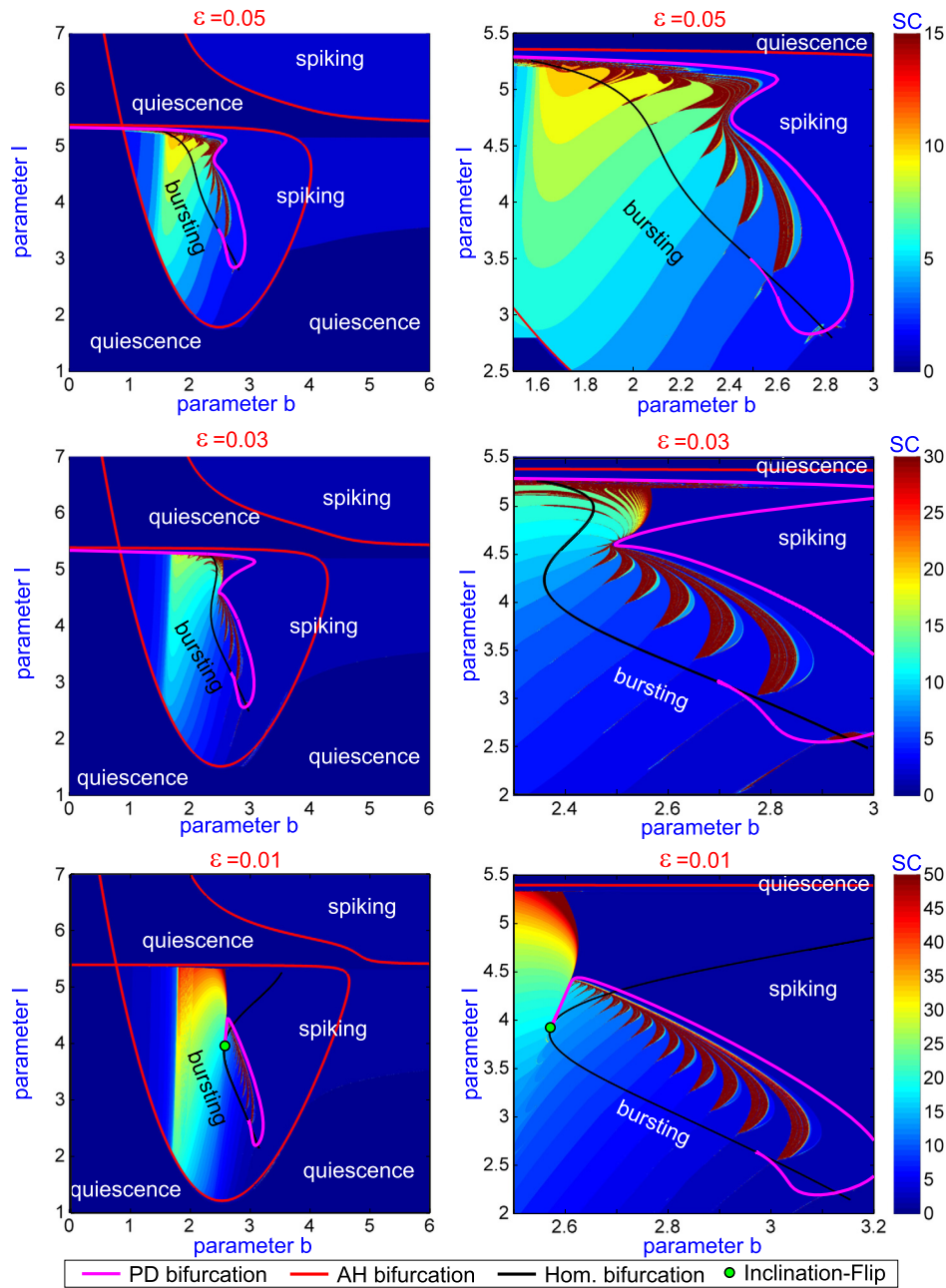


Fig. 4. Bi-parametric plot (plane (b, l)) of the HR-model at three values of ε , where the different colors indicate the number of spikes per period (spike-counting technique) and, superimposed, the bifurcation curves that demarcate the borderlines of the regions of colors ranging from blue to red and corresponding to spike numbers (vertical bar). Curves shown in pink, red and black correspond to period-doubling, Andronov–Hopf (AH) and primary homoclinic (Hom) bifurcations. The green dot corresponds to an Inclination-Flip codimension-two bifurcation point. Right column corresponds to a magnification of the bursting region. (For interpretation of the colors in this figure, the reader is referred to the web version of this article.)

qualitatively the structure of the parameter plane but compresses it. Therefore, for simplicity we do not consider values of $\varepsilon < 0.01$.

Detailed bifurcation analysis were presented in [6,12]. In this paper, as before, we just focus our attention into the AH and homoclinic bifurcations when different values of the small parameter ε are used. The AH-bifurcation curves do not change their shape, but, as shown in the previous section, the shape of the homoclinic bifurcation curve changes, passing from 1-fold (C-shape) in the b parameter to 2 (Z-shape) and later to 0. These changes originate also changes in the spike-adding process and in the chaotic regions. In all three cases, the spike-adding process follows the scheme shown in [2,6], but in the C-shape there is no spike-adding process in the upper branch, while in the other cases the spike-adding process continues and in the case of no “visible” folds

the spike-adding is continued by a spike-deleting process. Also, the chaotic “onion bulbs” are present in the lower branch for the C-shape, whereas in the other two cases they are present along all the homoclinic bifurcation curve. Moreover, the change in the number of “visible” folds is located in the range of values of the parameter ε where the disappearance of the IF points (green dots) occurs. To study its relation with the change of the global picture we present also the first period-doubling curve (pink curve) that delimits the spiking region and we observe how, as the IF is no more present, the curve goes far away for high values of ε , whereas for small values the IF point attracts all these bifurcation curves.

The influence of the fact that the bifurcation curves end at the IF, or not, gives rise to another important feature. In Fig. 5

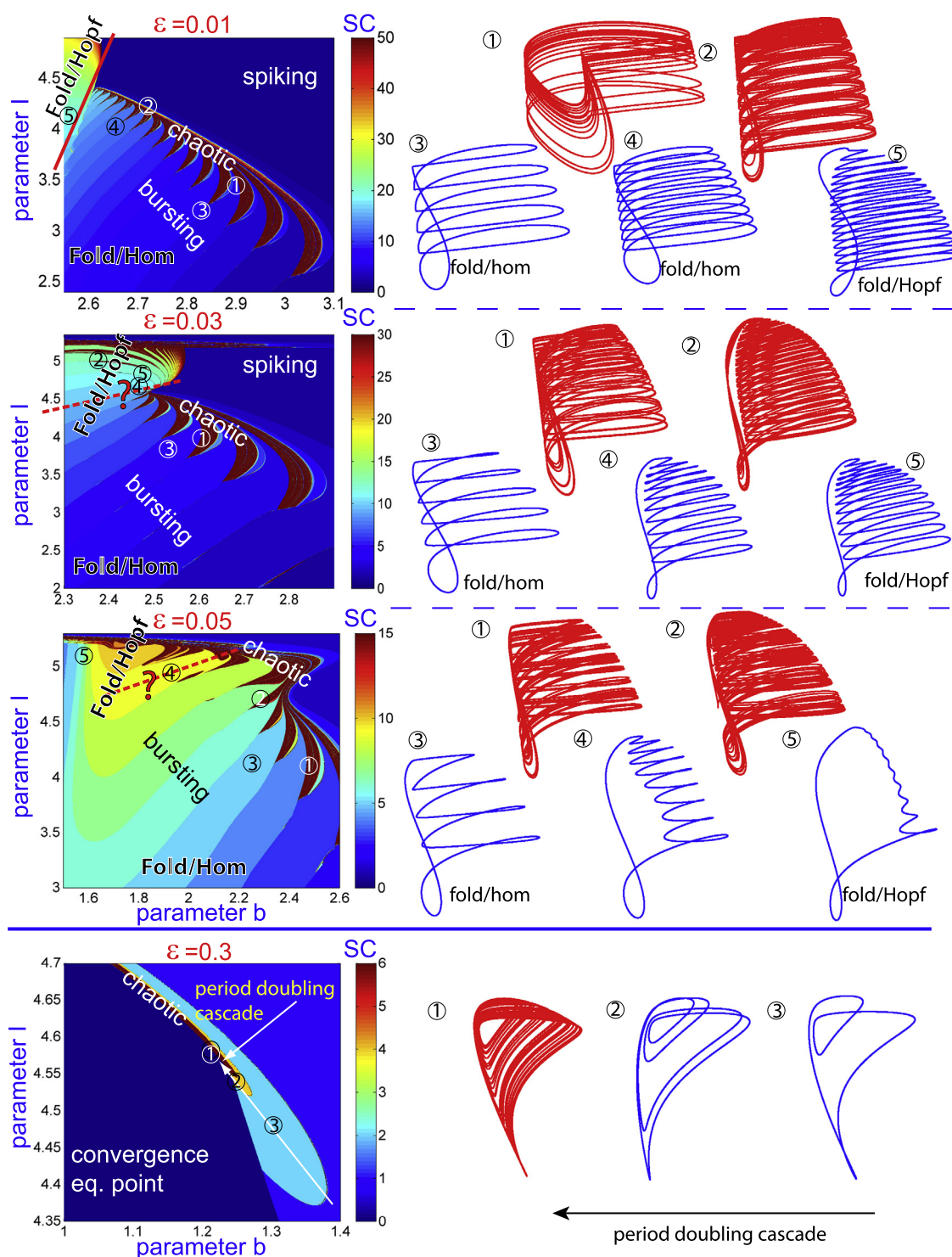


Fig. 5. Evolution of the orbits (stable periodic orbits (blue) and chaotic ones (red)) for different values of the parameter ε . On the left SC bi-parametric plots (plane (b, I)) showing the position of the different orbits and the change with ε in the spike-adding process and chaotic regions (in dark red). Regions with Fold/Hom and Fold/Hopf bursting behavior are shown (in case $\varepsilon = 0.01$ the regions are quite delineated, but in the other cases the change is more gradual without a clear boundary). (For interpretation of the colors in this figure, the reader is referred to the web version of this article.)

we present on the left the SC sweeping technique for four values of ε , in this case considering also a value clearly far from small ($\varepsilon = 0.3$). The case $\varepsilon = 0.01$ is clearly slow-fast, with the chaotic and periodic orbits with spikes around the fast spiking manifold M_{IC} . Moreover, if we observe the SC diagram there are two clearly defined areas in the bursting region (shown by the continuous straight red line that it is delined by the IF point and the bifurcation curves ending to it) of fold/hom (or square-wave) and fold/Hopf (or plateau-like) bursting behavior. The difference of the orbits is evident from the right figures. On the contrary, increasing the value of ε , as the IF point is no more present there is not a clear boundary. For $\varepsilon = 0.03$ and 0.05 we observe that now there is also fold/hom and fold/Hopf bursting behavior, but now we cannot give a precise limit of each behavior (so we have plotted a discontinuous red line with an interrogant on the area where the change seems to occur). This fact has clear biological interest as now there is a small change when varying the parameter as the geometry of the orbits is quite similar (when ε is small in the area of changing from fold/hom to fold/Hopf the difference is quite big). We also remark that, when ε grows, the dynamics of the system maintains some of the slow-fast features (spike-adding, chaotic stripes, ...) but now the spiking process is more and more similar to the funnel structures created around focus equilibria in Rössler-like systems (see [20]).

For large values of ε ($\varepsilon = 0.3$) we observe that the structure is not the same, and now the spike-adding process is not observed, being present a classical period-doubling phenomena giving rise to a small chaotic area, that is, now the system is not a slow-fast system, it is just another 3D dynamical system with oscillatory behavior around focus equilibria. The other three values of ε maintains some slow-fast dynamics.

A deep analysis of the changes from the limit case ($\varepsilon \searrow 0$) to the case $\varepsilon = \mathcal{O}(1)$ is part of our current research [21].

5. Conclusions

In this article, we present new approaches to study the dynamics arising in the HR model. Andronov–Hopf and homoclinic bifurcations play an essential role in the understanding of the whole picture. We have computed the singular limit of the Andronov–Hopf bifurcations in the family and checked that for each $\varepsilon > 0$ small, one of the Hopf bifurcation curves forms a loop which bounds all the rich variety of behaviors displayed by the system. This differs from other models considered in the literature where the Andronov–Hopf bifurcation curve (for fixed ε) adopts an U-shape as it tends to the singular limit (see [15]). On the other hand, although it is well known that homoclinic bifurcations of codimension-one or higher are key pieces in the organization of the bifurcations diagrams, this paper shows that this role extends from the singular limit up to, at least moderately, large values of ε . The variations in the shape of a principal homoclinic bifurcation curve were explored starting close to its singular limit and increasing the values of ε to get images of the behavior far from the slow-fast scenario. It becomes evident that close to the singular limit it adopts a C-shape with a unique principal “visible” folding point. As ε increases, the Inclination-Flip codimension-two points disappear, generating a smooth change from fold/hom and fold/Hopf bursting behavior. Moreover, although spike-adding and chaotic regions are present, the way in which new regions with differenced dynamics emerge is clearly different. The different shapes of the homoclinic bifurcation curves seem to be related to these changes in the dynamics.

As already mentioned, our current research is addressed to get a deeper insight in the manner in which the whole bifurcation diagram evolves as ε moves in a long interval. This should also gives us some enlightenment in the understanding of the slow-fast

mechanisms that explain the fascinating variety of neuronal activities. Regarding this point, it will be necessary to complete the study of singular limits, particularly, for the case of homoclinic bifurcation curves. Moreover, new codimension-two organizing centers need to be detected. For instance, it is still far from being clear which are the bifurcations existing at the terminal points of homoclinic bifurcation curves.

Acknowledgements

R.B. has been supported during this research by the Spanish Research projects MTM2012-31883 and MTM2015-64095-P (MINECO/FEDER) and the European Social Fund and Diputación General de Aragón (Grant E48). S.I. has been supported by the Spanish Research project MTM2014-56953-P. The authors thank the reviewers for their constructive remarks.

References

- [1] A.L. Hodgkin, A.F. Huxley, A quantitative description of membrane current and its application to conduction and excitation in nerve, *J. Physiol.* 117 (1952) 500–544.
- [2] D. Lino, A. Champneys, M. Desroches, M. Storace, Codimension-two homoclinic bifurcations underlying spike adding in the Hindmarsh–Rose burster, *SIAM J. Appl. Dyn. Syst.* 11 (3) (2012) 939–962.
- [3] M. Desroches, T.J. Kaper, M. Krupa, Mixed-mode bursting oscillations: dynamics created by a slow passage through spike-adding canard explosion in a square-wave burster, *Chaos* 23 (4) (2013) 046106, <http://dx.doi.org/10.1063/1.4827026>.
- [4] J.L. Hindmarsh, R.M. Rose, A model of neuronal bursting using three coupled first order differential equations, *Proc. R. Soc. Lond. B, Biol. Sci.* 221 (1222) (1984) 87–102, <http://dx.doi.org/10.1098/rspb.1984.0024>.
- [5] R. Barrio, A. Shilnikov, Parameter-sweeping techniques for temporal dynamics of neuronal systems: case study of Hindmarsh–Rose model, *J. Math. Neurosci.* 1 (2011) 6.
- [6] R. Barrio, M. Angeles-Martínez, S. Serrano, A. Shilnikov, Macro- and micro-chaotic structures in the Hindmarsh–Rose model of bursting neurons, *Chaos* 24 (2) (2014), <http://dx.doi.org/10.1063/1.4882171>.
- [7] J.M. González-Miranda, Observation of a continuous interior crisis in the Hindmarsh–Rose neuron model, *Chaos* 13 (3) (2003) 845–852, <http://dx.doi.org/10.1063/1.1594851>.
- [8] J.M. González-Miranda, Complex bifurcation structures in the Hindmarsh–Rose neuron model, *Int. J. Bifurc. Chaos* 17 (09) (2007) 3071–3083, <http://dx.doi.org/10.1142/S0218127407018877>.
- [9] G. Innocenti, A. Morelli, R. Genesio, A. Torcini, Dynamical phases of the Hindmarsh–Rose neuronal model: studies of the transition from bursting to spiking chaos, *Chaos* 17 (4) (2007) 043128, <http://dx.doi.org/10.1063/1.2818153>.
- [10] G. Innocenti, R. Genesio, On the dynamics of chaotic spiking-bursting transition in the Hindmarsh–Rose neuron, *Chaos* 19 (2) (2009) 023124, <http://dx.doi.org/10.1063/1.3156650>.
- [11] A. Shilnikov, M. Kolomiets, Methods of the qualitative theory for the Hindmarsh–Rose model: a case study. A tutorial, *Int. J. Bifurc. Chaos* 18 (8) (2008) 2141–2168.
- [12] M. Storace Lino, E. de Lange, The Hindmarsh–Rose neuron model: bifurcation analysis and piecewise-linear approximations, *Chaos* 18 (2008) 033128.
- [13] D. Terman, Chaotic spikes arising from a model of bursting in excitable membranes, *SIAM J. Appl. Math.* 51 (5) (1991) 1418–1450, <http://dx.doi.org/10.1137/0151071>.
- [14] A.R. Champneys, V. Kirk, E. Knobloch, B.E. Oldeman, J. Sneyd, When Shil'nikov meets Hopf in excitable systems, *SIAM J. Appl. Dyn. Syst.* 6 (4) (2007) 663–693, <http://dx.doi.org/10.1137/070682654>.
- [15] J. Guckenheimer, C. Kuehn, Homoclinic orbits of the FitzHugh–Nagumo equation: the singular-limit, *Discrete Contin. Dyn. Syst.* 2 (4) (2009) 851–872, <http://dx.doi.org/10.3934/dcds.2009.2.851>.
- [16] J. Guckenheimer, C. Kuehn, Homoclinic orbits of the FitzHugh–Nagumo equation: bifurcations in the full system, *SIAM J. Appl. Dyn. Syst.* 9 (1) (2010) 138–153, <http://dx.doi.org/10.1137/090758404>.
- [17] E.J. Doedel, R. Paffenroth, A.R. Champneys, T.F. Fairgrieve, Y.A. Kuznetsov, B.E. Oldeman, B. Sandstede, X.J. Wang, AUTO2000, <http://cmvl.cs.concordia.ca/auto>.
- [18] E. Doedel, AUTO: a program for the automatic bifurcation analysis of autonomous systems, in: *Proceedings of the Tenth Manitoba Conference on Numerical Mathematics and Computing*, Vol. I, Winnipeg, Man., 1980, vol. 30, 1981, pp. 265–284.
- [19] J. Guckenheimer, H.M. Osinga, The singular limit of a Hopf bifurcation, *Discrete Contin. Dyn. Syst.* 32 (8) (2012) 2805–2823, <http://dx.doi.org/10.3934/dcds.2012.32.2805>.

- [20] R. Barrio, F. Blesa, S. Serrano, Qualitative analysis of the Rössler equations: bifurcations of limit cycles and chaotic attractors, *Phys. D* 238 (2009) 1087–1100.
- [21] R. Barrio, S. Ibáñez, L. Pérez, Different spike-adding processes in neuron models, preprint.

4.2 Paper II

In the present article [5] we delve into the homoclinic structure of the Hindmarsh-Rose in the (b, I, ε) parameter space, completing the results obtained in paper I. An exhaustive study of the homoclinic bifurcation structure and its degeneracies is presented.

In particular, the homoclinic structures corresponding to the case of 1 to 2 spikes, 2 to 3 and 11 to 12 are considered. We investigate what happens with these structures with the system is far from the fast-slow scenario. The well-known software AUTO was used to compute sufficient homoclinic curves in the (b, I) plane for different values of ε so that the homoclinic surfaces could be visualised.

We have found numerical evidences showing that the homoclinic bifurcation curves in the (b, I) plane are isolas, with the exterior face corresponding to n spikes and the interior face to $n + 1$. For that reason we use the notation $hom^{(n, n+1)}$. The computation of $hom^{(n, n+1)}$ curves reveals that, in the cases $n > 1$, for small values of ε , there is not a unique isola but two, and when ε increases these two isolas joint each other forming a unique close curve. We have also observed that there is a correlation between the ε -level reached by each surface $hom^{(n, n+1)}$ in the (b, I, ε) parameter space and the existence of bursting of n spikes for the corresponding value of ε .

Special attention has been paid to the codimension-two degeneracies (namely orbit flips, inclination flips and Belyakov points). We have studied how the codimension-two points move on the homoclinic bifurcation curves in the (b, I) plane as ε increases, and how they disappear due to different mechanisms. These mechanisms include codimension-three phenomena, where different codimension-two curves in the (b, I, ε) parametric space collide; folding processes, which constitute the so-called 2+1 codimension phenomena; and the shrinking in the size of the homoclinic curves, which prevents homoclinic bifurcations whose corresponding equilibria have associated real eigenvalues (a necessary condition for the existence of orbit and inclination flips and Belyakov points).

It is found that the disappearance of codimension-two points due to a folding processes leads to relevant changes in the bifurcation diagram. In particular, it is illustrated how two different period-doubling curves, each arising from a different inclination flip point, joint each other forming a unique curve after the two inclination flips collide. This evolution in the arrangement of the codimension-one bifurcation curves may explain the deformation of the spike-counting map that occurs when ε increases.

Our findings allow us to propose a theoretical scheme of the global homoclinic structure that organises the bursting dynamics of the model.

Homoclinic organization in the Hindmarsh-Rose model: A three parameter study

Cite as: Chaos **30**, 053132 (2020); <https://doi.org/10.1063/1.5138919>

Submitted: 16 November 2019 . Accepted: 24 April 2020 . Published Online: 18 May 2020

Roberto Barrio , Santiago Ibáñez , and Lucía Pérez

COLLECTIONS

 This paper was selected as Featured



[View Online](#)



[Export Citation](#)



[CrossMark](#)



NEW!

Sign up for topic alerts
New articles delivered to your inbox



Homoclinic organization in the Hindmarsh–Rose model: A three parameter study

Cite as: Chaos 30, 053132 (2020); doi: 10.1063/1.5138919
Submitted: 16 November 2019 · Accepted: 24 April 2020 ·
Published Online: 18 May 2020



View Online



Export Citation



CrossMark

Roberto Barrio,^{1,a)}  Santiago Ibáñez,^{2,b)}  and Lucía Pérez^{2,c)}

AFFILIATIONS

¹Departamento de Matemática Aplicada and IUMA, University of Zaragoza, E-50009 Zaragoza, Spain

²Departamento de Matemáticas, University of Oviedo, E-33007 Oviedo, Spain

^{a)} Author to whom correspondence should be addressed: rbarrio@unizar.es

^{b)} Electronic mail: mesa@uniovi.es

^{c)} Electronic mail: perezplucia@uniovi.es

ABSTRACT

Bursting phenomena are found in a wide variety of fast–slow systems. In this article, we consider the Hindmarsh–Rose neuron model, where, as it is known in the literature, there are homoclinic bifurcations involved in the bursting dynamics. However, the global homoclinic structure is far from being fully understood. Working in a three-parameter space, the results of our numerical analysis show a complex atlas of bifurcations, which extends from the singular limit to regions where a fast–slow perspective no longer applies. Based on this information, we propose a global theoretical description. Surfaces of codimension-one homoclinic bifurcations are exponentially close to each other in the fast–slow regime. Remarkably, explained by the specific properties of these surfaces, we show how the Hindmarsh–Rose model exhibits isolas of homoclinic bifurcations when appropriate two-dimensional slices are considered in the three-parameter space. On the other hand, these homoclinic bifurcation surfaces contain curves corresponding to parameter values where additional degeneracies are exhibited. These codimension-two bifurcation curves organize the bifurcations associated with the spike-adding process and they behave like the “spines-of-a-book,” gathering “pages” of bifurcations of periodic orbits. Depending on how the parameter space is explored, homoclinic phenomena may be absent or far away, but their organizing role in the bursting dynamics is beyond doubt, since the involved bifurcations are generated in them. This is shown in the global analysis and in the proposed theoretical scheme.

Published under license by AIP Publishing. <https://doi.org/10.1063/1.5138919>

As a fundamental element in the study of nervous system dynamics, the analysis of behaviors and changes in isolated neurons is a first step in the theoretical/experimental research in mathematical/computational neuroscience. In addition, it is common to find synchronization in neuronal networks showing dynamical states that include different bursting regimes. From the physiological point of view, bursting is characterized by trains of spikes alternating with quiescent periods. Studying the different changes in the bursts fired by an isolated neuron will help provide detailed mathematical mechanisms to explain them. This work aims to understand the hidden mechanisms behind the processes that lead neurons to add (or subtract) spikes in a signal: the homoclinic bifurcations (in the case of fold/hom bursters). Their relationship with the processes of creation of new spikes has been discussed earlier in the literature, but the global picture is not yet fully understood. We work with the Hindmarsh–Rose (HR) neuron model, one of the most popular neuronal dynamics models. To perform the analysis, we use continuation techniques

and brute-force methods to locate and describe the changes. When exploring a three-dimensional space of parameters, we discover a complex structure of bifurcations that allows us to propose a new global structure, which we call, due to its geometry, homoclinic “mille-feuille” + “spines-of-the-book.” This skeleton of homoclinic bifurcations allows an explanation of the different phenomena observed in the literature, such as the influence of homoclinic bifurcations, even when not observed, the disappearance of bursting dynamics with a large number of spikes when the small parameter in the models grows (in fast–slow dynamics), and the spike-adding process.

I. INTRODUCTION

Fast–slow dynamics is a quite common phenomenon in theoretical and practical models in many disciplines where different time scales are present. Computational/mathematical neuroscience

is one of the fields where these models are more abundant. In neuroscience, to understand how an incredibly sophisticated system such as the brain *per se* functions dynamically, it is imperative to study the dynamics of its constitutive elements—neurons. Since Hodgkin and Huxley developed the first model of action potentials in the membrane,¹ the design of mathematical models for neurons has arisen as a trending topic in science for a few decades, and a lot of models and variations describing different kinds of neuron cells in numerous animals have been proposed in the literature. What all these systems have in common is the existence of fast–slow dynamics,² that is also quite usual in a lot of other practical applications, like in chemical reactions³ and laser dynamics.⁴ In all these models, one of the key magnitudes is the time that a neuron, or other dynamical system, is active, and this is related to the number of oscillations (spikes) in the fast subregime.

In order to help in the analysis of neuron models simulated realistically within the Hodgkin–Huxley framework,¹ a common approach is to use some simplified models. In particular, the 3D Hindmarsh–Rose (HR) model⁵ reproduces fairly well the basic oscillatory activities routinely observed in isolated biological cells and in neural networks. It fulfills the two basic conditions of being computationally simple but, at the same time, able to reproduce the main behavior (the rich firing patterns) exhibited by the real biological neuron. The HR model is described by three nonlinear ordinary differential equations,

$$\begin{cases} \dot{x} = y - ax^3 + bx^2 - z + I, \\ \dot{y} = c - dx^2 - y, \\ \dot{z} = \varepsilon[s(x - x_0) - z], \end{cases} \quad (1)$$

where x is the membrane potential, y the fast, and z the slow gating variables for ionic current. In our study, we will consider a typical choice of parameters: $a = 1$, $c = 1$, $d = 5$, $s = 4$, and $x_0 = -1.6$. Parameters b and I determine the bursting or spiking behavior and their values are considered in specific ranges where such phenomena are present. Parameter ε governs the fast–slow behavior and we will study dynamics for ε small, but including scenarios far from the singular limit $\varepsilon = 0$. In the sequel, we consider (1) as a family of vector fields depending on parameters (b, I, ε) , and, say, fast subsystem to refer to the z -family obtained after taking $\varepsilon = 0$.

Roughly speaking, we can say that a fast–slow system exhibits bursting when orbits exhibit periods of fast spiking followed by periods of quiescence. When the jump between these two different regimes can be explained by a fold bifurcation of equilibria and a homoclinic bifurcation of periodic orbits (both bifurcations occurring in the fast subsystem), we say that the bursting is of fold/hom type.⁶ In Sec. II (see Fig. 3), we will describe how fold/hom bursters arise in the HR model.

One of the big challenges regarding bursting phenomena is to understand the mechanisms explaining the variation in the number of spikes (Fig. 4 in Sec. II B provides an illustrative example in the HR model). These spike-adding processes have been studied for several mathematical neuron models (see, for example, Refs. 7–9), and also in other contexts such as laser dynamics, chemical reactions, or discrete maps, with the alternative name of period-adding.^{10–14} This process is quite important in that it progressively modifies the spectrum of periodic orbits of the system and the

structure of chaotic attractors.^{15–18} As argued by Terman,¹⁸ these transitions may be either continuous, with the period of the bursting solution increasing along the process or they may involve chaotic behaviors (see also Ref. 19). Recently, these transitions have been studied in detail²⁰ providing a theoretical scheme for ε fixed. The relevance of fold bifurcations of periodic orbits in this process was pointed out earlier in Ref. 21. Dealing with fold/hom bursting, the spike-adding process has also been related to the existence of canard orbits^{22–25} and with the existence of certain codimension-two homoclinic bifurcations.^{15,26,27} Working with a fixed value $\varepsilon = 0.01$, the role of homoclinic bifurcations of codimension-one and -two in the spike-adding mechanisms was discussed in Ref. 26 and some preliminary results were advanced. In particular, bifurcations of periodic orbits around flip and Belyakov bifurcations (see Sec. II A for background) were identified as crucial ingredients to understand some spike-adding transitions that are present in the HR model. Again, working with that fixed value of ε , codimension-two homoclinic bifurcations were again considered in Ref. 27, but providing a much more thorough study. Different homoclinic curves were discussed and their sharp fold points were already detected in that reference and linked to the spike-adding processes. Codimension-two homoclinic bifurcations in Refs. 26 and 27 are also organizing centers of chaotic regions in the bifurcation diagram. All these chaotic phenomena were discussed in Ref. 15.

What is missing in the literature is a global study of how homoclinic bifurcations are organized, and to that goal we need, at least, to describe them in a three-parameter space. Note that it is intrinsic to the notion of bifurcation the possibility of observing its effects without the bifurcation point being present. In the HR model, one can explore the parameter space without detecting homoclinic bifurcations (see Fig. 4), although their consequences (fold and period-doubling bifurcations) are exhibited. The organizing points (the codimension-two homoclinic bifurcations) may be placed far away in the space or parameters, and even, they may be outside a particular set of parameters that we are visualizing, but they continue being the organizing centers. Taking all of this into account, the goal of this article is to provide a model of the homoclinic organization that explains all these facts.

As already mentioned, previous work in the literature was focused in studying, for some ε fixed, the curves of homoclinic bifurcation at equilibria displayed by the system.^{15,26,27} A bifurcation diagram in a three-parameter space, including variation of ε , was first considered in Ref. 46. Changes in the spike-adding structures and the underlying bifurcations were observed. Moreover, foldings in the curves of inclination flip (IF) bifurcation were already detected. In Ref. 20, a theoretical scheme giving a complete scenario of bifurcations involved in the spike-adding processes in fold/hom bursters was introduced. This theoretical scheme provides a complete description of the connections of the different codimension-two points and the organization of the homoclinic curves for ε fixed. Also, in that paper, the validity of the scheme is checked for a pancreatic β -cell neuron model.

In this article, we are interested in understanding the global structure of the homoclinic surfaces in the three-parameter space. To that goal, a detailed numerical study with continuation techniques is required (we use the well-known software AUTO^{28,29})

as well as the spike counting (SC in the sequel) technique, as introduced in Refs. 15, 26, and 30.

Supported by numerical evidences, we conjecture that the intersection of each homoclinic surface with horizontal planes (with ε fixed) produces isolas in the plane of parameters (compare with results in Ref. 31 for the FitzHugh–Nagumo system), that is, simple closed curves in the corresponding slice. We show how, for each ε fixed, the model exhibits a finite number (number that grows when the small parameter decreases) of isolas corresponding to primary homoclinic bifurcations. Isolae are not only exponentially close to each other but they also exhibit a pair of extremely sharp folds so that the width of each isola is also exponentially small. These folds allow two sides of the isola to be distinguished (and also two faces of the surface of homoclinic bifurcations). On one of the faces, the corresponding homoclinic orbits on the fold/hom regime exhibit n spikes and, on the other face, $n + 1$. It is because of this fact that, from now on, we use the notation $hom^{(n,n+1)}$ to refer to the different homoclinic bifurcation surfaces (or isolae if working with two-parameter plots).

Remark 1. Notation $hom^{(n,n+1)}$ was already introduced in Ref. 20. In Refs. 26 and 27, the authors use a different option to label homoclinic bifurcation curves. In particular, they do not emphasize that a given homoclinic bifurcation curve can correspond to homoclinic orbits with a different number of spikes. For instance, in Ref. 27, the authors use the notation $hom^{(n)}$, where we use $hom^{(n,n+1)}$. Nevertheless, one should note that when required (see Figs. 4, 5, and 7 in Ref. 27), they also use two different notations for a unique curve of homoclinic bifurcation, changing the label from $hom^{(n)}$ to $hom^{(n+1)}$ after a sharp fold of the curve is crossed, pointing out that the number of spikes changes from n to $n + 1$.

Homoclinic surfaces are the main focus of this article. We show how they are disposed in the parameter space, taking into account that, as numerics show, they are exponentially close to each other when $\varepsilon \rightarrow 0$. Because of their tubular shape and the proximity of the surfaces, we can compare the whole structure with a “mille-feuille” pastry. There, we observe pencils of curves of fold and period-doubling (PD) bifurcations of periodic orbits generated on codimension-two bifurcation points. Moving ε , each of the curves in the pencil gives rise to a surface. Hence, we can compare the codimension-two bifurcation curves with the “spines-of-a-book” with pages correspondent to surfaces of bifurcations of periodic orbits. Besides, the ε -level reached by each surface $hom^{(n,n+1)}$ decreases as n increases. This allows us to explain the simplification mechanisms (bursting with a lower number of spikes) that can be observed as ε increases.

The article is organized as follows. In Sec. II, we provide general information about the HR model: fast–slow decomposition, spike-adding process linked to fold/hom bursters exhibited by the model, and a discussion about existence of equilibria in the full system. A short survey about homoclinic bifurcations is also provided in Sec. II. In Sec. III, we pay attention to some particular slices (with ε fixed) inside the three-parameter space. Here, we show how the base shape of the homoclinic curves evolves as ε varies, but much more significantly, how the codimension-two homoclinic bifurcation points move on the homoclinic curves and, in fact, how they disappear when ε grows. Section IV presents a three-parameter

study explaining some of the phenomena that are observed when ε is fixed and shows isolae of codimension-one homoclinic bifurcations. Section V introduces the global theoretical scheme creating the structure that we call “homoclinic mille-feuille,” bearing in mind the codimension-one bifurcation surfaces. In them, we find “spines-of-a-book,” bearing in mind the codimension-two bifurcation curves, holding pencils of bifurcations of periodic orbits. Both structures give rise to the theoretical model proposed in this article. Finally, we present some conclusions in Sec. VI.

II. BACKGROUND

In this section, we recall some basic aspects about homoclinic bifurcations and fast–slow dynamics, including a description of fold-hom bursters, one of the mechanisms exhibited by the HR model for the creation of bursting orbits. In addition, to facilitate further discussions, the equilibrium points displayed by the full system (1) are explained. In our revision on bifurcations, only those that play a relevant role in the global organization of dynamics in the HR model are included.

A. Homoclinic bifurcations

First, we review some theoretical features regarding homoclinic bifurcations. For additional details and references, see Ref. 37 or for the books Refs. 38 and 39. Refs. 40–43 are essential, but technical.

Consider a smooth family of vector fields X_μ on \mathbb{R}^3 with $\mu \in \mathbb{R}^k$ and suppose that there exist $\mu_0 \in \mathbb{R}^k$ and $p_0 \in \mathbb{R}^3$ such that p_0 is a saddle-type hyperbolic equilibrium of X_{μ_0} . Without loss of generality, we assume that $\mu_0 = 0$ and $p_0 = 0$. Let $W^s(0)$ [respectively, $W^u(0)$] be the stable (respectively, unstable) invariant manifolds of X_0 at 0. Up to time reversal, we can assume that $\dim(W^s(0)) = 1$.

To state certain conditions, we will need to use the notions of strong unstable manifold and center stable manifold. Assume that $DX_0(0)$ has real eigenvalues λ_s, λ_u and λ_{uu} with $\lambda_s < 0 < \lambda_u < \lambda_{uu}$. The strong unstable manifold $W^{uu}(0)$ is a one-dimensional invariant manifold whose tangent space at 0 is given by the eigenspace corresponding to the eigenvalue λ_{uu} (the so called strong unstable direction). On the other hand, the center stable manifold $W^{cs}(0)$ is a two-dimensional invariant manifold whose tangent space at 0 is given by the eigenspace corresponding to the eigenvalues λ_u and λ_s .

Let $\Gamma_0 \subset W^s(0) \cap W^u(0)$ be a homoclinic orbit. In the sequel, we assume that the family X_μ unfolds Γ_0 generically. To understand this condition, consider a cross section Σ at a point in Γ_0 and define the distance $\Delta(\mu)$ between the point $W^s(p_\mu) \cap \Sigma$ and the curve $W^u(p_\mu) \cap \Sigma$, where p_μ denotes the saddle type hyperbolic equilibrium of X_μ , which exists close to 0 for μ to be small enough. We say that Γ_0 is generically unfolded with respect to μ if $D_\mu \Delta(0) \neq 0$. Under this generic assumption, there always exists a hypersurface H in the parameter space such that $0 \in H$ and X_μ has a homoclinic orbit asymptotic to p_μ for all $\mu \in H$.

There exist four classes of codimension-one homoclinic orbits.

- Case 1 Eigenvalues of $DX_0(0)$ are λ_s, λ_u and λ_{uu} , with $\lambda_s < 0 < \lambda_u < \lambda_{uu}$ and $\lambda_s + \lambda_u > 0$.
- Case 2 Eigenvalues of $DX_0(0)$ are λ_s, λ_u and λ_{uu} , with $\lambda_s < 0 < \lambda_u < \lambda_{uu}$ and $\lambda_s + \lambda_u < 0$. Moreover,

(H1) $\Gamma_0 \not\subset W^{uu}(0)$.

(H2) $W^{cs}(0)$ intersects $W^u(0)$ transversally along Γ_0 .

Case 3 Eigenvalues of $DX_0(0)$ are $\lambda_s < 0$ and $\rho_u \pm \omega_u i$, with $\rho_u > 0$, $\omega_u \neq 0$ and $\lambda_s + \rho_u > 0$.

Case 4 Eigenvalues of $DX_0(0)$ are $\lambda_s < 0$ and $\rho_u \pm \omega_u i$, with $\rho_u > 0$, $\omega_u \neq 0$ and $\lambda_s + \rho_u < 0$.

Conditions $\lambda_s + \lambda_u \neq 0$ and $\lambda_s + \rho_u \neq 0$ are non-resonance hypothesis. Condition (H1) implies that Γ_0 is tangent to the weak unstable direction, that is, the direction given by the eigenspace associated with the weak unstable eigenvalue λ_u . Condition (H2) is a “non-inclination” property.

In Case 1 and Case 3, a single unstable (repelling) periodic orbit is born from the homoclinic connection for parameter values on one side of the hypersurface H . In Case 2, a saddle periodic orbit emerges from the homoclinic orbit. Its stable manifold is orientable or not, depending on the orientability of $W^u(0)$. In Case 4, there exist infinitely many saddle-type periodic orbits in any neighborhood of the homoclinic orbit. In fact, as argued in Ref. 44, there exist infinitely many horseshoes in any neighborhood of the homoclinic orbit Γ_0 . When the connection is destroyed, finitely many of the horseshoes persist and hence it follows the existence of an infinite number of periodic solutions. The appearance or disappearance of horseshoes is accompanied by unfoldings of homoclinic tangencies of saddle-type periodic orbits and hence, strange repellers should emerge.^{35,36,45} Readers can find more extended explanations about all these bifurcation results in Refs. 37 and 38.

Regarding codimension-two homoclinic bifurcations, we only pay attention to the inclination flip, orbit flip (OF), and Belyakov bifurcations because they are the only cases that we will discuss in the context of the Hindmarsh–Rose model. So, we distinguish the cases below.

Inclination Flip (IF): Assume all conditions in Case 2 except (H2), that is, we assume that the intersection between $W^{cs}(0)$ and $W^u(0)$ is non-transversal along Γ_0 .

Orbit Flip (OF): Assume all conditions in Case 2 except (H1), that is, we assume that $\Gamma_0 \subset W^{uu}(0)$.

Belyakov Point: Assume that the equilibrium point is a saddle-node (SN) with eigenvalues λ_s and λ_u with $\lambda_s < 0 < \lambda_u$. The eigenvalue λ_u has geometric multiplicity one and algebraic multiplicity two.

To characterize different types of inclination and orbit flip bifurcations, we need to introduce the following ratios between eigenvalues:

$$\alpha = -\frac{\lambda_{uu}}{\lambda_s}, \quad \beta = -\frac{\lambda_u}{\lambda_s}. \tag{2}$$

Note that $\alpha > \beta$.

Bifurcation diagrams corresponding to IF and OF bifurcation points are quite similar and they can be described simultaneously. First, we observe that the hypersurface H of homoclinic bifurcation splits into two regions separated by a manifold of codimension-two homoclinic bifurcations. The orientation of the unstable invariant manifold at the equilibrium point reverses when such manifold is crossed.

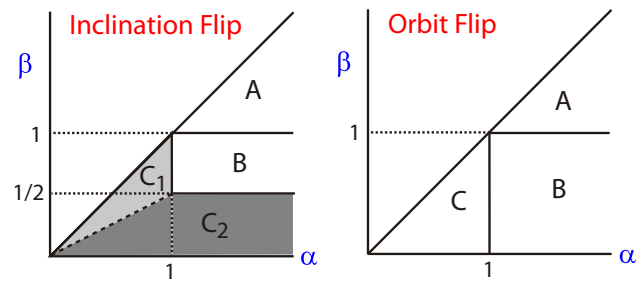


FIG. 1. Types of inclination and orbit flips. Values of the ratios α and β are given in (2).

For either IF or OF bifurcations, there are three cases (see Fig. 1):

	Inclination flip	Orbit flip
Case A	$\beta > 1$	$\beta > 1$
Case B	$\alpha > 1$ and $\frac{1}{2} < \beta < 1$	$\beta < 1$ and $\alpha > 1$
Case C	$\alpha < 1$ or $\beta < \frac{1}{2}$	$\alpha < 1$

We are only interested in Case C because the other two cases are not detected in our exploration of the HR model. Homoclinic flip bifurcations in Case C require additional generic assumptions. In particular, for inclination flips, we assume:

- (I1) $\beta \neq \frac{1}{2}\alpha$.
- (I2) If $\beta > \frac{1}{2}\alpha$ (region C_1 in the left panel of Fig. 1), the homoclinic orbit does not lie in the unique smooth leading unstable manifold.
- (I3) If $\beta < \frac{1}{2}\alpha$ (region C_2 in the left panel of Fig. 1), there is a quadratic tangency between $W^{cs}(0)$ and $W^u(0)$ along the homoclinic orbit.

Remark 2. Regions labeled SN1 (red) and SN2 (white) in the bottom panels shown for each ε in Figs. 5 and 6 correspond to saddle-node equilibria where conditions $\beta > \frac{1}{2}\alpha$ and $\beta < \frac{1}{2}\alpha$, respectively, are satisfied.

On the other hand, for orbit flips in Case C, we assume:

- (O1) $W^{cs}(0)$ intersects $W^u(0)$ transversally along Γ_0 .

Hypothesis (I2) [respectively, (I3)] makes sense in the region C_1 (respectively, C_2) depicted in Fig. 1. We do not extend in details about these two cases because they make no difference in the unfoldings. The essential distinction has to do with the way in which the unstable manifold approach the origin when it is followed along the homoclinic orbit by the forward flow (see Fig. 2 in Ref. 40).

There are two possible bifurcation diagrams in case C. In both cases, horseshoes exist in a region of the parameter space. We remark that chaotic regions have been observed in the HR model⁴⁶ connected with the infinite fans of period doubling and fold bifurcations of periodic orbits generated at these codimension-two points. Depending on how they are formed, cases C (in) and C (out) are

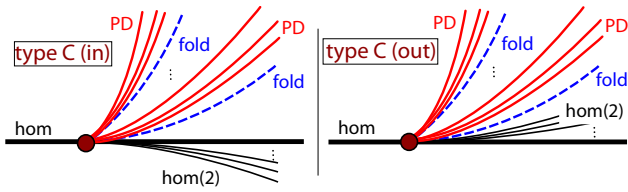


FIG. 2. Theoretical two-parameter unfolding of the codimension-two OF and IF homoclinic bifurcations of type C (in) and C (out) describing the fans of period doubling and fold bifurcations of periodic orbits. Bifurcation diagrams for Belyakov bifurcations are similar, but folds and period doublings accumulate from both sides of the primary homoclinic bifurcation (see details in Ref. 43). A fan of secondary homoclinic orbits [labeled hom(2)] is also depicted.

distinguished (see Fig. 2). In both, infinitely many one-sided curves of secondary N -homoclinic orbits emerge for each $N \geq 2$ from the flip point on the branch of primary homoclinic orbits (labeled hom in Fig. 2). These are homoclinic orbits that follow N times the primary one before closing up. Also, in both cases, the bifurcation diagram exhibits an infinite fan of bifurcation curves corresponding to period doublings and folds of periodic orbits. The horseshoe dynamics appear in between that cascade and the infinite fans of N -homoclinic orbits. In case C (in), shift dynamics and the homoclinic cascade are separated by the curve hom, whereas, in case C (out), the homoclinic cascade, the shift dynamics, and the fan of bifurcations of periodic orbits are located on the same side of the curve hom (see Fig. 2). A complete description of the bifurcation diagrams can be found in Refs. 37, 40, and 41.

Regarding Belyakov bifurcations, we remark that the hypersurface H of homoclinic bifurcation splits into two regions separated by a manifold of codimension-two homoclinic bifurcations. Saddles change from saddle-node type to saddle-focus (SF) type when such manifold is crossed. Additional generic conditions include global assumptions on the behavior of the invariant manifolds (see Refs. 37 and 43 for a complete description and particularly Fig. 14 in the second reference).

If $\lambda_s + \rho_u < 0$, a unique unstable limit cycle bifurcates from the homoclinic orbit (see Ref. 43). Otherwise, a two-parameter bifurcation diagram is quite similar to those in Fig. 2. Infinitely many one-sided curves of secondary N -homoclinic orbits emerge for each $N \geq 2$ from the Belyakov point and they are tangent at the flip point to the branch of primary homoclinic orbits corresponding to saddle-focus. The bifurcation diagram also exhibits infinite fans of bifurcation curves corresponding to period doublings and folds of periodic orbits, but, in contrary to what is shown in Fig. 2, they accumulate on the branch of saddle-focus homoclinic orbits from both sides (see Fig. 14 in Ref. 43).

Codimension-three homoclinic bifurcations have been studied in Ref. 40. In particular, transitions from Case A to Case B and also from Case B to Case C were discussed and conjectural bifurcation diagrams were provided. See also Ref. 42 regarding the case of the coalescence of resonances between eigenvalues with an orbit flip degeneracy. In both references, particular attention is devoted to the existence of homoclinic doubling cascades. Our study of the homoclinic phenomena in the HR model focuses on codimension-one and

codimension-two bifurcations, but, as expected in a three-parameter study, higher codimension configurations do exist. For instance, coalescence between IF and Belyakov bifurcations and transitions from C_1 to C_2 in Fig. 1 (left) are expected in the HR model. Nevertheless, although these codimension-three phenomena have not been previously considered in the literature, they are out of the scope of this paper. Despite this, none of the scenarios considered in Refs. 40 and 42 have been detected in the HR model, but the bifurcation diagrams there proposed should inspire our future analysis of such configurations. These diagrams show pencils of codimension-one bifurcations connecting codimension-two bifurcation points. This is similar to what is shown in Fig. 6 in Ref. 20.

B. Slow-fast dynamics and fold-hom bursters

Equilibrium points in the full system (1) are given, after substituting the parameter values, by the intersection of the plane

$$z = 4(x + 1.6) \tag{3}$$

and the curve

$$\begin{cases} 0 = 1 - 5x^2 - y, \\ 0 = y - x^3 + bx^2 - z + I. \end{cases} \tag{4}$$

They do not depend on ε , but there can be one, two, or three equilibrium points depending on the values of parameters b and I . Projections of the plane (3) and the curve (4) on the plane (z, x) are illustrated in Fig. 3 for $b = 2.7$ and $I = 2.2$; see the brown colored straight line and the green-red colored Z-shaped curve, respectively. For these parameter values, there is a unique equilibrium point in the full system (1).

A detailed discussion about local bifurcations was given in Ref. 26. In particular, the description provided in Ref. 26 (Fig. 3) is similar to the information given at the bottom panels in our Figs. 5 and 6. As a reference, we use the bottom panel in Fig. 6 for the value $\varepsilon = 0.08$. For parameters in the purple region, there are three equilibrium points. Outside this region (at least in the range of parameters under consideration) there is only one equilibrium point that is attracting for parameter values on the green region until it undergoes a Hopf bifurcation (yellow line). The pale blue region correspond to saddle-focus (SF) equilibria with stability index 1, that is, equilibria where the linear part has eigenvalues λ_s and $\rho_u \pm \omega$, with $\lambda_s < 0 < \rho_u$ and $\omega \neq 0$. The transition from the pale blue to the red region means the change from SF to saddle-node (SN) equilibria (with stability index 1), that is, equilibria where the linear part has eigenvalues λ_s , λ_u , and λ_{uu} such that $\lambda_s < 0 < \lambda_u < \lambda_{uu}$, with $\lambda_s < 0 < \lambda_u < \lambda_{uu}$. Note that $\lambda_u = \lambda_{uu}$ for parameters on the borderline between the pale blue and the red regions. This transition is related to the existence of Belyakov bifurcations, which were described in Sec. II A. The difference between red and white regions—labeled SN1 and SN2, respectively—has to do with conditions on the eigenvalues, which are used to characterize specific cases of flip bifurcations (see Remark 2). In any case, both regions correspond to SN equilibria with stability index 1.

The Hindmarsh–Rose model is a prototypical example of a fast–slow system. The bifurcation diagram of the fast subsystem,

$$\begin{cases} \dot{x} = y - x^3 + bx^2 - z + I, \\ \dot{y} = 1 - 5x^2 - y, \end{cases} \tag{5}$$

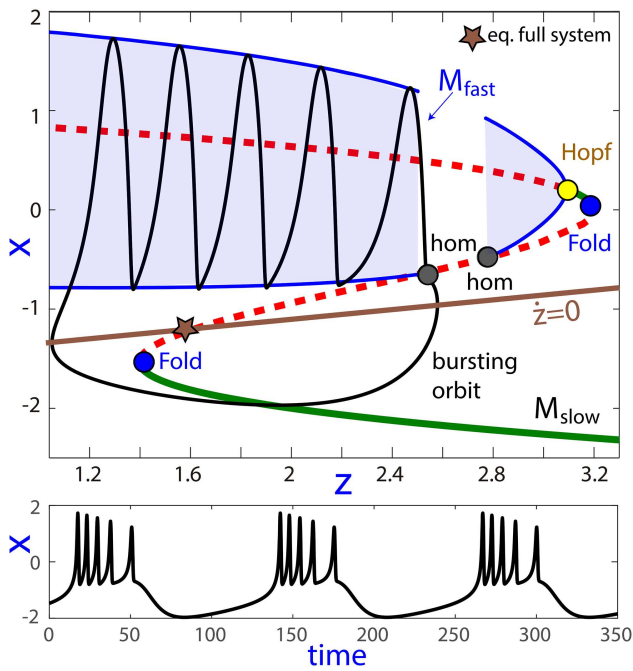


FIG. 3. Illustration of a slow-fast decomposition in the HR model with $b = 2.7$ and $I = 2.2$. Top panel shows a bifurcation diagram of the fast subsystem (5) when variable z is considered as a bifurcation parameter. Straight line $\dot{z} = 0$ is also depicted to visualize the equilibrium point that exists for the full system. A periodic orbit with five spikes is superimposed on the fast and slow manifolds. The time series of the x -component of the solution is shown in the bottom panel.

obtained when $\epsilon = 0$ is crucial to explain the dynamics when ϵ is small.² It should be remarked that each time that we refer to the fast subsystem (5), z is considered as an additional parameter. Fixing b and I , the model analysis provides two invariant objects: a curve of equilibrium points, with equations given in (4), and a manifold of limit cycles. As illustration, in Fig. 3, we show a partial bifurcation diagram of (5) with $b = 2.7$ and $I = 2.2$. The Z-shaped curve corresponds to equilibrium points: solid green lines correspond to stable equilibria, whereas dashed red lines correspond to unstable points. Note that the displayed curve corresponds to the projection of the curve with Eq. (4) on the plane (z, x) . Stability along the lower branch is lost at a fold bifurcation point. There is also a second fold where the equilibria recover their stability to become again unstable when they undergo a Hopf bifurcation. The emerging limit cycles disappear in a homoclinic bifurcation to emerge again for lower values of z through an additional homoclinic bifurcation. This second family of limit cycles disappears at a Hopf bifurcation point, which is not displayed in the figure. We also show the maximum and minimum values of the x variable along the periodic orbits with solid blue lines. So, in general, we identify two invariant manifolds. On the one hand, the fast manifold \mathcal{M}_{fast} , also named spiking manifold, is given by the second family of attracting limit cycles of the fast subsystem (5) and, on the other hand, the slow manifold \mathcal{M}_{slow} , formed by the equilibrium points of the fast subsystem (5).

It follows from the Fenichel theory that for values of z where these manifolds are normally hyperbolic, they perturb to invariant manifolds $\mathcal{M}_{fast}^\epsilon$ and $\mathcal{M}_{slow}^\epsilon$, which exist for ϵ small enough in the full system.

Bursting in the full system emerges because orbits repeatedly switch between $\mathcal{M}_{slow}^\epsilon$ and $\mathcal{M}_{fast}^\epsilon$. An example of a bursting orbit with 5 spikes for $\epsilon = 0.01$ is shown in Fig. 3. Top panel shows the bursting orbit projected on the plane (z, x) and superimposed on the picture of the fast-slow decomposition. The time series of the x component of the solution is displayed in the bottom panel. Note that the active regime begins close to a fold bifurcation of equilibria and finishes at a homoclinic bifurcation of limit cycles in the limit case. Due to this reason, following the Izhikevich⁶ classification of bursting types, we say fold/hom bursting (also named square-wave bursting) to refer to the case illustrated in Fig. 3. The classification in Ref. 6 is based on the fast/slow decomposition (first developed in Ref. 32) of the model. Detailed explanations about the previous description of the bursting phenomena in the HR model can be found, for instance, in Refs. 15 and 33.

In the literature, there are a lot of papers devoted to the study of the variation in the number of spikes that can be observed when one parameter is changed. Thus, plots similar to Fig. 4 are obtained (see also, for instance, Fig. 4 of Ref. 34), where the number of spikes in the neuronal response increases from two to six as a parameter is varied, and where each spike-adding transition is characterized by a strong increase in the L_2 integral norm of the orbit. By spike-adding process, we mean any mechanism leading to the formation of extra excursions around the tubular invariant manifold \mathcal{M}_{fast} (and therefore the addition of one spike to the bursting orbit).

In Fig. 4, we use the HR model to exemplify a process of spike-adding. We fix $\epsilon = 0.01$ and $I = 2.2$ and let b vary as the continuation parameter of a periodic orbit. It is clear from the picture that a sequence of fold bifurcations (blue dots in the figure) is involved, giving rise to hysteresis phenomena and the appearance of bistability regions (in Fig. 4, we show two examples of coexisting stable periodic orbits). Although they are not shown, period-doubling bifurcations may also be present. As shown in Refs. 15, 20, 26, and 27, at least in the case of the HR model, all these bifurcations of periodic orbits are related to homoclinic phenomena.

III. ANALYSIS WITH ϵ FIXED

In this section, we begin our analysis by describing all the information provided by a selection of horizontal slices with the small parameter ϵ fixed. These selected slices will show us the different scenarios that we can find by changing ϵ , and it will help us later to develop a complete three-dimensional bifurcation diagram in the parameter space (b, I, ϵ) shown in Secs. IV–VI. Also, these two-parameter plots will show the connection of the spike-adding process with the “far-away” codimension-two homoclinic bifurcation points. Recall that the notation $hom^{(n, n+1)}$ was already introduced in Sec. I to refer to codimension-one homoclinic bifurcation curves.

As a first analysis, Figs. 5 and 6 show the results we have obtained in the plane (b, I) for different values of ϵ . In total, eight different values of ϵ are considered and for each value, two panels are exhibited. The selected values cover all the different possibilities

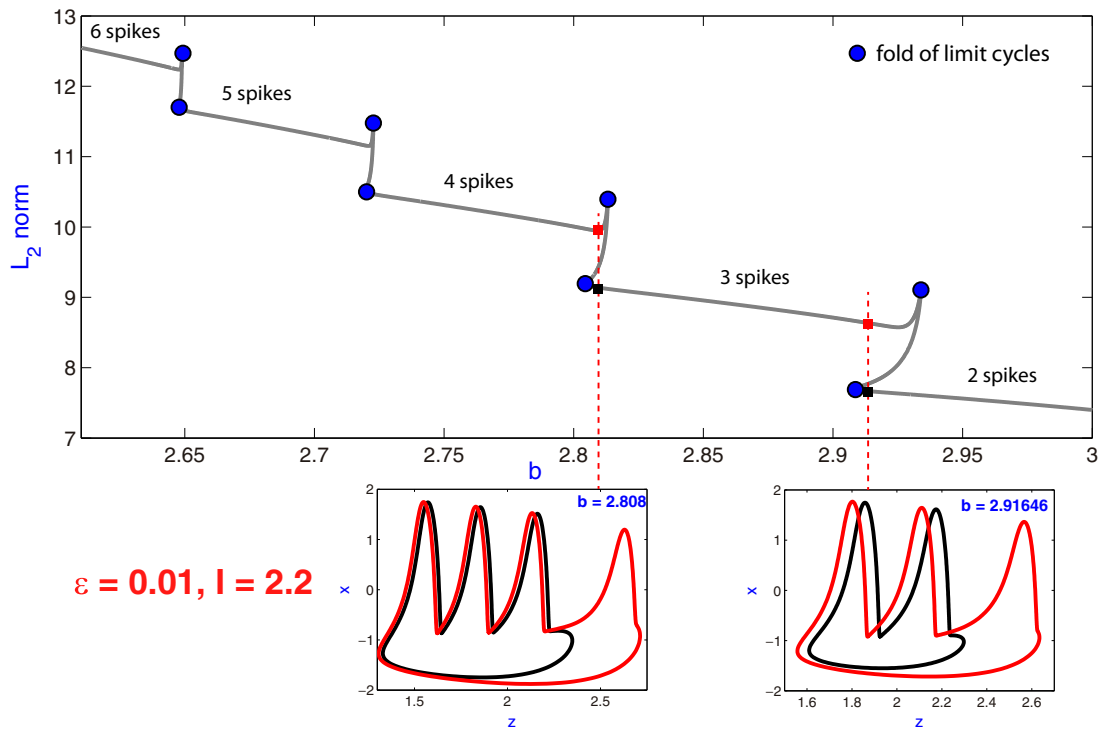


FIG. 4. Example of a spike-adding process in the HR model. A periodic orbit is continued with b varying when $\epsilon = 0.01$ and $l = 2.2$. As b decreases, the change in the L_2 integral norm can be seen. The increase in the number of spikes is illustrated by showing a collection of orbits corresponding to specific positions along the bifurcation curve. We observe how this type of spike-adding process is associated to fold bifurcations of periodic orbits. Two coexisting stable periodic orbits are shown in the small plots for two values of b .

found in the tests. The upper panel combines a two-parameter sweep done with the SC technique (that counts the number of spikes per burst of the stable periodic orbit) with a parameter continuation of bifurcation curves as in Refs. 15 and 27. The lower panel provides information about the number and type of equilibrium points in different regions of the parameter plane (see Subsection II B).

All the ingredients that we need in our description of dynamical and topological changes are shown in Figs. 5 and 6. The displayed bifurcations are the following: *black lines* correspond to $hom^{(1,2)}$ bifurcation curves; *red lines* represent period-doubling bifurcation curves; *yellow lines* stand for Hopf bifurcation curves; *red points* are Belyakov bifurcation points and *green* and *gray points* represent, respectively, IF and OF bifurcation points. When displayed all together, the homoclinic bifurcation curves $hom^{(n,n+1)}$ are not distinguishable because for low values of ϵ , they are exponentially close and the largest is $hom^{(1,2)}$, the one shown. Therefore, the IF and Belyakov bifurcation points corresponding to different homoclinic curves are superimposed (they are in different homoclinic curves but at a very small distance). The OF bifurcation points also correspond to several homoclinic curves (to be studied later), but they are clearly distinguished. In Fig. 7, we provide an alternative schematic view. Taking four representative values of ϵ , we show separately the homoclinic curves $hom^{(1,2)}$, $hom^{(2,3)}$, and $hom^{(11,12)}$ and some

connected bifurcations. These figures illustrate the changes that can be expected in our global study and that we should explain.

In each lower panel of Figs. 5 and 6, the parameter plane is partitioned in different regions corresponding to different types of equilibrium points. As already explained in Subsection II B, this classification does not depend on ϵ . There is either a unique equilibrium point (purple region labeled 1EP and only displayed for $\epsilon = 0.07$ and $\epsilon = 0.08$) or three equilibrium points (3EP). In fact, we only need to pay attention to regions where the unique equilibrium point is a saddle-focus (region SF in the plots) or a saddle-node (regions SN1 and SN2 in the plots). Distinction between regions SN1 and SN2 has to do with two different cases for IF bifurcations characterized in Subsection II A. In particular, if a Case C of IF bifurcation is detected for parameter values on SN1 (respectively, SN2), hence eigenvalues correspond to the region C_1 (respectively, C_2) shown in Fig. 1 (left). Moreover, eigenvalues at the saddle-node point for parameter values in regions SN1 and SN2 correspond to region C in Fig. 1 (right), where the cases for the OF bifurcations are shown. In short, all IF and OF bifurcations are in Case C. Lower panels also display the curve $hom^{(1,2)}$ to understand all different types of homoclinic bifurcations: saddle-focus homoclinic orbits along sections contained in region SF and saddle-node homoclinic orbits along sections contained in regions SN1 and SN2.

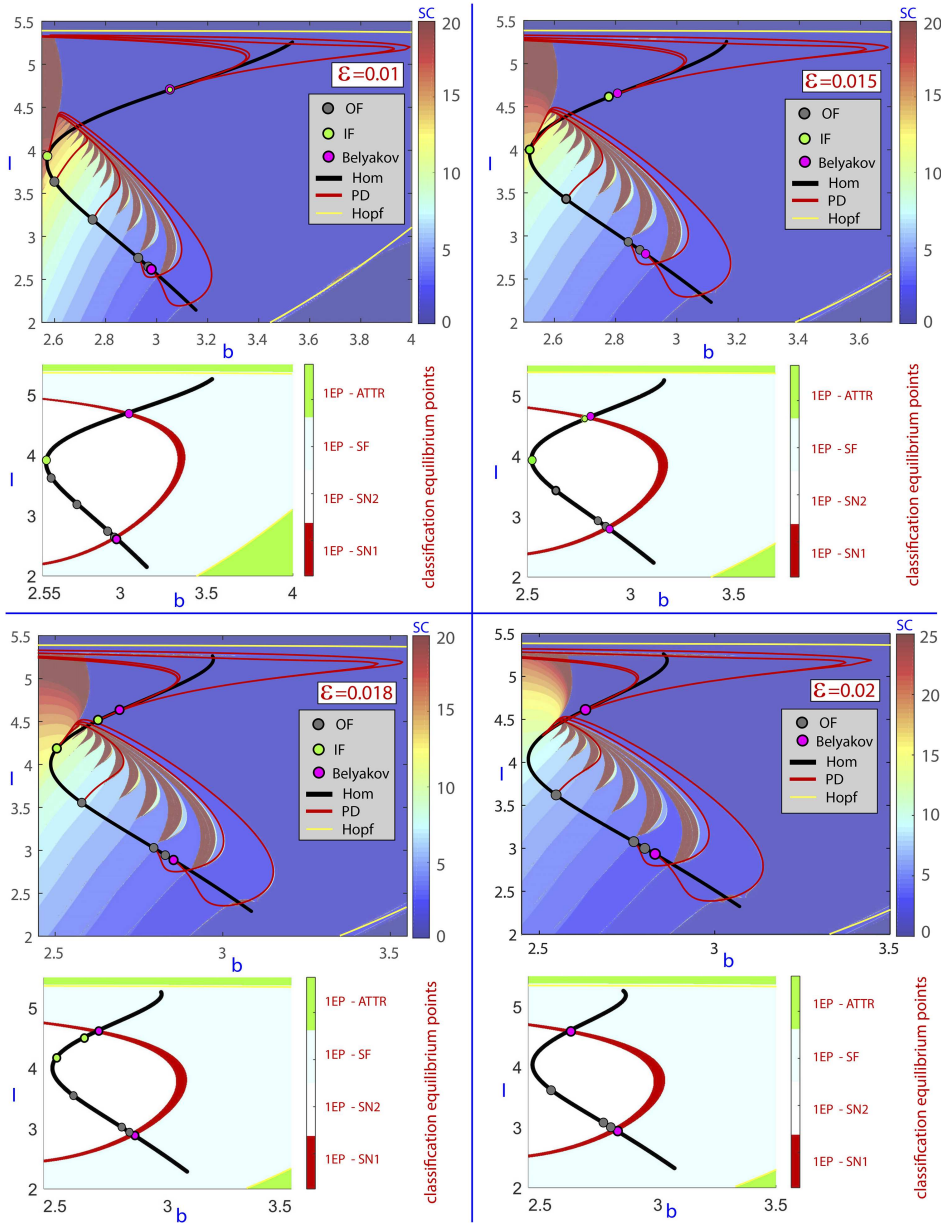


FIG. 5. Parametric plane (b, l) for $\varepsilon = 0.01, 0.015, 0.018, 0.02$. In the upper panel, and for each ε , a SC sweep is overlaid with several bifurcation curves and points. In the lower panel, the parameter plane is partitioned in different regions corresponding to different types of equilibrium points. See the text for details about the curves and points displayed.

Several changes can be observed as ε increases. First of all, as we have already noted in Ref. 46, there is an evolution in the shape of the homoclinic bifurcation curves. For lower values of ε , the homoclinic bifurcation curves have a C-shape, with just one visible fold (as we can see in the case $\varepsilon = 0.01$). For intermediate values of ε ,

the C-shape transforms into a Z-shape, with two visible folds (see $\varepsilon = 0.03$). Last, for higher values of ε , the homoclinic bifurcation curves have no visible folds ($\varepsilon = 0.07$). As shown in Refs. 22, 23, 46, and 47, the C-shape is typical of the homoclinic bifurcation curves in the fast–slow regime.

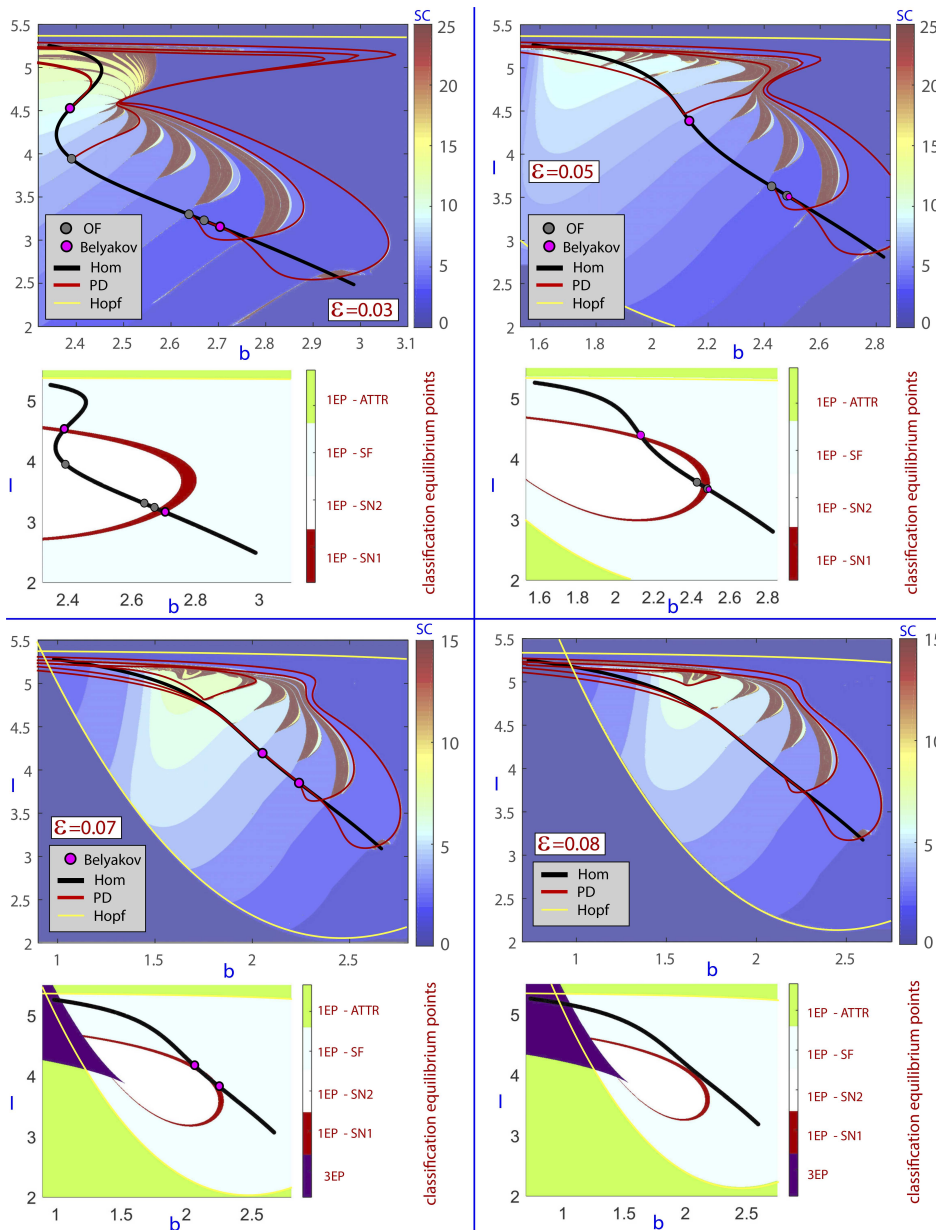


FIG. 6. Parametric plane (b, l) for $\varepsilon = 0.03, 0.05, 0.07, 0.08$. In the upper panel, and for each ε , a SC sweep is overlaid with several bifurcation curves and points. In the lower panel, the parameter plane is partitioned in different regions corresponding to different types of equilibrium points. See the text for details about the curves and points displayed.

Another apparent change is the disappearance of some codimension-two bifurcations. Regarding IF points, when ε is small enough (for instance, $\varepsilon = 0.00918$), there is only one IF point. When ε increases a little ($\varepsilon \approx 0.01$), there are two IF points. When $\varepsilon = 0.01$ (see Fig. 5), the uppermost IF point is superimposed to the Belyakov point. For smaller values of ε , the role of the IF point is taken by the Belyakov bifurcation point. Besides, for large values of the small parameter ($\varepsilon \geq 0.02$), there are no IF points. Obviously, these facts need a more detailed analysis provided by the three-parameter study done in Sec. IV as one may ask him/herself

about codimension-three bifurcation points. Regarding OF bifurcation points, for $\varepsilon = 0.015$ (see Fig. 5), we show four OFs, one for each homoclinic bifurcation curve $hom^{(1,2)}$, $hom^{(2,3)}$, $hom^{(6,7)}$, and $hom^{(11,12)}$ (there are more OF points on each curve but we just present one to show a scheme). For $\varepsilon = 0.03$ (see Fig. 6), only three OFs remain, due to the disappearance of the one on $hom^{(11,12)}$. In fact, the complete homoclinic curve $hom^{(11,12)}$ disappears, together with the strip corresponding to 11 spikes per burst. For $\varepsilon = 0.05$, there are two OF points placed on $hom^{(1,2)}$ and $hom^{(2,3)}$ (more strips have disappeared). Finally, for $\varepsilon = 0.07$, no OFs have been found

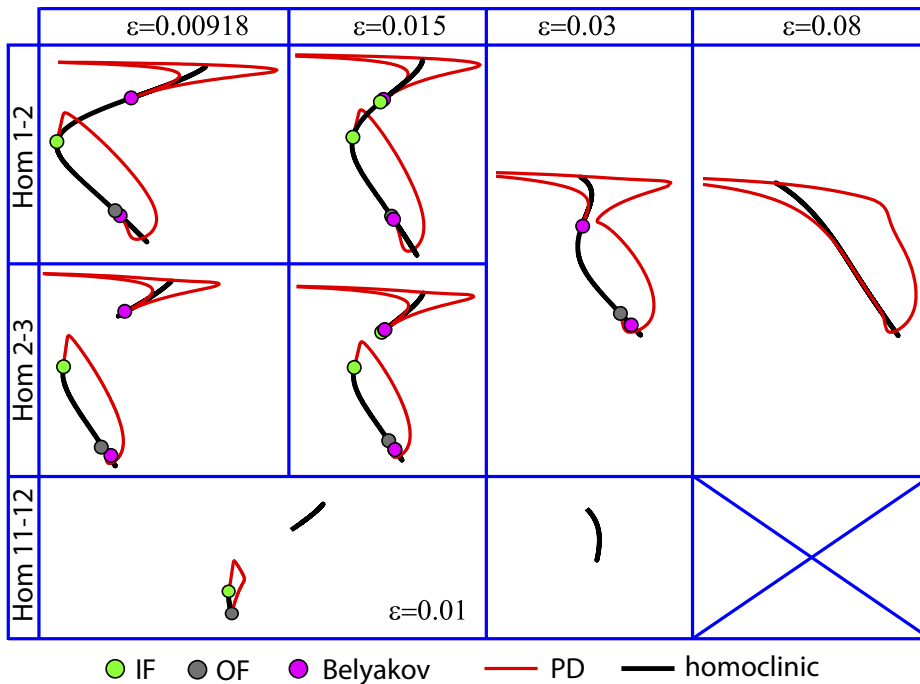


FIG. 7. Global schemes with the different possibilities on the plane (b, I) when the small parameter ϵ changes. The schemes shown correspond to the obtained results from AUTO for particular values of ϵ .

(although there are some bands with bursting dynamics). Again, all these changes ask for a detailed three-parameter study. Recall that attending to the lower panels of Figs. 5 and 6, we can conclude that all OF and IF bifurcations are in Case C. This fact implies the birth of an infinite number of fold and period-doubling bifurcation curves emerging from these points, as well as infinitely many secondary homoclinic bifurcation curves with extra passages close to the equilibrium point (see Fig. 2).

The bifurcation diagrams in Figs. 5 and 6 also show the disappearance of the Belyakov bifurcation points. As ϵ increases, the distance between the two Belyakov points shrinks until they collapse; for $\epsilon = 0.08$, there are no Belyakov bifurcation points. Lower panels help to understand how the Belyakov bifurcation points disappear. As ϵ increases, the homoclinic bifurcation curve has a smaller portion in regions SN1 and SN2. Note that the Belyakov bifurcation points appear when the homoclinic bifurcation curve intersects the borderline between regions SN1 and SF.

As it can be observed in the upper panels of $\epsilon = 0.018, 0.02, 0.03$, qualitative changes in the period-doubling (PD) bifurcation curves occur for values of ϵ near to the value for which IF bifurcation points disappear ($\epsilon \approx 0.0197$). For $\epsilon = 0.015$, we have plotted just one of the PD bifurcation curves emerging from each IF bifurcation point and for each one of the homoclinic bifurcation curves (in fact, the theory³⁷ regarding IF bifurcation points shows that infinitely many one-sided PD bifurcation curves emerge; see Fig. 2). A continuation of these curves in the plane (b, ϵ) shows that pairs of PD bifurcation curves are transformed into a single curve that persists for higher values of ϵ . This fact is a direct consequence of the disappearance of IF points where the pencils of PD and fold bifurcation curves are

born. Therefore, the curves do not have a mechanism to finish and so they have to continue connecting both branches. Effects of this type have been already reported in the literature in other contexts (e.g., Refs. 48 and 49).

In order to summarize all the previous results, we show in Fig. 7 the complete global schemes with the different possibilities on the parameter plane (b, I) when the parameter ϵ changes. The schemes correspond to the results obtained for particular values of ϵ , but each bifurcation diagram is persistent, that is, it is qualitatively equivalent on any close enough horizontal slice. In the figure, we show a table in which each row corresponds to a certain transition from n to $n + 1$ spikes, while each column corresponds to a given value of ϵ . For each n and for each value of ϵ , we show the corresponding homoclinic bifurcation curve(s), the codimension-two homoclinic bifurcation points and some PD bifurcation curves. Color codes are those used in Figs. 5 and 6. When two adjacent boxes share the same diagram, we mean that the corresponding two cases are qualitatively the same. When a certain box appears crossed out, it means that there is no homoclinic structure for the corresponding transition in the number of spikes and for the given value of ϵ . This organization allows the reader to have a clear sight of all the different situations and to understand how the homoclinic structures vary as ϵ moves and different number of spikes are considered.

The first row of the table, i.e., the cases associated with 1 spike, has been already discussed. As it can be easily observed, the main difference between the case $n = 1$ (change from 1 to 2 spikes) and the other cases is that in the latter cases there is no longer a unique homoclinic curve for all values of ϵ , but two homoclinic curves exist for low values (this is the first time this fact is observed in the HR

model). Second, it is also important to note that the number and the type of codimension-two bifurcation points vary significantly with n . In the case $n = 2$, for all the values of ε , the codimension-two points present a similar situation to their analogs of 1–2 spikes. However, in the case $n = 11$, some of the codimension-two points that appear in the former cases do not exist (see, for example, the Belyakov points for $\varepsilon = 0.00918$ and 0.015). Last, the case $n = 11$ reveals that the persistence of the homoclinic structure as ε increases depends on the number of spikes to which it is associated (see the fourth column, corresponding to $\varepsilon = 0.08$). This fact suggests the existence of a mechanism of disappearance of the global structures for large number of spikes when ε grows. All these numerical findings and hypothesis underlying these differences will be discussed in Secs. IV–VI.

Note that all the previous discussions make clear that when dealing with fast–slow systems, the understanding of the mechanisms of creation and destruction of spikes requires studies in spaces of parameters which include the “small parameters.” It is essential to have a global view of the bifurcations and Secs. IV–VI will stress the relevance of this goal.

IV. GLOBAL ANALYSIS CHANGING ε

As shown in Sec. III, a higher dimensional analysis is needed in the parameter space in order to explain the changes in the bifurcation diagrams observed in planes (b, I) . In this section, we will

discuss the three-dimensional structures associated to the different homoclinic bifurcation curves we have observed.

In Figs. 8–10, we provide bifurcation diagrams in the three-parameter space (b, I, ε) . Codimension-one homoclinic bifurcations are shown in black, Belyakov bifurcations in magenta, IF bifurcations in green, and OF bifurcations in gray, as in previous pictures of this article. We have calculated curves of codimension-one homoclinic bifurcations with a step of 0.001 in the parameter ε using AUTO software, in order to visualize surfaces. For each case, the three-dimensional diagram is shown, as well as projections in the planes (b, I) and (I, ε) . These representations allow us to understand the mechanisms of appearance or disappearance of the different codimension-two bifurcation curves. It must be remarked that we have found difficulties for the continuation of OF bifurcation curves with AUTO in the HR model. For that reason, the continuation of OF curves is only partial in Figs. 8 and 9. In the parametric zones, where we have been able to obtain the OF points, we provide an interpolated curve in gray color. We conjecture, taking into account the points already calculated and the rest of bifurcation curves, that the full OF bifurcation curve in these two cases will be similar in shape to the IF curve. They will show a fold for large ε values, and for $\varepsilon \searrow 0$, they can continue or they can end in either a codimension-three point (such as the IF curve in Fig. 8) or at one turning point of the homoclinic codimension-one curves when they have two components (such as the IF curve in Figs. 9 and 10 and the OF curve in Fig. 10). In any case, the numerical results show us a complete picture of the global dynamics of the system.

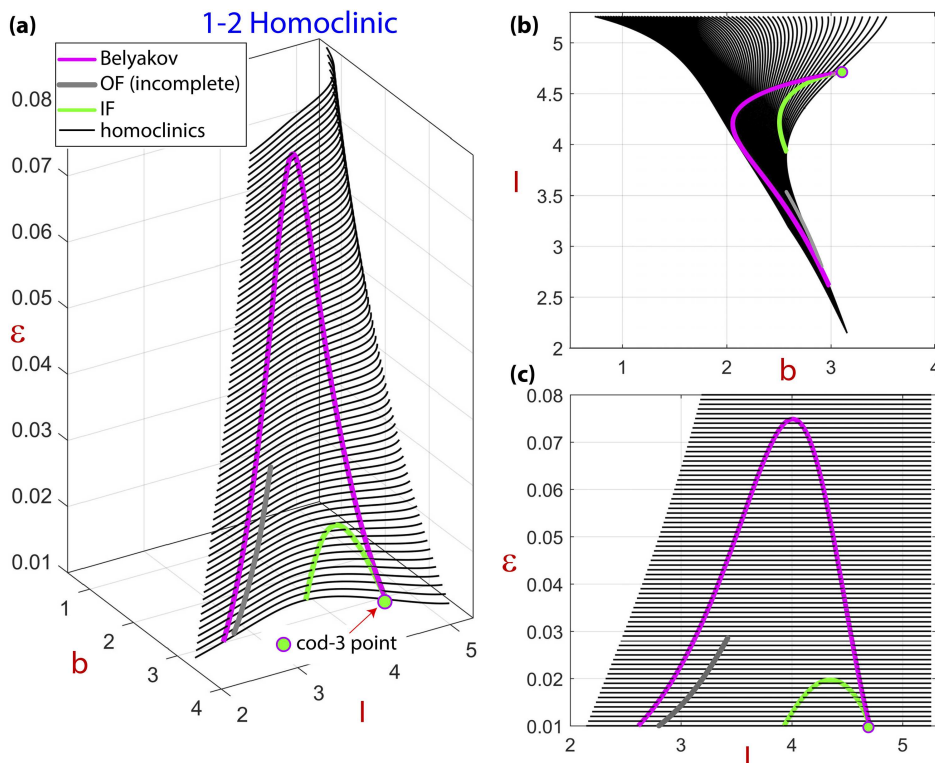


FIG. 8. (a) Three-parameter plot (b, I, ε) for the $hom^{(1,2)}$ homoclinic case; (b) and (c) plane projections. Homoclinic bifurcations of codimension-one and two are shown. The OF bifurcation curve in gray is only part of the complete curve.

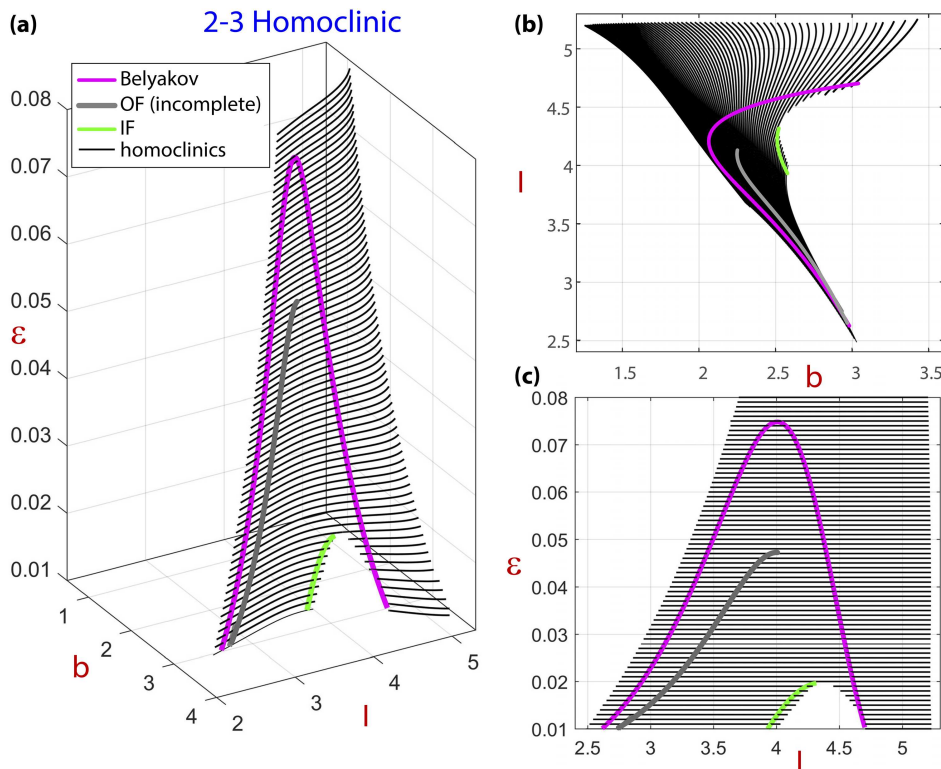


FIG. 9. (a) Three-parameter plot (b, I, ε) for the $hom^{(2,3)}$ homoclinic case; (b) and (c) plane projections. Homoclinic bifurcations of codimension-one and two are shown. The OF bifurcation curve in gray is only part of the complete curve.

Looking at the first two cases in Fig. 5, we observe how a IF bifurcation point appears close to the upper Belyakov point. If we observe now Fig. 8, we clearly see that it seems that the IF and Belyakov bifurcation curves collide at the numerically obtained parameter values,

$$\varepsilon \approx 0.009189, \quad b \approx 3.102, \quad I \approx 4.713.$$

This “collision” would give rise to a codimension-three point that it is not studied in the literature, but it is out of the scope of this article. Besides, it is clear that, in the case $hom^{(1,2)}$ (Fig. 8), the Belyakov bifurcation points and also the IF bifurcation points disappear due to a folding of the bifurcation curve with respect to ε (the maxima we can observe in the 3D plots) of their corresponding bifurcation curves in the three-dimensional parameter space. Specifically, the Belyakov bifurcation curve has its folding point at $\varepsilon \approx 0.0748$ and the IF bifurcation curve at $\varepsilon \approx 0.0197$. In the case of $hom^{(2,3)}$ (Fig. 9), the Belyakov bifurcation curve presents a similar behavior to the $hom^{(1,2)}$ case. However, there is a very important difference in the way the IF bifurcation curve disappears. Note that curves forming the surface $hom^{(2,3)}$ have two disconnected components for (fixed) low values of ε . In addition, the system ceases to exhibit homoclinic connections in one of the regions in the parameter space where the

geometry of the flow is the appropriate for the formation of IF bifurcations. This situation appears again in all the codimension-two curves in the case of $hom^{(11,12)}$ (Fig. 10). Therefore, we can observe a clear difference between $hom^{(1,2)}$ and all the other cases. This change in the topology of the homoclinic surfaces will be explained in more detail in Sec. V.

There is also another remarkable difference regarding the values of the small parameter for which each homoclinic surface disappears. In the cases $hom^{(1,2)}$ and $hom^{(2,3)}$, it can be seen that the homoclinic curves clearly persist for all the values of ε we have studied, namely, up to $\varepsilon = 0.08$. Note that for larger values, we cannot consider the system as a fast-slow one. However, in the case $hom^{(11,12)}$, the homoclinic surface has disappeared at $\varepsilon \approx 0.038$. Using the SC technique, we discover band structures in the parameter planes with ε fixed, as shown in Figs. 5 and 6. Each band is associated to a given number of spikes per burst. The spike-adding process in fold/hom bursters was connected recently^{25,50} with saddle-type canards.^{51,52} Besides, the necessary fold bifurcations of periodic orbits of the spike-adding process for fold/hom bursters were also recently connected with codimension-two homoclinic bifurcation points and also the homoclinic orbits experiment canard phenomena on one turning point of the homoclinic bifurcation curves.^{15,27} Our numerical findings also support this idea, as they show clearly

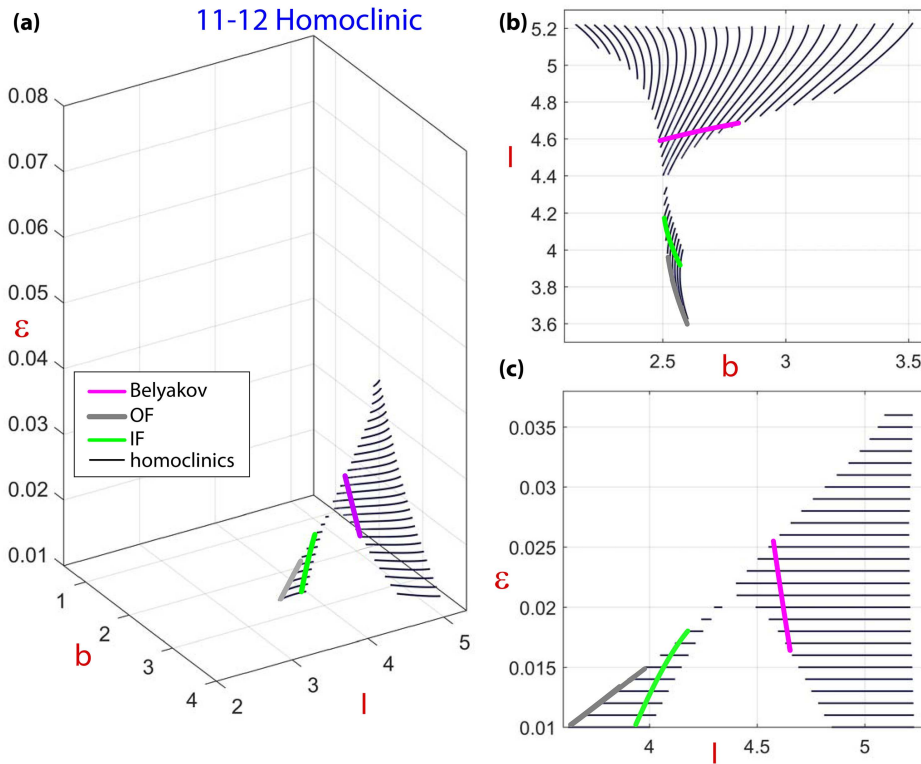


FIG. 10. (a) Three-parameter plot (b, l, ε) for the $hom^{(11,12)}$ homoclinic case; (b) and (c) plane projections. Homoclinic bifurcations of codimension-one and two are shown.

that the disappearance of a band corresponding to n spikes is linked to the disappearance of the corresponding homoclinic curves (surfaces) $hom^{(n,n+1)}$. This is a quite important consequence of the three-parameter plots, as they explain the simplifications that are observed in the band structure of the fold/hom regime as ε increases, giving rise to burst phenomena with a small number of spikes (see in Figs. 5 and 6 how the number of color stripes decreases when ε grows).

All the above mentioned features, together with the SC sweeps, suggest that the bigger the number n of spikes is, the smaller is the value of ε for which the corresponding homoclinic curve vanishes. Moreover, the numerical results show that the different homoclinic curves are stacked in a certain direction, being $hom^{(1,2)}$ the first one, providing an upper bound for “length and shape.” The other homoclinic surfaces are disposed, exponentially close each other, as slabs in increasing order with respect to number of spikes per burst, but decreasing their size.

We have checked that Belyakov and IF bifurcation curves of different numbers of spikes overlap with each other in all the points in the (b, l, ε) where they coexist (they are exponentially close each other, like the homoclinic bifurcation surfaces). One can understand that the magenta (Belyakov) and green (IF) curves are placed in a fixed location in all the diagrams due to the requirements for their existence, and the existence or not of bifurcation points for some of the ε values depends if the corresponding homoclinic bifurcation curves (black curves) cut them. However, OF bifurcation curves corresponding to different numbers of spikes do not coincide with

each other, and in fact they are quite far. This behavior is consistent with the role of OF bifurcation points in the spike-adding process as stated in Refs. 15, 20, and 27.

What remains in the numerical tests is to reveal what is the aspect of the homoclinic surface in all cases, that is, if it is just a one leave surface or it has folds and it is a two (or more) leaves surface. This is in fact a relevant question as it will give the global structure of the homoclinic leaves. We are going to show the structure of isolas displayed by the different homoclinic bifurcation curves, once the parameter ε is fixed. We do not pay much attention to explain the transitions from n to $n + 1$ spikes on a given curve or surface (for details of this process, see Refs. 27 and 31) on both sharp folds of the isolas. Isolal are isolated closed curves of solution branches; hence, the curve is homotopic to a circle. In the literature, there are several examples of isolas of equilibria^{53,54} or limit cycles.^{55–57} Computing many isolas is tedious and requires an adequate strategy. For instance, in Ref. 53, the authors develop a strategy for locating families of isolas of equilibria. In this article, we focus on the detection of isolas of homoclinic orbits (see also Ref. 58) in the parameter space.

By performing sections on the surface $hom^{(2,3)}$ and using AUTO, with a large number of points and steps to guarantee some numerical precision in the computations, we have obtained the results given in Fig. 11. The pictures show codimension-one homoclinic isolas in the parameter plane (b, l) for $\varepsilon = 0.03$ (panel A) and $\varepsilon = 0.07$ (panel B). In the case $\varepsilon = 0.03$, the AUTO software is not able to connect one side of the isola, and adjusting different parameters of the software, just slight increments in the length of

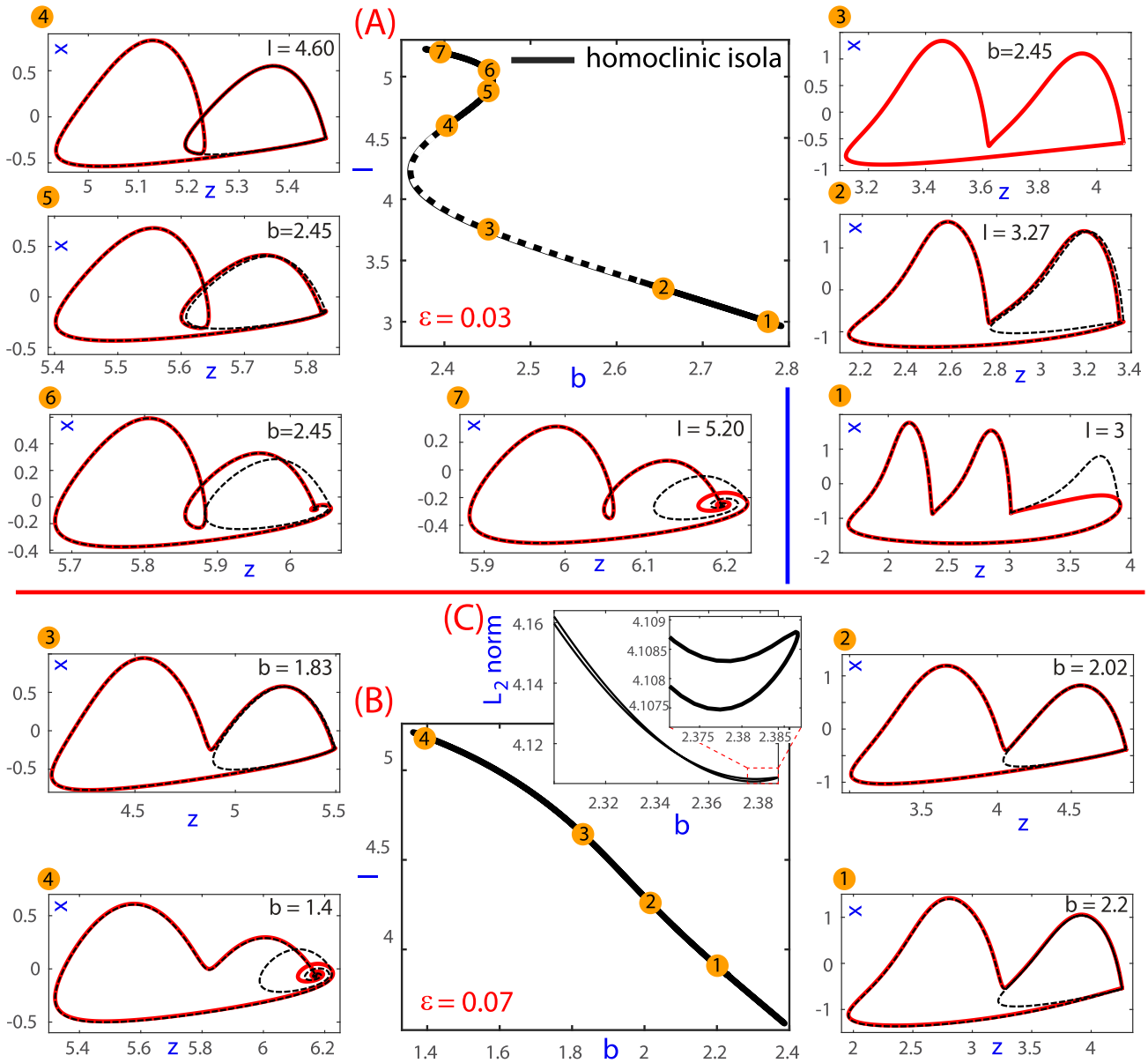


FIG. 11. Codimension-one homoclinic isolas in the parameter plane (b, l) for the surface $hom^{(2,3)}$. Sections $\epsilon = 0.03$ (A) and $\epsilon = 0.07$ (B) are shown. In both cases, several xz projections of two homoclinic orbits on the curve for fixed values of either l or b parameter are displayed. In the case $\epsilon = 0.03$, the black-and-white portion denotes where the AUTO software is not able to connect one side of the isola. Displayed in panel C, we observe magnifications of the sharp fold located on the left side of the isola, but on a plane $(b, \|\cdot\|_2)$.

the bifurcation curve are obtained (the black-and-white portion of the homoclinic curve denotes where the AUTO software stops the computation in one side). On the other hand, for higher values of ϵ , like $\epsilon = 0.07$ shown on panel B, the software is able to connect both sides of the isola giving a close curve. In both cases, several

xz projections of two homoclinic orbits on the curve for fixed values of either l or b are displayed. The study of what happens at the right sharp fold of the homoclinic curve is explained in detail in Fig. 6 of Ref. 27 (this corresponds with the subplot -1- of the case $\epsilon = 0.03$), but the complete evolution along the isola is not given in that article.

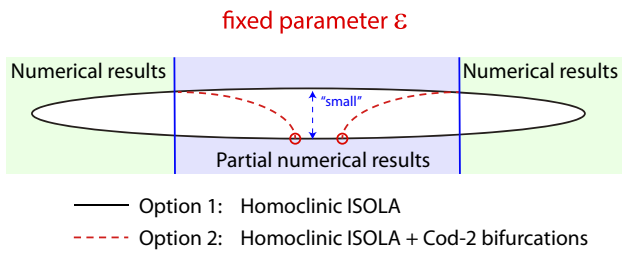


FIG. 12. Theoretical scheme of the codimension-one homoclinic isolas for ϵ fixed.

For $\epsilon = 0.03$, the passage through the milder visible folds (compared with the sharp U-turns of both extremes of the isolas) of the homoclinic curve exhibit no bifurcations as the plots xz along the isola show $(-3-$ to $-4-$ and $-5-$ to $-6-$). It is important to remark that taking the homoclinic orbits close to the values of the parameter where the continuation software stops for $\epsilon = 0.03$, subplots $-2-$ and $-4-$, the different orbits show exactly the same behavior, with just small modifications (as it also shows the intermediate subplot $-3-$ for one side). Therefore, it is perfectly logical to conjecture in this case that both sides of the curve are connected giving an isola, even more taking into account the results for $\epsilon = 0.07$ where the isola is fully obtained. Note that in Ref. 27, the homoclinic isolas and the homoclinic organization were not detected as their main interest was the spike-adding and canard process of the homoclinic orbits on the lower-right sharp fold of the homoclinic bifurcation curve for ϵ fixed. In panel C (Fig. 11), we show two magnifications of the lower sharp fold of the isola for $\epsilon = 0.07$. In these zooms, instead of plotting on the parametric plane (b, I) , we use the plane with b and the AUTO norm L_2 to get a clearer image of the fold, showing two curves, and thus it illustrates one extreme of the isola.

In any case, the numerics only can give strong evidences of the existence of the isola. This fact is shown in the theoretical scheme shown in Fig. 12. The black curve is our conjectured isola (based in our numerical results), but, as the observed phenomena is on a small distance in the parameter space (the isola is very “thin,” with a width about 10^{-8}), other options can be possible, like the existence of foldings in both sides and also some extra homoclinic codimension-two points, that is, two connected isolas, that are able to give rise to

the folds (one option can be the dotted curve in Fig. 12). In any case, all of our numerical results show that it seems that we really have isolas, that is, the topological structure of the black curve in Fig. 12.

If one looks at the theoretical unfolding of the OF and IF codimension-two points shown in Fig. 2, there is an infinite fan of secondary codimension-one homoclinic bifurcation curves. None of the numerical simulations on the system (our studies in this article and in Refs. 15, 20, and 46, and in Refs. 26 and 27 of other authors) show any of these bifurcations and any dynamical effect that can be related to them. This fact allows us (as also done in Ref. 27) to conjecture that the secondary homoclinics are inside the very thin homoclinic isola, and, therefore, it is not computationally possible to observe any of them. With these elements, we propose in Fig. 13 a theoretical scheme of the secondary homoclinic bifurcation curves and their connections (in a similar way as in Ref. 40) in the cases of having an even or odd number of pairs of codimension-two points.

As already remarked, it is apparent that there is an overlap between the different $hom^{(n,n+1)}$ bifurcation curves (in fact, they are exponentially close to each other as commented above), except for the higher values of ϵ where a slight separation can be observed. This separation of the curves occurs progressively as ϵ increases, and it can be appreciated for $\epsilon > 0.07$. In Fig. 14, we show superimposed the three homoclinic isolas $hom^{(1,2)}$, $hom^{(2,3)}$ and $hom^{(11,12)}$ for $\epsilon = 0.036$ and $\epsilon = 0.07$ to show that the isolas are outside of each other but exponentially close.

V. THEORETICAL SCHEME: THE HOMOCLINIC “MILLE-FEUILLE”

In Sec. IV, we have explored the three-dimensional parameter space of the HR model considering in detail the homoclinic structure. What it remains is to provide a complete theoretical scheme that connects all the basic ingredients of the spike-adding process in fold/hom bursters. That is, on the one hand, we have that in the parameter space the system experiments the spike-adding process far from the homoclinic bifurcations. On the other hand, the spike-adding process requires of two fold bifurcations to give rise to hysteresis phenomena and canards on one side to generate the extra spike (see Refs. 20, 25, and 50). However, where are these fold bifurcation points generated? These points form bifurcation curves that

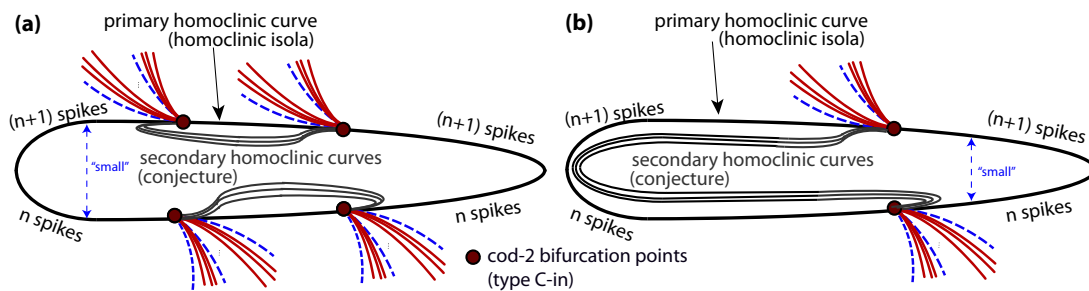


FIG. 13. Conjectured theoretical scheme of the codimension-one secondary homoclinic bifurcation curves for ϵ fixed for cases with an (a) even or (b) odd number of pairs of codimension-two points.

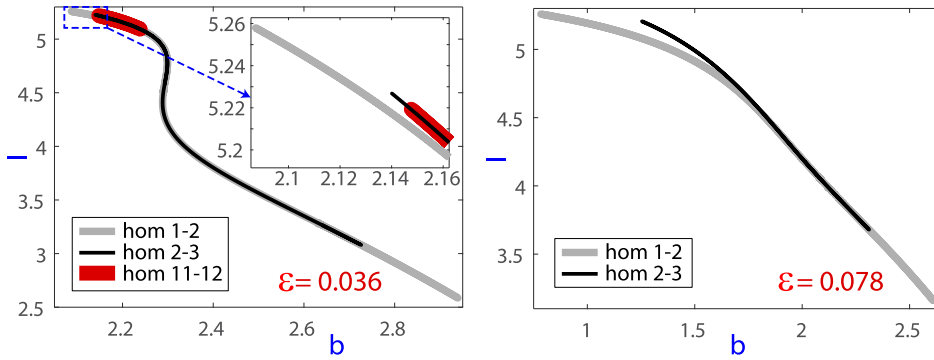


FIG. 14. Homoclinic isolas $hom^{(1,2)}$, $hom^{(2,3)}$, and $hom^{(11,12)}$ for $\epsilon = 0.036$ and $\epsilon = 0.07$ showing their relative position.

are born at codimension-two bifurcation points located on the “far-away” homoclinic bifurcation lines. All the bifurcation lines, in fact pencils of fold and PD bifurcation lines, are born, like the “pages-of-a-book” at the OF and IF points of the $hom^{(n,n+1)}$ curves as shown in Figs. 5 and 6 and in Refs. 15 and 27. But there is no reference on the literature (to our knowledge), where it is explained globally in

the parameter space why we have more spike-adding phenomena as $\epsilon \rightarrow 0$.

The numerical findings shown in Secs. III and IV permit us to establish a global theoretical scheme to describe the whole picture (see Figs. 15–17). First, in Fig. 15, we show the different homoclinic surfaces. All of them are composed of one or two tubular structures.

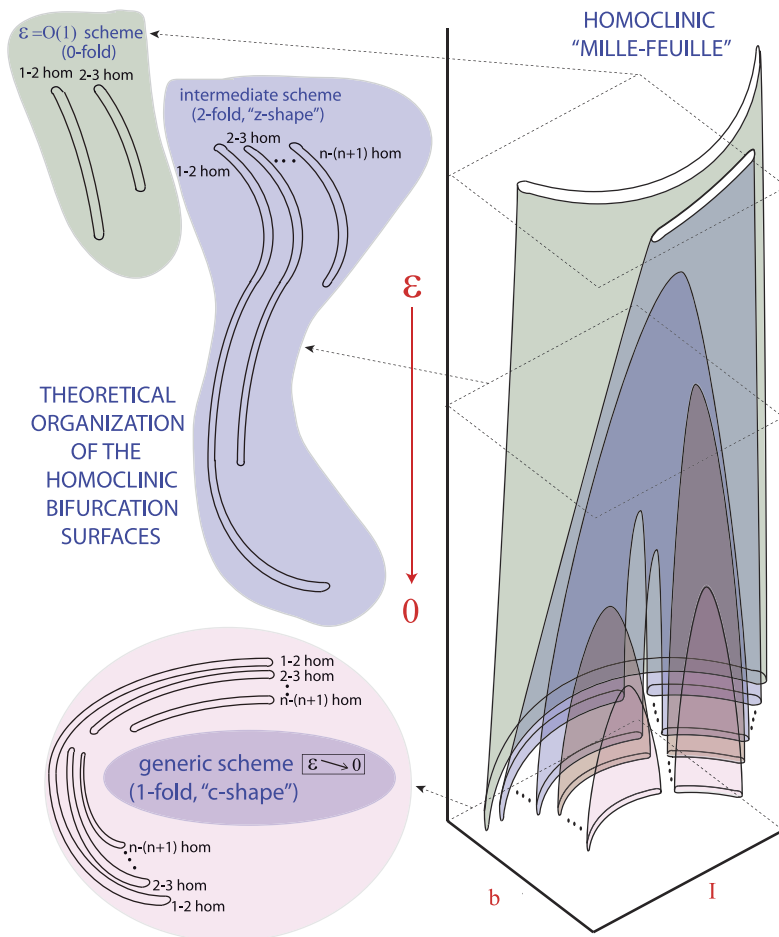


FIG. 15. Homoclinic “mille-feuille” organization in fold/hom bursters.

As the number of spikes of the homoclinic orbit grows, we distinguish three types, either a tubular surface ($hom^{(1,2)}$) or two tubular surfaces connected ($hom^{(2,3)}, \dots, hom^{(k,k+1)}$) or, finally, surfaces that disappear when ε grows ($hom^{(k+1,k+2)}, \dots$). Note that Figs. 8–10 also illustrate numerically each one of these three types of surfaces. In the scheme, the different homoclinic surfaces are clearly separated from one another, but in the real parameter space, they are extremely close when ε is small, being organized in shape and size by the $hom^{(1,2)}$ surface. When ε is large, the separation becomes evident, showing that, indeed, these homoclinic surfaces have no contact point when $\varepsilon > 0$ (see Fig. 14).

If we take a section fixing the value of ε , we find three different situations, already partially described in Ref. 46, depending on the value of ε . When ε is large [$\mathcal{O}(1)$], the slices just show a few homoclinic isolas corresponding to a small number of spikes and without visible folds. For intermediate values of ε , the isola corresponding to $hom^{(1,2)}$ has Z-shape with two visible folds. The other isolas complete a Z-shape, or not, depending on their length. Finally, for small ε , that is, in the generic situation when we are concerned with fast-slow systems, the principal isola for $hom^{(1,2)}$ has a C-shape with one visible fold. The curves corresponding to $hom^{(n,n+1)}$, with $n \geq 2$, split into two isolas also disposed in such a way that they are adapted to the C-shape of the principal isola. In this case, all the homoclinic curves have two components (isolas) but the first one $hom^{(1,2)}$ and all of them have folds with branches exponentially close to each other.

Due to the fact that, from a certain point of view, homoclinic surfaces are piled up one upon another, we refer to this conjectured global theoretical structure as the *fold/hom homoclinic “mille-feuille” organization*. Note that for fixed ε , we have a finite

number of homoclinic curves, but the number of them grows as ε decreases.^{25,33}

Codimension-one homoclinic bifurcations that form each surface $hom^{(n,n+1)}$ must be understood as primary bifurcations. These surfaces contain curves of codimension-two homoclinic bifurcation: IF, OF, and Belyakov points. Emerging from these curves, there exist surfaces of bifurcation of periodic orbits: PD or folds, some of them involved in the spike-adding process. Also attached to these curves there are surfaces of secondary homoclinic bifurcations arising in the inner side of the surface, that is, separated from the surfaces of bifurcation of periodic orbits by the surface of primary homoclinic bifurcations [see case $C(in)$ in Fig. 2]. Note that this scenario is covered by the classical unfolding theory of codimension-two homoclinic bifurcations.^{37,38} We remark that these unfoldings have to be “glued” to the homoclinic surfaces given by the “homoclinic mille-feuille.” Figure 16 illustrates the described scenario. Each of these curves of codimension-two bifurcations behaves as the “spine-of-a-book” located on the homoclinic surface (like the “bookshelves” of a “bookcase”), whose “pages” consist of surfaces of bifurcations of periodic orbits and secondary homoclinic bifurcations. Plot 16.A provides the theoretical scheme of a homoclinic surface with the curve of codimension-two bifurcation points that form the “spine-of-a-book” structure creating the pencils of surfaces of fold and PD bifurcations. In plots 16.B and 16.C, we show some numerical results illustrating such a theoretical scheme. The plot 16.B presents a projection of the homoclinic structure for three values of ε . Also, in plot 16.C, we see the global three-parametric view illustrating the theoretical scheme proposed in 16.A.

Finally, Fig. 17 illustrates the complete “mille-feuille” organization together with the “books” of bifurcation of periodic orbits. Now,

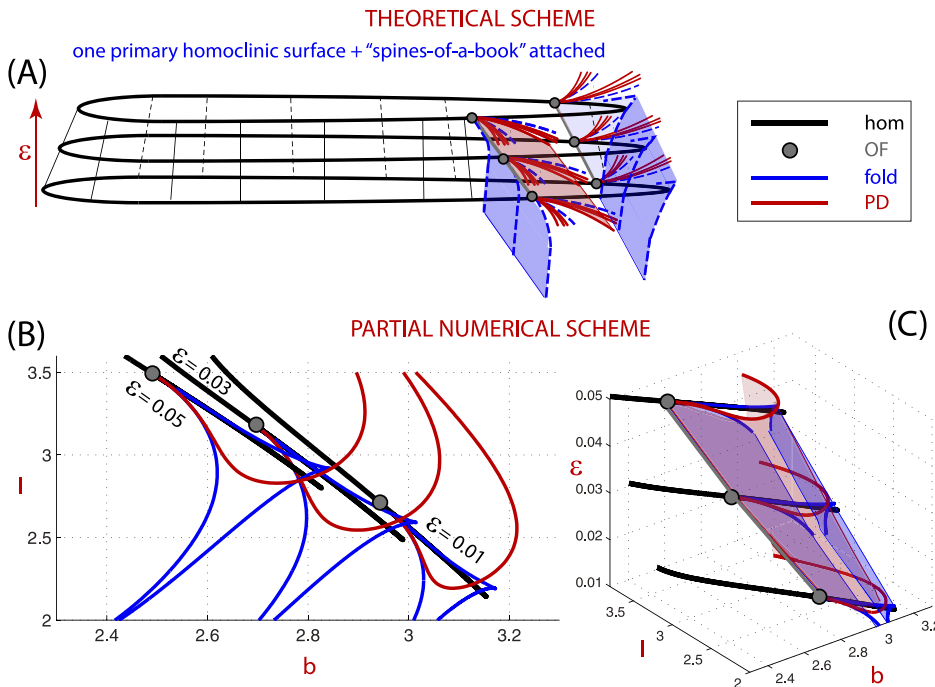


FIG. 16. Theoretical and numerical illustration of the “spines-of-a-book” structure on the $hom^{(1,2)}$ homoclinic surface. Each of the curves of codimension-two homoclinic bifurcations is identified with the “spine-of-a-book” gathering “pages” of fold bifurcations, period-doubling (PD) bifurcations, and also (not showed) secondary homoclinic bifurcations. Panel A shows this theoretical model in the case of a “spine” of orbit flip (OF) points. Panels B and C show numerical results illustrating typical “pages” of one of these “books.” In particular, panel B shows numerical slices of a “book” projected on the (b, I) plane. A three-dimensional view is given in panel C. Attached to each “spine,” we see two “pages” of fold bifurcation and one “page” of period-doubling.

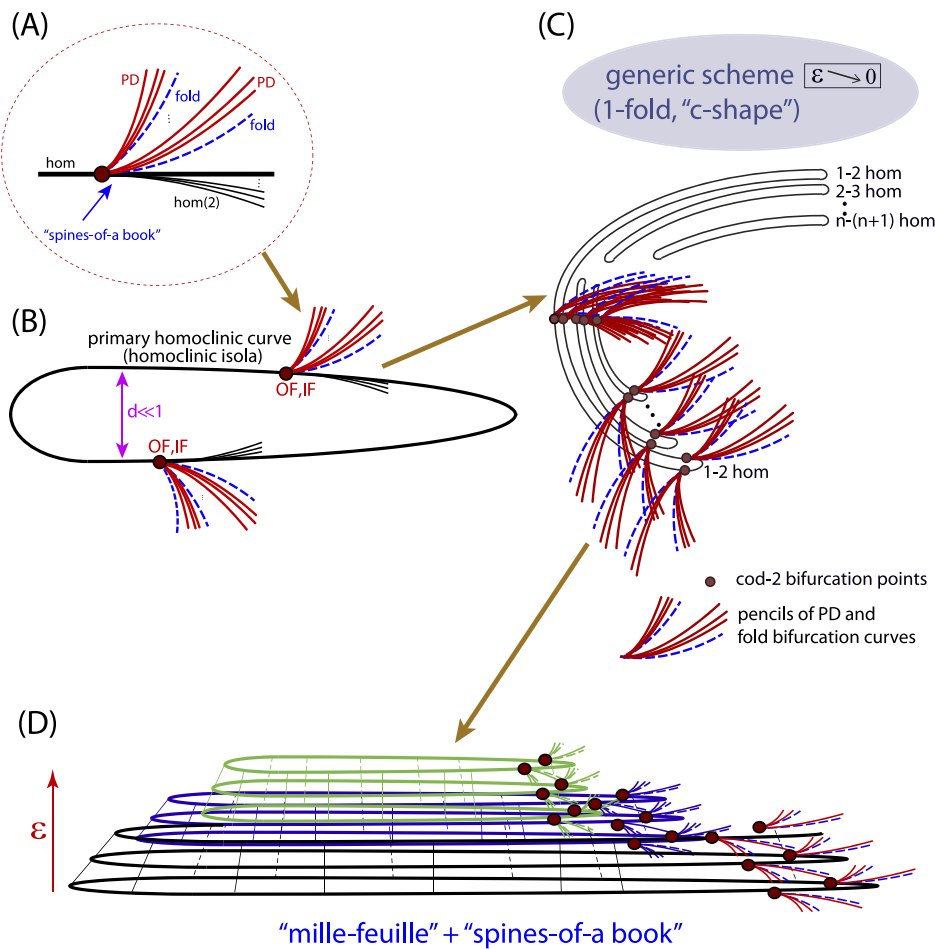


FIG. 17. Complete “mille-feuille” and “spines-of-a-book” theoretical structure. In panel A, we recall the unfolding of the bifurcation diagram associated to a OF bifurcation: there are pencils of PD and fold bifurcation of periodic orbits and also a pencil of secondary homoclinic bifurcations. In panel B, we see how these pencils are attached along a primary homoclinic curve. The isola has an exponentially small width d . Panel C illustrates a collection of isolas for a small value of ϵ . Finally, a three-dimensional scheme is provided in panel D. We see three “bookshelves” (homoclinic surfaces) and with some “books” (codimension-two points and the bifurcations generated) on them.

we can identify each layer of the “mille-feuille” with a “bookshelf” keeping as many “books” as “spines” of codimension-two homoclinic bifurcations it contains. So, we have a complete “bookcase” of bifurcations of periodic orbits. Moreover, we must notice that each surface in the “mille-feuille” has their own collection of “spines,” that is, their own collection of “books.” This figure gives an idea of how much entangled the bifurcations involved in the spike-adding process is. As illustrated in Fig. 17 (panel B), there are “pages” of the “books” involved in the spike-adding process. We remark that Fig. 17 provides a complete theoretical explanation of all the numerical findings obtained in this article (and in the literature). Our conjectured theoretical structure permits to link the global three-parameter structure (the homoclinic surfaces) with the spike-adding phenomena that can be observed on parameter regions that are quite far from the homoclinic curves. In addition, if we use another set of parameters, we can also observe the fold/hom spike-adding processes, even without homoclinic bifurcations in the entire parametric plane. This is easily explained from Fig. 15, as if our parameters do not cut the homoclinic surface we cannot observe the homoclinic orbits themselves. But what remains are the fold and PD surfaces generated on the codimension-two points attached

to the homoclinic surfaces, as shown in Figs. 16 and 17. Following with the “bookcase” analogy, this will be the case if we have “books” wider than the “bookshelves,” and we observe it without seeing the bookcase.

Obviously, our theoretical scheme is necessarily a partial one, as other bifurcations and phenomena may be present on the complete global picture, but it englobes all the current numerical and theoretical analysis in literature. This article provides new insights into the spike-adding process and the global parametric study of the Hindmarsh–Rose model. We hope that it may be applied to other fold/hom bursters, and this is part of our future work.

VI. CONCLUSIONS

In this article, we have presented a three-parameter study of homoclinic bifurcations in the canonical Hindmarsh–Rose neuron model when it evolves in the fold/hom bursting regime. We have introduced a new structure, the homoclinic “mille-feuille” connected with the fold/hom spike-adding process. Fold/hom bursting is found in numerous fast–slow models, and we expect that most of the findings of this article will be present in many similar problems.

Exploration of other fold/hom bursters is a goal for our future work, but a preliminary study as well as the theoretical scheme of the spike-adding process was introduced in Ref. 20.

Our numerical analysis using different techniques allows us to conjecture the global theoretical homoclinic organization. There exists a “mille-feuille” structure of tubular-like homoclinic surfaces. Each of them corresponds to a transition where the homoclinic orbit increases the number of spikes by one, that is, taking the appropriate paths of parameters, one could observe in the phase-space how the orbits pass from n to $n + 1$ spikes for certain n . Moreover, as ϵ increases, the disappearance of a homoclinic surface associated to the transitions from n to $n + 1$ spikes means the “de facto” disappearance in the surroundings of the band of periodic orbits with $n + 1$ spikes. This structure provides a theoretical explanation of why there is not a regular fold/hom bursting regime with a large number of spikes when the small parameter grows. Moreover, due to the tubular structures, an analysis for fixed values of the small parameter gives rise to the appearance of isolas of homoclinic bifurcation points.

Note that previous relevant studies in the literature^{15,26,27} focus their attention on the spike-adding and canard process of the homoclinic orbits on the lower-right sharp fold of the homoclinic bifurcation curve for ϵ fixed. The other sharp fold, the isolas, and also the complete bifurcation scheme were not identified and studied.

Located on each homoclinic surface, we find curves of codimension-two homoclinic bifurcation. These curves act as the organizing centers for the framework of fold and period-doubling bifurcations of periodic orbits, which is behind one of the main spike-adding mechanisms. The discovery of the global structure of orbit flip, inclination flip, and Belyakov bifurcations is one of our main motivations. Homoclinic surfaces can be compared with “bookshelves,” where the “books” of bifurcation of periodic orbits are kept. Hence, curves of codimension-two homoclinic bifurcations can be compared with the “spines-of-a-book.”

The global structure (homoclinic “mille-feuille” + “spines-of-a-book”), which is revealed in the three-parameter space, is a motivation for further study of higher codimension bifurcation points, which appear on the homoclinic bifurcation surfaces. In fact, the global structure we have uncovered gives clues about part of the bifurcations, which should be expected when dealing with such bifurcation points (and their connections, in a similar way as some codimension-three phenomena provides a global theoretical picture in Ref. 40). These relevant open problems are out of the scope of this article but they are part of our current research.

ACKNOWLEDGMENTS

The authors thank stimulating discussions with Professors Bernd Krauskopf, Hinke Osinga, and Jonathan Rubin that have contributed to improve the clarity of the article. R. Barrio has been supported by the Spanish Ministry of Economy and Competitiveness (Grant No. PGC2018-096026-B-I00), the European Social Fund (EU) and Aragón Government (Grant No. LMP124-18 and Group No. E24-17R), and the University of Zaragoza-CUD (Grant No. UZCUD2019-CIE-04). S. Ibáñez and L. Pérez have been supported by the Spanish Research Projects (Nos. MTM2014-56953-P and MTM2017-87697-P). L. Péhas been supported by Programa de

Ayudas “Severo Ochoa” of Principado de Asturias (Grant PA-18-PF-BP17-072).

REFERENCES

- A. L. Hodgkin and A. F. Huxley, “A quantitative description of membrane current and its application to conduction and excitation in nerve,” *J. Physiol.* **117**, 500–544 (1952).
- G. B. Ermentrout and D. H. Terman, *Mathematical Foundations of Neuroscience*, Interdisciplinary Applied Mathematics Vol. 35 (Springer, New York, 2010), pp. xvi+422.
- M. Broens and K. Bar-Eli, “Canard explosion and excitation in a model of the Belousov–Zhabotinskii reaction,” *J. Phys. Chem.* **95**, 8706–8713 (1991).
- S. Wicczorek, B. Krauskopf, and D. Lenstra, “Multipulse excitability in a semiconductor laser with optical injection,” *Phys. Rev. Lett.* **88**, 063901 (2002).
- J. L. Hindmarsh and R. M. Rose, “A model of the nerve impulse using three coupled first-order differential equations,” *Proc. R. Soc. Lond.* **B221**, 87–102 (1984).
- E. Izhikevich, *Dynamical Systems in Neuroscience* (MIT Press, Cambridge, MA, 2007).
- J. Nowacki, H. M. Osinga, and K. Tsaneva-Atanasova, “Dynamical systems analysis of spike-adding mechanisms in transient bursts,” *J. Math. Neurosci.* **2**, 7 (2012).
- K. Tsaneva-Atanasova, H. M. Osinga, T. Riess, and A. Sherman, “Full system bifurcation analysis of endocrine bursting models,” *J. Theor. Biol.* **264**, 1133–1146 (2010).
- A. Shilnikov and G. Cymbalyuk, “Transition between tonic spiking and bursting in a neuron model via the blue-sky catastrophe,” *Phys. Rev. Lett.* **94**, 048101 (2005).
- F. A. Cardoso Pereira, E. Colli, and J. C. Sartorelli, “Period adding cascades: Experiment and modeling in air bubbling,” *Chaos* **22**, 013135 (2012).
- A. Granados, L. Alsedá, and M. Krupa, “The period adding and incrementing bifurcations: From rotation theory to applications,” *SIAM Rev.* **59**, 225–292 (2017).
- M. Levi, “A period-adding phenomenon,” *SIAM J. Appl. Math.* **50**, 943–955 (1990).
- V. S. M. Piassi, A. Tufaile, and J. C. Sartorelli, “Period-adding bifurcations and chaos in a bubble column,” *Chaos* **14**, 477–486 (2004).
- M. Rachwalska and A. L. Kawczynski, “Period-adding bifurcations in mixed-mode oscillations in the Belousov–Zhabotinsky reaction at various residence times in a CSTR,” *J. Phys. Chem. A* **105**, 7885–7888 (2001).
- R. Barrio, M. A. Martínez, S. Serrano, and A. Shilnikov, “Macro- and micro-chaotic structures in the Hindmarsh–Rose model of bursting neurons,” *Chaos* **24**, 023128 (2014).
- Y. Hirata, M. Oku, and K. Aihara, “Chaos in neurons and its application: Perspective of chaos engineering,” *Chaos* **22**, 047511 (2012).
- H. Korn and P. Faure, “Is there chaos in the brain? II. Experimental evidence and related models,” *C. R. Biol.* **326**, 787–840 (2003).
- D. Terman, “Chaotic spikes arising from a model of bursting in excitable membranes,” *SIAM J. Appl. Math.* **51**, 1418–1450 (1991).
- X. Wang, “Genesis of bursting oscillations in the Hindmarsh–Rose model and homoclinicity to a chaotic saddle,” *Physica D* **62**, 263–274 (1993).
- R. Barrio, S. Ibáñez, L. Pérez, and S. Serrano, “Spike-adding structure in fold/hom bursters,” *Commun. Nonlinear Sci. Numer. Simul.* **83**, 105100 (2020).
- W. Govaerts and A. Dhooge, “Bifurcation, bursting and spike generation in a neural model,” *Int. J. Bifurcation Chaos* **12**, 1731–1741 (2002).
- J. Guckenheimer and C. Kuehn, “Homoclinic orbits of the FitzHugh–Nagumo equation: The singular-limit,” *Discrete Contin. Dyn. Syst. Ser. S* **2**, 851–872 (2009).
- J. Guckenheimer and C. Kuehn, “Homoclinic orbits of the FitzHugh–Nagumo equation: Bifurcations in the full system,” *SIAM J. Appl. Dyn. Syst.* **9**, 138–153 (2010).
- G. Innocenti, A. Morelli, R. Genesio, and A. Torcini, “Dynamical phases of the Hindmarsh–Rose neuronal model: Studies of the transition from bursting to spiking chaos,” *Chaos* **17**, 043128 (2007).

- ²⁵M. Desroches, T. J. Kaper, and M. Krupa, "Mixed-mode bursting oscillations: Dynamics created by a slow passage through spike-adding canard explosion in a square-wave burster," *Chaos* **23**, 046106 (2013).
- ²⁶M. Storace, D. Linaro, and E. de Lange, "The Hindmarsh–Rose neuron model: Bifurcation analysis and piecewise-linear approximations," *Chaos* **18**, 033128 (2008).
- ²⁷D. Linaro, A. Champneys, M. Desroches, and M. Storace, "Codimension-two homoclinic bifurcations underlying spike adding in the Hindmarsh–Rose burster," *SIAM J. Appl. Dyn. Syst.* **11**(3), 939–962 (2012).
- ²⁸E. Doedel, "AUTO: A program for the automatic bifurcation analysis of autonomous systems," *Congr. Numer.* **30**, 265–284 (1981).
- ²⁹E. J. Doedel, R. Paffenroth, A. R. Champneys, T. F. Fairgrieve, Y. A. Kuznetsov, B. E. Oldeman, B. Sandstede, and X. J. Wang, "Auto2000," see <http://cmvl.cs.concordia.ca/auto>.
- ³⁰R. Barrio and A. Shilnikov, "Parameter-sweeping techniques for temporal dynamics of neuronal systems: Case study of Hindmarsh–Rose model," *J. Math. Neurosci.* **1**, 6:1–6:22 (2011).
- ³¹P. Carter and B. Sandstede, "Unpeeling a homoclinic banana in the FitzHugh–Nagumo system," *SIAM J. Appl. Dyn. Syst.* **17**, 236–349 (2018).
- ³²J. Rinzel, "A formal classification of bursting mechanisms in excitable systems," in *Mathematical Topics in Population Biology, Morphogenesis and Neurosciences: Proceedings of an International Symposium held in Kyoto, 10–15 November 1985*, edited by E. Teramoto and M. Yumaguti (Springer, Berlin, 1987), pp. 267–281.
- ³³A. Shilnikov and M. Kolomiets, "Methods of the qualitative theory for the Hindmarsh–Rose model: A case study. a tutorial," *Int. J. Bifurcation Chaos* **18**(8), 2141–2168 (2008).
- ³⁴H. M. Osinga and K. T. Tsaneva-Atanasova, "Geometric analysis of transient bursts," *Chaos* **23**, 046107 (2013).
- ³⁵F. Drubi, S. Ibáñez, and J. A. Rodríguez, "Coupling leads to chaos," *J. Differ. Equ.* **239**, 371–385 (2007).
- ³⁶F. Drubi, S. Ibáñez, and P. Pilarczyk, "Nilpotent singularities and chaos: Tritrophic food chains," *Chaos Solitons Fractals* (submitted).
- ³⁷A. J. Homburg and B. Sandstede, "Homoclinic and heteroclinic bifurcations in vector fields," *Handb. Dyn. Syst.* **3**, 379–524 (2010).
- ³⁸L. P. Shilnikov, A. L. Shilnikov, D. Turaev, and L. O. Chua, *Methods of Qualitative Theory in Nonlinear Dynamics. Part II* (World Scientific Publishing Co. Inc., 2001).
- ³⁹Y. A. Kuznetsov, *Elements of Applied Bifurcation Theory*, 3rd ed., Applied Mathematical Sciences Vol. 112 (Springer-Verlag, New York, 2004), pp. xxii+631.
- ⁴⁰A. J. Homburg and B. Krauskopf, "Resonant homoclinic flip bifurcations," *J. Dyn. Differ. Equ.* **12**, 807–850 (2000).
- ⁴¹B. E. Oldeman, B. Krauskopf, and A. R. Champneys, "Death of period-doublings: Locating the homoclinic-doubling cascade," *Phys. D Nonlinear Phenom.* **146**, 100–120 (2000).
- ⁴²A. J. Homburg, H. Kokubu, and V. Naudot, "Homoclinic-doubling cascades," *Arch. Ration. Mech. Anal.* **160**, 195–243 (2001).
- ⁴³Y. A. Kuznetsov, O. De Feo, and S. Rinaldi, "Belyakov homoclinic bifurcations in a tritrophic food chain model," *SIAM J. Appl. Math.* **62**, 462–487 (2001).
- ⁴⁴C. Tresser, "About some theorems by L. P. Shilnikov," *Ann. Inst. H. Poincaré Phys. Théor.* **40**, 441–461 (1984).
- ⁴⁵L. Mora and M. Viana, "Abundance of strange attractors," *Acta Math.* **171**, 1–71 (1993).
- ⁴⁶R. Barrio, S. Ibáñez, and L. Pérez, "Hindmarsh–Rose model: Close and far to the singular limit," *Phys. Lett. A* **381**, 597–603 (2017).
- ⁴⁷A. R. Champneys, V. Kirk, E. Knobloch, B. E. Oldeman, and J. Sneyd, "When Shil'nikov meets Hopf in excitable systems," *SIAM J. Appl. Dyn. Syst.* **6**, 663–693 (2007).
- ⁴⁸A. Algaba, F. Fernández-Sánchez, M. Merino, and A. J. Rodríguez-Luis, "Structure of saddle-node and cusp bifurcations of periodic orbits near a non-transversal T-point," *Nonlinear Dyn.* **63**, 455–476 (2011).
- ⁴⁹S. Wicczorek and B. Krauskopf, "Bifurcations of n -homoclinic orbits in optically injected lasers," *Nonlinearity* **18**, 1095–1120 (2005).
- ⁵⁰G. Innocenti and R. Genesio, "On the dynamics of chaotic spiking-bursting transition in the Hindmarsh–Rose neuron," *Chaos* **19**, 023124 (2009).
- ⁵¹M. Desroches, J. Guckenheimer, B. Krauskopf, C. Kuehn, H. M. Osinga, and M. Wechselberger, "Mixed-mode oscillations with multiple time scales," *SIAM Rev.* **54**, 211–288 (2012).
- ⁵²T. Vo and M. Wechselberger, "Canards of folded saddle-node type I," *SIAM J. Math. Anal.* **47**, 3235–3283 (2015).
- ⁵³D. Avitabile, M. Desroches, and S. Rodrigues, "On the numerical continuation of isolas of equilibria," *Int. J. Bifurcation Chaos* **22**, 1250277 (2012).
- ⁵⁴T. Erneux and E. L. Reiss, "Brusselator isolas," *SIAM J. Appl. Math.* **43**, 1240–1246 (1983).
- ⁵⁵E. J. Doedel and C. L. Pando, "Isolas of periodic passive Q -switching self-pulsations in the three-level: Two-level model for a laser with a saturable absorber," *Phys. Rev. E* **84**, 056207 (2011).
- ⁵⁶J. C. Englund and W. C. Schieve, "Laser isolas," *J. Opt. Soc. Am. B* **2**, 81–83 (1985).
- ⁵⁷T. Namba, "Bifurcation phenomena appearing in the Lotka–Volterra competition equations: A numerical study," *Math. Biosci.* **81**, 191–212 (1986).
- ⁵⁸A. Algaba, M. Merino, F. Fernández-Sánchez, and A. J. Rodríguez-Luis, "Closed curves of global bifurcations in Chua's equation: A mechanism for their formation," *Int. J. Bifur. Chaos Appl. Sci. Eng.* **13**, 609–616 (2003).

4.3 Paper III

In this paper [3] we deepen into the relationship between the homoclinic bifurcation structure of the Hindmarsh-Rose model and the spike-adding phenomena. Small values of ε are considered.

We provide a global scheme that allows to locate continuous and chaotic spike-adding processes with respect to the homoclinic bifurcation curves. The side of the homoclinic curve on which the system is placed determines which are the bifurcations involved, and thus, how the process takes place. We consider different cuts in the (b, I) plane and illustrate the different spike-adding processes in detail. Different elements are involved in these processes: homoclinic isolas, canards, pencils of period-doubling bifurcations, codimension-two homoclinic bifurcation points, etc. The bifurcation structure underlying these phenomena is shown to persist for small values of ε (when the model is biophysically plausible).

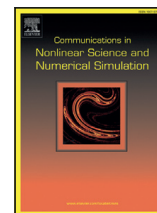
We combined different techniques (spike-counting, continuation, IBD's), which allows to connect the different views of the spike-adding processes provided in previous works, where the role of the homoclinic bifurcations is not evident. Our results highlight that a dynamical behaviour can be a consequence of a bifurcation that is not visible in the chosen parameter space. For instance, we provide an in-depth analysis of the diagonal band structure in the (x_0, I) found in previous works. Our exploration allows us to identify continuous and chaotic spike-adding and explain the passage from one to another from the homoclinic bifurcation structure.

We also illustrate that structures similar to those of the Hindmarsh-Rose model are found in the Sherman model of pancreatic β -cells. In particular, the spike-counting map for the Sherman model is also structured in bands corresponding to bursting of different number of spikes, and there are also chaotic lobes arranged in a similar fashion to the chaotic lobes of the Hindmarsh-Rose model. We have found homoclinic bifurcation curves with codimension-two degeneracies, from which fold and period-doubling bifurcation emanate. These fold and period-doubling bifurcation curves constitute borders of the different qualitative regions of the spike-counting map. All these findings suggest that the theoretical scheme that we proposed may be universal for generic fold/hom bursters.



Contents lists available at ScienceDirect

Commun Nonlinear Sci Numer Simulat

journal homepage: www.elsevier.com/locate/cnsns

Research paper

Spike-adding structure in fold/hom bursters

R. Barrio^{a,*}, S. Ibáñez^b, L. Pérez^b, S. Serrano^a^a IUMA and Dpto. Matemática Aplicada, Universidad de Zaragoza, Zaragoza E-50009, Spain^b Departamento de Matemáticas, University of Oviedo, Oviedo E-33007, Spain

ARTICLE INFO

Article history:

Available online 5 November 2019

MSC:

37Mxx

37Gxx

Keywords:

Spike-adding

Fold/hom bursting

Fast-slow dynamics

Neuron models

Homoclinic bifurcations

ABSTRACT

Square-wave or fold/hom bursting is typical of many excitable dynamical systems, such as pancreatic or other endocrine cells. Besides, it is also found in a great variety of fast-slow systems coming from other neural models, chemical reactions, laser dynamics, and so on. We focus on the spike-adding process and its connection with the homoclinic structure of the system. The creation of new fast spikes on a bursting neuron is an important phenomenon as it increases the duty cycle of the neuron. Here we mainly work with the Hindmarsh-Rose neuron model, a prototype of fold/hom bursting, but also with the pancreatic β -cell model, where, as already known from the literature, homoclinic bifurcations play an important role in bursting dynamics. Based on several numerical simulations, we present a theoretical scheme that provides a complete scenario of bifurcations involved in the spike-adding process and their connection with the homoclinic bifurcations on the parametric space. The global scheme explains the different phenomena of the spike-adding processes presented in literature (continuous and chaotic processes after Terman analysis) and moreover, it also indicates where each kind of spike-adding process occurs. Different elements are involved in the theoretical scheme, such as homoclinic isolas, canard orbits, inclination and orbit flip codimension-two bifurcation points and several pencils of period doubling and fold bifurcations, all of them illustrated with different numerical techniques. Some of these bifurcations needed in the process may be not visible on some numerical simulations because the organizing points are in different parametric planes due to the high dimension of the whole parameter space, but their effects are present. Therefore, we introduce a mechanism of the spike-adding process in fold/hom bursters in the whole space of parameters, even if apparently no role is played by the “far-away” homoclinic bifurcations. This fact is illustrated showing how the theoretical scheme provides a theoretical explanation to the different interspike-interval bifurcation diagrams (IBD) that have appeared in the literature for different models.

© 2019 Elsevier B.V. All rights reserved.

1. Introduction

One of the most active research lines today is neuroscience, and a part of it is devoted to the study of its basic elements, neurons. Models in this field exhibit fast slow dynamics [1], a feature which is shared with many other models in practical applications as the case of some chemical reactions [2] or, in the field of technology, laser devices [3]. An essential measure is the time that a neuron, or any other system, is active. This is related with the number of oscillations (spikes) in the

* Corresponding author.

E-mail addresses: rbarrio@unizar.es (R. Barrio), mesa@uniovi.es (S. Ibáñez), perezplucia@uniovi.es (L. Pérez), sserrano@unizar.es (S. Serrano).

fast subregime. In the literature there is a large number of articles dedicated to study the mechanisms involved in the spike-adding processes and also how the number of spikes changes when one parameter is varied.

This paper studies the spike-adding process focusing on the Hindmarsh-Rose [4] neuron model, as a well known example and prototype of square-wave (or fold/hom) bursting [5]. Literature concerning this model is really impressive and, only in relation to our interests, we can quote [6–17]. We contribute to the general understanding of the spike-adding process in fold/hom bursters, one of the most common ones. Namely, we put forward a theoretical scheme to describe the mechanisms involved in the formation of spikes in the context of such model. Later, we also show how these mechanisms are also observed in the Sherman et al. model of the pancreatic β -cell [18].

Since the pioneering work by Hodgkin and Huxley [19], many proposals have been made to encapsulate a qualitative description of the neuronal dynamics in a family of differential equations. The Hindmarsh–Rose model:

$$\begin{cases} \dot{x} = y - ax^3 + bx^2 - z + I, \\ \dot{y} = c - dx^2 - y, \\ \dot{z} = \varepsilon[s(x - x_0) - z], \end{cases} \quad (1)$$

is able to reproduce the most significant behaviours: quiescence, spiking and also bursting, either regular or irregular. Variable x represents the membrane potential, whereas y and z correspond to ionic currents. We consider a typical choice of parameters $a = 1$, $c = 1$, $d = 5$ and $s = 4$, discussing the spike-adding processes for different choices of the others [20]. The parameter ε is the small parameter of the model, giving rise to a fast-slow system with two fast and one slow variables.

This model is a prototypical example of fast-slow system. Bifurcations in the fast subsystem (limit case $\varepsilon = 0$) are essential elements of the fast-slow decomposition (first developed by Rinzel [21]) to explain the dynamics when ε is small. The study of the fast subsystem provides the spiking (or fast) manifold \mathcal{M}_{fast} , formed by stable limit cycles of the limit case, and the slow manifold \mathcal{M}_{slow} , formed by the equilibria of the limit case. The stable periodic orbits of the complete model behave following the well-known phenomenon, explained by singular perturbation theory and Fenichel's theorems [22], that the orbits (for small enough parameter ε) exhibit jumps from one manifold to the another one along its trajectory. Note that, when $\varepsilon = 0$, z is an additional parameter of system (1). Choosing b and I in suitable regions one can check that the curve of equilibrium points (slow manifold) exhibits a S-shape with two Hopf and fold bifurcations splitting the curve in stable and unstable branches (see [1] for more details).

We call bursting oscillation a time evolution consisting of bursts of rapid spikes (any excursion around the tubular manifold \mathcal{M}_{fast}), alternated by phases of relative quiescence (following \mathcal{M}_{slow}). The kind of bursting that we study here is said fold/hom [23] because the family of limit cycles displayed by the fast subsystem ends at a homoclinic bifurcation, where trajectories of the full system jump to the slow manifold.

By spike-adding process we understand any mechanism leading to the formation of additional turnings. The spiking rate and the time between spikes are essential elements in the understanding of the codifications in the neurons. As a result, spike-adding has been studied in many fold/hom neuron models [24–27], including the Hindmarsh-Rose system as a prototypical one. It should be noted that in the literature one can find other types of spike addition processes that arise in bursting models of different nature, such as systems with external multiple frequency forcings, in which new bursting patterns can be observed [28,29]. In these models, the effects of forcing frequencies must be taken into account. As well, phenomena of mixed mode burst oscillations (MMBO), that is, solutions that exhibit small amplitude oscillations and bursts consisting of one or multiple large amplitude oscillations, have been observed in some fourth order systems [10].

As explained in [30], the spike-adding transition may be either continuous, with a period which increases along the process, or discontinuous, involving chaotic phenomena. Relevance of fold bifurcations of periodic orbits was pointed out numerically in [31]. Dealing with fold/hom bursting, the spike-adding has also been related with canard orbits [14,16,32,33], already anticipated in [30] when the increasing of the period was pointed out, and also with the existence of certain codimension-two homoclinic bifurcations [7,8,10,16,17]. Spike-adding cascades were also discussed in [25] for a modified version of the Hindmarsh-Rose model. Authors identified two different routes which were determined by the location of the equilibrium point in the full system with respect to the homoclinic bifurcation in the fast subsystem. One involves fold bifurcations of periodic orbits. In the second route the spike-adding cascade is organized by isolas.

As already mentioned, spike-adding mechanisms have been linked to the occurrence of certain codimension-two homoclinic bifurcations. Namely, fold and period doubling bifurcations have been shown to arise from codimension-two bifurcation points located along homoclinic bifurcation curves exhibited by the full system for fixed values of ε and with b and I varying. In this paper, we aim at showing the mechanism of the spike-adding process by proposing, based on our bifurcation results, a possible theoretical scheme that completes and provides answers to open questions related to the first scheme given in [16]. Moreover, the proposed scheme permits to locate theoretically both spike-adding processes studied by Terman [30], a connection which is missed in the literature.

All these spike-adding processes are usually illustrated by means of interspike-interval bifurcation diagrams (IBD) of stable bursting orbits as one parameter changes (see [9,13,25]). That kind of pictures shows different cascades of spike-adding (or period-adding) phenomena, crossing or not chaotic zones. The involved chaotic transitions have been discussed in several papers [8,13,15,17], but what is missing is a connection with a theoretical framework. In Section 3 it is shown how the introduced global scheme provides a theoretical explanation to the different IBD diagrams that have appeared in the literature.

This paper is organized as follows. Section 2 presents a global three-parametric numerical study of the Hindmarsh-Rose model focusing on the 2–3 spike-adding process (from 2 to 3 spikes per burst) and on the 6–7 one. Section 3 provides a theoretical scheme of the fold/hom spike-adding area with the different bifurcations involved in the process. Also, once the theoretical scheme is given we show how it provides an explanation for the typical IBD pictures shown in literature. An example using a more realistic model, the pancreatic β -cell neuron model of Sherman et al.[34], is presented in Section 4, showing that the same bifurcations as in the Hindmarsh-Rose model are present. Finally, we give some conclusions.

2. Global analysis

In this section we study the structure of the parametric space of the system by using different numerical techniques.

As an introduction, in Fig. 1 we use the HR model to exemplify two processes of spike-adding usually shown in literature [13,25]. Panel (a) shows an interspike-interval bifurcation diagram (IBD) of stable bursting orbits as I varies when $\varepsilon = 0.01$, $x_0 = -1$ and $b = 2.7$. Similar bifurcation diagrams are given in [9], where the spike-adding process is clearly shown. For high values of I , from right to left, the model exhibits tonic spiking which precedes a cascade of period doubling bifurcations leading to chaos. After crossing the chaotic zone the bifurcation diagram is wider and it starts an inverted cascade of period doubling bifurcations, and later a regular bursting regime with 12 spikes is observed. This transition is named a continuous interior crisis [11,13] (compare also with [30] when Terman shows that a transition from n to $n + 1$ spikes can be chaotic). When I decreases there is a sequence of spike-deletions between which there is a well-defined bursting regime. In [12,13] it is said that the dynamics is block structured. Note that the transition between blocks can be again chaotic. As already mentioned, this type of diagram is shown quite frequently in literature for different models but, although chaotic transitions are discussed, no connection with a theoretical framework is available.

Right side panel (b) shows another IBD. In this case b varies whereas $\varepsilon = 0.01$, $x_0 = -1.6$ and $I = 2.2$. From now on, unless indicated, we fix the value $x_0 = -1.6$. We also provide the continuation of a periodic orbit (plotting the $\|\cdot\|_2$ norm against b using AUTO continuation software [35]) along the whole process of spike-adding. Note that the periodic orbits evolve continuously with respect to the parameter (a similar evolution could be shown for the case of the left panel, at least for the transition from 2 spikes to 11 spikes). This spike-adding mechanism with a continuous evolution of the periodic orbit was already anticipated in [30]. Note that the sequence of bifurcations involved in the transition from n to $n + 1$ spikes is always the same: two fold bifurcations give rise to an hysteresis phenomenon. These fold bifurcations are the key features of this spike-adding process. They have already been shown in some examples in [8,14,16].

As illustrated in Fig. 1, spike-adding cascades determine, following the notion introduced in [13], a block structure in the bifurcation diagrams. But this analysis uses just one parameter, and other techniques are more suitable to provide results in higher dimensional parameter spaces. Fig. 2 shows how these blocks give rise to bands when two- and three-dimensional parameter spaces are explored. Spike-counting technique [9], which counts the number of spikes in a burst, is used to obtain two-parameter sweeps on certain parameter planes: a vertical one with I fixed and five horizontal planes with ε fixed. Putting everything together on a three-dimensional parameter space (b, I, ε), we obtain the two pictures displayed in Fig. 2 (front and back views). Clearly visualized, we observe a band structure which goes through a simplification process as ε increases: note how the number of colors (related with the number of spikes per burst) decreases. The simplification of the band structure is explained in [7] by means of a parallel process of simplification in the homoclinic structure in the system. The dark red regions denote chaotic areas or, due to the chosen color scale, they correspond to bursting orbits with a large number of spikes (see bottom part). For further understanding, one should place the bifurcation diagrams shown in Fig. 1 in the context of Fig. 2, where the IBD shown in the plot (b) of Fig. 1 corresponds to a line in the three-parametric

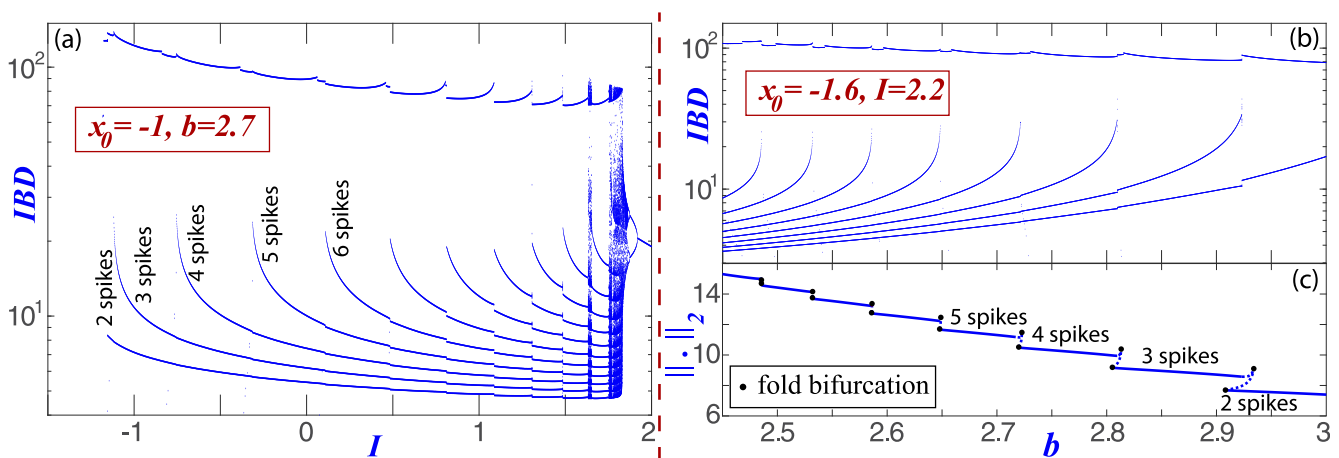


Fig. 1. Two typical examples of spike-adding processes. Left: interspike-interval bifurcation diagram (IBD) with $x_0 = -1$, $b = 2.7$, $\varepsilon = 0.01$ and I as bifurcation parameter. Right: continuation of a periodic orbit with b varying and $x_0 = -1.6$, $I = 2.2$, $\varepsilon = 0.01$. This left panel shows the IBD and the $\|\cdot\|_2$ norm of the periodic orbit as a function of b , where solid (resp. dashed) refers to stable (resp. unstable) orbits.

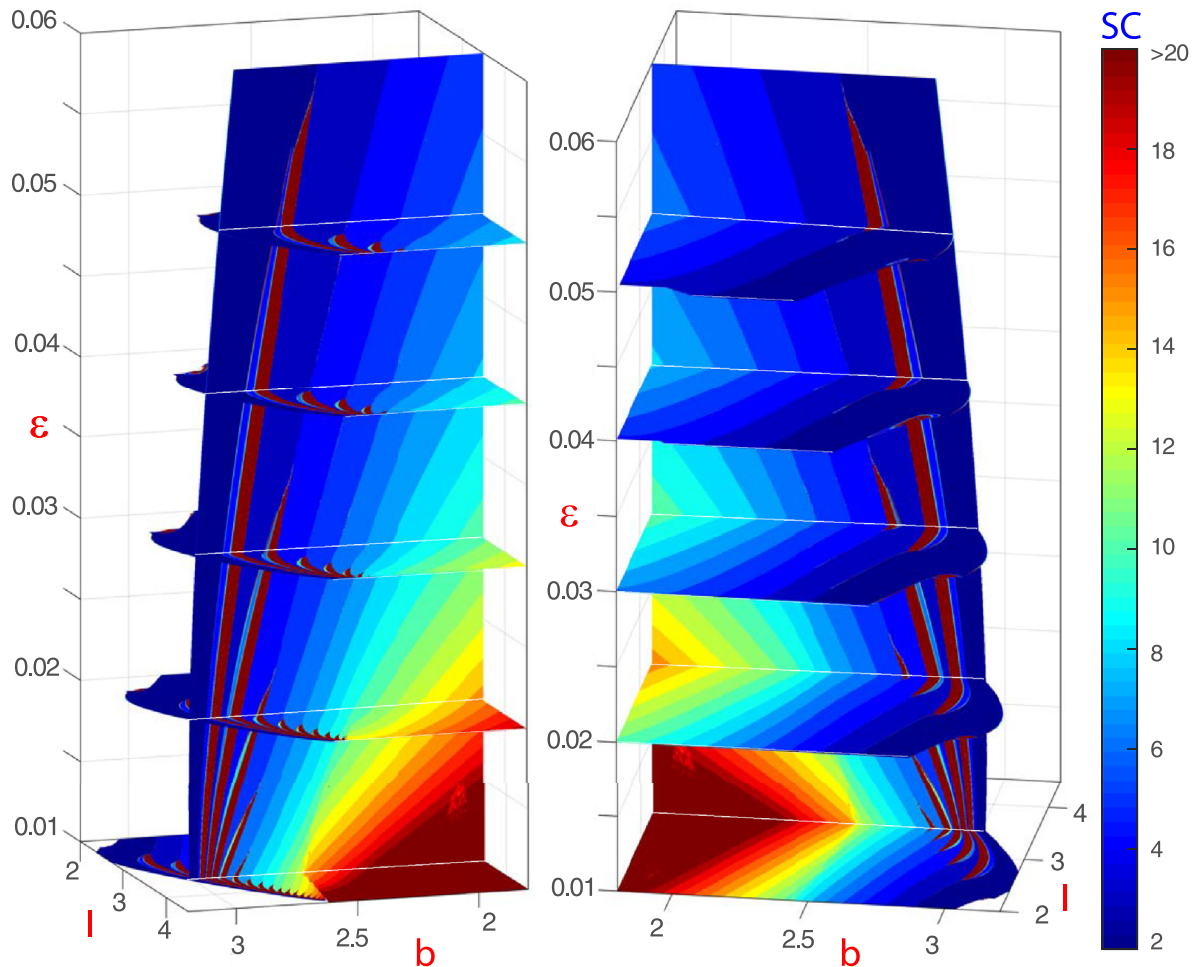


Fig. 2. Three-parametric (b, l, ε) diagram showing the spike-counting (SC) sweeping technique, number of spikes per burst of the attractor, in different biparametric planes. The pictures show how the number of spikes per burst decreases when the small parameter ε grows and how less and less color bands appear. The global structure seems to be similar for any small value of the parameter, but with more color bands.

study of Fig. 2 that crosses the different bands on the spike-adding process. Now the question is to focus on detecting the main ingredients that give rise to the structures observed in Fig. 2.

In the sequel, we use the notation $hom^{(n, n+1)}$ to refer to a homoclinic bifurcation surface (or curve) where the homoclinic orbit evolves from n to $n+1$ spikes. In [6,7], we showed how these homoclinic bifurcation surfaces overlap each other forming a structure of “mille-feuille”. In turn, arising from these surfaces we find bifurcations of periodic orbits that are essential ingredients in the mechanisms of spike-adding. As already mentioned, bifurcations of periodic orbits involved in the spike-adding mechanisms in the Hindmarsh-Rose model were linked to the existence of certain codimension-two homoclinic bifurcations in [14,16].

In Fig. 3 we show bifurcation diagrams on parametric planes (b, l) , fixing different values of ε . All of them show similar techniques and elements: spike-counting, a homoclinic bifurcation curve, codimension-two homoclinic bifurcation points, folds of periodic orbits and curves of period doubling bifurcation. Although three types of homoclinic bifurcations of codimension-two can appear, now we only pay attention to inclination flips (IF) and orbit flips (OF). In our case, at both bifurcations the linear part at the equilibrium point has real eigenvalues λ^s , λ^u and λ^{uu} with $\lambda^s < 0 < \lambda^u < \lambda^{uu}$. Passing through an inclination flip, the orientation of the global two-dimensional unstable manifold changes. Whereas through an orbit flip, there is a switching when, following the backward flow, the homoclinic orbit approaches the equilibrium over the leading unstable manifold; namely, the entrance branch is reversed. Reference [36] contain extended discussions regarding these codimension-two homoclinic bifurcations. There are three classes of flip homoclinic bifurcations: A, B and C. Those exhibited in the Hindmarsh-Rose model are all of type C. The corresponding theoretical bifurcation diagram is well-known in literature (see [36] and references therein). There exist pencils consisting of fold bifurcations of periodic orbits, period doubling bifurcations and wedge-shaped regions of chaotic behaviour.

Left and right panels in Fig. 3 show diagrams which include (black coloured lines) the curve $hom^{(2,3)}$ and $hom^{(6,7)}$, respectively. From top to bottom the values of ε are 0.01, 0.015 and 0.03. Note that, as already known from [16], the endpoints of the homoclinic bifurcation curve are only apparent ends. There, the curve is folded onto itself so that, actually, there is a

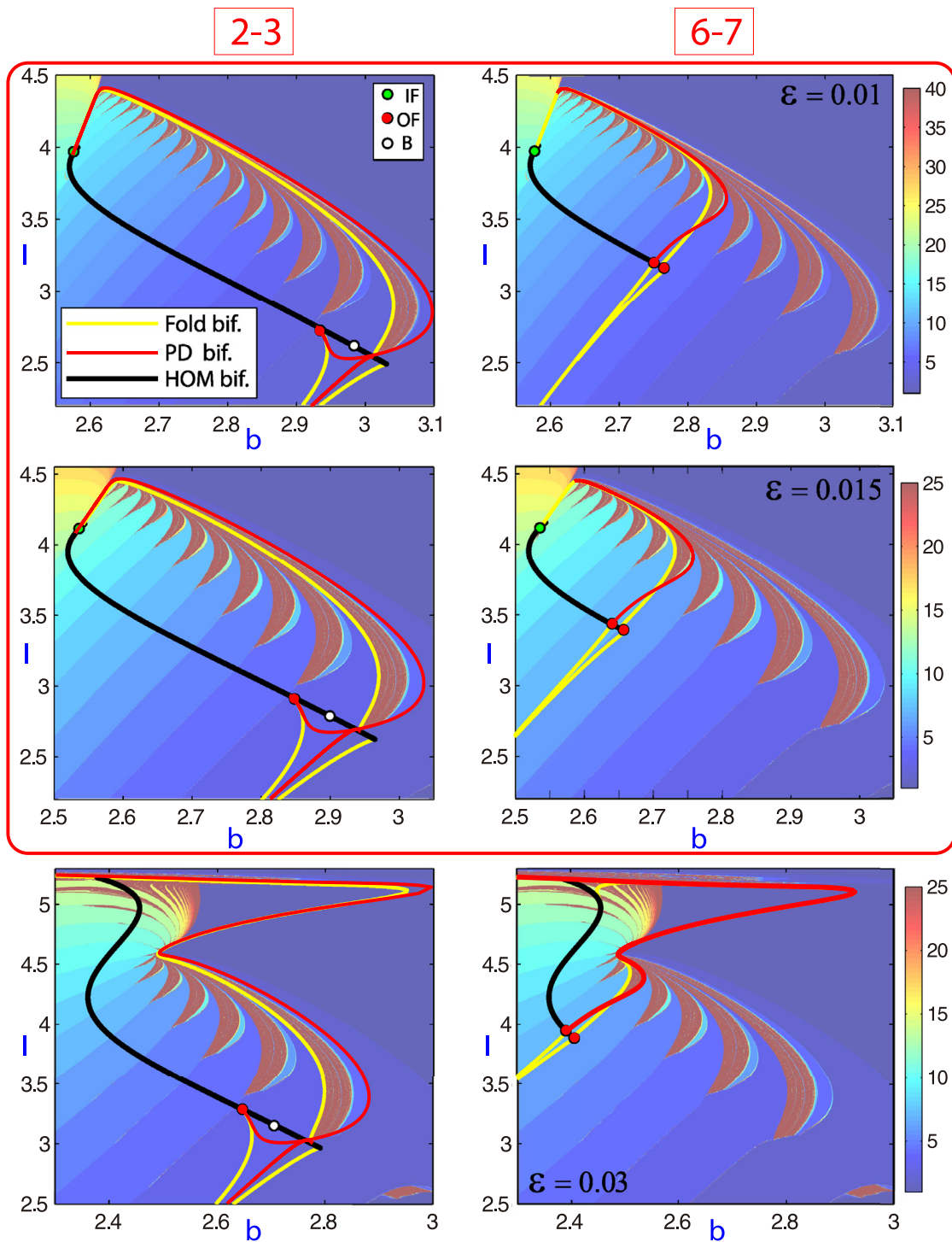


Fig. 3. Three biparametric (b, l) spike-counting diagrams (for $\varepsilon = 0.01, 0.015$ and 0.03) and the main bifurcation lines detailed for the 2–3 and 6–7 spike-adding processes. The square remarked area shows the structure for small parameter values of ε (similar pictures for any $\varepsilon \ll 1$ exist but with more and more stripes). The PD and Fold bifurcations shown are the ones that delimit the spike-adding structure. Some codimension-2 homoclinic bifurcation points are marked on the corresponding homoclinic bifurcation lines. See the text for more details.

double covering with two branches. In fact, it is argued in [7] that these curves are closed and hence it makes sense to refer to isolas limited by homoclinic bifurcations. To illustrate this fact, in Fig. 4 we show (central panel) the curve $hom^{(6,7)}$ on the two-parameter plane (b, l) for $\varepsilon = 0.07$. It seems to be just a line, but this cannot be the case, as long as the bifurcation curve cannot stop suddenly, unless a codimension-two point or another singularity appears. If we follow the bifurcation curve with continuation techniques (using the software AUTO in our case) we really see that the continuation process produces foldings on the visible segment. To study what happens, we consider three values of the parameter l and we show the homoclinic orbits obtained in each one of the branches. At each value of l we have obtained two different homoclinic orbits

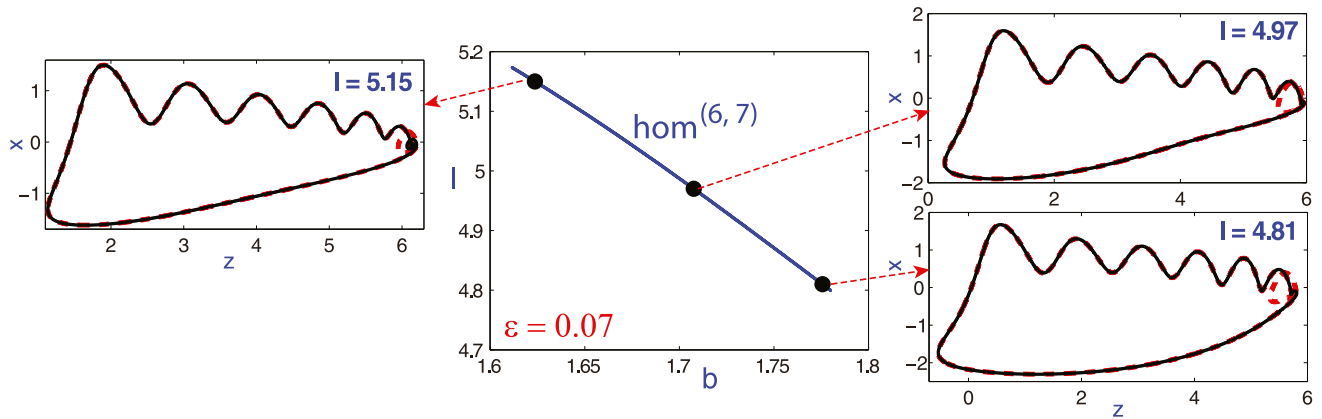


Fig. 4. Center: Parameter plane (b, l) for $\varepsilon = 0.07$ showing the isola of the codimension-one homoclinic curve that gives 6–7 spikes per burst. Left and right: xz projections of two homoclinic orbits for three fixed values of l .

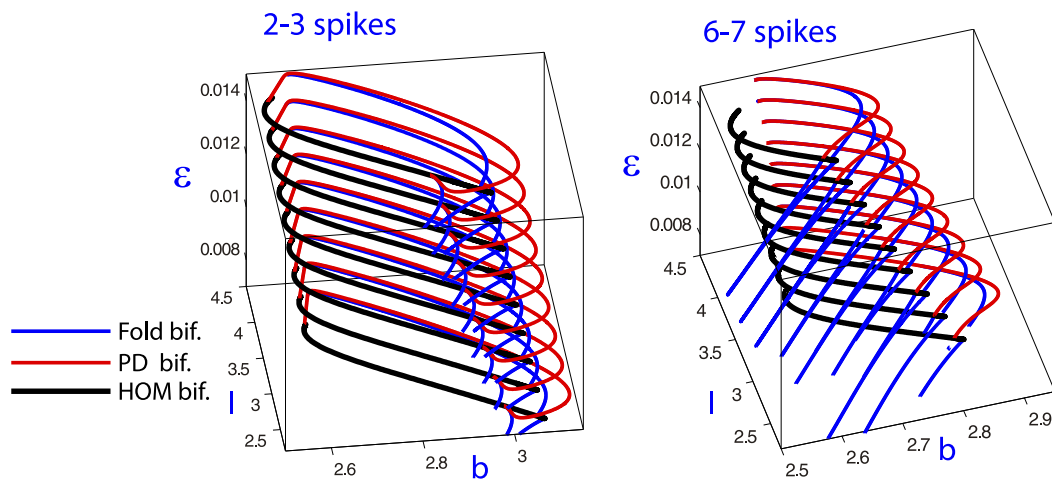


Fig. 5. Three-parametric (b, l, ε) plots of homoclinic bifurcation curves corresponding to $hom^{(2,3)}$ and $hom^{(6,7)}$ for low values of the small parameter ε , including also the main PD and Fold bifurcations.

(left and right panels in Fig. 4). One has an extra loop around the equilibrium far from the burst activity, namely, there is a homoclinic orbit with six spikes (black color), and another one (red color) with seven spikes, but organized in two groups, one of six spikes and another one of just one. This provides a numerical evidence of the existence of the homoclinic isola.

In this paper we focus on small values of ε because we want to provide a study of the generic case when $\varepsilon \ll 1$. That is the reason why the bifurcation diagrams for $\varepsilon = 0.01$ and $\varepsilon = 0.015$ are remarked in Fig. 3. Note that the main difference between small and large values of ε has to do with left ends of folds and period doubling bifurcations. Whereas for small values these curves emerge from inclination flip bifurcations placed on the left side of the homoclinic curve, for larger values these bifurcation curves extend far from the homoclinic structure.

To understand the theoretical scheme that we propose below in Section 3, one should pay attention to some of the differences observed in Fig. 3. The most remarkable one is that, whereas $hom^{(6,7)}$ exhibits two orbit flips (OF), the left one located on the lower branch of the homoclinic curve and the right one on the upper one, $hom^{(2,3)}$ only exhibits one, located on the lower branch. We remark that the behaviour exhibited by $hom^{(6,7)}$ is the generic one, that is, it corresponds to the behaviour that we found along $hom^{(n,n+1)}$ for ε small and $n > 2$. Nevertheless, as already argued in [16], we stress that $hom^{(2,3)}$ behaves differently, although the global picture is similar, except in a very small region around the homoclinic curve. We will come back to this later, when we discuss the scheme provided in Fig. 6.

In Fig. 5 we show that the structures observed in Fig. 3 for some values of ε are the generic ones for ε small enough. The bifurcation curves build up surfaces in the three-parameter space (b, l, ε) . Later on, this global structure will allow us to understand, from a slightly different perspective, the different explorations on spike-adding processes provided in the literature.

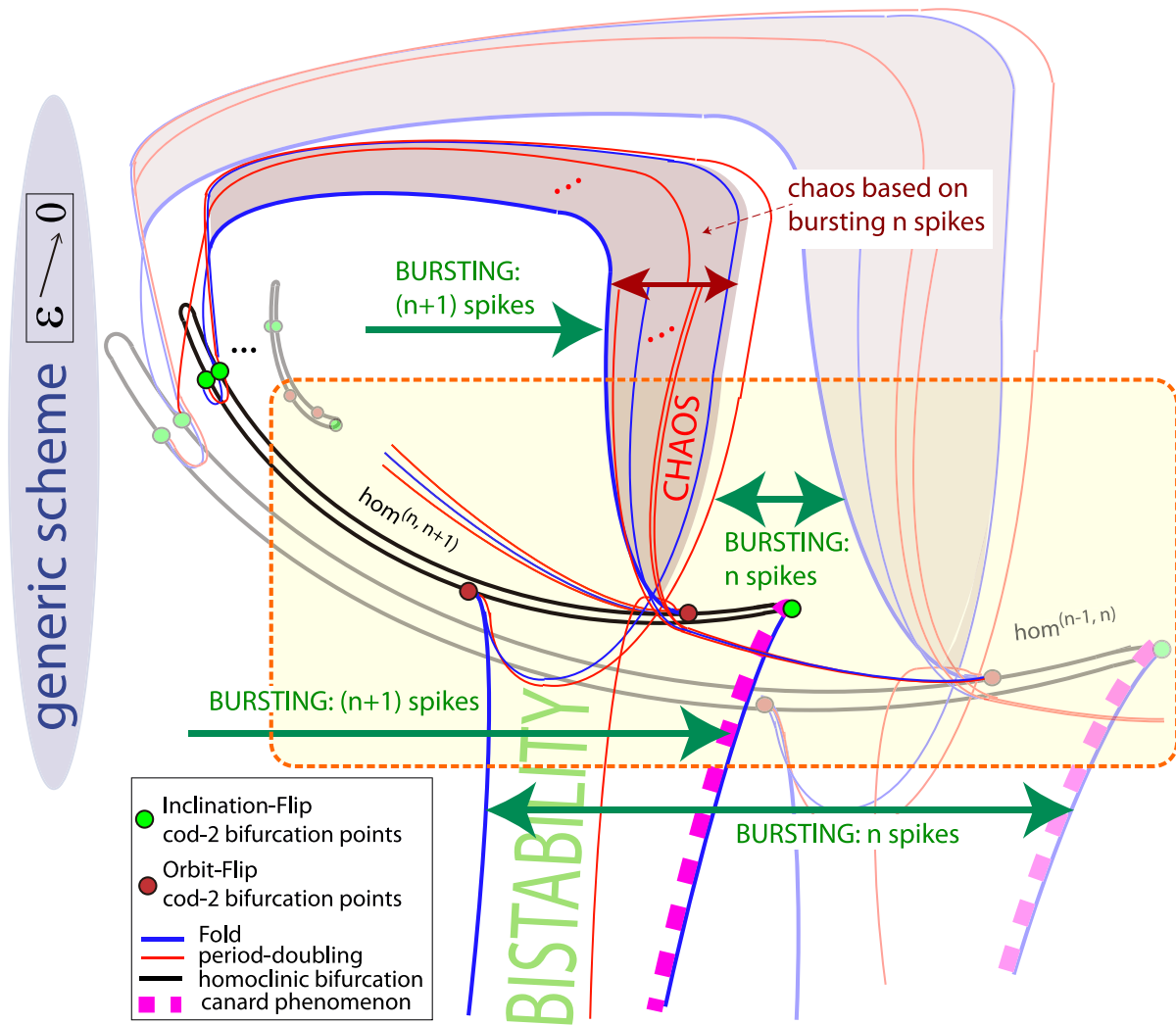


Fig. 6. Generic theoretical scheme ($n > 2$) showing the entwined bifurcation diagram involved in the spike-adding mechanisms. See the text for explanation.

3. Global theoretical scheme

In Section 2 we have seen numerically how the main bifurcations (period doublings and folds of periodic orbits) which are involved in the spike-adding mechanism are organized with respect to the homoclinic structures exhibited in the system. Next, we introduce a theoretical scheme providing a fully general overview of the process.

3.1. Global theoretical scheme: biparametric case (ε fixed)

Using the numerical simulations shown in Section 2 and previously in [7,8,16], we provide in Fig. 6 a more complete generic scenario of the transition in fold/hom bursters from n to $n + 1$ spikes when ε is small. Note that the homoclinic isola component was illustrated in the previous section exploring the $hom^{(6,7)}$ case. As already explained in [7], the homoclinic isolas are piled up and their size decreases as the number of spikes increases. In each homoclinic curve we find some significant degenerations: three inclination flips and two orbit flips. The two inclination flips on the left side are terminal points for fold and period doubling bifurcations, but they do not play a relevant role in the discussion below. Depending on the location, either above or below the isola, the mechanisms to create extra spikes are different. Note that the scheme is partial as more bifurcations and codimension-two points should be present.

In Fig. 6 we have remarked the complete structure for the n to $n + 1$ ($n > 2$) spike-adding process. Suppose we follow the evolution of a periodic orbit with n spikes as we move from the right side of the parameter plane and below the homoclinic curve (see right plots of Fig. 1). This orbit undergoes through two fold bifurcations which give rise to a hysteresis phenomena (a Z-shaped continuation curve). The first one is on the left, where the orbit becomes unstable and later the continuation goes back to the right till the fold bifurcation on the right is reached. There, the periodic orbit becomes stable again and, as we will shortly explain, exhibits an extra spike. The stability is lost later through several period doubling and fold bifurcations (due to some pencils of these bifurcations generated on codimension-two bifurcation points) till another

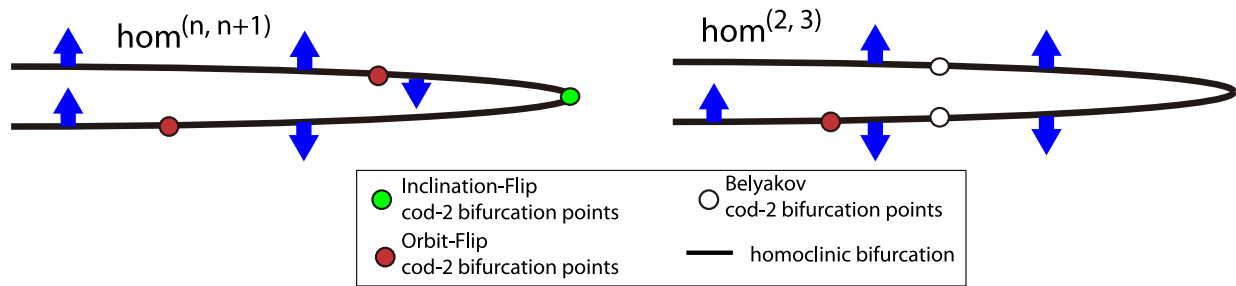


Fig. 7. Directions in which the saddle periodic orbits emerge from the homoclinic connection as we move along the homoclinic bifurcation curve. In the generic case ($n > 2$) there are three changes of direction, two of them are explained by the existence of orbit flips, whereas, the other can be explained by the presence of an inclination flip. In the case of the curve $hom^{(2,3)}$ there is only one change which is explained by the existence of just an orbit flip.

period doubling, located in between both main fold bifurcations, is reached. Hysteresis explains the existence of a region of bistability, where orbits with n spikes coexist with orbits with $n + 1$ spikes. The addition of the extra spike is explained by a canard transition [10,14] which occurs while the orbit undergoes through the second fold bifurcation on the right side. On the other hand, the transition from n to $n + 1$ spikes above the homoclinic isola involves a chaotic region. Note that the theoretical scheme includes the two types of spike-adding processes introduced by Terman in [30] and also described in [13,14,16]. The main original contributions of the scheme are, first to establish what areas will produce each kind of spike-adding, and second to provide an overall explanation of the origin of the bifurcations involved in each type of spike-adding process. Later, in Fig. 8, we will provide numerical explorations to illustrate both, continuous and chaotic spike-adding processes. We remark that the boxed area of Fig. 6 contains the main ingredients for the spike-adding process in a fold/hom burster (as it is shown later in Section 4 for the pancreatic β -cell model), while the complete panel explains the complete structure for the Hindmarsh-Rose model.

Next, we describe in detail the location of the codimension-one bifurcations of periodic orbits proposed in Fig. 6. Let us first pay attention to the bifurcations involved in the continuous spike-adding process (below the homoclinic isola). The fold bifurcation on the left emerges from the orbit flip on the left, located on the lower branch of the homoclinic curve. At this orbit flip the homoclinic connection exhibits n spikes. This fits with the fact that, at the fold bifurcation on the left, the periodic orbit also has n spikes. On the other hand, the fold bifurcation on the right emerges from an inclination flip located on the folding of the homoclinic isola [16]. Note again that this fits with the fact that at this fold bifurcation the periodic orbit is still evolving from n to $n + 1$ spikes. Indeed, as we will illustrate later in Fig. 9, while the periodic orbit undergoes through the fold bifurcation on the right the head of a canard orbit is starting to develop and, as a consequence, an extra spike is being formed. It makes sense to think that this mechanism is related to its counterpart behaviour along the homoclinic curve. In addition, as we will see later, the existence, conjectured in [16] but not numerically detected (due to precision limitations of any available numerical continuation software), of the inclination flip on the folding of the homoclinic isola, is explained by arguments related to the way in which periodic orbits are created from the homoclinic curve. On the other hand, the chaotic lobe is related to several codimension-two homoclinic bifurcations. The fold and period doubling bifurcations at the right, separating the chaotic zone from the region corresponding to bursting with n spikes, emerge from the orbit flip located on the lower (n -spikes) branch of $hom^{(n, n+1)}$. The fold bifurcation at the left, that is, the frontier between the chaotic zone and the region corresponding to bursting with $n + 1$ spikes, emerges from the orbit flip located on the upper ($n + 1$ spikes) branch of $hom^{(n, n+1)}$. In Fig. 8 we will show that the chaotic behaviour inside the upper chaotic lobe is based on bursting behaviour with n -spikes, and so the pencils of bifurcations associated with that phenomena have to be generated on a codimension-two point related with n -spikes behaviour. Therefore, we conjecture that the period doubling and fold bifurcations inside the chaotic lobe emerge from the orbit flip located on the upper branch (n -spikes) of the previous homoclinic curve $hom^{(n-1, n)}$.

As already mentioned, AUTO is not able to detect the inclination flip located at the right end of the isolas. Nevertheless, as reasoned in [16], there is an argument to show that there must be another degeneracy in between the orbit flips when we move from one to the other side of the isola along the right side of the curve. Arrows in Fig. 7 indicate the direction in which single saddle periodic orbits emerge [37] from the homoclinic bifurcation curve (determined using AUTO software). Left panel shows the generic case where we see that there are, at least, three changes of direction. Following [16,38], there are three codimension-two homoclinic bifurcations which can explain the side-switching: orbit flip, inclination flip and resonant eigenvalues. The latter one is excluded and moreover, following the homoclinic orbit from one orbit flip to the other along the right side, there is no change in the direction along which the homoclinic orbit leaves the equilibrium point and, hence, no additional orbit flip may exist in between. The only option to explain the change in the direction of the arrows is the existence of an inclination flip. The same situation can be found in literature in a different model [38].

Right panel in Fig. 7 corresponds to the curve $hom^{(2,3)}$. In this case only one change of direction is observed. This fits with the fact that in this case (and also along $hom^{(1,2)}$) only one orbit flip exists. In fact, the existence of an inclination flip at the right tip of the isola in these two cases is discarded because there exist two Belyakov bifurcation points and the

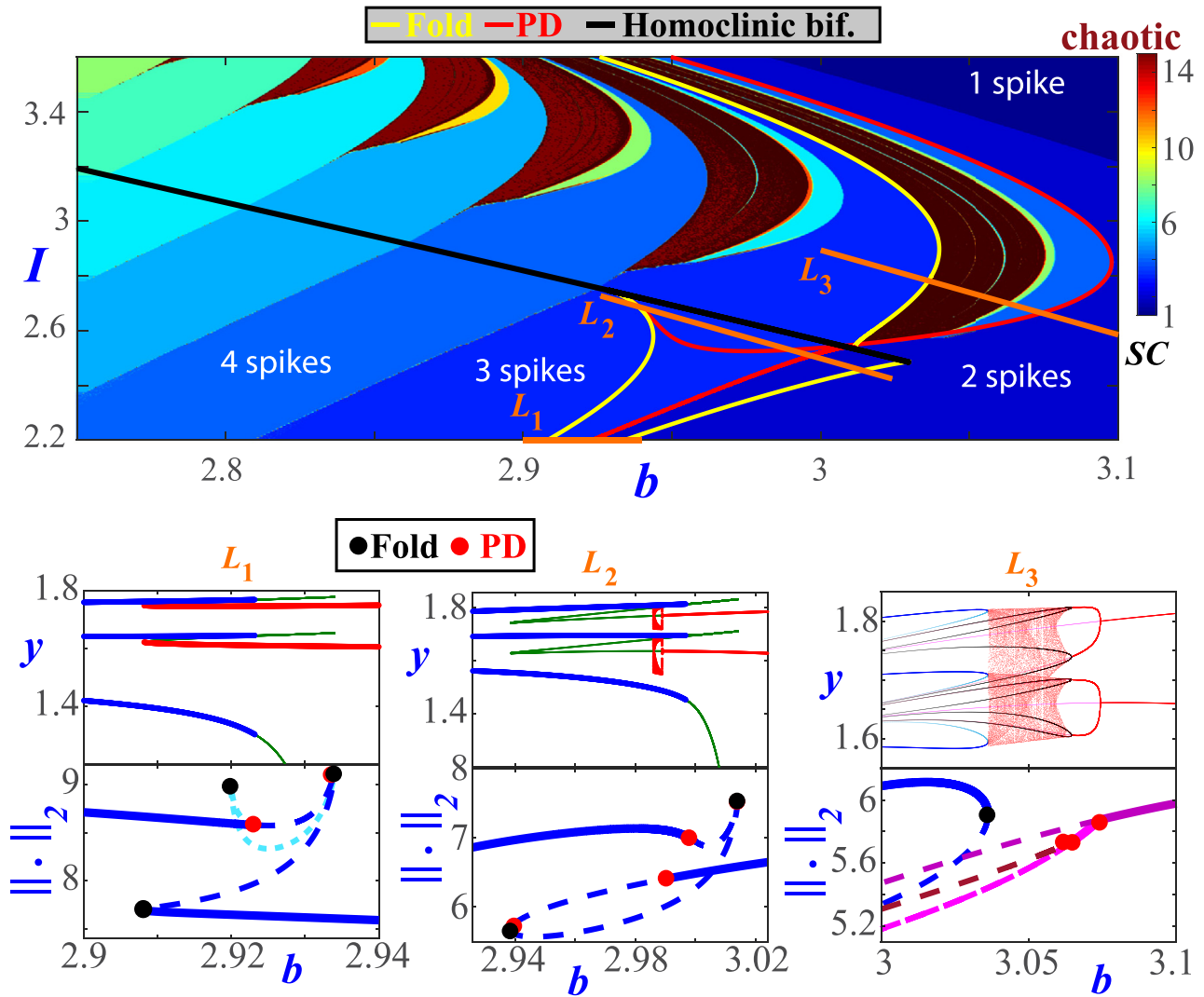


Fig. 8. Analysis of the spike-adding process from 2 to 3 spikes for $\varepsilon = 0.01$. Top: Biparametric diagram with the spike-counting technique and main bifurcation curves for the transition along selected spike-adding process. Bottom: Bifurcation diagrams for segments marked on top picture ($L_1 \equiv I = 2.2$; $L_2 \equiv I = 2.727 - 3.0918(b - 2.926)$; $L_3 \equiv I = 2.891 - 3.0918(b - 3.001)$). Two pictures have been performed for each segment: one plot with the standard bifurcation continuation diagram given by AUTO showing the $\|\cdot\|_2$ norm of the orbit and another one with the y value of the points where the corresponding orbit has a maximum for variable x .

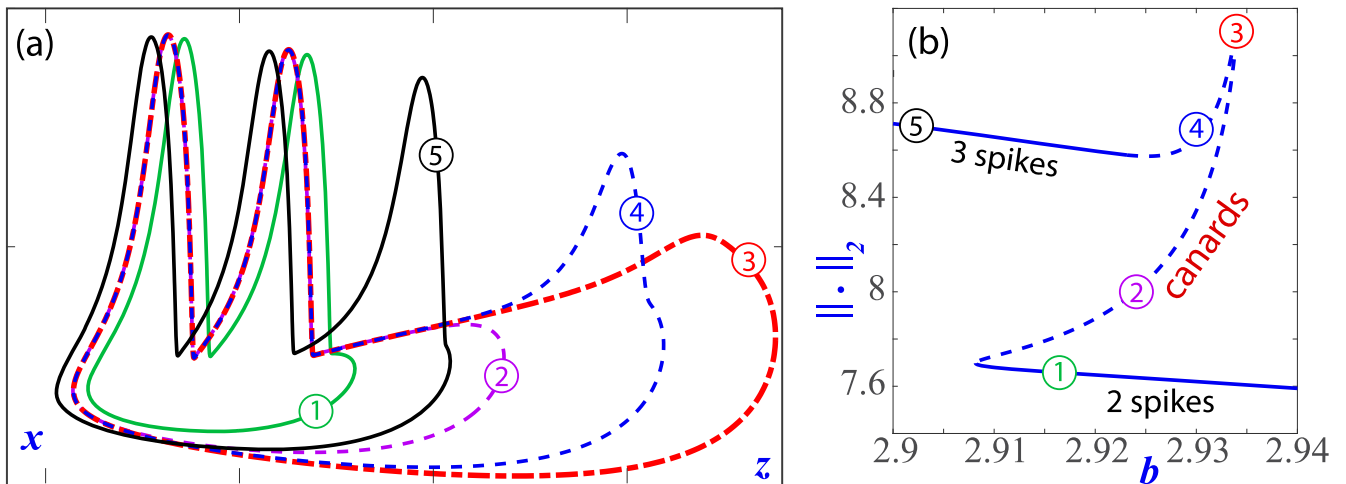


Fig. 9. (a): Evolution of periodic orbits throughout the process of spike-adding. (b): Bifurcation diagram obtained by continuation corresponding to the segment L_1 on Fig. 8. The coloured numbers mark the points in the diagram corresponding to the selected values. Along the continuation of the bifurcation lines we observe periodic orbits with two spikes (orbit 1), later headless canards (orbit 2), maximal canard (orbit 3), canards with head (orbit 4), and finally orbits with three spikes (orbit 5).

right side of the homoclinic curve in between the Belyakov points corresponds to saddle-focus equilibrium points and so, flip bifurcations make no sense.

We remark that our theoretical scheme of Fig. 6 is valid for the generic case of $hom^{(n,n+1)}$ with $n > 2$. As already explained, in the generic case, one of the fold bifurcations involved in the continuous spike-adding emerges from the inclination flip at the tip on right side of the homoclinic isola, as well as one of the folds involved in the chaotic spike-adding emerges from the orbit flip located on the upper branch of the curve $hom^{(n,n+1)}$. When $n = 2$, there are only one OF point on the lower branch of the curve $hom^{(2,3)}$. In any case, the macroscopic global view is similar to the generic case, as shown in Fig. 3.

Both cases, continuous and chaotic spike-adding transitions, are illustrated in Fig. 8 for the case of the transition from 2 to 3 spikes (we have chosen this case as globally the process is the same but it is easier and better visualized due to the bigger area involved). A periodic orbit is continued along three different segments of parameters: L_1 , L_2 and L_3 as displayed in the top panel. Bottom panels show the corresponding bifurcation diagrams: on the vertical axis we plot the value of y (top diagrams) at the points where the variable x has a maximum and the $\|\cdot\|_2$ norm (bottom diagrams) of the periodic orbit.

Along the segment L_1 we observe a continuous spike-adding process. From right to left, we see how a periodic orbit with 2 spikes undergoes a fold bifurcation at which it loses its stability. Later, now for b moving to right, the periodic orbit increases its length until it reaches a second fold at which b starts to decrease again. The periodic orbit recovers the stability after a period doubling bifurcation. Note that in this area there are pencils of bifurcations very close each other, and so it is quite difficult to observe them and their effects. Just to show this, the doubled periodic orbit emerging at that point ($b \simeq 2.922$) is also continued with AUTO. It undergoes through a fold bifurcation where parameter b starts to increase until a second period doubling is reached, and so on (note that the unstable orbit is connected with bifurcated orbits close to the fold on the right). This process only can be detected using continuation techniques because the stable region is very small and it has no real effects in the dynamics.

The behaviour along the segment L_2 , very close to the homoclinic curve but below, exhibits some differences to that already described along the segment L_1 , but the process is still continuous. The main difference is that in this case there is a microchaotic structure coexisting with stable periodic orbits due to the segment L_2 crosses pencils of period doublings and fold bifurcations generated on the orbit flip point located on the left (see [8] for additional details).

Finally, along the segment L_3 , the spike-adding process is discontinuous, going through a chaotic area. Starting from the right we see how a 2-spikes periodic orbit goes through a chaotic window after which only one stable orbit persists, but exhibiting 3 spikes. Note that the chaotic window is generated via a period doubling cascade originated from a bursting orbit with 2 spikes, as shown on the picture on the right for the segment L_3 . Note that the determining characteristic for the process of spike-adding to be continuous or discontinuous is on which side of the homoclinic curve the system is located and, therefore, what are the bifurcations that affect it.

A picture of the transition from 2 to 3 spikes along the segment L_1 is given in Fig. 9. Following the bifurcation curve depicted in the plane $(b, \|\cdot\|_2)$ displayed in the right panel, the excursion starts on the lower branch of the bifurcation curve where the 2-spikes periodic orbit is stable. After undergoing through a fold bifurcation, the periodic orbit becomes unstable and its length starts to increase as b decreases. This is the beginning of the canard transition already mentioned. The increment in the length of the periodic orbit occurs as it extends following the piece of the slow manifold. The orbit evolves from “headless” canard to a maximal canard, giving finally a bursting orbit with an extra spike (for details, see [10,14]). Homoclinic orbits undergo similar transformations as they evolve from the orbit flip located in the lower branch of the homoclinic curve and they pass the right-folding (see [16] for an example showing the transition from 3 to 4 spikes).

3.2. Global theoretical scheme: global case

The structure provided by the theoretical scheme is robust with respect to ε for small values of this parameter. In Fig. 10 the theoretical scheme of Fig. 6 is visualized into a three-parameter space. Note that the surfaces of fold bifurcation and period doubling involved in the spike-adding process emerge from the homoclinic bifurcation curves. A green plane is marked to emphasize that, in principle, it would be possible to take two-parameter slides hiding the whole homoclinic structure, but in any case, as we have argued, the spike-adding process cannot be fully understood without realizing the full bifurcation diagram. Particularly, all previous explorations recorded in the literature fit with our scheme, although in some of them it is not possible to see any homoclinic bifurcation (it depends on the selected parameters and regions as argued from Fig. 10). In fact, all the situations detected in previous studies can be explained with a single global theoretical scheme shown in Fig. 10.

In order to see how the theoretical scheme given in Fig. 6 is valid for the classical 1D views provided in literature, we take again the pictures of Fig. 1. Plots (b) and (c) have been already studied in Figs. 8 and 9 linking them with the results of Fig. 6. Now, we intend to explain the theoretical facts of the 1D simulation shown on plot (a) of Fig. 1 (we recall that this type of 1D visualization was already considered in [9,13], among others). Top panel in Fig. 11 shows how the three-parametric global scheme does not only extends adding ε but also other parameters as, for instance, x_0 (compare also with Fig. 2). In this case we observe that moving parameter x_0 just makes a translation of the global picture in the parameter space, and therefore the biparametric picture (I, x_0) just shows a parallel band structure as presented in plot (b). On that picture we also add some bifurcation lines (fold and homoclinic bifurcations), that obviously follow the band structure,

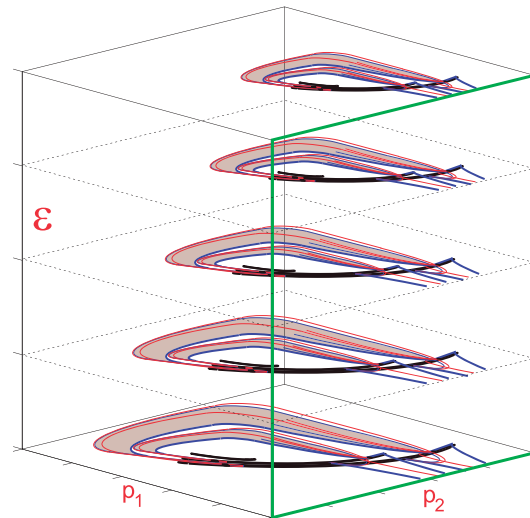


Fig. 10. Scheme of a three-dimensional view of the theoretical scheme (only essential elements are displayed). The structure persists for small values of ε .

giving straight lines. Taking now a segment fixing $b = 2.7$, $x_0 = -1$ and $\varepsilon = 0.01$ as that depicted in panel (b), we obtain the bifurcation diagrams displayed in panels (c), (d) and (e). Note that plot (e) corresponds to the IBD right panel of Fig. 1.

It is important to remark that when one studies the interspike-interval bifurcation diagram shown in panel (e), and we note that this is the most standard visualization of this kind of systems in literature, the relevance of the homoclinic bifurcation remains hidden, in spite of the segment crosses the homoclinic surface. In order to reveal the internal structure of the spike-adding process in that line, we need to use continuation techniques. To that goal, we pay now attention to the other two 1D bifurcation diagrams of panels (c) and (d), where we show the $\|\cdot\|_2$ norm and the period of the stable (continuous line) and unstable (discontinuous line) periodic orbits for the given parametric values computed using AUTO software. Starting from the left, we see that there exists a spike-adding cascade, but moving to the right, the role of the homoclinic orbit is again hidden because we are now following the stable branch of periodic orbits. Only when we continue the orbit up to the last fold bifurcation we see that an unstable periodic orbit persists as I decreases up to it undergoes a homoclinic bifurcation on the value marked by a dotted vertical line. So, attending to this exploration, we can say that it is at the homoclinic orbit where the periodic orbit involved in the continuous spike-adding is created, but when the periodic orbit bifurcates from the homoclinic orbit it is unstable and only recovers the stability through period doubling or fold bifurcations.

Note that to the right of the homoclinic bifurcation the spike-adding is chaotic: the segment crosses chaotic lobes, most of them very narrow, and so difficult to detect. In that region the bands of periodic orbits with a fix number of spikes are in fact formed by isolas of periodic orbits disconnected one each other. The periodic orbits experiment a period doubling cascade (we just depict the first period doubling with a red dot) generating the chaotic region. One should also compare with the continuation along the segment L_3 in Fig. 8. Recall that, when explained by a chaotic process, the spike-adding is discontinuous (see [30]). Discontinuities are apparent in the inter-spike interval bifurcation diagram depicted in Fig. 11 (panel (e)). In panels (c) and (d) we observe that the bifurcation curves emerging from the cascade of folds located to the right of the homoclinic bifurcation create isolas with a fold bifurcation point located to the right side of the bifurcation diagram. In fact, close to the value of I for which the segment enters in the region with one spike, there is a collection of fold bifurcation curves. Note that all of these bifurcation points are in fact the intersection with the pencils of bifurcations created on the orbit-flip and inclination-flip points located on the homoclinic bifurcation curve but on different parametric planes.

Finally, we remark that the global scheme presented in this paper explains most of the phenomena of the spike-adding process as it relates the different bifurcation lines, that are present in Figs. 8 and 11, with the pencils of bifurcations created on the codimension-two homoclinic bifurcation points that are in different parametric planes and that cannot be seen in the selected set of parameters. As illustrated on Fig. 10, when we have a large parametric phase space, it depends on how and where we make a section in order to better visualize the real organizing points of the studied phenomena.

4. Pancreatic β -cell neuron model

In this section we briefly illustrate that similar structures, as the ones observed for the Hindmarsh–Rose neuron model, are observed in other fold/hom neuron bursting models. Different models of pancreatic β -cells are usually based on the standard Hodgkin–Huxley formalism including different phenomena [34,39,40], like the intracellular storage of Ca^{2+} , the glucose metabolism, the influence of ATP, and so on. The most simple model of pancreatic β -cells which generates a realistic bursting behaviour is a three-dimensional model with two fast variables and one slow variable. In this paper we consider

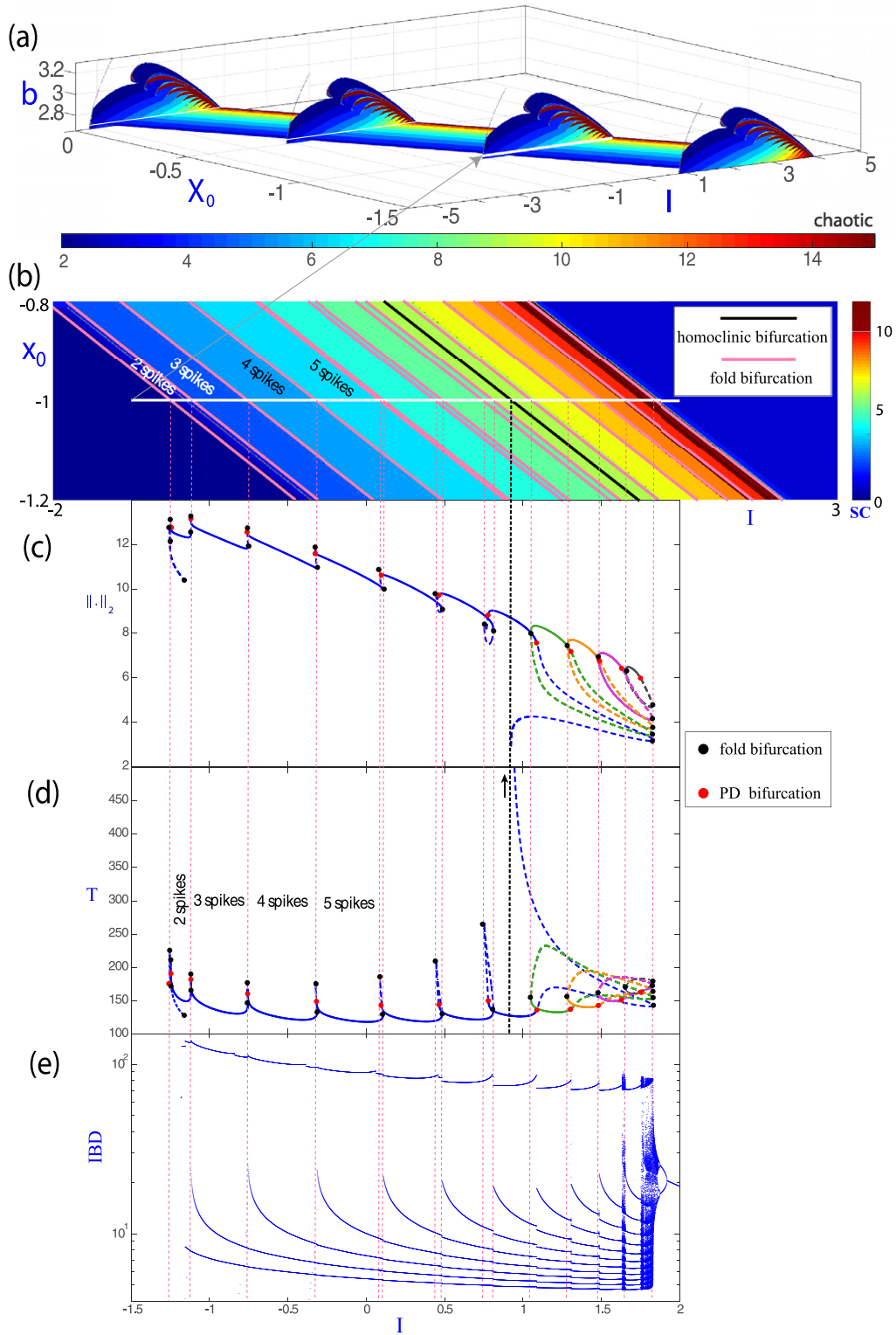


Fig. 11. (a) Three-parametric (I, x_0, b) diagram showing the spike-counting (SC) sweeping technique in different biparametric planes using $\varepsilon = 0.01$. (b) Biparametric (I, x_0) diagram with $b = 2.7$. And (c), (d) and (e), 1D cuts on the line $x_0 = -1$ showing the $\|\cdot\|_2$ norm, the period and the IBD of the orbit, respectively. Several bifurcation lines and points are depicted.

the model of Sherman et al. [34] given by

$$\begin{cases} \tau \dot{V} = -[I_{Ca}(V) + I_K(V, n) + g_S S(V - V_K)] + I_{app}, \\ \tau \dot{n} = \sigma [n_\infty(V) - n], \\ \tau_S \dot{S} = S_\infty(V) - S, \end{cases} \quad (2)$$

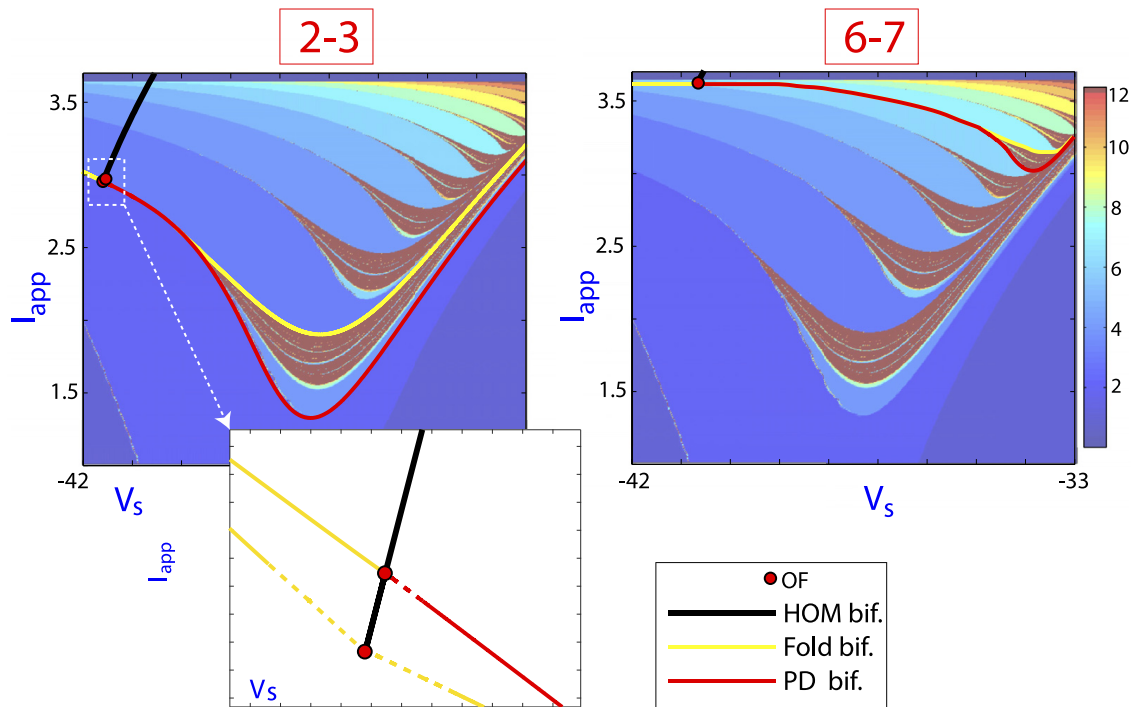


Fig. 12. Biparametric (V_S, I_{app}) spike-counting diagrams of the β -cell neuron model (for $k_S = 0.004$) and the main bifurcation lines detailed for the 2–3 and 6–7 spike-adding processes. Some codimension-2 homoclinic bifurcation points are marked on the corresponding homoclinic bifurcation lines. See the text for more details.

with the auxiliary ionic current functions defined by I_{app} (the external current) and

$$I_{Ca}(V) = g_{Ca} m_{\infty}(V) (V - V_{Ca}), \quad I_K(V, n) = g_K n (V - V_K),$$

and where the different steady state gating variables take the forms

$$m_{\infty}(V) = \left[1 + \exp\left(\frac{V_m - V}{\theta_m}\right) \right]^{-1}, \quad n_{\infty}(V) = \left[1 + \exp\left(\frac{V_n - V}{\theta_n}\right) \right]^{-1},$$

$$S_{\infty}(V) = \left[1 + \exp\left(\frac{V_S - V}{\theta_S}\right) \right]^{-1}.$$

In this model, V represents the membrane potential, n the opening probability of the potassium channels and I_{Ca} and I_K are the calcium and potassium currents, (for more details see [27,34]). The fixed parameters values that we use are taken from reference [27] and they are given by

$$\begin{aligned} \tau = 0.02, \quad \tau_S = 5, \quad V_{Ca} = 25, \quad V_K = -75, \quad g_{Ca} = 3.6, \quad g_K = 10.0, \quad g_S = 4, \\ \sigma = 0.85, \quad V_m = -20, \quad V_n = -16, \quad \theta_m = 12, \quad \theta_n = 5.6, \quad \theta_S = 10. \end{aligned}$$

The ratio $k_S = \tau/\tau_S$, in our case $k_S = 0.004$, defines the ratio of the time parameters for the fast (V and n) and the slow (S) variables. The parameter V_S is the main bifurcation parameter and it defines the membrane potential at which the steady-state value for the gating variable S attains one-half of its maximum value.

In Fig. 12 we show bifurcation diagrams on the parametric plane (V_S, I_{app}) . These pictures are similar to the ones shown in Fig. 3 for the Hindmarsh–Rose model. The main difference is that for this model it is much more difficult to locate numerically the different elements that are clearly shown in the Hindmarsh–Rose model. Besides, in the β -cell neuron model we do not have Belyakov points for the 2–3 spike-adding process, and so now this case also follows the generic theoretical scheme of the boxed area of Fig. 6 with two orbit flip codimension-two points. As in the Hindmarsh–Rose model, an inclination flip point is conjectured in the sharp fold of the homoclinic curves. The 2–3 spike-adding process is detailed with a magnification of the bifurcation lines. On the left side of the homoclinic curve the main fold bifurcations that create the spike-adding region go to one OF and to the conjectured IF. On the right side, the period doubling and fold bifurcation lines that delimit the chaotic lobe go each one to different OF points as shown in the generic theoretical scheme of Fig. 6. On the magnification on Fig. 12 the continuous lines are the ones computed with AUTO, and the discontinuous ones are the conjectured continuation of the lines.

On the 6–7 spike-adding process the numerical continuation software is not able to compute some of the curves close to the codimension-two points (AUTO detects the two OF points, but they are very close each other).

Therefore, from this brief analysis on the β -cell neuron model, it is plausible that the fold/hom spike-adding process in mathematical neuron models follows the theoretical scheme shown in Fig. 6. Note that the Fig. 6 provides the complete

scheme for the Hindmarsh–Rose model, while the boxed area the generic scheme for fold/hom bursters. The great advantage of using the Hindmarsh–Rose model is that it makes easier to detect the different elements of the spike-adding process.

5. Conclusions

We propose a global scheme to understand the spike-adding process in fold/hom bursting models, exemplified in the Hindmarsh–Rose neuron model. In the analysis we use different numerical techniques such as spike-counting, Lyapunov exponents and bifurcation continuation methods. Our simulations, and those of literature, allow us to introduce a global theoretical scheme that completes the previous ones that appeared recently (see [16]). The global framework connects the different types (continuous and chaotic) of spike-adding processes introduced by Terman [30]. It determines the regions of the parametric space where each kind of process occurs, and provides a general explanation of the origin of the bifurcations involved in them. Finally, being a global and multiparametric scheme, it allows to give an explanation to the different interspike-interval bifurcation diagrams (IBD) that have appeared in the literature for different models. This is an important point, since in most papers the spike-adding process is illustrated only with IBD plots, but without connecting to any region or bifurcation. In addition, an example has been presented that uses a more realistic model, the pancreatic β -cell neuron model of Sherman et al., which shows the same scheme as in the Hindmarsh–Rose model. Therefore, there are indications of the universality of this theoretical scheme for the generic fold/hom spike-adding process.

Acknowledgments

RB and SS have been supported by the Ministerio de Ciencia, Innovación y Universidades (Spain) projects MTM2015-64095-P, PGC2018-096026-B-I00, the [Universidad de Zaragoza](#)–CUD project [UZCUD2019-CIE-04](#) and [European Regional Development Fund](#) and Diputación General de Aragón (E24-17R and LMP124-18). SI and LP have been supported by Ministerio de Ciencia, Innovación y Universidades (Spain) projects MTM2014-56953-P and MTM2017-87697-P. LP has been partially supported by the Gobierno de Asturias project PA-18-PF-BP17-072.

References

- [1] Ermentrout GB, Terman DH. *Mathematical foundations of neuroscience*. Vol. 35 of interdisciplinary applied mathematics. New York: Springer; 2010.
- [2] Broens M, Bar-Eli K. Canard explosion and excitation in a model of the Belousov-Zhabotinskii reaction. *J Phys Chem* 1991;95(22):8706–13.
- [3] Wiczeorek S, Krauskopf B, Lenstra D. Multipulse excitability in a semiconductor laser with optical injection. *Phys Rev Lett* 2002;88:063901.
- [4] Hindmarsh JL, Rose RM. A model of the nerve impulse using three coupled first-order differential equations. *Proc R Soc Lond* 1984;B221:87–102.
- [5] Izhikevich EM. Neural excitability, spiking and bursting. *Int J Bifur Chaos Appl Sci* 2000;10(06):1171–266.
- [6] Barrio R, Ibáñez S, Pérez L. Hindmarsh–Rose model: close and far to the singular limit. *Phys Lett A* 2017;381(6):597–603.
- [7] Barrio R, Ibáñez S, Pérez L. Homoclinic organization in fold/hom bursters: the Hindmarsh–Rose model, preprint.
- [8] Barrio R, Martínez MA, Serrano S, Shilnikov A. Macro- and micro-chaotic structures in the Hindmarsh–Rose model of bursting neurons. *Chaos* 2014;24(2):023128.
- [9] Barrio R, Shilnikov A. Parameter-sweeping techniques for temporal dynamics of neuronal systems: case study of Hindmarsh–Rose model. *J Math Neurosci* 2011;1 6:1–6:22.
- [10] Desroches M, Kaper TJ, Krupa M. Mixed-mode bursting oscillations: dynamics created by a slow passage through spike-adding canard explosion in a square-wave burster. *Chaos* 2013;23(4):46106.
- [11] González-Miranda JM. Observation of a continuous interior crisis in the Hindmarsh–Rose neuron model. *Chaos* 2003;13(3):845–52.
- [12] González-Miranda JM. Block structured dynamics and neuronal coding. *Phys Rev E* 2005;72:51922.
- [13] Gonzalez-Miranda JM. Complex bifurcation structures in the Hindmarsh–Rose neuron model. *Int J Bifur Chaos Appl Sci* 2007;17:3071.
- [14] Innocenti G, Morelli A, Genesio R, Torcini A. Dynamical phases of the Hindmarsh–Rose neuronal model: studies of the transition from bursting to spiking chaos. *Chaos* 2007;17(4):43128.
- [15] Innocenti G, Genesio R. On the dynamics of chaotic spiking-bursting transition in the Hindmarsh–Rose neuron. *Chaos* 2009;19(2):023124.
- [16] Lınaro D, Champneys A, Desroches M, Storace M. Codimension-two homoclinic bifurcations underlying spike adding in the Hindmarsh–Rose burster. *SIAM J Appl Dyn Syst* 2012;11(3):939–62.
- [17] Storace M, Lınaro D, de Lange E. The Hindmarsh–Rose neuron model: bifurcation analysis and piecewise-linear approximations. *Chaos* 2008;18:33128.
- [18] Sherman A, Rinzel J, Keizer J. Emergence of organized bursting in clusters of pancreatic β -cells by channel sharing. *Biophys J* 1988;54:411–25.
- [19] Hodgkin AL, Huxley AF. A quantitative description of membrane current and its application to conduction and excitation in nerve. *J Physiol* 1952;117:500–44.
- [20] Shilnikov A, Kolomiets M. Methods of the qualitative theory for the Hindmarsh–Rose model: a case study. a tutorial. *Int J Bifur Chaos Appl Sci* 2008;18(8):2141–68.
- [21] Rinzel J. A formal classification of bursting mechanisms in excitable systems. In: Teramoto E, Yumaguti M, editors. *Mathematical Topics in population biology, morphogenesis and neurosciences: proceedings of an international symposium held in Kyoto, November 10–15, 1985*. Berlin, Heidelberg: Springer Berlin Heidelberg; 1987. p. 267–81.
- [22] Fenichel N. Geometric singular perturbation theory for ordinary differential equations. *J Differ Equ* 1979;31(1):53–98.
- [23] Izhikevich E. *Dynamical systems in neuroscience. The geometry of excitability and bursting*. Cambridge, Mass: MIT Press; 2007.
- [24] Nowacki J, Osinga HM, Tsaneva-Atanasova K. Dynamical systems analysis of spike-adding mechanisms in transient bursts. *J Math Neurosci* 2012;2(1):7.
- [25] Tsaneva-Atanasova K, Osinga HM, Riess T, Sherman A. Full system bifurcation analysis of endocrine bursting models. *J Theor Biol* 2010;264(4):1133–46.
- [26] Shilnikov A, Cymbalyuk G. Transition between tonic spiking and bursting in a neuron model via the blue-sky catastrophe. *Phys Rev Lett* 2005;94:48101.
- [27] Mosekilde E, Lading B, Yanchuk S, Maistrenko Y. Bifurcation structure of a model of bursting pancreatic cells. *BioSystems* 2001;63(1):3–13.
- [28] Han X, Yu Y, Zhang C, Xia F, Bi Q. Turnover of hysteresis determines novel bursting in duffing system with multiple-frequency external forcings. *Int J Non Linear Mech* 2017;89:69–74.
- [29] Han X, Zhang Y, Bi Q, Kurths J. Two novel bursting patterns in the duffing system with multiple-frequency slow parametric excitations. *Chaos* 2018;28(4):43111.
- [30] Terman D. Chaotic spikes arising from a model of bursting in excitable membranes. *SIAM J Appl Math* 1991;51(5):1418–50.
- [31] Govaerts W, Dhooge A. Bifurcation, bursting and spike generation in a neural model. *Int J Bifur Chaos Appl Sci* 2002;12(08):1731–41.
- [32] Guckenheimer J, Kuehn C. Homoclinic orbits of the FitzHugh–Nagumo equation: the singular-limit. *Discrete Contin Dyn Syst Ser S* 2009;2(4):851–72.
- [33] Guckenheimer J, Kuehn C. Homoclinic orbits of the FitzHugh–Nagumo equation: bifurcations in the full system. *SIAM J Appl Dyn Syst* 2010;9(1):138–53.

- [34] Sherman A, Rinzel J, Keizer J. Emergence of organized bursting in clusters of pancreatic β -cells by channel sharing. *Biophys J* 1988;54(3):411–25.
- [35] Doedel E.J., Paffenroth R., Champneys A.R., Fairgrieve T.F., Kuznetsov Y.A., Oldeman B.E., Sandstede B., Wang X.J.. *Auto2000*. <http://cmvl.cs.concordia.ca/auto>.
- [36] Homburg AJ, Sandstede B. Homoclinic and heteroclinic bifurcations in vector fields. *Handbook Dyn Syst* 2010;3:379–524.
- [37] Shilnikov L. On the birth of a periodic motion from a trajectory bi-asymptotic to an equilibrium state of the saddle type. *Soviet Math Sbornik* 1968;35:240–64.
- [38] Champneys A, Kirk V, Knobloch E, Oldeman B, Rademacher J. Unfolding a tangent equilibrium-to-periodic heteroclinic cycle. *SIAM J Appl Dyn Syst* 2009;8(3):1261–304.
- [39] Chay T, Keizer J. Minimal model for membrane oscillations in the pancreatic β -cell. *Biophys J* 1983;42(2):181–90.
- [40] Sherman A, Rinzel J. Model for synchronization of pancreatic β -cells by gap junction coupling. *Biophys J* 1991;59(3):547–59.

4.4 Paper IV (submitted)

The present work is devoted to the mechanisms underlying the different spike-adding processes found in the Hindmarsh-Rose model and completes the results provided in Paper III. We address the case of ε taking small values, so $\varepsilon = 0.01$ is fixed. The dynamics in the (b, I) plane are investigated.

The model exhibits fold/hom and fold/Hopf bursting. Fold/hom bursting is known to present two types of spike-adding: continuous and chaotic, following Terman notation [44]. We refer to them as canard-induced continuous spike-adding and chaos-induced spike-adding, respectively. Only one spike-adding process have been observed for fold/Hopf bursting, which we refer to as Hopf-induced continuous spike-adding.

We determine a map in the (b, I) plane locating the spike-adding processes exhibited by the model, illustrating them thoroughly and discovering novel aspects of the dynamics. Transitions from one process to another (transition spike-adding states) are analysed. For instance, we show how the passage from canard-induced to Hopf-induced continuous spike-adding is located far from the homoclinic bifurcation curve, in regions where the fold bifurcations arising at codimension two points are vanishing. Cusp bifurcations have a key role separating both processes.

There also exist parametric regions where the Izhikevich classification does not hold, since the fast-slow skeleton corresponds to fold/Hopf bursting but the orbits clearly resemble fold/homoclinic bursting, despite $\varepsilon = 0.01$ is usually considered as a value compatible with the fast-slow dissection. Mixed orbits combining bursts resembling fold/hom behaviour and bursts resembling fold/Hopf dynamics are also found.

We provide a theoretical explanation for the Hopf-induced spike-adding, employing a toy model to show analytically how the number of spikes is related with the space being available for the production of oscillations. More precisely, the distance between the fold bifurcations along the manifold of equilibria determines the number of spikes per burst.

Classification of fold/hom and fold/Hopf spike-adding phenomena

Roberto Barrio,^{1, a)} Santiago Ibáñez,^{2, b)} Lucía Pérez,^{2, c)} and Sergio Serrano^{1, d)}

¹⁾*Departamento de Matemática Aplicada and IUMA. Computational Dynamics group. University of Zaragoza. E-50009. Spain.*

²⁾*Departamento de Matemáticas. University of Oviedo. E-33007 Oviedo. Spain.*

(Dated: 30 January 2021)

Hindmarsh-Rose neural model is widely accepted as an important prototype for fold/hom and fold/Hopf burstings. In this paper we are interested in the mechanisms for the production of extra spikes in a burst, and we show the whole parametric panorama in an unified way. In the fold/hom case two types are distinguished, the continuous one, where the bursting periodic orbit goes through bifurcations, but persists along the whole process, and the discontinuous one, where the transition is abrupt and happens after a sequence of chaotic events. In the former case we speak about canard-induced spike-adding and, in the second one, about chaos-induced. For fold/Hopf bursting, a single (and continuous) mechanism is distinguished. Separately, all these mechanisms are, up to some extent, presented in literature. Nevertheless, our full perspective allows us to build a spike-adding map and, more significant, to understand the dynamics which are exhibited when frontiers are crossed, a crucial point not studied previously.

Keywords: neuron models, fold/hom bursting, fold/Hopf bursting, spike-adding mechanisms

AMS codes: 37B10, 65P20, 92B20

Among the elements that allow communication between neurons, spikes or action potentials are major pieces. Not the isolated ones, but the spike trains are those that allow the brain to build a language for the transmission of information. A burst is a signal with a higher probability of being picked up by neighbouring neurons than an isolated spike.¹ Moreover, the number and the temporal pattern of spikes provide a system for encoding messages. Facing this context, understanding how spikes can be gained (or lost) becomes a central question. This is the goal of this work, taking the Hindmarsh-Rose equations as a paradigm for certain classes of bursting, we analyse three different types of spike-adding processes. Although most of the involved dynamics and bifurcations are well known, we will be able to discover some novel characteristics. Our classification of the different spike-adding mechanisms determines maps in the parameter space. But maps are not useful if one is not able to understand the frontiers between different regions. Indeed, in this work we deal with the dynamics that characterize the transitions from one to another type of spike-adding. Challenges in neuroscience and, in particular, the problems that still remain to be solved in deciphering the language of neurons are impressive, but, without doubt, the classification of the different mechanisms involved in the genesis of extra action potentials is one of those essential basic steps.

I. INTRODUCTION

Bursting is one of the most relevant phenomena that can be observed in a neuron. Roughly speaking, bursting is charac-

terized by the appearing of sequences of spikes, corresponding to fast discharges, alternating with periods of quiescence. Moreover, when dealing with a bursting neuron, one of the major challenges is to understand how spikes are added to a given train of signals.

This paper studies the spike-adding mechanisms exhibited in the Hindmarsh-Rose² neuron model, a well known example and prototype of fold/hom (or square-wave) and fold/Hopf bursting^{3,4}. It is able to reproduce the most significant behaviors: quiescence, spiking and also bursting, either regular or irregular (chaotic). Literature concerning this model is really impressive and, only in relation to our interests, we can quote Refs. 5–18.

The Hindmarsh-Rose (HR) model is described by the following set of equations:

$$\begin{cases} \dot{x} = y - ax^3 + bx^2 - z + I, \\ \dot{y} = c - dx^2 - y, \\ \dot{z} = \varepsilon[s(x - x_0) - z]. \end{cases} \quad (1)$$

Variable x represents the membrane potential, whereas y and z correspond to ionic currents. We consider a typical choice of parameters with $a = 1$, $c = 1$, $d = 5$ and $s = 4$, discussing the spike-adding processes for different choices of the others b , I and ε ¹⁸. We assume that ε is a small parameter in the model, giving rise to a fast-slow system with two fast (x and y), and one slow (z) variables.

When $\varepsilon = 0$ in model (1), we obtain a reduced system which is usually called fast subsystem. Note that the fast subsystem is a family of planar vector fields where z is an additional parameter. Fixing b and I (still with $\varepsilon = 0$), we obtain a bifurcation diagram with respect to z that is illustrated in Fig. 1. There is a curve formed by equilibria which is named the slow manifold (\mathcal{M}_{slow}) and a surface containing limit cycles which is said the fast manifold (\mathcal{M}_{fast}). Recall that, in a general setting, slow-fast decompositions were first described in Ref. 3. For $I = 2.2$, $b = 2.91646$ (top) and for $I = 2.75$ and $b = 2.39$ (bottom) the slow manifold is shown in dark red (resp. orange) for stable (resp. unstable) equilibria and the fast manifold is shown in gray. Intuitively, one can un-

^{a)}Electronic mail: rbarrio@unizar.es

^{b)}Electronic mail: mesa@uniovi.es

^{c)}Electronic mail: perezplucia@uniovi.es

^{d)}Electronic mail: sserrano@unizar.es

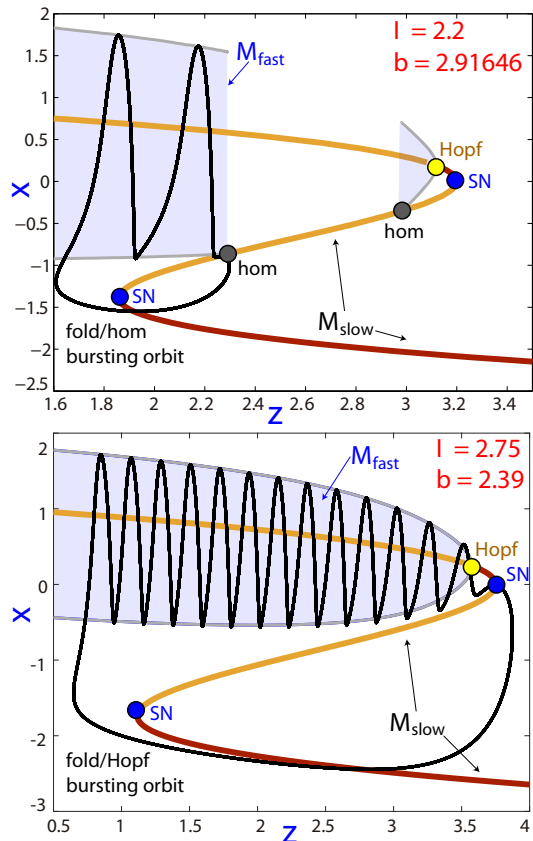


FIG. 1. 2D projection of fold/hom (top) and fold/Hopf (bottom) bursting orbits ($\epsilon = 0.01$) superimposed (in black) over classical slow-fast decomposition ($\epsilon = 0$) of the HR model (1) formed by the 1D slow manifold of stable (dark red) and unstable (orange) equilibria (\mathcal{M}_{slow}) and the 2D fast (spiking) manifold (\mathcal{M}_{fast}) of limit cycles of the fast subsystem of the model (in gray). *SN* stands for saddle-node bifurcations of equilibria, *Hopf* denotes the Hopf bifurcation points and “*hom*” the homoclinic bifurcation points.

derstand how burst patterns emerge. Fig. 1 also shows stable periodic orbits of the full system (black) superimposed to the bifurcation diagram of the fast subsystem. The slow dynamics in the complete model is such that $\dot{z} < 0$ when fast variables are moving close to the lower branch of \mathcal{M}_{slow} , whereas $\dot{z} > 0$ when they do close to \mathcal{M}_{fast} .

Indeed, as singular perturbation theory and Fenichel’s theorems explain¹⁹, orbits (for small enough ϵ) follow both manifolds on some parts of its trajectory. Following the terminology in Ref. 4, in the first case (top panel), the bursting orbit is said of fold/homoclinic type, because the termination of the fast subregime is due to the existence of a homoclinic bifurcation in the phase space of the fast subsystem. In the second case (bottom panel), the bursting orbit is said of fold/Hopf type because the amplitude of oscillations during the bursting is decreasing as the limit cycles of the reduced model approach the Hopf bifurcation.

As already mentioned, the main goal of this paper is to explain the processes (spike-adding) that lead a bursting orbit to change its number of spikes per period. More precisely, we

provide a classification of the different types of spike-adding processes in fold/hom and fold/Hopf bursters. From Terman²⁰, in the general context of fold/hom bursting, two spike-adding mechanisms are considered. On the one hand, there can arise extra excursions around the fast manifold which are generated through a discontinuous process linked to a chaotic phenomenon. On the other, there also can happen that extra excursions are created through a continuous process linked to orbits that transit through phase space following the unstable branch of the slow manifold. We will refer to the first scenario as chaos-induced spike-adding, and the second one as canard-induced spike-adding. Both cases have been recently studied in the literature^{5,7,14,16,21}. The spike-adding mechanism in the case of fold/Hopf bursting is completely different and is related to the distance between saddle-node (left SN bifurcation point of Fig. 1(bottom)) and Hopf bifurcation points in the fast subsystem, see Fig. 1. Namely, the number of spikes depends on the length of the oscillation tube which is accessible for orbits after they jump to the fast manifold from the slow manifold. It also depends on the characteristic rotation speed at the Hopf bifurcation point. We will refer to this mechanism for spike-adding as Hopf-induced. Of course, in all cases, the number of spikes also increases as ϵ decreases, but this is not our interest, we will consider fixed small values of ϵ . Discussions in the literature about the spike-adding mechanism involved in the fold/Hopf bursters are not so common as those about the mechanisms linked to fold/hom scenario.

We will see how the Hindmarsh-Rose model exhibits the three spike-adding mechanisms that we have just described. As said, all have already been considered, to a greater or a lesser extent, in the literature. However, in this paper the treatment is unified, which allows to understand the differences between them. Besides, we pay special attention to the transition dynamics between scenarios, a problem not well studied in literature. Having in mind that different spike-adding processes are feasible in a model (HR model in our case), the question is: where and why they are produced?

The frontier between the two spike-adding mechanisms linked to fold/hom bursters will be shown sharp. Namely, it will be marked by homoclinic surfaces in the three-parameter bifurcation space.⁶ Nevertheless, the separation between Hopf-induced processes and either chaos-induced or canard-induced will appear fuzzy. Coming from the region of chaos-induced spike-adding, a fan of bifurcations must be crossed to enter into the region corresponding to Hopf-induced processes. These bifurcations arise from a codimension-two homoclinic bifurcation point. As we will recall later, in the case of a canard-induced spike-adding, the periodic orbit must undergo several periodic orbit bifurcations (bistability and hysteresis are present), among them two curves of fold bifurcations which disappear at cusp bifurcation points. These codimension-two bifurcation points will play the role of boundary stones separating the canard domains from the Hopf ones. In other words, continuous spike-adding can be canard-induced or Hopf-induced. The first case happens when the continuation of the periodic orbit includes paths of instable regime. When this course is not realizable because no bifurcation is accessible (the continuation curve is

far from the cusp boundary stones), the gaining of extra spikes can be explained through a Hopf bifurcation process.

All the different types of spike-adding mechanisms are detailed in Section II, showing how they indeed arise in the Hindmarsh-Rose model. Transitions between these mechanisms will also be described in II. Results are summarized and discussed in Section III, where a theoretical classification parametric map is proposed. Conclusions are provided in Section IV.

II. CLASSIFICATION OF SPIKE-ADDING PHENOMENA

In this section we describe the different spike-adding phenomena present in the HR model. On Fig. 2, regions with periodic attractors with a different number of spikes are represented in different colors (spike-counting technique). From dark blue, indicating spiking, towards red, the number of spikes of the periodic orbit grows. Dark red indicates that the maximum number of spikes considered in the method has been exceeded, meaning that in a large part of that region the dominant behavior is chaotic⁹.

This figure shows a typical situation for small ε values (in this case $\varepsilon = 0.01$). There exist a finite collection of homoclinic bifurcation curves, the black curve represented in the figure being one of them. All the other are so close that, if they were also depicted, they would overlap with each other (see details in Ref. 6). Located on such curves there also arise codimension-two homoclinic bifurcations from which many of the elements involved in the spike-adding processes emerge. As an illustration, Fig. 2 includes some codimension-one bifurcations of periodic orbits: fold (yellow) and period-doubling (red) curves. Below the homoclinic bifurcation curve, there are wedges corresponding to bistability regimes. These regions are bounded by a pair of fold bifurcations connecting through a cusp. Above the homoclinic bifurcation curve, lobes of chaotic dynamics are formed containing pencils of period-doubling cascades. These lobes are limited by a fold bifurcation curve of periodic orbits and the first period-doubling cascade.

Figure 3 presents two different techniques for the study of the segment $R1$ of Fig. 2, that crosses regions of the bi-parametric plane showing the three types of spike-adding detected in the model: chaos-induced discontinuous spike-adding (right), canard-induced continuous spike-adding (middle) and Hopf-induced continuous spike-adding (left). On the plot on the top it is shown the interspike-interval bifurcation diagram (IBD) showing clearly the number of spikes and the time length among spikes. Red color represents coexistence of two periodic attractors with n and $n + 1$ spikes. The bottom plot presents the parametric evolution of the periodic orbits using continuation techniques. Along this article all the continuation analysis has been done using the well known software AUTO^{22,23}. The figure shows the $\|\cdot\|_2$ norm of the periodic orbit along the selected segment $R1$. On the continuation line, the blue color line changes from Hopf-induced continuous spike-adding (left part) to canard-induced continuous spike-adding (middle part). Note that, on the right side,

the purple color line represents an isola (simple closed curves in the corresponding slice) of 3-spikes periodic orbits and green and other colors represent the basic 2-spikes periodic orbit and its period-doubling bifurcated orbits on the region of chaos-induced discontinuous spike-adding. We can also observe how the change from the discontinuous spike-adding to the continuous spike-adding occurs sharply when crossing the homoclinic curve. On the other hand, while canard-induced continuous spike-adding is occurring, the segment $R1$ crosses wedges of bistability, limited by a fold point and period-doubling bifurcation. When the last wedge has been crossed, the Hopf-induced continuous spike-adding occurs. Bistability regions occur only for the canard-induced continuous spike-adding. Segments $R1a$, $R2$ and $R1b$ from Fig. 2 have been selected to illustrate with more detail each kind of spike-adding process. We will dedicate the following subsections to that description.

In addition, we include (Subsection IID) detailed studies of the transition processes between different types of spike-adding. As we have just mentioned, the boundary between chaotic processes and canard-induced mechanisms will be clearly located at the homoclinic curves. The separation between chaos induced and Hopf-induced mechanisms is not so sharp but clearly linked to the passage through a cascade of bifurcations that arise at a codimension-two homoclinic bifurcation.

Note that in Fig. 3 we have included a vertical line (in green) indicating the value of b for which, according to the Izhikevich classification, the bursting change from fold/Hopf to fold/hom. That is, the value of b at the point where the homoclinic bifurcation curve folds in the direction of b for the limit case ($\varepsilon = 0$). Of course, this association is worst as ε increases. For $\varepsilon = 0.01$ we can see how the spike-adding is classified as canard-induced to the left of the green line (up to the red line) because bifurcations of periodic orbits are still detected. The change happens when one crosses the red line corresponding to the cusp bifurcation. Therefore, we have marked this region with an interrogant symbol on the top of the figure, as more details are required. This transition will be explained in more detail in Subsection IID. The limitations of the Izhikevich classification when one transits from fold/Hopf to fold/hom will be discussed in III.

A. Chaos-induced discontinuous spike-adding

The first type of spike-adding process that we are going to analyze is the chaos-induced discontinuous one. As we have already mentioned, this process occurs in the region above the homoclinic curve, this curve being a boundary of such region. On Fig. 4 we consider segment $R1a$ of Fig. 2 and we zoom in on the surrounding region with the spike counting technique. Below that picture, we show the IBD of this segment and the $\|\cdot\|_2$ norm of the periodic orbits obtained with continuation techniques (AUTO).

As we can see in the figure, to the right of the segment there is a bursting periodic attractor with 2 spikes. As b decreases, a typical scenario is present. Firstly, the periodic attractor

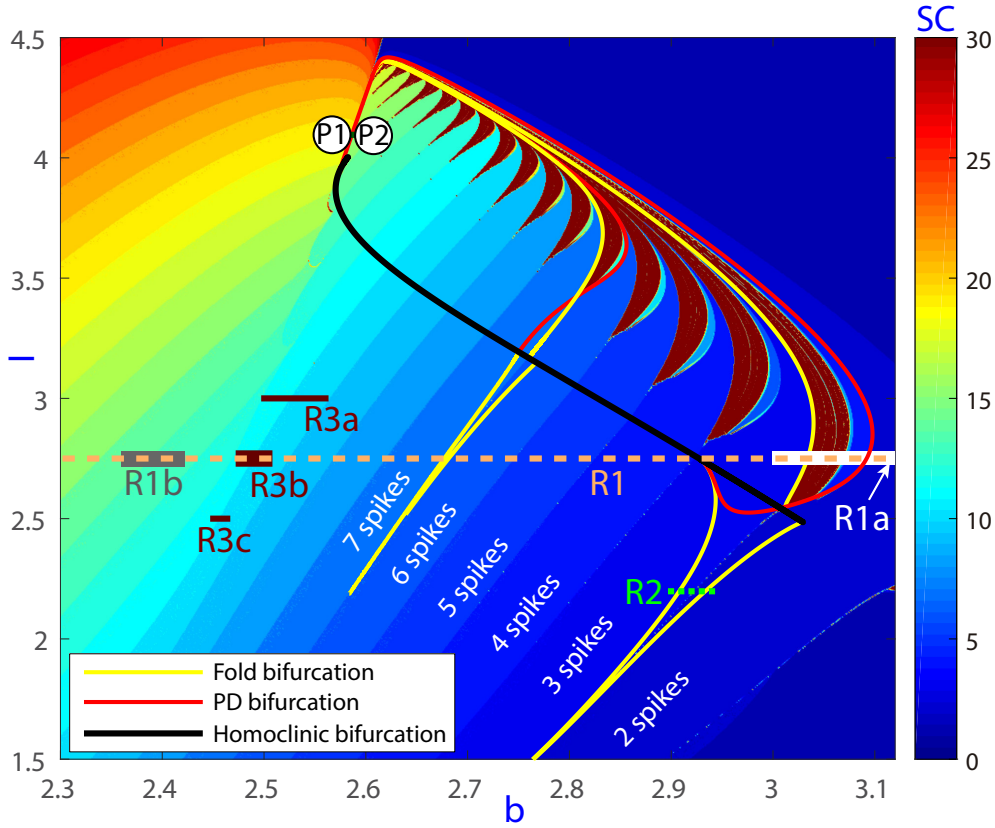


FIG. 2. Biparametric spike-counting bifurcation diagram for $\varepsilon = 0.01$. Different segments are selected to illustrate (on later figures) three different spike-adding processes: chaos-induced discontinuous spike-adding, canard-induced continuous spike-adding and Hopf-induced continuous spike-adding. Along the long segment $R1$ all of them appear; a discontinuous chaos-induced transition from 2 to 3 spikes along segment $R1a$; a continuous Hopf-induced transition from 13 to 14 spikes along segment $R1b$ and continuous canard-induced in between, although segment $R2$ will offer a more detailed illustration showing a transition from 2 to 3 spikes between fold/hom bursters. Transitions from $P1$ to $P2$ and along the segments $R3a$, $R3b$ and $R3c$ will be described to explain how dynamics evolve to change from one scenario to another.

undergoes through a cascade of period-doubling bifurcations, until a chaotic attractor is generated. Within the chaotic region, narrow windows of regular behavior appear where new periodic orbits are generated. They will go through new bifurcations where they will become unstable joining to the chaotic set. Finally, at a fold bifurcation, the chaotic set stop being attractor and two periodic orbits (one stable and one unstable) with 3 spikes are generated.

To show how the attractors evolve throughout this spike-adding phenomenon, on Fig. 5 we present the complete process. The central picture shows the bifurcation diagram obtained by continuation (AUTO) corresponding to the segment $R1a$ on Fig. 2. We have selected several values of b (marked in the central picture with small colored squares and numbers) for which we have plotted these orbits. For these values, the periodic orbits (solid line for stable, and dashed for unstable ones) and a chaotic attractor (for square $-6-$) are shown around the central picture. Orbit $-1-$ represents the basic periodic orbit of 2 spikes. After the first period-doubling bifurcation, the orbit $-1-$ becomes unstable and a stable periodic orbit ($-2-$) with two bursts with 2 spikes (2×2 orbit) is generated. A second period-doubling bifurcation repeats the

former mechanism from 2×2 to 4×2 orbit ($-3-$). So, the same mechanism is developed again and again (to a 8×2 orbit $-4-$, 16×2 orbit $-5-$, and so on), a countably infinite number of times giving place to a typical period-doubling route to chaos that generates a chaotic attractor ($-6-$). After a fold bifurcation, the chaotic set becomes unstable and two periodic orbits ($-7-$) with 3 spikes are born (the spike-adding). One of them is stable, the other one unstable, both are indistinguishable at the fold bifurcation and they run along the outer edge of the chaotic set. When b moves away from the value at which the bifurcation occurs, both orbits are separated from each other.

It is worth paying attention to certain qualitative aspects that can be observed in the chaotic transition illustrated in Figure 5. As the attracting periodic orbits that arise through period-doublings build the chaotic attractor ($-6-$), spikes arrange visually in four groups inside phase space, although two of them, those placed in central positions, seem to compete to fill the same area. This process is typical in period-doubling cascades giving rise first to thin Feigenbaum chaotic attractors that later merge in thicker and larger ones via boundary crisis phenomena. When the chaotic attractor is fully created,

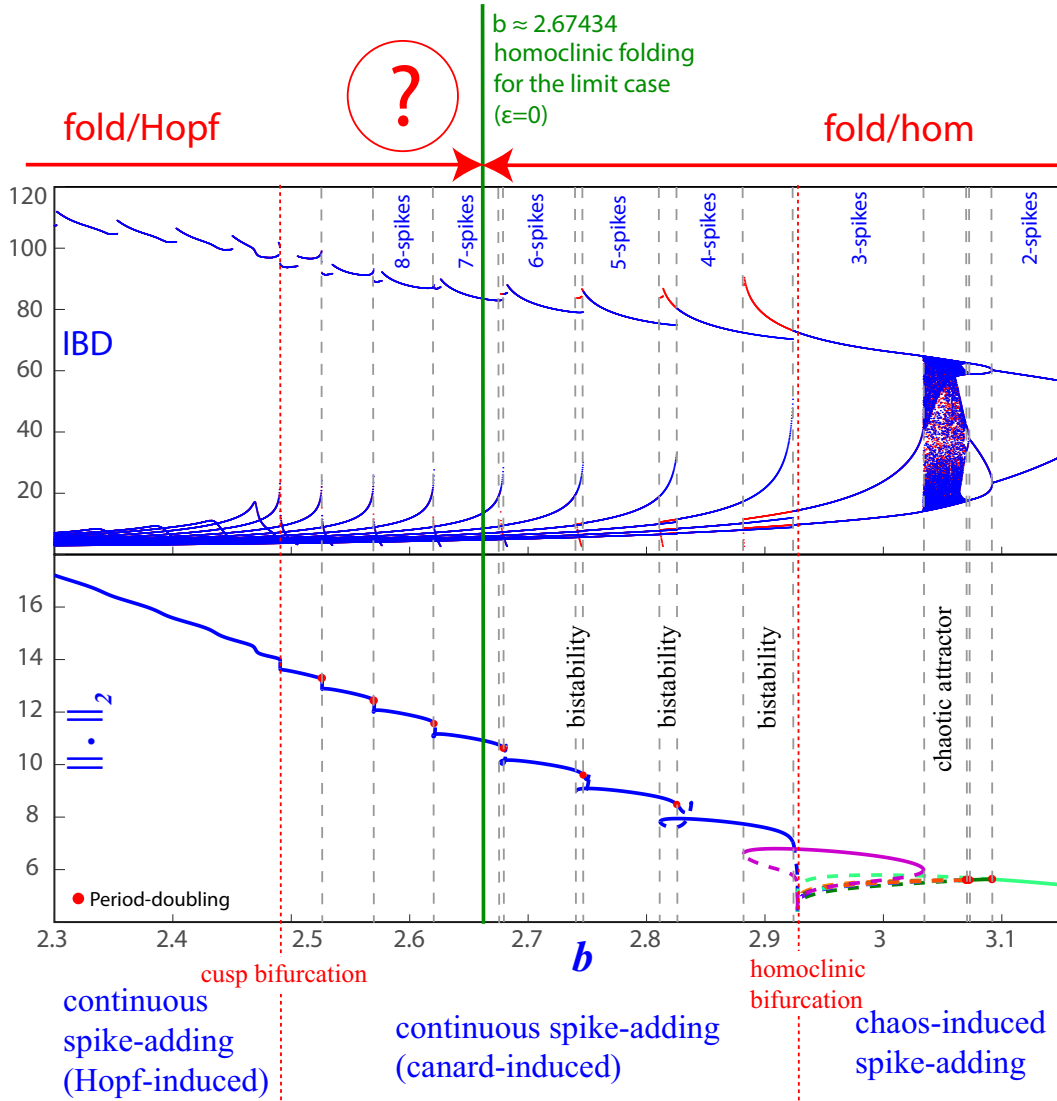


FIG. 3. Analysis of transitions along segment $R1$ (on Fig. 2) with $\epsilon = 0.01$, $I = 2.75$ and b as bifurcation parameter. Top: Interspike-interval bifurcation diagram (IBD). Red color represents coexistence of two periodic attractors with n and $n + 1$ spikes. Bottom panel shows the $\|\cdot\|_2$ norm of the periodic orbit along the process, obtained with continuation techniques (AUTO). Purple represents an isola of 3-spikes periodic orbits; in blue, the continuous spike-adding process is shown; green and other colors represent the basic 2-spikes periodic orbit and its period-doubling bifurcated orbits. More details are given in the text and on later figures.

we clearly see how the groups of spikes give rise to three, not to four, areas within the attractor, characterized by a denser flow. When the fold bifurcation occurs, the three-spiked stable periodic orbit takes the place of the chaotic attractor, flowing through the denser areas previously swept by the chaotic trajectory. The fold bifurcation marks the beginning of a periodic window: the chaotic attractor becomes an unstable saddle chaotic invariant set that embeds, among other unstable periodic orbits, the unstable orbit itself that is born at the fold bifurcation.

As already pointed out in Ref. 8, the process we have just described is what is known in the literature as Type I intermittency transition to chaos, as introduced in Refs. 24 and 25. In Ref. 8, authors explore a segment of parameters which cuts

the whole sequence of chaotic lobes. The scenario here presented is common to each spike-adding. As b decreases, periodic orbits with n spikes go through a period-doubling cascade which precedes the formation of a horseshoe. The dynamics enters into a chaotic window which disappears through a Type I intermittency transition. Chaotic transitions have been studied in Refs. 20 and 26. Working in a general framework, which includes the Hindmarsh-Rose model, Terman explains how the passage from n to $n + 1$ spikes can be accompanied by the creation of horseshoes. In that sense, we understood that each passage through a chaotic lobe includes a Terman's transition.

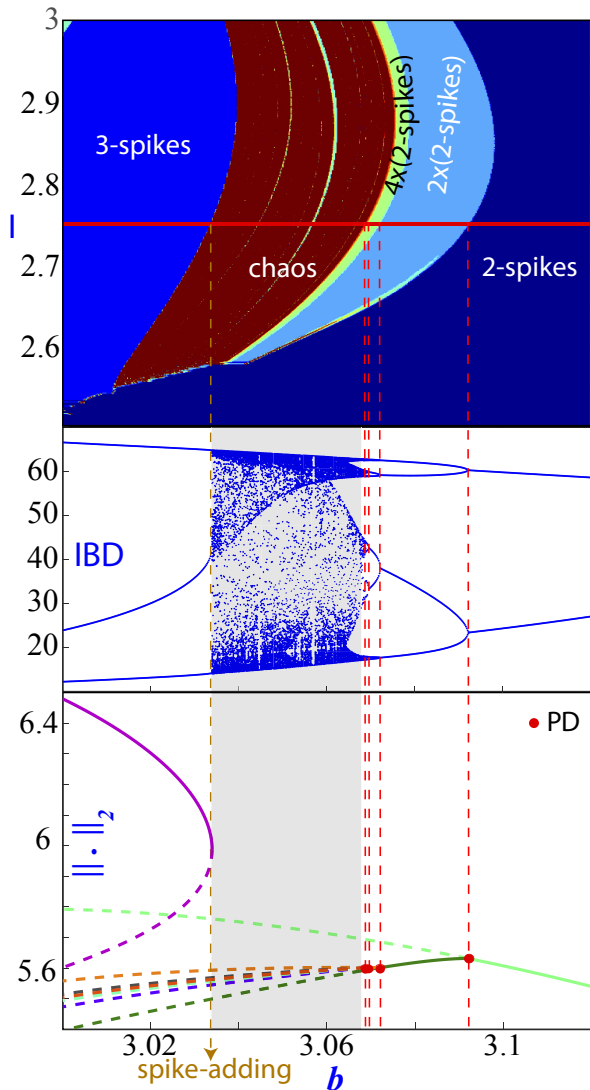


FIG. 4. Analysis of segment $R1a$ (on Fig. 2) with $\varepsilon = 0.01$, $I = 2.75$ and b as bifurcation parameter. Top: Biparametric bifurcation spike-counting diagram around the segment $R1a$. Dark red represents chaos, different colors represent periodic orbits with different bursting. Middle and bottom pictures show magnifications of Fig. 3 for the segment $R1a$. Gray region marks chaotic behavior and red points period-doubling bifurcations.

B. Canard-induced continuous spike-adding

A full detailed picture of the continuous transition from 2 to 3 spikes between fold/hom bursters along the segment $R2$ (Fig. 2) is given in Figure 6. In the central panel, the bifurcation curve obtained by continuation is displayed. Solid curve represents stable periodic orbits, while dashed curve indicates unstable periodic orbits. Squares with different colors over the curve mark different values of parameter b selected to show their corresponding periodic orbits (pictures around). These periodic orbits are plotted over the slow \mathcal{M}_{slow} and fast \mathcal{M}_{fast} manifolds of the limit case to explain the canard transition

generating the new spike^{7,10,14}. In the upper left corner of the central picture, all the selected orbits are represented together to see their relative position. Starting from the lower branch of the bifurcation curve, where the 2-spikes periodic orbit is stable, and decreasing the value of b , the curve reaches a fold bifurcation (marked with a square inside a circle). There, the periodic orbit becomes unstable and its length starts to increase as b decreases. This is the beginning of the canard transition: The increment in the length of the periodic orbit occurs as it extends following the piece of the slow manifold close to the unstable part of the manifold of equilibria between both fold bifurcations (see Fig. 1 top). Along the middle branch of the bifurcation curve, “headless” canards evolve up to a second fold bifurcation is reached. There, the orbit overcomes the right-fold of the equilibrium manifold in the fast subsystem and an additional turn around the tubular fast manifold arises; the canard orbit is said maximal and the canard “head” starts to be developed (second fold bifurcation marked with a square in a circle). This “head” moves to the left as b increases and the orbit recovers its stability after a period-doubling bifurcation (marked with a square inside a circle), when the orbit already has an extra spike. Therefore, the new spike has travelled from the neighbourhood of the right piece of \mathcal{M}_{fast} to the neighbourhood of the left piece of \mathcal{M}_{fast} . This process that we have just described is the essential mechanism behind the continuous spike-adding for fold/hom bursters^{7,10,14}.

In the sense in which we have travelled the curve, the bifurcation where the orbit with three spikes regains its stability is actually a period-halving bifurcation. Keep in mind that in a small interval to the right of this bifurcation there are pencils of bifurcations very close each other, and so it is quite difficult to observe them and their effects. Just to show this, the doubled periodic orbit emerging at that point is also continued with AUTO and both bifurcation curves are displayed on Fig. 7 (light blue color lines). The curve for the double period orbit undergoes through a fold bifurcation where parameter b starts to increase until a second period-doubling is reached, and so on (note that the unstable orbit is connected with bifurcated orbits close to the fold on the right). This process only can be detected using continuation techniques because the stable region is very small and it has no real effects in the dynamics. However, once the phenomenon is detected, the orbits obtained can be carefully integrated to observe the chaotic behavior in that narrow parametric region (see red dots on the IBD on the top picture of Fig. 7).

This canard-induced spike-adding mechanism had already been discussed in the literature.^{7,10,14,16} Some micro-chaos zones had already been detected and discussed in Ref. 8, but for segments very close to the homoclinic bifurcation curves, and not on the generic spike-adding process. Here we observe how small chaotic windows are detected far from the homoclinic skeleton. It follows that the fan of bifurcations of periodic orbits extends widely in parameter space. In fact, the chaotic window is associated with a cascade of period-doubling. The tangled bifurcation diagram formed by the codimension one bifurcations that arise from the codimension-two homoclinic bifurcation points have been discussed in Ref. 6, where it is also explained how the spike-

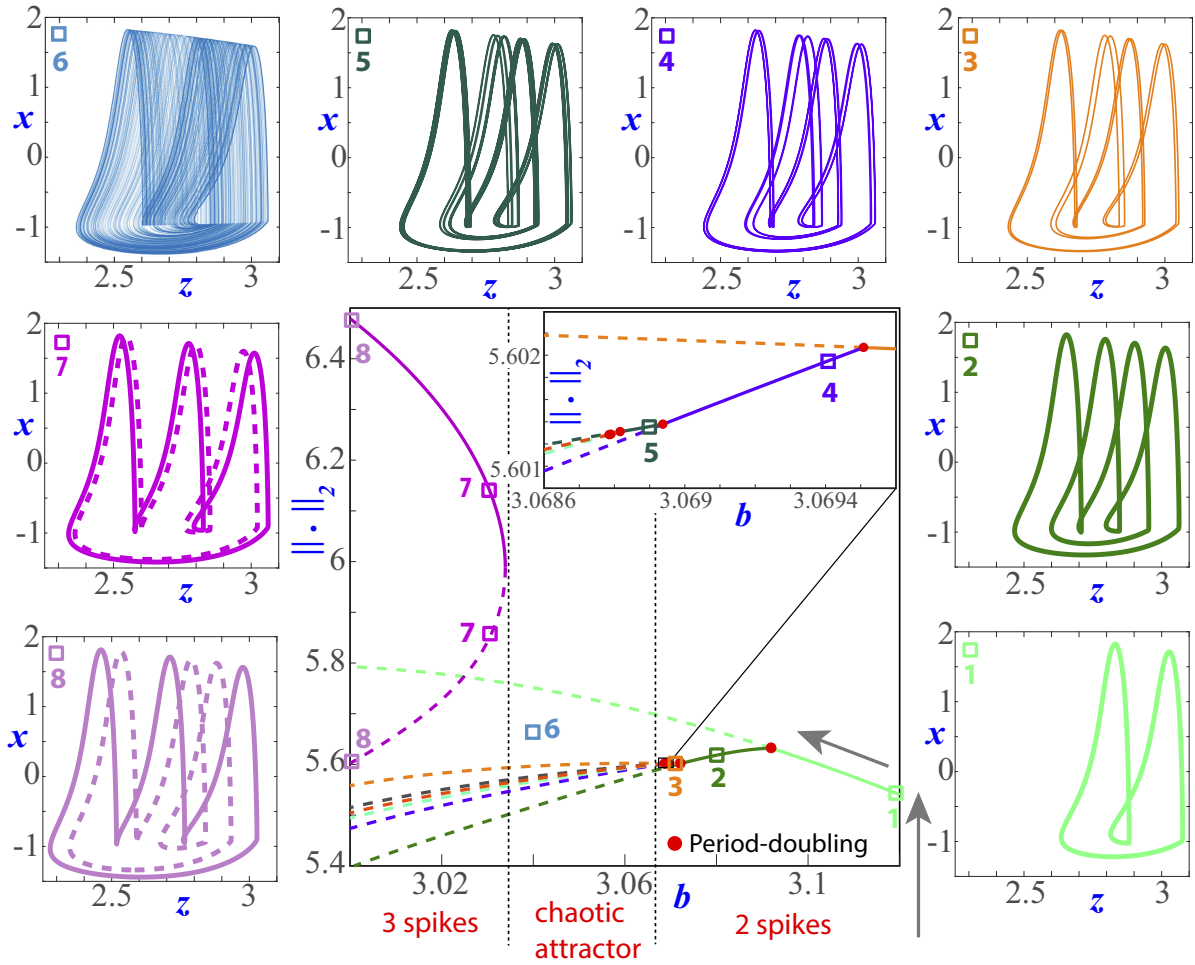


FIG. 5. Evolution of periodic orbits throughout the process of chaos-induced discontinuous spike-adding. Central picture shows the bifurcation diagram obtained by continuation corresponding to the segment $R1a$ on Fig. 2. The coloured squares mark the points in the diagram corresponding to the selected values. For these values, the periodic orbits (solid line for stable, and dashed for unstable ones) and a chaotic attractor (for square $-6-$) are shown around the central picture. Along the continuation of the bifurcation lines we observe periodic orbits with two spikes ($-1-$), later a period-doubling cascade ($-2-$ to $-5-$) originates a chaotic attractor ($-6-$) and, finally, after a fold bifurcation, two periodic orbits with three spikes appear ($-7-$ and $-8-$). In the upper right corner of the central picture, a magnification of the region where the first period-doubling cascade occurs is shown.

adding mechanisms fit into the whole web.

C. Hopf-induced continuous spike-adding

The Hindmarsh-Rose model presents a variation of continuous spike-adding, where bistability and canards are not present. The spike-adding occurs without the periodic orbits losing their stability, but still increasing their length by adding an extra cycle to their turns around the fast manifold.

Unlike what happens in the fold/hom cases, in the process of Hopf-induced spike-adding, period-doubling and fold bifurcations do not appear. Nor is chaotic behavior observed, nor do canards appear. The complete process is shown in Fig. 8, presenting again in the central panel the continuation bifurcation diagram of segment $R1b$ of Fig. 2. The coloured

squares mark the points in the diagram corresponding to the selected values. For these values, the stable periodic orbits are shown over the slow \mathcal{M}_{slow} and fast \mathcal{M}_{fast} manifolds (see Fig. 1 for more details). As shown on Fig. 8, the process is straightforward. That is, what happens in this case is that, as b decreases, almost the entire orbit is moving toward smaller values of z . But the point of re-entry of the orbit around the fast manifold, after passing through the stable lower branch of the slow manifold, does not move. This means that more space is generated in the corner of the slow manifold where the upper saddle-node is located. Thus, there comes a time when there is room for a new spike in the orbit, which is occupied. As b continues to decrease, the displacement of most of the orbit continues, causing the amplitude of the new spike to increase. Along the continuation of the bifurcation line we observe how periodic orbits with thirteen spikes move to the

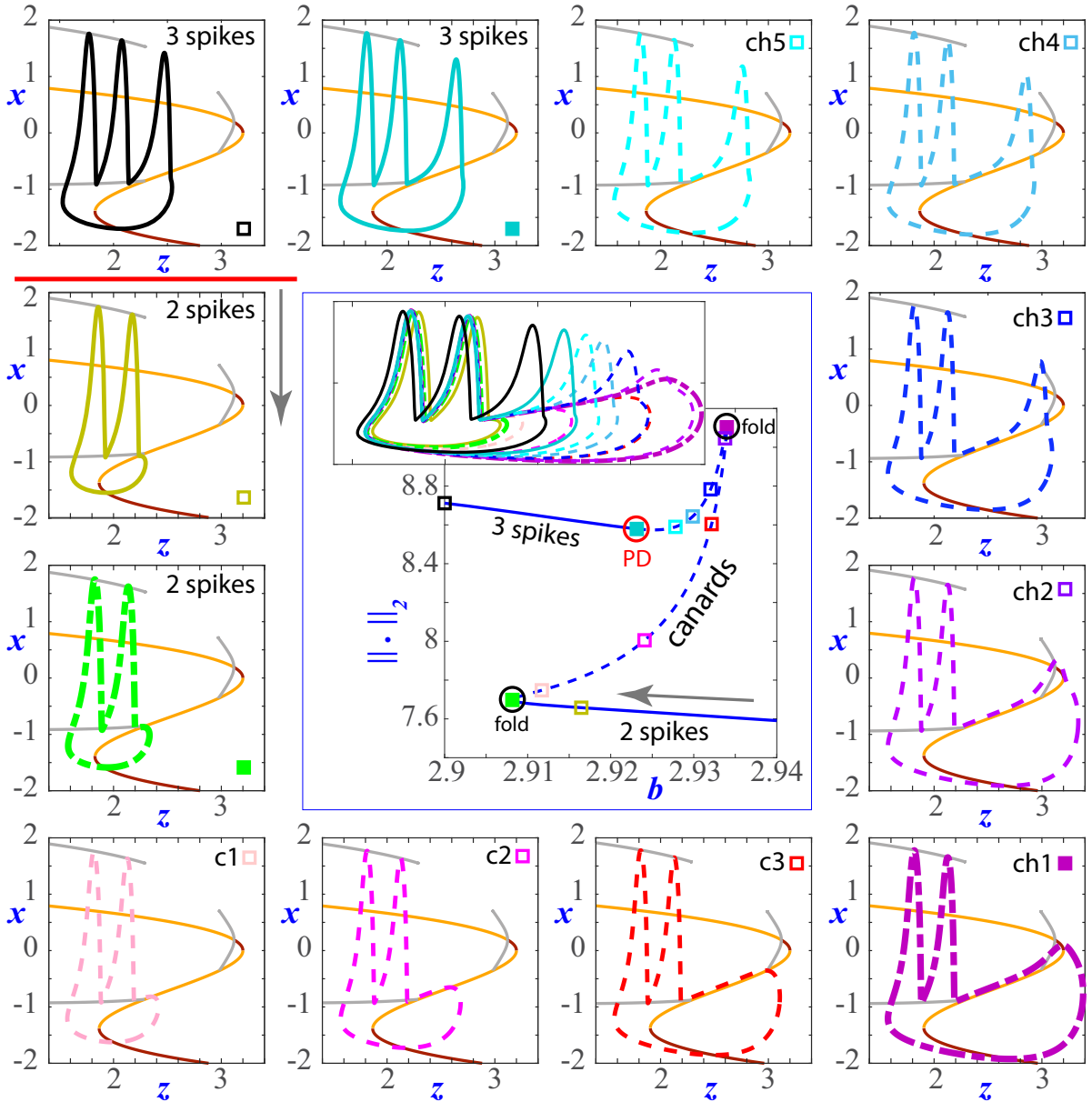


FIG. 6. Evolution of periodic orbits throughout the process of canard-induced continuous spike-adding. Central picture shows the bifurcation diagram obtained by continuation (AUTO) corresponding to the segment R2 on Fig. 2. The coloured squares mark the points in the diagram corresponding to the selected values. For these values, the periodic orbits (solid line for stable, and dashed for unstable ones) are shown over the slow and fast manifolds (\mathcal{M}_{slow} and \mathcal{M}_{fast} , see Fig. 1 for more details). The grey arrow indicates the direction in the process of adding a new spike. In the upper left corner of the central picture, all the selected orbits are represented together to see their relative position. Along the continuation of the bifurcation line we observe periodic orbits with two spikes, later headless canards (orbits numbered with -c-), canards with head (-ch- orbits), and, finally, orbits with three spikes.

left so that space is generated for the appearance of a new spike on the right side of the orbit giving rise to a burster with fourteen spikes instead of thirteen. If b continues to decrease sufficiently, this spike-adding process will be repeated in the same way.

As already mentioned in the introduction, any process of spike-adding where periodic orbits do not cross any bifurcation, just a smooth change allowing an extra spike, will be

referred as Hopf-induced, even in the case where the fast dynamics does not correspond to a fold/Hopf bursting from the Izhikevich classification.

In the Appendix we explain theoretically, using a simple model, how the number of spikes depends on the distance between the two saddle-node bifurcation points of the slow manifold of equilibria \mathcal{M}_{slow} . In the case of a fold/Hopf burster, the number of spikes exhibited by an orbit is strongly linked to

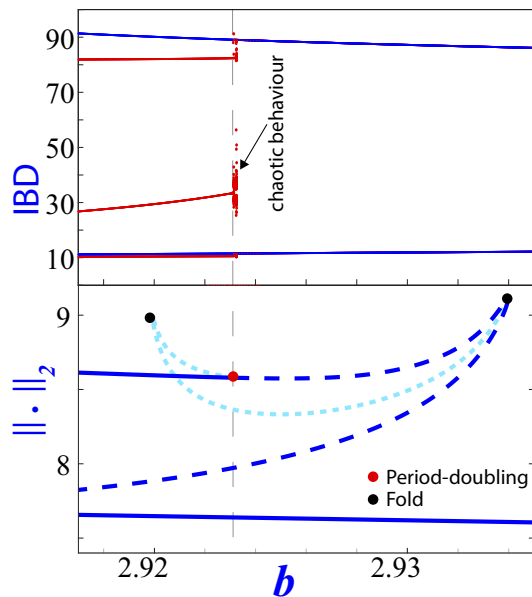


FIG. 7. IBD (top) and continuation diagram (bottom) of a magnification of segment $R2$. On the top picture, blue represents periodic orbits with two spikes while red line represents periodic orbits with three spikes and some bifurcated orbits from them coexisting with the two spikes periodic orbits. In the pointed thin region there exists chaotic behaviour (dotted red points) originated via a very narrow period-doubling cascade.

the size of the oscillation region in the phase space. The trajectory around the fast manifold is longer as greater is the width of that region in the direction of variable z and that width corresponds to the distance between the saddle-node bifurcation points, at least for small values of ε . As b decreases, that distance increases. To be precise, observe how the lower saddle-node point moves to left as b decreases, but the upper one seems to remain fixed.

D. Transition spike-adding states

In the previous subsections we have identified three different spike-adding processes, namely, mechanisms induced by chaotic behaviors, canard explosions or Hopf bifurcations. Recall that the former is a discontinuous evolution, whereas the latter two are continuous transitions. Now we explain how the dynamics is transformed to change from one type to another.

We begin by discussing the transition between the two types of continuous spike-adding. In this case we cannot visually identify a sharp border marking the passage from one to the other. Fig. 9 shows the spike-adding process from bursting periodic orbits with 10 spikes to periodic orbits with 11 spikes along the three small segments $R3a$, $R3b$ and $R3c$ (see Fig. 2). Along the first segment, the process clearly corresponds to canard-induced continuous spike-adding. In the case of the third segment, however, the process clearly is Hopf-induced

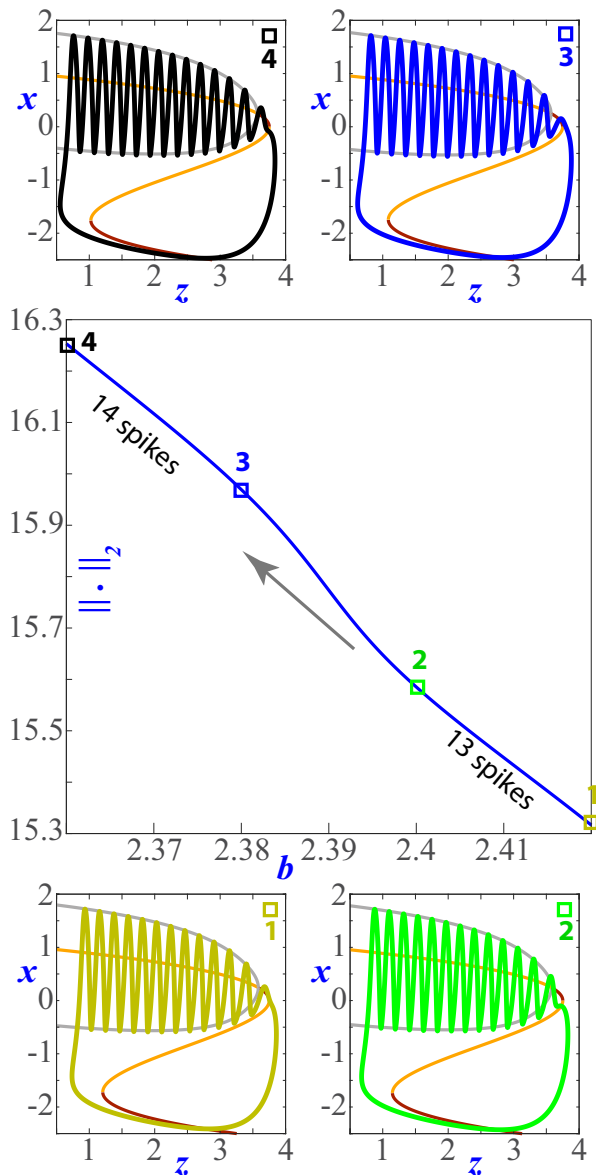


FIG. 8. Evolution of periodic orbits throughout the process of Hopf-induced continuous spike-adding. Central picture shows the bifurcation diagram obtained by continuation corresponding to the segment $R1b$ of Fig. 2. The coloured squares mark the points in the diagram corresponding to the selected values. The stable periodic orbits are shown over the slow \mathcal{M}_{slow} and fast \mathcal{M}_{fast} manifolds. The grey arrow indicates the direction in the process of adding a new spike. Along the continuation of the bifurcation line we observe how periodic orbits with thirteen spikes move to the left so that space is generated for the appearance of a new spike on the right side of the orbit. Finally, periodic orbits have fourteen spikes.

continuous spike-adding. It is evident that, between these two segments, a bifurcation has to occur that generates the change between both types of spike-adding. However, for this value of ε we are not able to detect it numerically as the continuation software stops the calculation of the fold bifurcations.

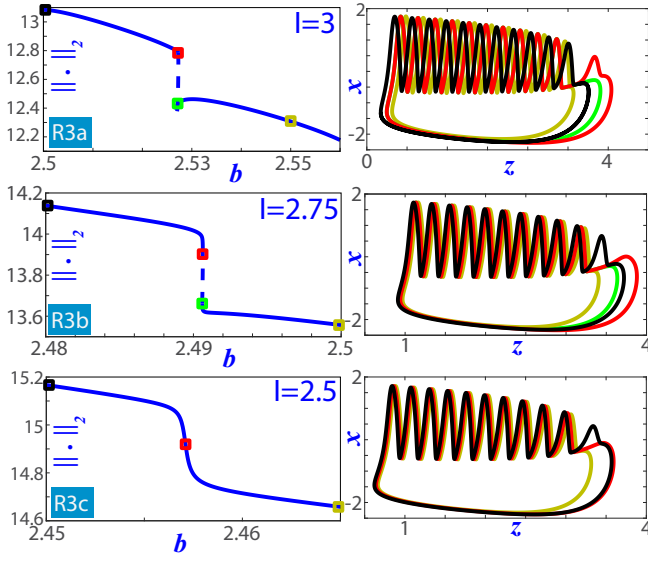


FIG. 9. Variations of the spike-adding processes along segments R3a, R3b and R3c (Fig. 2). Along segment R3a (top) the spike-adding is canard-induced, but along segment R3c (bottom) the bifurcation curve has been stretched and from now on the spike-adding process is Hopf-induced.

We show an intermediate segment (R3b) where the passage through the canard is not so apparent.

In order to illustrate more clearly the transition between these two types of spike-adding, we study one case for a higher value of the small parameter ($\varepsilon = 0.05$) to help in the visualization. For this ε value, the two fold bifurcations involved in the spike-adding from 2 to 3 spikes between fold/hom bursters that occur in the upper part of the region below the homoclinics can be fully continued numerically. Fold bifurcation curves are plotted in yellow on Fig. 10, they arise from codimension-two bifurcation points located on the homoclinic curves. Segments A and B cut both curves and, as it can be seen on the bottom pictures, the spike-adding process is canard-induced. If we compare the continuation bifurcation curves (left pictures) for both segments, we can observe how, as l decreases, the curve is stretched. As a consequence, the two fold bifurcation curves get closer to each other, until they reach a point (cusp bifurcation) where both coincide and disappear. Segment C goes through that point. This is the bifurcation point where canard-induced continuous spike-adding ends to give rise to Hopf-induced continuous spike-adding. Segments D and E cross this type of spike-adding, as can be seen on bottom pictures.

Once we understand how a cusp bifurcation of periodic orbits allows us to explain the passage from a canard-induced spike-adding towards a Hopf-induced type, we can conjecture that this is what happens for smaller values of ε and, in particular, in the case illustrated in Fig. 9, although the fold bifurcation curves involved are not easy to detect and to continue. It is important to remark here one main difference among both continuous spike-adding phenomena: in the canard-induced

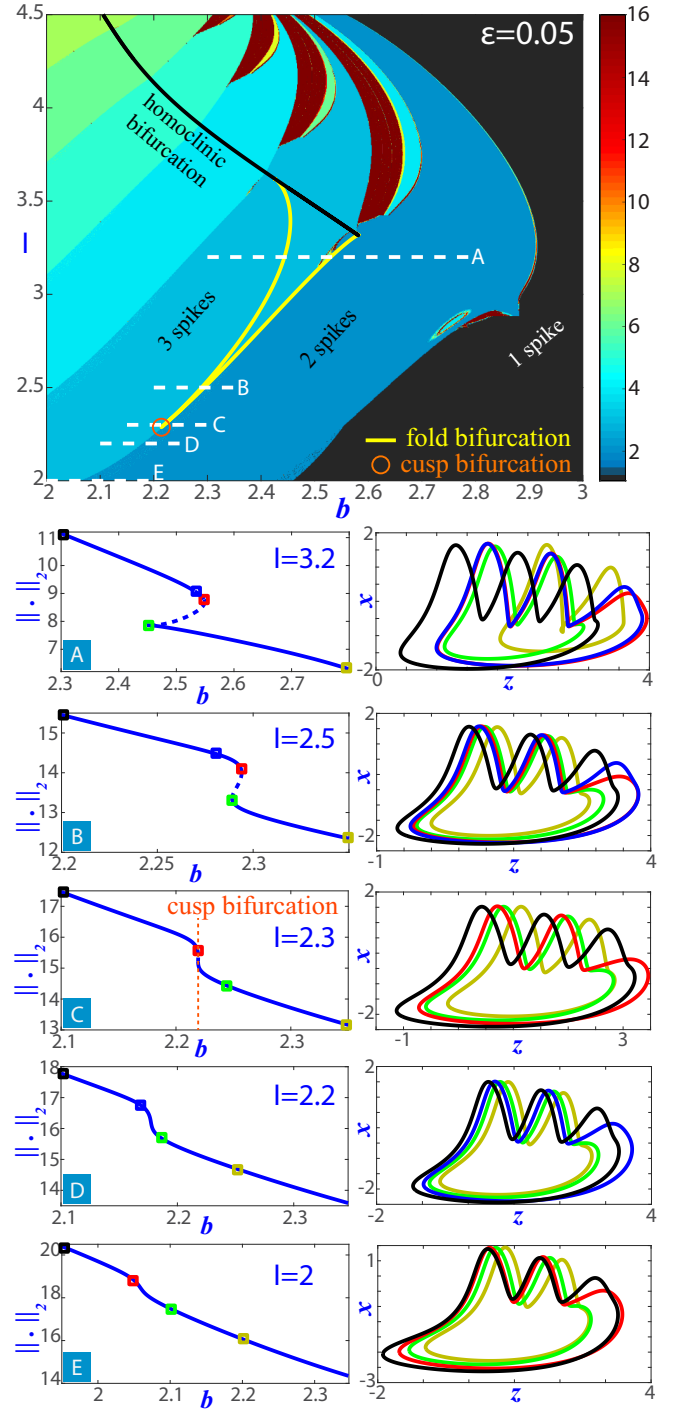


FIG. 10. Top: Biparametric bifurcation spike-counting diagram for $\varepsilon = 0.05$. Different segments are selected to illustrate the evolution from canard-induced continuous spike-adding (segments A and B) to Hopf-induced continuous spike-adding (segments D and E) through a cusp (segment C). Bottom: Left column shows bifurcation diagrams obtained by continuation corresponding to the selected segments. In the right column, some periodic orbits along the segment are plotted together to see their relative position and shape. The colors of the orbits correspond with coloured squares in the left bifurcation diagrams.

case the canard orbit in the process to obtain an extra spike makes a “go-and-come-back” excursion, whereas in the Hopf-induced case the orbit that is obtaining an extra spike grows but it does not come back. This is clearly seen on Figures 9 and 10.

As already mentioned, the transition from the region where spike-adding is induced by chaotic dynamics to the zones exhibiting continuous processes is determined, one way or another, by the homoclinic skeleton of the model. Two cases are clearly distinguished according to whether the dynamics change to either a canard-mediated mechanism or a Hopf-induced one.

If we pay attention to the transition towards a canard-induced spike-adding, the homoclinic bifurcation curve itself becomes a sharp frontier with the region governed by the chaotic machinery. Indeed, if we consider any horizontal line in the parameter space such that it crosses the homoclinic curve, as the segment $R1$ in Fig. 2, the passage through the homoclinic curve is clearly that event which marks the change of behavior. The spike-adding cascade showed in Fig. 3 illustrates this fact. Moving from right to left, one can observe how the chaotic windows (see Section II A) are replaced by instability/bistability windows (see II B) as mechanisms producing the spike-adding transitions, but once the homoclinic curve is crossed, (macro-)chaos is no longer observed.

The transformation of discontinuous spike-addings into Hopf-induced ones is quite different. To describe how dynamics evolves, we have selected a short segment in the parameter space fixing $I = 4.1$ and $b \in [2.58, 2.6]$. We denote by $P1$ and $P2$ the left and right ends, respectively, of the segment shown in Fig. 2. The transition process starts when the segment crosses an ultimate fan of bifurcation curves of periodic orbits arising from the type-C inclination-flip (IF) codimension-two homoclinic bifurcation point located in the fold of the homoclinic curve (see the theoretical unfolding²⁷ and the numerically computed bifurcation curves displayed at the bottom-right panel in Fig. 11). As showed at top panels of Fig. 11, for $P1$ and $P2$ we observe a fold/Hopf and a fold/hom bursting, respectively. Some of the changes that occur in the attractor can be seen in the IBD bifurcation diagram (central panel of Fig. 11). By decreasing parameter b , a bistability zone is detected, which leads to the gaining of a new spike. It is formed as a consequence of the passing through fold and period-doubling bifurcation curves. Shortly after crossing this bistability zone, there is an abrupt change in the number of spikes that precedes the entrance into the domain of Hopf-induced spike-adding (see the green vertical band in the IBD). The time series and the orbit exhibited at the bottom-left panel in Fig. 11 show a phenomenon of intermittency where the fold/Hopf and the fold/Hom bursting alternate (the sum of the spikes of both types explains the abrupt jump observed in the IBD). We can understand this peculiar behavior appealing to the fast-slow decomposition. Along the transition from fold/Hopf to fold/hom bursting (see Fig. 1), the 2D fast manifold of limit cycles becomes tangent to the 1D slow manifold of equilibria. Close to this tangency, orbits can show the alternation between the two types of bursting, exhibiting phases where the orbit follows the fast manifold up

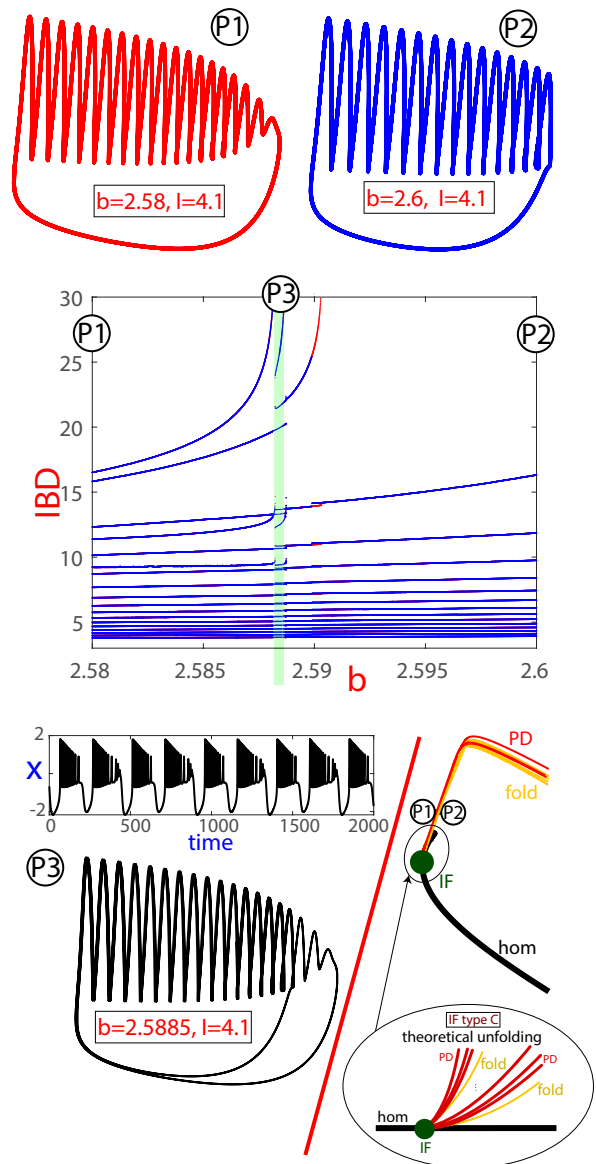


FIG. 11. Crossing the bridge between Hopf-induced (top-left) and chaos-induced (top-right) spike-adding. Orbits correspond to points $P1$ and $P2$, respectively, of Fig. 2. Inter-spike bifurcation diagram for $I = 4.1$ and $b \in [2.58, 2.6]$ is provided in central panel, where the green vertical band separates the two types of spike-adding. Transition through the green band is illustrated at the bottom-left panel. Bottom-right panel provides the location of $P1$ and $P2$, and also the numerically calculated bifurcation curves and the theoretical unfolding of a type-C inclination-flip.

to the Hopf bifurcation point and phases where orbits behave as if the fast manifold were split. The presence of the pencils of bifurcations that converge to the IF point helps in this mixed behavior.

III. DISCUSSION

Throughout the previous section we have provided a unified perspective of several of the spike-adding mechanisms that are unfolded in the Hindmarsh-Rose model and the transitions that occur between the different types. Panel (b) in Figure 12 provides a schematic illustration of the catalogue. Specifically, we have identified

- **Chaos-induced spike-adding:** (translucent red region) discontinuous spike-adding formed by isolas of bursting periodic orbits with cascades of period-doubling bifurcations leading to chaos. This case corresponds to the chaotic scenario studied by Terman²⁰.
- **Canard-induced continuous spike-adding:** (translucent dark-green region) continuous spike-adding created in hysteresis areas limited by fold bifurcations of periodic orbits and canards being involved in the genesis of extra spikes.
- **Hopf-induced continuous spike-adding:** (translucent pale-green region) continuous spike-adding with a Hopf bifurcation being involved in the processes generating new extra spikes (see also Appendix).
- **Transition spike-adding states:** there are three possible transitions. Translucent light-green regions in Fig. 12 correspond to the mixing of Hopf-induced and canard-induced continuous spike-addings near a cusp bifurcation where the two fold bifurcations of periodic orbits collapse. On the other hand, the black curve (homoclinic) marks the transitions from chaos-induced to canard-induced spike-adding. The change from chaos to Hopf-induced spike-adding is also evident: it involves bifurcation curves of periodic orbits arising from codimension-two homoclinic bifurcations.

At panel (a) in Fig. 12 one can see how the isolas of periodic orbits and the chaotic region are located to the right of the vertical line that marks the passage through the homoclinic bifurcation curves.

Fig. 12 also shows the vertical line ($b = 2.67434$) that, according to the fast-slow dynamics and the Izhikevich classification, corresponds to the passage from fold/hom to fold/Hopf bursting. Namely, that vertical line is tangent to the homoclinic bifurcation curve for the fast subsystem at the point where the curve folds in the b -direction. Of course, this theoretical frontier works the better as smaller the value of ϵ is and, in fact, already for $\epsilon = 0.01$ we observe how the Izhikevich criterion is no longer applicable in some regions (as expected).

Paying attention to the cascade of bifurcations shown at panel (a) of Fig. 12, it is still observed how on the left side of the vertical line of homoclinic folding, the canards are involved in the genesis of new spikes. That is the case throughout the entire vertical pale-pink band, limited to the left side by a cusp bifurcation of periodic orbits. On this complete band, the Izhikevich analysis classifies the bursting as fold/Hopf, but this only manifests for smaller values

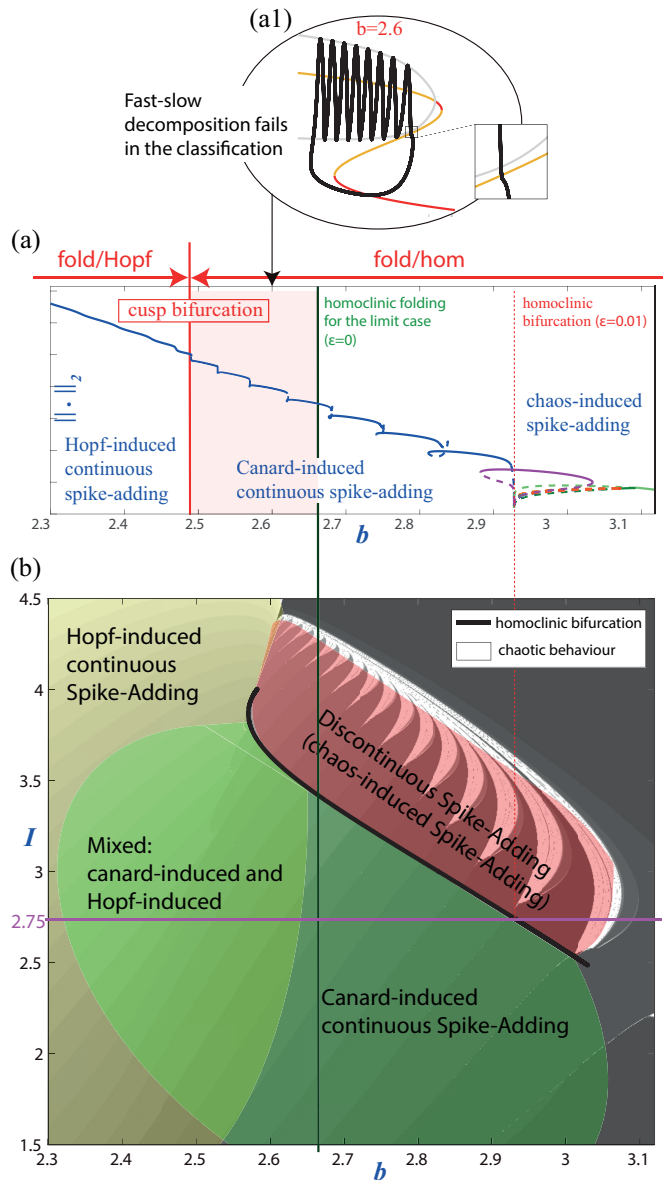


FIG. 12. (a) Extra details in the bifurcation diagram for the continuation of the periodic orbit through the cascade of spike-addings along segment R1 (see Fig. 2). Compare with bottom panel of Fig. 3. (b) Classification scheme of regions with different type of spike-adding process superimposed on the biparametric bifurcation spike-counting diagram for $\epsilon = 0.01$. White color represents regions with chaotic behavior; different shades of gray represent regions with periodic orbits with different number of spikes; translucent colors represent (schematically) regions with different types of spike-adding. The homoclinic bifurcation (black curve) marks the boundary between the region with discontinuous spike-adding and the other regions.

of parameter b (on the left-side of the cusp bifurcation line, to be precise). The reason lies in the fact that for a higher dimensional parameter space, like in a three-dimensional bifurcation diagram, including ϵ , the transition bifurcation surfaces exhibit some inclination, that is, they are not completely

vertical (see recent Ref. 6 for a complete three dimensional analysis). Panel (a1) in Figure 12 illustrates one example of the limits with Izhikevich's classification. Superimposed on the fast-slow decomposition, a bursting orbit is shown. Fast-slow decomposition is fold/Hopf type, but bursting is clearly of fold/hom type. In any case this fact is what is expected as this useful classification is based on the limit cases.

IV. CONCLUSIONS

Neural communication takes place through action potentials or spikes. In addition, it is when the spikes travel in packets that the exchange of information is more fluent and efficient. The number and tempo of the spikes in each burst are main ingredients to build neural messages. These are the reasons that justify the importance of the analysis of the spike-adding mechanisms. In this paper we deal with bursting in single-neurons activity. Among the most popular models, we chose the Hindmarsh-Rose, as it is the simplest one that is able to exhibit bursting behavior. We show and classify the different mechanisms of spike-adding: chaos-induced, canard-induced and Hopf-induced. Besides, we study the transition mechanisms from one type of spike-adding process to another. This classification leads to a map where frontiers are sometimes clear and other times fuzzy. We have identified the key ingredients of each spike-adding process and transitions among them. For further research, it would be interesting to explore whether this classification is valid in other models exhibiting fold/hom and fold/Hopf bursting, where we honestly believe that is the case. Particularly, it would be interesting to know if different transition dynamics along frontiers are possible. More challenging, Izhikevich's catalogue for the types of bursting is extensive and one must wonder which spike-adding mechanisms are available in each case and also which are the transitional dynamics.

ACKNOWLEDGMENTS

RB and SS have been supported by the Spanish Research projects PGC2018-096026-B-I00 and PID2019-105674RB-I00, the Universidad de Zaragoza-CUD project UZCUD2019-CIE-04 and the European Regional Development Fund and Diputación General de Aragón (E24-17R and LMP124-18). SI and LP have been supported by Spanish Research project MTM2017-87697-P. LP has been partially supported by the Gobierno de Asturias project PA-18-PF-BP17-072.

DATA AVAILABILITY

Data available on request from the authors. The simulations have been done using the AUTO^{22,23} and the TIDES^{28,29} softwares.

¹F. Zeldenrust, W. J. Wadman, and B. Englitz, *Frontiers in Computational Neuroscience* **12**, 48 (2018).

²J. L. Hindmarsh and R. M. Rose, *Proc. Roy. Soc. Lond.* **B221**, 87 (1984).

- ³J. Rinzel, in *Mathematical Topics in Population Biology, Morphogenesis and Neurosciences: Proceedings of an International Symposium held in Kyoto, November 10–15, 1985*, edited by E. Teramoto and M. Yumaguti (Springer Berlin Heidelberg, Berlin, Heidelberg, 1987) pp. 267–281.
- ⁴E. M. Izhikevich, *Int. J. Bifur. Chaos Appl. Sci.* **10**, 1171 (2000).
- ⁵R. Barrio, S. Ibáñez, and L. Pérez, *Phys. Lett. A* **381**, 597 (2017).
- ⁶R. Barrio, S. Ibáñez, and L. Pérez, *Chaos* **30**, 053132, 20 (2020).
- ⁷R. Barrio, S. Ibáñez, L. Pérez, and S. Serrano, *Commun. Nonlinear Sci. Numer. Simul.* **83**, 105100, 15 (2020).
- ⁸R. Barrio, M. A. Martínez, S. Serrano, and A. Shilnikov, *Chaos* **24**, 023128 (2014).
- ⁹R. Barrio and A. Shilnikov, *Journal of Mathematical Neuroscience* **1**, 6:1 (2011).
- ¹⁰M. Desroches, T. J. Kaper, and M. Krupa, *Chaos* **23**, 046106 (2013).
- ¹¹J. M. González-Miranda, *Chaos* **13**, 845 (2003).
- ¹²J. M. González-Miranda, *Physical Review E* **72**, 051922 (2005).
- ¹³J. M. Gonzalez-Miranda, *Int. J. Bifur. Chaos Appl. Sci.* **17**, 3071 (2007).
- ¹⁴G. Innocenti, A. Morelli, R. Genesio, and A. Torcini, *Chaos* **17**, 043128 (2007).
- ¹⁵G. Innocenti and R. Genesio, *Chaos* **19**, 023124 (2009).
- ¹⁶D. Linaro, A. Champneys, M. Desroches, and M. Storace, *SIAM J. Appl. Dyn. Syst.* **11**(3), 939–962 (2012).
- ¹⁷M. Storace, D. Linaro, and E. de Lange, *Chaos* **18**, 033128 (2008).
- ¹⁸A. Shilnikov and M. Kolomiets, *Int. J. Bifur. Chaos Appl. Sci.* **18**(8), 2141 (2008).
- ¹⁹N. Fenichel, *J. Differential Equations* **31**, 53 (1979).
- ²⁰D. Terman, *SIAM J. Appl. Math.* **51**, 1418 (1991).
- ²¹J. Nowacki, H. M. Osinga, and K. Tsaneva-Atanasova, *The Journal of Mathematical Neuroscience* **2**, 7 (2012).
- ²²E. Doedel, in *Proceedings of the Tenth Manitoba Conference on Numerical Mathematics and Computing, Vol. 1 (Winnipeg, Man., 1980)*, Vol. 30 (1981) pp. 265–284.
- ²³E. J. Doedel, R. Paffenroth, A. R. Champneys, T. F. Fairgrieve, Y. A. Kuznetsov, B. E. Oldeman, B. Sandstede, and X. J. Wang, <http://cmv1.cs.concordia.ca/auto>.
- ²⁴Y. Pomeau and P. Manneville, *Comm. Math. Phys.* **74**, 189 (1980).
- ²⁵E. Ott, *Chaos in dynamical systems*, 2nd ed. (Cambridge University Press, Cambridge, 2002) pp. xii+478.
- ²⁶X. Wang, *Physica D* **62**, 263 (1993).
- ²⁷A. J. Homburg and B. Sandstede, *Handbook of Dynamical Systems* **3**, 379 (2010).
- ²⁸A. Abad, R. Barrio, F. Blesa, and M. Rodríguez, <https://sourceforge.net/projects/tidesodes/>.
- ²⁹A. Abad, R. Barrio, F. Blesa, and M. Rodríguez, *ACM Transactions on Mathematical Software* **39**, 5:1 (2012).
- ³⁰Y. A. Kuznetsov, *Elements of applied bifurcation theory*, 3rd ed., Applied Mathematical Sciences, Vol. 112 (Springer-Verlag, New York, 2004) pp. xxii+631.

APPENDIX

In this Appendix we just show analytically with a simple example how the distance between the saddle-node bifurcations of equilibria in the fast subsystem of the HR model allows the increment of the number of spikes, and so, it generates the Hopf-induced spike-adding process.

Let us consider the following family of vector fields:

$$\begin{cases} x' = -zx - \omega y - Lx(x^2 + y^2), \\ y' = \omega x - zy - Ly(x^2 + y^2), \\ z' = \varepsilon. \end{cases} \quad (2)$$

This is a toy-model for a Hopf bifurcation, where the bifurcation parameter z varies with respect to time at a constant ratio ε , which we assume to be a small parameter ($\varepsilon \ll 1$). Coeffi-

cient L corresponds to the first Lyapunov coefficient³⁰ and we assume that $L > 0$.

Using polar coordinates $x = r \cos \theta$, $y = r \sin \theta$ in (2), we get:

$$\begin{cases} r' = -zr - Lr^3, \\ \theta' = \omega, \\ z' = \varepsilon. \end{cases} \quad (3)$$

Let

$$\varphi(t, r_0, \theta_0, z_0) = (\varphi^r(t, r_0, \theta_0, z_0), \varphi^\theta(t, r_0, \theta_0, z_0), \varphi^z(t, r_0, \theta_0, z_0))$$

be the flow defined by equations (3). Clearly,

$$\begin{aligned} \varphi^\theta(t, r_0, \theta_0, z_0) &= \theta_0 + \omega t, \\ \varphi^z(t, r_0, \theta_0, z_0) &= z_0 + \varepsilon t. \end{aligned}$$

Fixing time $t = \frac{2\pi}{\omega}$ and angle $\theta_0 = 0$ we get the first return map from the half-plane $\theta_0 = 0$ on itself. Namely,

$$P(r_0, z_0) = (P^r(r_0, z_0), P^z(r_0, z_0))$$

with

$$P^r(r_0, z_0) = \varphi^r\left(\frac{2\pi}{\omega}, r_0, 0, z_0\right)$$

and

$$P^z(r_0, z_0) = \varphi^z\left(\frac{2\pi}{\omega}, r_0, 0, z_0\right) = z_0 + \frac{2\pi\varepsilon}{\omega}.$$

In what follows, we assume that

$$(r_0, z_0) \in [0, R] \times \{-\delta\},$$

for some $\delta > 0$ and $R > \sqrt{\frac{\delta}{R}}$, and define

$$(r_n, z_n) = ((P^r)^n(r_0, z_0), (P^z)^n(r_0, z_0)).$$

Constant δ stands for the maximum allowed change in parameter z . We say that the orbit of the point $(r_0, 0, z_0)$ has N spikes if N is the maximum number of iterations of the first return map which remain in the rectangle $[0, R] \times [-\delta, \delta]$. Since $R > \sqrt{\frac{\delta}{R}}$, it follows by construction that $r_n < R$ for all $n \in \mathbb{N}$. On the other hand

$$z_n = -\delta + \frac{2\pi\varepsilon n}{\omega},$$

and, in order to have $z_n > \delta$, the condition

$$n > \frac{2\delta\omega}{2\pi\varepsilon},$$

must be fulfilled. We obtain the expected results, that is, the number n of allowed spikes increases as either δ or the rotation speed ω increase. Bearing in mind the Hindmarsh-Rose model, the number of spikes in the fold/Hopf bursting increases as the distance (measured in the z -direction) between the two saddle-node bifurcation points in the fast subsystem (2δ in the toy model) increases.

4.5 Paper V

The goal of this article [7] is the study of the dynamical mechanisms underlying pathological phenomena in cardiac activity. As in the case of neurons, the activity of the heart presents different time-scales and exhibits oscillatory phenomena, which is of spiking type in healthy individuals, and bursting-like in pathological cases. Due to these elements in common, we can use sweeping and continuation techniques to study the dynamics as a function of parameters. We considered a simplified version of the Luo-Rudy cardiac model, which consists of the following system of ODE's:

$$\begin{cases} C_m \dot{V} &= -(I_{Ca} + I_K) + I_{sti} \\ \dot{f} &= \frac{f_\infty - f}{\tau_f} \\ \dot{x} &= \frac{x_\infty - x}{\tau_x} \end{cases}$$

with the ionic currents

$$I_{Ca} = G_{Ca} d_\infty(V) f(V - E_{Ca}); \quad I_K = G_K x(V - E_K)$$

being the steady state functions

$$f_\infty(V) = \frac{1}{1 + \exp\left(\frac{V - E_f}{\theta_f}\right)}, \quad x_\infty(V) = \frac{1}{1 + \exp\left(\frac{E_x - V}{\theta_x}\right)}, \quad d_\infty(V) = \frac{1}{1 + \exp\left(\frac{E_d - V}{\theta_d}\right)}$$

The variable V represents the transmembrane potential of the heart, and f and x are auxiliary variables, corresponding to inactivation gates of the ionic currents. We study the dynamics of the system in the planes (G_K, G_{Ca}) and (G_K, C_m) , fixing the rest of the parameters to biophysically plausible values. Our focus is the generation of arrhythmogenic early afterdepolarizations (EADs), which consist of an elongation of the plateau phase of the normal beat accompanied by small oscillations. EADs are a pathological behaviour that can lead to sudden cardiac death.

We consider a 1 fast, 2 slow variable decomposition to analyse the dynamics of the model, which allows us to relate the evolution of the solutions with the critical manifold of the system. We employ sweeping techniques to generate maps in the (G_K, G_{Ca}) and (G_K, C_m) planes that allow us to identify parametric regions associated with healthy beats and abnormal beats with one or more extra oscillations. We considered a one-parameter cut and investigated the bifurcation diagram of the system. The regions corresponding to the appearance of EADs are organised by isolas of periodic orbits, each isola corresponding to an abnormal beat with a different number of extra oscillations. The isolas have stable and unstable sections, and the stable sections delimitate the appearance of the corresponding pathological beats.

Article

Bifurcations and Slow-Fast Analysis in a Cardiac Cell Model for Investigation of Early Afterdepolarizations

Roberto Barrio ^{1,*} , M. Angeles Martínez ¹, Lucía Pérez ² and Esther Pueyo ³ 

¹ IUMA and Departamento Matemática Aplicada, University of Zaragoza, E-50009 Zaragoza, Spain; gelimc@unizar.es

² Departamento Matemáticas, University of Oviedo, E-33007 Oviedo, Spain; perezplucia@uniovi.es

³ I3A, University of Zaragoza, IIS Aragón and CIBER-BBN, E-50018 Zaragoza, Spain; epueyo@unizar.es

* Correspondence: rbarrio@unizar.es

Received: 24 April 2020; Accepted: 23 May 2020; Published: 1 June 2020



Abstract: In this study, we teased out the dynamical mechanisms underlying the generation of arrhythmogenic early afterdepolarizations (EADs) in a three-variable model of a mammalian ventricular cell. Based on recently published studies, we consider a 1-fast, 2-slow variable decomposition of the system describing the cellular action potential. We use sweeping techniques, such as the spike-counting method, and bifurcation and continuation methods to identify parametric regions with EADs. We show the existence of isolas of periodic orbits organizing the different EAD patterns and we provide a preliminary classification of our fast–slow decomposition according to the involved dynamical phenomena. This investigation represents a basis for further studies into the organization of EAD patterns in the parameter space and the involved bifurcations.

Keywords: cardiac dynamics; early afterdepolarizations (EADs); bifurcations; isolas; fast–slow decomposition

MSC: 92B05; 34C23; 34C60

1. Introduction

In a healthy heart, the sinoatrial node sends out an electrical impulse, which spreads cell to cell throughout the heart, activating all cardiomyocytes to produce an electrical response called the action potential (AP). Upon being stimulated, cardiomyocytes in the lower chambers of the heart, the ventricles, suddenly increase their transmembrane voltage (depolarization). This increase is followed by a small partial voltage decrease (transient repolarization) and a prolonged plateau phase where voltage remains approximately constant. In the final part of the AP, transmembrane voltage decreases (repolarization) while returning to the resting potential level, which is maintained until receiving the next stimulus.

Under some circumstances, the normal sequence of AP phases can be reversed due to inward currents raising the transmembrane voltage during the plateau or repolarization phases of the AP, producing so-called phase-2 or phase-3 early afterdepolarizations (EADs). Drug side effects, ion channel dysfunction or oxidative stress, among others, can lead to the genesis of EADs [1–3]. In heart failure and genetic syndromes, EADs have been documented to be an important cause for lethal ventricular arrhythmias [4–6], but further knowledge is required to understand the mechanisms underlying EAD generation and the relationship between these cellular abnormalities and the occurrence of arrhythmias at tissue and whole-organ level that could eventually lead to sudden cardiac death.

Computational models of cardiac electrical activity have greatly contributed to shed light into varied cardiac phenomena, including EADs. Multiple models of mammalian ventricular cardiomyocytes have been used in the literature. Some of these are highly detailed, complex models with tens of state variables and hundreds of parameters, while there are other simpler models with just a few variables and parameters. Whereas complex (high-dimensional) models allow for greater realism in reproducing experimental observations and facilitating biophysical interpretation, simple (low-dimensional) models aid in isolating the dynamical mechanisms underlying a particular phenomenon and in performing a comprehensive theoretical study. In the present work, we use a low-dimensional approach based on a reduced three-variable cardiomyocyte model.

In 1991, Luo and Rudy [7] introduced a mathematical model of the membrane AP of a mammalian ventricular cell based on experimental data recently available at that time. This model, differently from subsequent models developed by the same authors, is called “passive” because all ionic concentrations, except for intracellular calcium, remain unchanged rather than varying dynamically over time. Due to its simple formulation and its ability to represent phenomena involving both depolarization and repolarization of ventricular cell, this model, either as such or with some simplifications, has been extensively used. In [8], a reduction in the number of variables of the Luo–Rudy model was proposed to investigate the mechanisms of EADs when decreasing the stimulation frequency. Initially, a model able to produce EADs was considered that contained three ionic currents, namely a fast Na current, an intermediate time-scale Ca current, and a slow K current. Later, the fast Na current was discarded due to it having little effect on EAD generation, as it is activated mostly during the AP upstroke and is practically null during the plateau and repolarization AP phases. In our analysis, we use this reduced model to simplify the number of state variables at its maximum and, thus, facilitate a theoretical study.

From a mathematical point of view, this is a *fast–slow dynamical system* with multi-timescale phenomena. A fast–slow analysis of a reduced version of the Luo–Rudy model is presented in [8], considering a system with one slow and two or three fast variables. In that paper, the presence of a subcritical Poincaré–Andronov–Hopf bifurcation is shown as a signature of pseudo-plateau bursting. Similar analyses were published based on mathematical neuron models [9–11], where the classification of bursting models and the generation of new oscillations (spikes) were related, among others, with Poincaré–Andronov–Hopf and homoclinic bifurcations in the fast subsystem of two variables (dimension 2). While this approach has been successfully used in a variety of cardiac studies to investigate the causes for the presence or absence of EADs, it has recently been shown to fail in explaining the lack of certain types of EADs [12]. Considering the reduced three-variable version of the Luo–Rudy model presented in [8], a 1-fast, 2-slow decomposition is proposed [12,13] to provide more insight into the facilitation or inhibition of EADs as a function of the pacing frequency or pharmacological interventions. In this paper, we use this approach for the fast–slow decomposition and we characterize dynamical behaviors by introducing a sweeping technique, namely the spike-counting method. Besides, by using continuation techniques, we describe some bifurcations of the system and we show, for the first time to the best of our knowledge, the presence of isolas of families of periodic orbits in the reduced Luo–Rudy model.

The paper is organized as follows. In Section 2, the reduced model used to describe the electrical behavior of a mammalian ventricular cardiomyocyte is presented. In Section 3, the dynamical analysis performed to identify parametric regions with EADs and generate associated bifurcation diagrams is described. In Section 4, the discussion and conclusions of the study as well as recapitulating classification figures regarding EAD generation are presented.

2. The Reduced Luo–Rudy Mammalian Ventricular Cell Model

Following a Hodgkin and Huxley formalism [14], Luo and Rudy proposed a mathematical model of a mammalian ventricular cell (LR91) [7]. The rate of change of the transmembrane potential (V) is given by

$$dV/dt = -(1/C_m)(I_i + I_{sti})$$

where C_m is the membrane capacitance, in this study set at $0.5 \mu\text{F}/\text{cm}^2$, as in [13], and subsequently varied to investigate its role in facilitating the generation of EADs. In the above equation, I_{sti} is an external stimulus current and I_i is the sum of the ionic currents in the cell. All ionic currents were computed for a membrane area of 1cm^2 . Six ionic currents were defined in the LR91 model: I_{Na} , a fast sodium current; I_{Ca} , a slow inward current; I_K , a time-dependent potassium current; I_{K1} , a time-independent potassium current; I_{Kp} , a plateau potassium current; and I_b , a time-independent background current.

Since here we focus on EAD generation, we follow the approach proposed in [8] and we discard the fast I_{Na} current for the reduced version of the LR91 model. Although some studies have described a role for the sodium current in the generation of EADs [2,3], it should be noted that this current has two components, namely the fast sodium current and the late sodium current. While the late sodium current flows throughout the AP plateau and its involvement in EAD generation has been well documented, the fast sodium current contributes to the AP depolarization and has a more limited contribution to EADs. In the reduced model used in this work, only the fast sodium current is included and, thus, we discard it based on its reduced contribution to the investigated phenomenon. The other two ionic currents in the reduced model are: $I_{Ca} = G_{Ca} \cdot d \cdot f \cdot (V - E_{Ca})$, which is a calcium current with an activation gating variable d and an inactivation gating variable f ; and $I_K = G_K \cdot x \cdot x_i \cdot (V - E_K)$, which is a time-dependent potassium current with a time-dependent activation gating variable x and a time-independent inactivation gating variable x_i set to one for simplification. The reversal potential of calcium was set at $E_{Ca} = 100\text{mV}$, rather than being time-dependent as in the LR91 model.

The values of the gating variables used to define the ionic currents are obtained as the solution of a coupled system of nonlinear ordinary differential equations (ODEs) of the form $dy/dt = (y_\infty(V) - y)/\tau_y(V)$, where y represents any gating variable, τ_y is its time constant, and y_∞ is the steady-state value of y [7].

An additional simplification to the four-variable system (V, d, f , and x) proposed in [8] was later described by Kügler [15]. The gating variable d was replaced with its steady-state function $d_\infty(V)$ and the time-constant functions $\tau_f(V)$ and $\tau_x(V)$ were assumed to be constant, thus being represented by τ_f and τ_x .

With all these simplifications, the three-variable model used here [12] was described by the following ODE system:

$$\begin{cases} C_m \frac{dV}{dt} = -(I_{Ca} + I_K) + I_{sti} \equiv h(V, f, x), \\ \frac{df}{dt} = \frac{f_\infty(V) - f}{\tau_f} \equiv g_1(V, f), \\ \frac{dx}{dt} = \frac{x_\infty(V) - x}{\tau_x} \equiv g_2(V, x), \end{cases} \tag{1}$$

with the inward ionic calcium current I_{Ca} (with the calcium channel conductance G_{Ca} and the dynamic inactivation variable f) and the outward ionic potassium current I_K (with the potassium channel conductance G_K and the dynamic activation variable x) defined by:

$$I_{Ca} = G_{Ca} \cdot d_\infty(V) \cdot f \cdot (V - E_{Ca}); \quad I_K = G_K \cdot x \cdot (V - E_K). \tag{2}$$

The steady-state functions were given by:

$$f_\infty(V) = \frac{1}{1 + e^{\frac{V - E_f}{\theta_f}}}, \quad x_\infty(V) = \frac{1}{1 + e^{\frac{E_x - V}{\theta_x}}}, \quad d_\infty(V) = \frac{1}{1 + e^{\frac{E_d - V}{\theta_d}}}.$$

The fixed parameter values used in this study, unless otherwise stated, were:

$$\begin{aligned}
 C_m &= 0.5 \mu\text{F}/\text{cm}^2, & \tau_f &= 80 \text{ ms}, & \tau_x &= 300 \text{ ms}, & G_{Ca} &= 0.025 \text{ mS}/\text{cm}^2, & E_{Ca} &= 100 \text{ mV}, \\
 G_K &= 0.04 \text{ mS}/\text{cm}^2, & E_K &= -80 \text{ mV}, & E_f &= -20 \text{ mV}, & \theta_f &= 8.6 \text{ mV}, & E_x &= -40 \text{ mV}, \\
 \theta_x &= 5 \text{ mV}, & E_d &= -35 \text{ mV}, & \theta_d &= 6.24 \text{ mV}.
 \end{aligned}$$

It should be noted that, whereas the LR91 model well represents the behavior of a ventricular cardiomyocyte with constant resting membrane potential during Phase 4, the reduced model described above presents a Phase 4 with slowly increasing transmembrane potential. Thus, an external stimulus is required to depolarize the AP in the LR91 model, but the AP depolarizes spontaneously when transmembrane potential reaches a threshold in the case of the reduced model. Consequently, $I_{sti} = 0$ in the above equations for the three-variable model.

3. Dynamical Study

We showed that the reduced version of the LR91 model described above presents a behavior comparable to that of typical spiking-bursting activity [9–11]. To achieve a better understanding of the model dynamics, we performed a detailed numerical analysis using both a spike-counting technique and numerical continuation to detect the main bifurcations. Numerical simulations were performed using a variable-stepsize variable-order Taylor series method (software TIDES (<https://sourceforge.net/projects/tidesodes/>) [16,17]), which provides a highly accurate numerical ODE solver, using $TOL = 10^{-12}$ as error tolerance.

3.1. Spike-Counting Sweeping

When EADs are generated, extra spikes can be seen in the plateau of the AP. Figure 1 shows a normal beat with no EADs, a beat with one EAD and a beat with several EADs (more than 2 spikes).

The spike-counting technique consists of detecting the number of spikes of the limit cycles of the system, when these exist [18]. Regions of parameter values with the same number of spikes per beat are represented with the same color. This allows appreciating different bands in the parameter space, which characterize the structure of the model. The detection of the number of spikes per orbit is performed by computing all relative maxima and minima and by counting the spikes where the relative difference between the maxima and minima in the voltage variable is higher than a threshold. Here, the threshold is set at 10^{-2} so as not to include very small oscillations that occur in action potentials such as the one represented on the right panel of Figure 1. The number of counted spikes is clearly sensitive to the selection of the threshold value, but the global behavior in terms of the occurrence of EADs is generally well captured, as all main voltage changes during the AP plateau are detected.

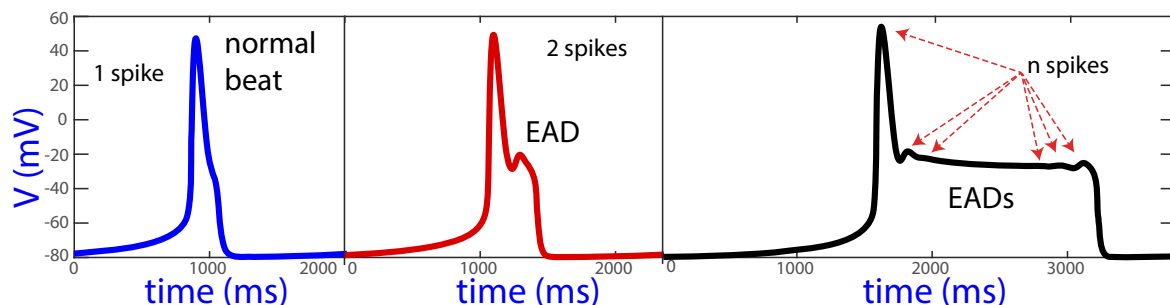


Figure 1. Normal beat and beats with one or more EADs.

In our analysis, we used the conductances of the calcium and potassium currents, G_K and G_{Ca} , as the main set of parameters to investigate their involvement in EAD occurrence. We also investigated variations in the cell capacitance, C_m . This represents a further step from previous studies that considered variations only in G_{Ca} [8] or both G_{Ca} and G_K [12] to determine the presence of

EADs. While using a reduced model facilitates theoretical understanding on the mechanisms for EAD generation, future works should be conducted with more complex and more realistic cardiomyocyte models that allow meaningful interpretations regarding the parameters involved in the occurrence of EADs.

Figure 2 shows the results of the spike-counting technique for the biparametric plane (G_K, G_{Ca}), with the upper left inset presenting a magnification of a specific area. Colors indicate different cellular behaviors. Darkest blue denotes cases where no beats are generated. Slightly lighter blue corresponds to normal beats without EADs, an example of which is illustrated in Figure 3b for the parameter values of Point I. In the region of Point II, the periodic orbit shows one EAD, as exemplified in Figure 3d. When the parameters move to the lightest blue and red regions, more EADs are present, as shown in Figure 3f for Point III and in Figure 4c,f for Points IV and V, respectively. In particular, Point III corresponds to the default values $G_{Ca} = 0.025$ and $G_K = 0.04$, for which EADs are present. Based on the different cellular behaviors indicated by the color band structure in Figure 2, further analyses were performed for the default value of $G_{Ca} = 0.025$ while varying G_K along the horizontal red line, as described in the following sections.

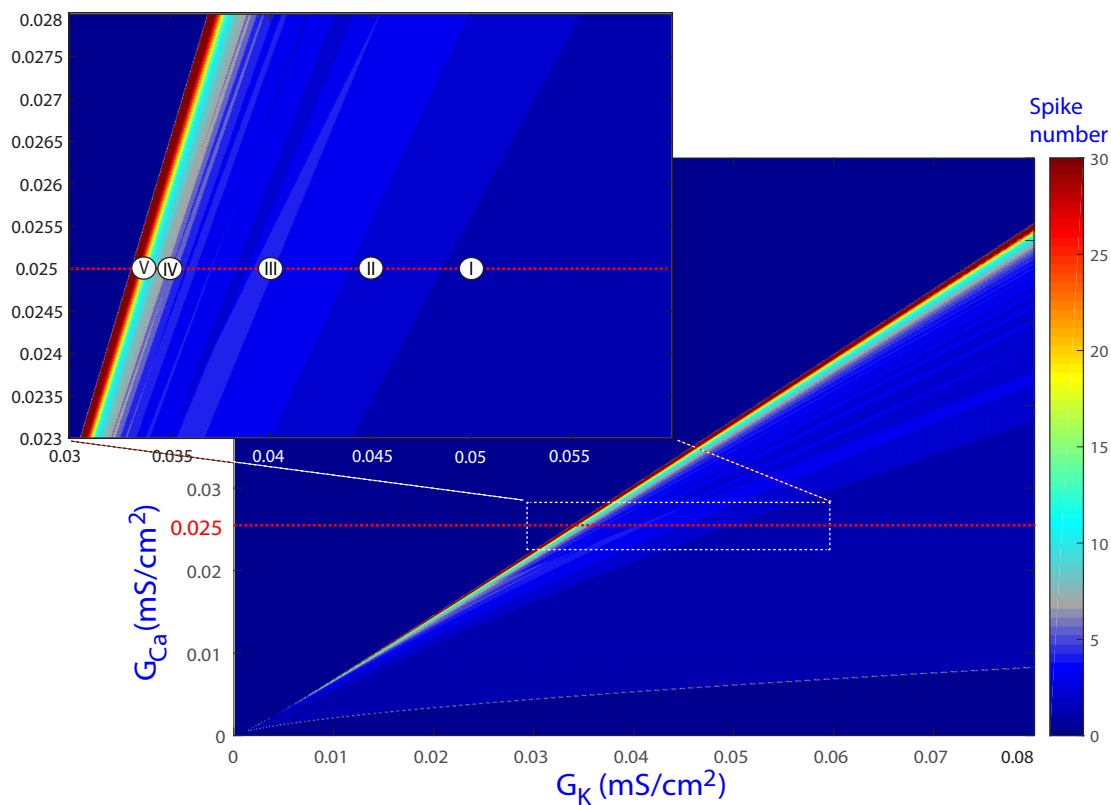


Figure 2. Regions of the spike-counting analysis for the biparametric plane (G_K, G_{Ca}). In the upper left inset, a magnification of a specific region is shown. Different colors mark different numbers of spikes in the attracting orbit. A triangular shape region delimits the regions of beats with and without EADs. Point I corresponds to a normal beat without EADs (illustrated in Figure 3b). In the region of Point II, the periodic orbit shows one EAD (illustrated in Figure 3d). More EADs are present when the parameters move to the lightest blue and red regions (illustrated in Figure 3f for Point III and in Figure 4c,f for Points IV and V, respectively). The horizontal red dashed line corresponds to the default value $G_{Ca} = 0.025$.

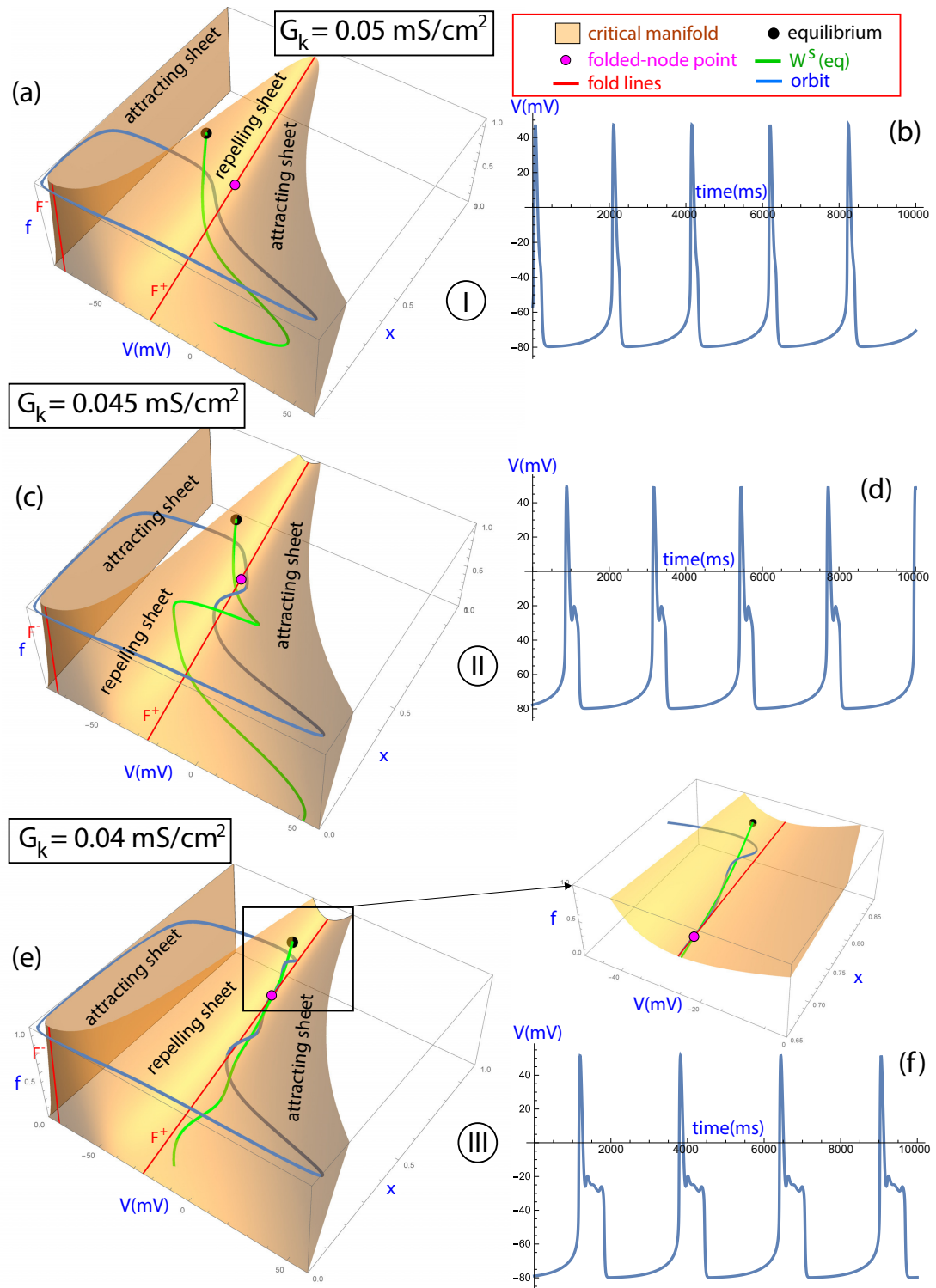


Figure 3. Analysis of cases I, II, and III on the line $G_{Ca} = 0.025$. Plots (a,c,e): the critical manifold $\mathcal{M}_{\text{critical}}$ (orange) is shown with the attracting and repelling sheets separated by the fold lines, F^+ and F^- (red). The periodic orbit is shown in blue. As the bifurcation parameter G_k is varied, the periodic orbit and the number of EADs change depending on the position of the equilibrium point (black), the folded-node point (magenta), and the stable manifold of the equilibrium (green). Plots (b,d,f): the temporal evolution in milliseconds of the variable V of the periodic orbit is shown.

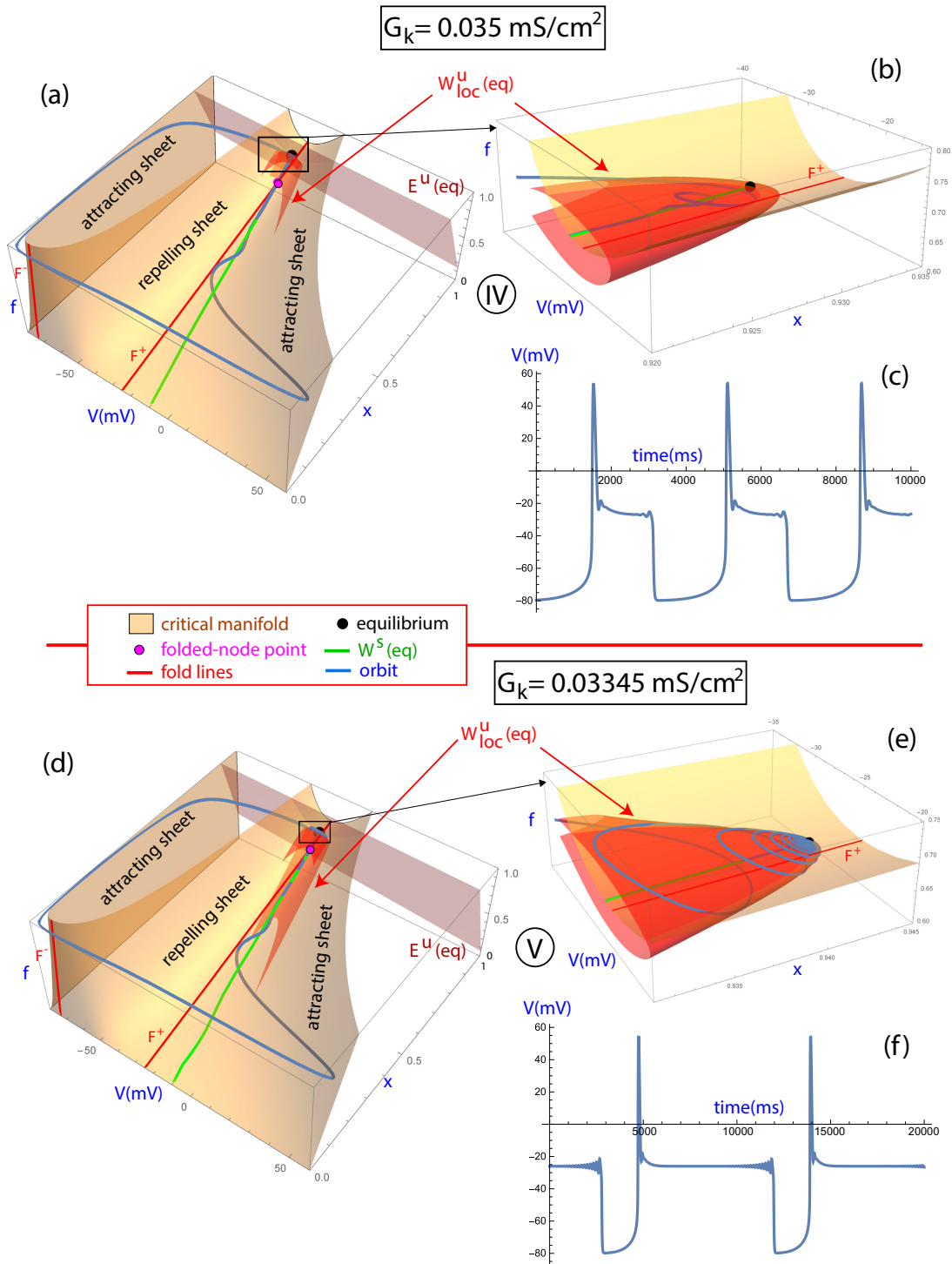


Figure 4. Analysis of cases IV and V on the line $G_{Ca} = 0.025$. Plots (a,b,d,e): the critical manifold $\mathcal{M}_{critical}$ (orange) is shown with the attracting and repelling sheets separated by the fold lines, F^+ and F^- (red). The periodic orbit is shown in blue. As the bifurcation parameter G_k is varied, the periodic orbit and the number of EADs change depending on the position of the equilibrium point (black), the folded-node point (magenta) and the stable manifold of the equilibrium (green). The local two-dimensional unstable manifold $W^u_{loc}(eq)$ and the unstable subspace $E^u(eq)$ of the equilibrium point are plotted. Plots (c,f): the temporal evolution in milliseconds of the variable V of the periodic orbit is shown. In this case the periodic orbit shows a longer activation time because of AP plateau prolongation and there is a remarkable increment in the number of EADs per beat.

Figure 5 shows additional spike-counting results for the biparametric (G_K , C_m) plane, with the horizontal red line corresponding to the default value $C_m = 0.5$ (and $G_{Ca} = 0.025$). In this case as well, color bands can be observed, rendering similar structures to those shown for the (G_K , G_{Ca}) plane in Figure 2. Based on the results shown in the two figures, bounded regions in the global parameter space can be expected in the characterization of EAD dynamics.

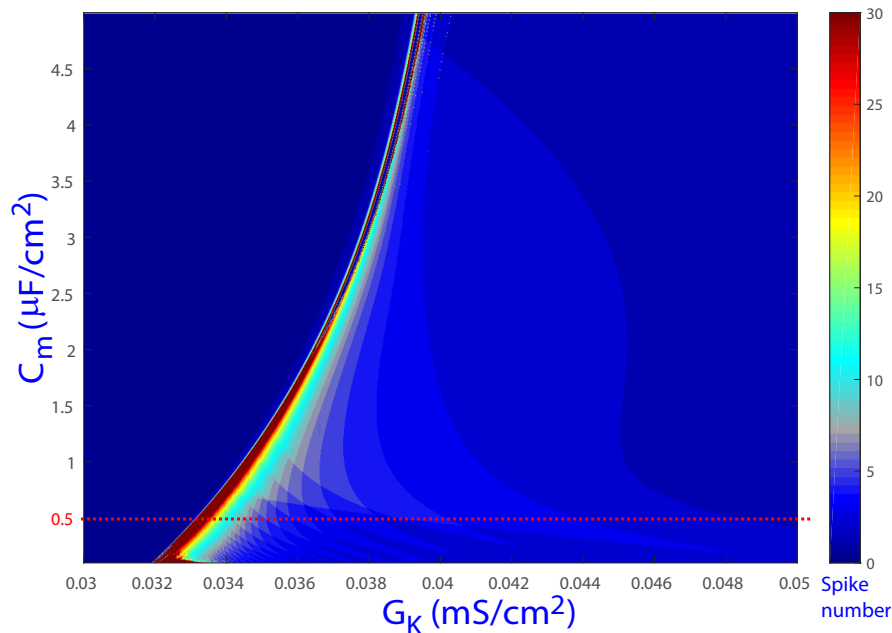


Figure 5. Regions of the spike-counting analysis for the biparametric plane (G_K , C_m). Different colors mark different numbers of spikes in the attracting orbit. A similar structure to that shown in Figure 2 can be observed. The red dashed line represents the value of $C_m = 0.5$, studied below in detail.

3.2. Fast–Slow Analysis

The reduced version of the LR91 model used in this study is a fast–slow system, since its state variables change at different time scales. When analyzing a fast–slow system, it is of major relevance to investigate the bifurcation diagrams of the limit cases (when the parameters responsible for the difference in time scales are considered to be zero) [10]. This approach uses geometric singular perturbation methods and allows (partially) explaining the dynamics when such parameters are small enough (see [19] for a review and [9] for the basic theory and for classification of bursting mechanisms).

The default values of the time constant parameters characterizing the state variables f and x in the reduced LR91 model are $\tau_f = 80\text{ms}$ and $\tau_x = 300\text{ms}$. An estimate of the time constant for the state variable V can be obtained by $\tau_V = \frac{C_m}{G_{Ca} + G_K} = 7.7\text{ms}$ [12]. This means that V is the fastest state variable and x is the slowest one, while the state variable f can be considered as a fast or a slow one. In [8], the four-variable (V , d , f , and x) system was decomposed into a fast three-variable (V , d , and f) subsystem and a slow one-variable (x) subsystem, thus including f as a fast variable. In [15], a simpler three-variable (V , f , x) model was considered, as d was replaced with its steady-state function $d_\infty(V)$. The fast subsystem was defined to contain two variables (V and f), thus again taking f as a fast state variable. On this basis, a fast two-variable and a slow one-variable subsystems were analyzed and their information was combined to characterize the dynamics of the full three-variable system. By fixing x , the model analysis provides two invariant objects: a curve of equilibrium points and a manifold of limit cycles. The main issue with this approach is that it does not explain some changes in the system, as illustrated in [12]. To solve this issue, some studies have decomposed the same three-variable system into a fast one-variable (V) and a slow two-variable (f and x) subsystems [12,13]. A systematic analysis of the geometric singular perturbation methods for 1-fast, 2-slow variables is given in [20,21].

In this study, we considered, on the one hand, the reduced LR91 model (Equation (1)) using the fast time scale $\tau = t/C_m$:

$$\frac{dV}{d\tau} = h(V, f, x), \quad \frac{df}{d\tau} = \varepsilon \cdot g_1(V, f), \quad \frac{dx}{d\tau} = \varepsilon \cdot g_2(V, x). \tag{3}$$

where ε is a parameter that takes small values ($C_m/\tau_f, C_m/\tau_x$) and $h(V, f, x) = -(I_{Ca} + I_K)$, as no external stimulus was considered ($I_{sti} = 0$), as in [12,13]. When ε decreases to zero ($\varepsilon \rightarrow 0$), the system described in Equation (3) defines orbits that converge during fast dynamics to solutions of the *fast subsystem or layer equations* given by:

$$\frac{dV}{d\tau} = h(V, f, x), \quad \frac{df}{d\tau} = 0, \quad \frac{dx}{d\tau} = 0. \tag{4}$$

On the other hand, when the orbits have slow dynamics, the fast variable moves so rapidly that it can be considered to have already reached steady-state. Thus, changing to the time scale $\tilde{t} = \tau/\varepsilon$ and taking the limit case, the orbits converge to solutions of the differential algebraic equation (DAE) system, called the *slow-flow* system, given by:

$$0 = h(V, f, x), \quad \frac{df}{d\tilde{t}} = g_1(V, f), \quad \frac{dx}{d\tilde{t}} = g_2(V, x). \tag{5}$$

The solutions of Equation (5) evolve on the manifold given by $h(V, f, x) = 0$, which is called the *critical manifold* and is denoted by $\mathcal{M}_{critical}$. Besides, this gives the manifold where the equilibria of the fast subsystem are. It follows from Fenichel theory [22] that this manifold perturbs to invariant manifolds that exist for small enough ε in the full system.

In the following, a detailed investigation of the geometry of the bursting orbit dynamics for the reduced LR91 model, and in particular the orbits for the set of parameters corresponding to Points I–V in Figure 2, is performed. Taking the model equations defined by Equation (1), the critical manifold is given by the cubic-shaped surface:

$$\mathcal{M}_{critical} := \{(V, f, x) \mid h(V, f, x) = 0\} \rightarrow \mathcal{M}_{critical} = \left\{ (V, f, x) \mid f = -\frac{G_K x (V - E_K)}{G_{Ca} d_\infty(V) (V - E_{Ca})} \right\}. \tag{6}$$

Figure 3 shows the outer sheets of the surface, which are attracting ones, and the middle sheet, which is a repelling one. The different sheets are separated by curves F^\pm corresponding to fold bifurcations of the fast subsystem:

$$F^\pm = \left\{ (V, f, x) \in \mathcal{M}_{critical} \mid \frac{\partial h(V, f, x)}{\partial V} = 0, \frac{\partial^2 h(V, f, x)}{\partial^2 V} \neq 0 \right\}. \tag{7}$$

From the analysis of limit cases and Fenichel theory, the solutions of the global system were found to evolve in the slow epochs close to one of the attracting sheets of the critical manifold. The evolution on the attracting sheets was found to give the stable hyperpolarized and stable depolarized steady-states. Close to the fold bifurcations, the orbits quickly fell down to the other attracting sheet. The rapid transitions between the attracting sheets were approximated by solutions of the fast one-variable subsystem in Equation (4).

As described above, the equations of the slow motion on the critical manifold are given by Equation (5), where differential equations describe the motions of the variables f and x , whereas the fast variable V is implicitly described by the first algebraic equation in Equation (5). Through several

manipulations (see [12,13,19] for details), the slow subsystem can be transformed into the so-called *desingularized system*:

$$\begin{aligned} \frac{dV}{dt_d} &= \frac{\partial h}{\partial f}g_1 + \frac{\partial h}{\partial x}g_2, \\ \frac{dx}{dt_d} &= -\frac{\partial h}{\partial V}g_2. \end{aligned} \tag{8}$$

Folded singularities are equilibria of the desingularized system only, but not of the slow subsystem in Equation (5) or the initial model in Equation (1). Thus, they lie on a fold curve and satisfy:

$$FN = \left\{ (V, f, x) \in F^\pm \mid \frac{\partial h}{\partial f}g_1 + \frac{\partial h}{\partial x}g_2 = 0 \right\}. \tag{9}$$

A study of their linear stability suggested they are folded-node equilibria in this system. These special points give a route to the solutions of the slow subsystem to cross the folds from an attracting sheet and to move some time on the repelling sheet. Therefore, these points may generate the so-called singular canards (see [19,23] for details).

The existence of canard orbits have relevant consequences in many different systems, as they allow uncovering mechanisms of sudden changes. For instance, they were linked to the spike-adding phenomena in the Hindmarsh-Rose neuron model [24,25]. In a reduced LR91 model, canard orbits were shown to organize the first EADs generated on the orbits in phase space [12]. This is well explained in references [12,13] and therefore here we focus on the different geometric characterizations of the periodic orbits of the system showing where EADs are produced by the canard orbits and where different phenomena are also present.

In Figure 3, the fast–slow geometry is described for the orbits with labels I, II, and III in Figure 2 on the parametric line $G_{Ca} = 0.025$. The critical manifold is shown in orange, with the attracting and repelling sheets separated by the fold lines, F^+ and F^- , in red and with the periodic orbits in blue. The temporal evolution of the variable V of the periodic orbit is shown on the right panels. It can be observed that in Case I for $G_K = 0.05$ the orbit presents a normal beat without any EADs (Figure 3a,b). In this case, the orbit presents the “nominal behavior”, remaining most of the time on the critical manifold of the slow motion and fast transitioning between the attracting sheets close to the fold lines. Note that the orbit is far from the folded-node singular point in magenta and, therefore, there is no canard orbit. By moving forward on the line $G_{Ca} = 0.025$ towards Point II corresponding to $G_K = 0.045$, it can be observed that the orbit has one EAD (Figure 3c,d). In this case, the orbit passes near the folded-node singular point and this allows the orbit to make a loop on the repelling sheet before progressing to the other attracting sheet (see [13]). By further moving on the parametric line towards Point III corresponding to $G_K = 0.04$, more EADs are generated by the maximal canards (Figure 3e,f). Maximal canards are given by the intersections of the depolarized attracting and the repelling sheets of the slow manifold of the system and extended by the flow (for more details, see [12,13,26]). The equilibrium point, which is a saddle-node of type (1,2) with eigenvalues $\lambda_1 = -3.91295$, $\lambda_2 = 0.0928806$, and $\lambda_3 = 4.27207$, is attracting the orbit along the stable manifold $W^s(eq)$ of the equilibrium (in green) at the same time that the canard orbits generate new EADs until the orbit progresses to the other attracting sheet (see inset in Figure 3e). This phenomenon has been previously observed in other 1-fast, 2-slow variables systems [27–29].

Figure 4 shows how further variations in the bifurcation parameter G_k lead to higher numbers of EADs as the orbit approaches the equilibrium point shown in black. The two orbits presented in Figure 4 contain a large number of EADs, particularly the second one. The mathematical mechanism explaining such a large number of EADs is twofold: the described canard phenomenon that gives rise to EADs when the orbit passes near the folded-node and the stable manifold $W^s(eq)$ of the equilibrium that increasingly pulls the orbit closer to that point. On the orbit of Point IV corresponding to $G_K = 0.035$, there is a saddle-focus equilibria of type (1, 2) with eigenvalues $\lambda_1 = -0.00436926$, $\lambda_2 = 0.00861114 + 0.035771 i$, and $\lambda_3 = 0.00861114 - 0.035771 i$. It can be observed in Figure 4

how such an orbit oscillates due to the canard orbits around the stable manifold of the equilibria $W^s(eq)$ until reaching a point close to the equilibrium point (Figure 4a,b). Consequently, the orbit remains more time active as the orbit approaches the equilibrium and it subsequently spirals outward (last spikes of the orbit). This can be appreciated in the two-dimensional local unstable manifold $W_{loc}^u(eq)$ of the equilibrium shown in Figure 4. In a previous study, this phenomenon was observed as a first approximation using the unstable linear subspace $E^u(eq)$ of the equilibrium [15]. In addition, similar observations hold for the last investigated point, i.e., Point V corresponding to $G_K = 0.03345$ (Figure 4d,e). As before, the first oscillations are due to the canard phenomena and the fact of passing near the folded-node singularity, while subsequent oscillations can be explained by the orbit approaching the saddle-focus equilibria of type (1,2) with eigenvalues $\lambda_1 = -0.0040745$, $\lambda_2 = 0.00137656 + 0.0399119i$ and $\lambda_3 = 0.00137656 - 0.0399119i$. It can be noted that in this case the ratio $|\lambda_1|/\text{Re}\lambda_{2,3} = 2.95991$, which makes the attracting dynamics strong and prolongs the approach towards the equilibrium point. When the orbit is already close enough to the equilibrium point, the unstable manifold takes control of its escape dynamics and the orbit follows this manifold. This is illustrated in the inset of Figure 4d, which shows how the orbit spirals the two-dimensional local unstable manifold $W_{loc}^u(eq)$. The small variations in the plateau phase of the AP closely resemble the oscillations present in pseudo-plateau bursting, whose dynamics has also been studied for 1-fast, 2-slow variables systems [21].

As the parameter G_K takes decreasing values, the orbit approaches more and more the saddle-focus equilibria. As shown above, more and more small spikes are then generated. The fact of setting a threshold on voltage when counting the number of spikes may render the algorithm unable to detect a small spike, as shown in Figure 6, which can be additionally influenced by the enlargement of the orbit approaching the saddle-focus equilibria. This may generate transitions between areas of different colors, which would seem to indicate a change in the number of spikes by one or more spikes even if this is not actually the case.

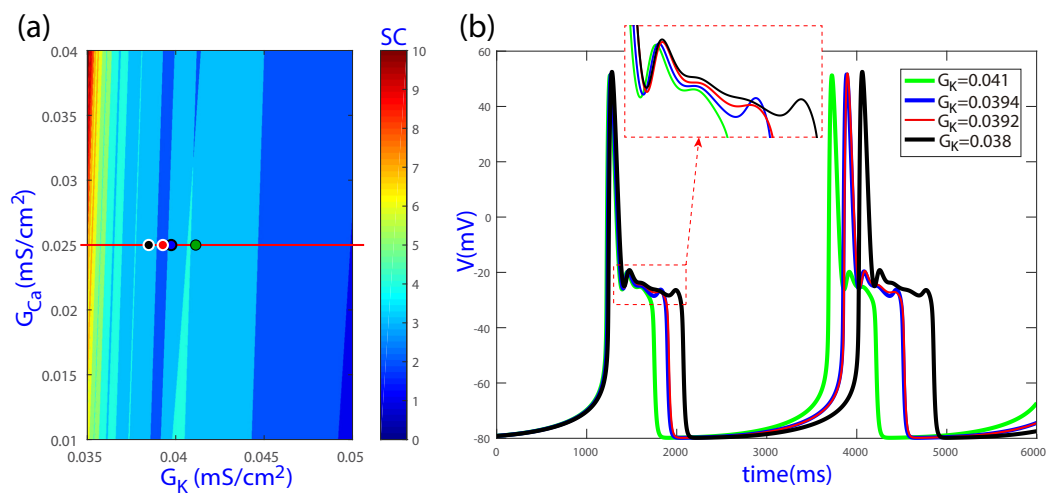


Figure 6. (a) Magnification of the spike-adding plot of Figure 2 using a different color scale; and (b) some selected beats illustrating how the number of counted spikes can decrease due to the threshold on voltage set in the spike-counting algorithm, even if the number of oscillations is not decreased.

3.3. Isolats of Periodic Orbits

To investigate bifurcations on the parametric line $G_{Ca} = 0.025$, numerical analysis with continuation techniques was performed using the software AUTO [30,31]. The main focus of this study was to explore the presence of isolats of periodic orbits, that is, simple closed curves of families of periodic orbits. These isolats have been described for other models, such as the Koper model of

chemical reactions with mixed-mode oscillations (see Figure 19 in [19]). For the reduced LR91 model used in this study, some bifurcations are identified in [12] but no isolas are shown.

Figure 7 shows the bifurcation diagram obtained with the software AUTO using G_k as the continuation parameter on the line $G_{Ca} = 0.025$. The bifurcation diagram shows the maximum (the highest peak of the orbit) and minimum (resting membrane potential) values of the transmembrane voltage variable V for different periodic orbits corresponding to a range of given values of the continuation parameter. The continuation of the equilibria (black thick line) and limit cycles (color lines) are shown too. Continuous lines are stable invariants while discontinuous lines are unstable ones. In the figure, presenting a large parametric interval $G_k \in [0.02, 0.46]$, two Poincaré–Andronov–Hopf bifurcations can be observed, a subcritical one on the left part and a supercritical one on the right part. As G_k decreases, the stable periodic orbits generated at the supercritical Hopf bifurcation move to the left towards the subinterval for G_k with associated EADs.

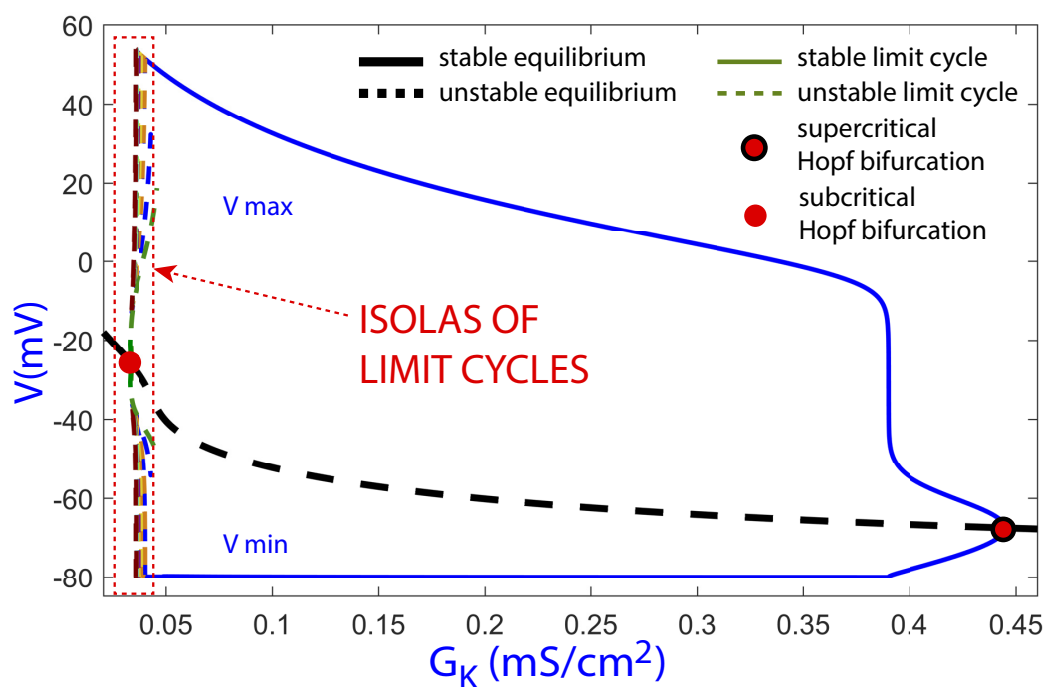


Figure 7. Bifurcation diagram using G_k as the continuation parameter for a large interval of G_k values to show the Hopf bifurcations. Black thick lines correspond to equilibria, while color lines correspond to limit cycles. Continuous lines represent stable invariants, while discontinuous lines represent unstable invariants.

In the subinterval with several EADs, shown in Figure 8b, families of periodic orbits can be observed, which are plotted in different colors. These families are organized in isolas, that is, closed family curves of periodic orbits with different numbers of oscillations in the form of EADs. The different isolas have a section formed by stable limit cycles placed mainly on the top (and bottom, as it is the maxima and minima) of the isola. These stable periodic orbits lose their stability at fold bifurcations (or saddle-node bifurcations of limit cycles), as indicated in [12]. However, the stable line is in fact a discontinuous one, as it is formed by the top subintervals of stable periodic orbits of the different isolas, and not a continuous line with several bifurcations. The unstable parts of the isolas shown in the figure evolve with similar maximum and minimum values, which explains why they are so closely represented in Figure 8b, while they are formed by different limit cycles, as can be appreciated in Figure 8a. Besides, there are fold and period-doubling bifurcations on the bifurcated periodic orbits from the subcritical Hopf bifurcation.

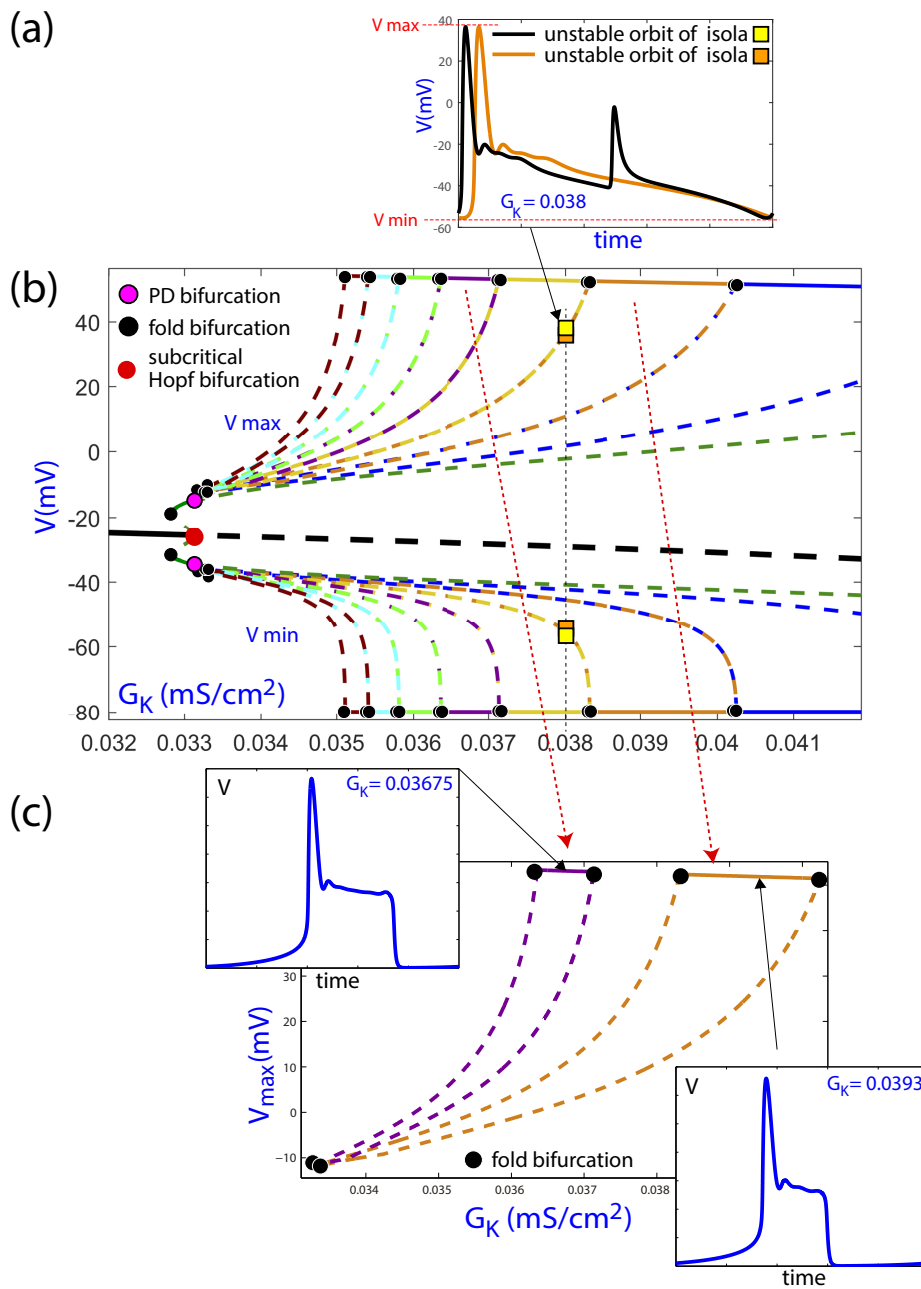


Figure 8. (b) Magnification of the bifurcation diagram of Figure 7 using G_k as the continuation parameter on the subinterval with isolas. (a) Two orbits on two consecutive isolas (orange and yellow ones) for the same value of the parameter $G_k = 0.038$. (c) A zoom of the V_{max} component of two isolas. Black thick lines correspond to equilibria, while color lines correspond to limit cycles. Continuous lines represent stable invariants, while discontinuous lines represent unstable invariants. Several bifurcations are pointed (fold and period-doubling bifurcations of limit cycles).

Two of the isolas in Figure 8b are represented separately in Figure 8c only for the maximum value of voltage. Now, the fold bifurcations are clearly seen as the limit of the stable periodic orbits. The temporal evolution of voltage along the heartbeat is represented for the two parametric values marked with a black dot in each of the two isolas, each showing a different number of EADs. The stable part of the isolas is located on the flat top segment, which corresponds to the observed limit cycles. These results confirm that the reduced LR91 model exhibits isolas of periodic orbits, as reported for other fast–slow models in the literature [19]. This can be the basis for further studies into the organization of EAD patterns in the parameter space and the involved bifurcations.

4. Discussion, Conclusions, and Future Work

In this study, we investigated the dynamical mechanisms for EAD generation in the reduced LR91 mammalian ventricular cell model. As in recent studies [12,13], we considered a fast–slow decomposition of the system with 1-fast and 2-slow variables rather than 2-fast and 1-slow variables [8], and we analyzed the influence of maximal canard orbits. We used sweeping techniques (the spike-counting method) as well as continuation techniques. The former allowed us to identify different parametric regions with EADs (see a summary in Figure 9), whereas the latter was used to generate bifurcation diagrams for the mentioned parametric regions. We showed the existence of isolas of periodic orbits and we performed a preliminary classification of the fast–slow decomposition in various cases according to the involved dynamical phenomena.

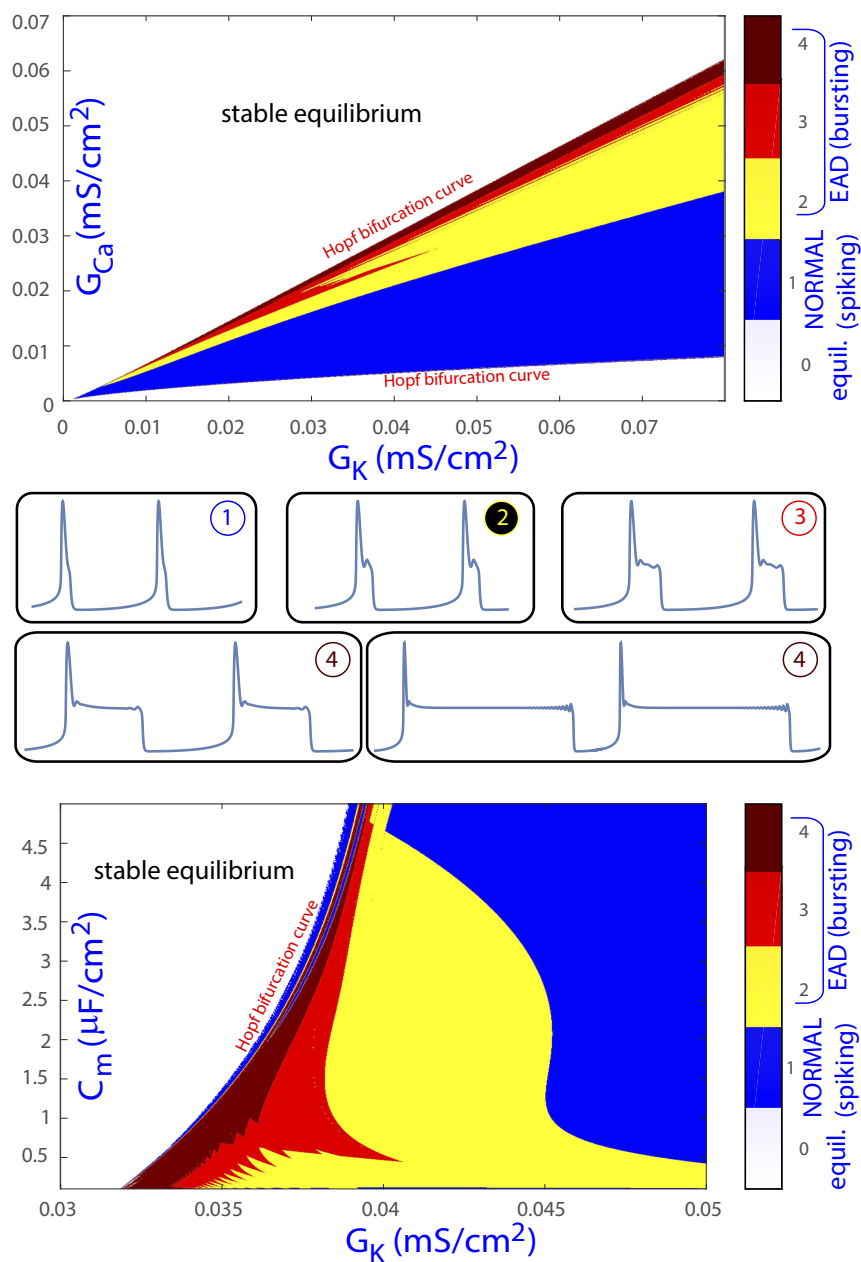


Figure 9. Classification of the different dynamical behaviors of the orbits on the parametric planes (G_K, G_{Ca}) and (G_K, C_m) .

As a summary, based on the dynamics on the critical manifold and near the unstable equilibrium point, several regions in the (G_K, G_{Ca}) and (G_K, C_m) parametric planes associated with different dynamical behaviors can be identified. Specifically, regarding EADs, the first region corresponds to cases where the orbit has an EAD due to a maximal canard orbit. As more canards take part in the process, more EADs are generated. When the orbit approaches the equilibrium, this gives rise to additional oscillations. When the equilibrium point is of saddle-focus type, the orbit gets closer and closer to the equilibrium and spirals following its unstable manifold. These mechanisms create EADs corresponding to small oscillations of voltage during the course of the AP, commonly in association with AP prolongation. Figure 9 recapitulates our classification of the dynamical behaviors of the orbits in the (G_K, G_{Ca}) and (G_K, C_m) parametric planes: **white** is associated with no activity, that is, the equilibria is an attractor; **blue** corresponds to normal beats; **yellow** denotes EADs created by the maximal canards; **red** corresponds to the attracting behavior of the equilibria on the stable manifold direction with AP prolongation; and **maroon** is for very elongated APs remaining close to the saddle-focus equilibria. Color regions, associated with active cell status, are delimited by two Hopf bifurcations that make the equilibrium point unstable in the middle parametric interval. As can be noted from the two panels in Figure 9, results for both (G_K, G_{Ca}) and (G_K, C_m) parametric planes render bands that allow making a parametric description of the areas in the parameter space that lead to EAD generation. This sets the basis to investigate actions able to move the system, i.e., the mammalian ventricular cell, to parameter regions far from areas prone to arrhythmogenic EADs. Part of our future research in this line focuses on studying the effects of including an external stimulus in this model and the dynamics of other, more complex and realistic cardiomyocyte models. This would allow more meaningful interpretations regarding the parameters involved in the occurrence of EAD.

Author Contributions: Conceptualization, R.B.; software, R.B. and L.P.; formal analysis, R.B., M.A.M., L.P., and E.P.; writing—original draft preparation, R.B. and M.A.M.; and writing—review and editing, R.B., M.A.M., L.P., and E.P. All authors have read and agreed to the published version of the manuscript.

Funding: R.B. and M.A.M. have been supported by the European Social Fund (EU), Aragón Government (Grant LMP124-18 and Group E24-17R), and the University of Zaragoza-CUD (grant UZCUD2019-CIE-04). R.B. has been supported by the Spanish Ministry of Economy and Competitiveness (grant PGC2018-096026-B-I00). M.A.M. has been supported by the Spanish Ministry of Economy and Competitiveness (grant DPI2016-75458-R). L.P. has been supported by the Spanish Ministry of Economy and Competitiveness (grant MTM2017-87697-P) and by Programa de Ayudas “Severo Ochoa” of Principado de Asturias (Grant PA-18-PF-BP17-072). E.P. has been supported by the European Research Council (Grant ERC-638284), Spanish Ministry of Economy and Competitiveness (grant DPI2016-75458-R), European Social Fund (EU), and Aragón Government (grant LMP124-18 and Group T39-17).

Conflicts of Interest: The authors declare no conflict of interest.

Abbreviations

The following abbreviations are used in this manuscript:

EADs	Early AfterDepolarizations
LR91	Luo–Rudy model (1991)
AP	Action Potential

References

1. January, C.T.; Riddle, J.M. Early afterdepolarizations: Mechanism of induction and block. A role for L-type Ca^{2+} current. *Circ. Res.* **1989**, *64*, 977–990. [[CrossRef](#)] [[PubMed](#)]
2. Song, Y.; Shryock, J.; Belardinelli, L. An increase of late sodium current induces delayed afterdepolarizations and sustained triggered activity in atrial myocytes. *Am. J. Physiol. Heart and Circ. Physiol.* **2008**, *294*, 2031–2039. [[CrossRef](#)] [[PubMed](#)]
3. Xie, L.; Chen, F.; Karagueuzian, H.; Weiss, J. Oxidative-stress-induced afterdepolarizations and calmodulin kinase II signaling. *Circ. Res.* **2008**, *104*, 79–86. [[CrossRef](#)] [[PubMed](#)]

4. Antzelevitch, C.; Sicouri, S. Clinical Relevance of Cardiac Arrhythmias Generated by Afterdepolarizations. Role of M Cells in the Generation of U Waves, Triggered Activity and Torsade De Pointes. *J. Am. Coll. Cardiol.* **1994**, *23*, 259–277. [[CrossRef](#)]
5. Huffaker, R.B.; Weiss, J.N.; Kogan, B. Effects of early afterdepolarizations on reentry in cardiac tissue: A simulation study. *Am. J. Physiol. Heart Circ. Physiol.* **2006**, *292*, 3089–3102. [[CrossRef](#)] [[PubMed](#)]
6. Sato, D.; Xie, L.H.; Sovari, A.A.; Tran, D.X.; Morita, N.; Xie, F.; Karagueuzian, H.; Garfinkel, A.; Weiss, J.N.; Qu, Z. Synchronization of chaotic early afterdepolarizations in the genesis of cardiac arrhythmias. *Proc. Natl. Acad. Sci. USA* **2009**, *106*, 2983–2988. [[CrossRef](#)] [[PubMed](#)]
7. Luo, C.; Rudy, Y. A model of the ventricular cardiac action potential. Depolarization, repolarization, and their interaction. *Circ. Res.* **1991**, *68*, 1501–1526. [[CrossRef](#)] [[PubMed](#)]
8. Tran, D.X.; Sato, D.; Yochelis, A.; Weiss, J.N.; Garfinkel, A.; Qu, Z. Bifurcation and Chaos in a Model of Cardiac Early Afterdepolarizations. *Phys. Rev. Lett.* **2009**, *102*, 258103. [[CrossRef](#)]
9. Rinzel, J. A Formal Classification of Bursting Mechanisms in Excitable Systems. In *Mathematical Topics in Population Biology, Morphogenesis and Neurosciences, Proceedings of the International Symposium, Kyoto, Japan, 10–15 November 1985*; Teramoto, E.; Yumaguti, M., Eds.; Springer: Berlin/Heidelberg, Germany, 1987; pp. 267–281.
10. Ermentrout, G.B.; Terman, D.H. *Mathematical Foundations of Neuroscience*; Springer: New York, NY, USA, 2010; Volume 35.
11. Barrio, R.; Martínez, M.A.; Serrano, S.; Shilnikov, A. Macro- and micro-chaotic structures in the Hindmarsh–Rose model of bursting neurons. *Chaos* **2014**, *24*, 023128. [[CrossRef](#)]
12. Kügler, P.; Erhardt, A.H.; Bulelzi, M.A. Early afterdepolarizations in cardiac action potentials as mixed mode oscillations due to a folded node singularity. *PLoS ONE* **2018**, *13*, e0209498. [[CrossRef](#)]
13. Vo, T.; Bertram, R. Why pacing frequency affects the production of early afterdepolarizations in cardiomyocytes: An explanation revealed by slow-fast analysis of a minimal model. *Phys. Rev. E* **2019**, *99*, 052205. [[CrossRef](#)] [[PubMed](#)]
14. Hodgkin, A.L.; Huxley, A.F. A quantitative description of membrane current and its application to conduction and excitation in nerve. *J. Physiol.* **1952**, *117*, 500–544. [[CrossRef](#)] [[PubMed](#)]
15. Kügler, P. Early Afterdepolarizations with Growing Amplitudes via Delayed Subcritical Hopf Bifurcations and Unstable Manifolds of Saddle Foci in Cardiac Action Potential Dynamics. *PLoS ONE* **2016**, *11*, e0151178. [[CrossRef](#)]
16. Barrio, R.; Blesa, F.; Lara, M. VSVO formulation of the Taylor method for the numerical solution of ODEs. *Comput. Math. Appl.* **2005**, *50*, 93–111. [[CrossRef](#)]
17. Abad, A.; Barrio, R.; Blesa, F.; Rodriguez, M. TIDES: A Taylor series integrator for differential equations. *ACM Trans. Math. Softw. (TOMS)* **2012**, *39*, 5. [[CrossRef](#)]
18. Barrio, R.; Shilnikov, A. Parameter-sweeping techniques for temporal dynamics of neuronal systems: case study of Hindmarsh-Rose model. *J. Math. Neurosci.* **2011**, *1*, 6. [[CrossRef](#)] [[PubMed](#)]
19. Desroches, M.; Guckenheimer, J.; Krauskopf, B.; Kuehn, C.; Osinga, H.M.; Wechselberger, M. Mixed-Mode Oscillations with Multiple Time Scales. *SIAM Rev.* **2012**, *54*, 211–288. [[CrossRef](#)]
20. Vo, T.; Bertram, R.; Wechselberger, M. Multiple Geometric Viewpoints of Mixed Mode Dynamics Associated with Pseudo-plateau Bursting. *SIAM J. Appl. Dyn. Syst.* **2013**, *12*, 789–830. [[CrossRef](#)]
21. Vo, T.; Bertram, R.; Wechselberger, M. Bifurcations of canard-induced mixed mode oscillations in a pituitary Lactotroph model. *Discret. Contin. Dyn. Syst. A* **2012**, *32*, 2879. [[CrossRef](#)]
22. Fenichel, N. Geometric singular perturbation theory for ordinary differential equations. *J. Differ. Equ.* **1979**, *31*, 53–98. [[CrossRef](#)]
23. Szmolyan, P.; Wechselberger, M. Canards in \mathbb{R}^3 . *J. Differ. Equ.* **2001**, *177*, 419–453. [[CrossRef](#)]
24. Desroches, M.; Kaper, T.J.; Krupa, M. Mixed-mode bursting oscillations: Dynamics created by a slow passage through spike-adding canard explosion in a square-wave burster. *Chaos* **2013**, *23*, 046106. [[CrossRef](#)]
25. Barrio, R.; Ibáñez, S.; Pérez, L.; Serrano, S. Spike-adding structure in fold/hom bursters. *Commun. Nonlinear Sci. Numer. Simul.* **2020**, *83*, 105100. [[CrossRef](#)]
26. Wechselberger, M. À propos de canards (Apropos canards). *Trans. Amer. Math. Soc.* **2012**, *364*, 3289–3309. [[CrossRef](#)]
27. Guckenheimer, J. Singular Hopf Bifurcation in Systems with Two Slow Variables. *SIAM J. Appl. Dyn. Syst.* **2008**, *7*, 1355–1377. [[CrossRef](#)]

28. Guckenheimer, J.; Meerkamp, P. Unfoldings of Singular Hopf Bifurcation. *SIAM J. Appl. Dyn. Syst.* **2012**, *11*, 1325–1359. [[CrossRef](#)]
29. Mujica, J.; Krauskopf, B.; Osinga, H.M. Tangencies Between Global Invariant Manifolds and Slow Manifolds Near a Singular Hopf Bifurcation. *SIAM J. Appl. Dyn. Syst.* **2018**, *17*, 1395–1431. [[CrossRef](#)]
30. Doedel, E.J. AUTO: A program for the automatic bifurcation analysis of autonomous systems. *Congr. Numer.* **1981**, *30*, 265–284.
31. Doedel, E.J.; Paffenroth, R.; Champneys, A.R.; Fairgrieve, T.F.; Kuznetsov, Y.A.; Oldeman, B.E.; Sandstede, B.; Wang, X.J. AUTO2000. Available online: <http://cmvl.cs.concordia.ca/auto> (accessed on 1 December 2019).



© 2020 by the authors. Licensee MDPI, Basel, Switzerland. This article is an open access article distributed under the terms and conditions of the Creative Commons Attribution (CC BY) license (<http://creativecommons.org/licenses/by/4.0/>).

4.6 Poster

The poster entitled "Homoclinic organization in fold/hom bursters: the Hindmarsh-Rose model" was presented by the PhD candidate at the 5th International Conference on Mathematical NeuroScience (ICMNS) held in Copenhagen in June of 2019. It summarizes the main results presented in Paper II regarding the homoclinic structure of the Hindmarsh-Rose model in the three-dimensional space (b, I, ε) .

Homoclinic organization in fold/hom bursters: the Hindmarsh-Rose model.

L. Pérez^a (lperezp@uniovi.es), R. Barrio^b (rbarrio@unizar.es), S. Ibáñez^a (mesa@uniovi.es)

^a Department of Mathematics, University of Oviedo

^bIUMA and Department of Applied Mathematics, University of Zaragoza

1. The Hindmarsh-Rose neuron model

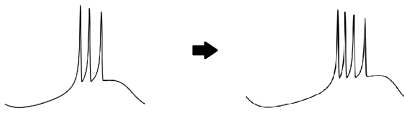
The Hindmarsh-Rose (HR) model is a classic model for the behaviour of individual neurons. It mimics the main activities found in biological neurons, namely, quiescence, spiking and bursting. The nice balance between simplicity and realism makes it a good choice to study the details of the dynamics of bursting, which has a prominent role in neuronal communication.

$$\begin{cases} \dot{x} = y - ax^3 + bx^2 + I - z & \rightarrow x \text{ represents the membrane potential} \\ \dot{y} = c - dx^2 - y & \rightarrow y \text{ represents the fast ionic currents} \\ \dot{z} = \varepsilon(s(x - x_{rest}) - z) & \rightarrow z \text{ represents the slow ionic currents} \end{cases}$$

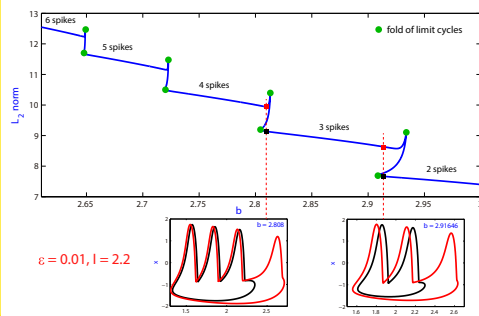
It is clear that the HR model is a fast-slow system (due to the presence of the parameter ε , usually set positive and very close to 0). Thus, for small values of ε , the structure of the manifolds of equilibria and limit cycles of the fast subsystem determines a great part of the dynamics in the whole system.

2. Spike-adding

When changing a parameter, the system can go from n spikes per burst to $n + 1$. This process is known as *spike-adding*.

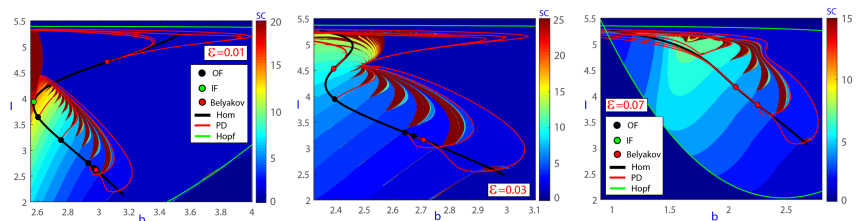


The spike-adding process of periodic orbits is known to be related to the hysteresis phenomena shown in the figure below, where a periodic orbit is continued in one parameter. The fold bifurcations are key features of the evolution of periodic orbits to gain spikes.



3. Homoclinic structure

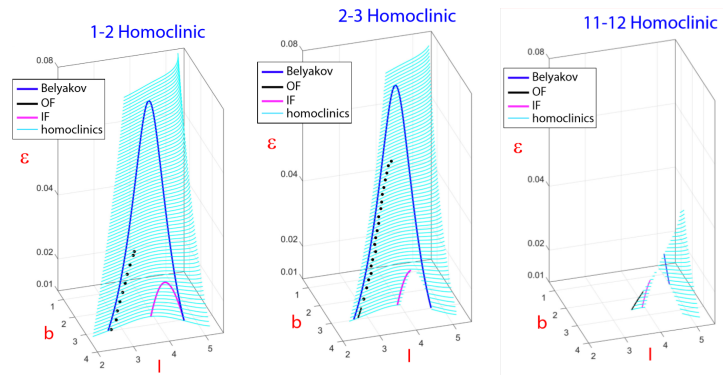
For each n , the spike-adding process from n to $n + 1$ spikes is associated with an homoclinic bifurcation curve in (b, I) , since the relevant bifurcation curves in the spike-adding process (namely, folds of periodic orbits and period-doublings) are born from the codimension-two points lying in the corresponding homoclinic curve.



Fixing all parameters up to b and I , numerical techniques allow us to calculate the typical number of spikes in each point of the parametric plane (b, I) , obtaining a *map* of the system. Stripes associated to different number of spikes exhibit a complicated structure, which is closely related to the bifurcation curves of the system, specially homoclinic bifurcation curves. When considering different values of ε , this *map* is deformed. One of our goals is to study the evolution of the homoclinic structure when ε increases.

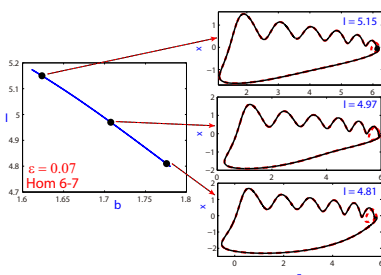
4. Some 3D insight

We have performed a numerical study of the homoclinic structure in the parameter space (b, I, ε) in order to visualize the evolution of the bifurcation diagram when ε increases. Some remarkable features are the following: the shape of the homoclinic curves in (b, I) varies when ε takes different values; the codimension-two points disappear via folding processes when ε increases; except in the case of $1 \rightarrow 2$ spikes, there is a *hole* in the bottom part of the homoclinic surface: for intermediate values of ε , two homoclinic bifurcation curves approach each other until they collide and form a bigger homoclinic bifurcation curve; lastly, for bigger n , the corresponding homoclinic surface ends for smaller values of ε . The simplification of the *spikes map* is associated to a simplification of the homoclinic structure of the system.



5. Isola structure

The homoclinic bifurcation curves have an isola structure: their extreme points are actually turning points where the curve has a very sharp fold. In these folds a spike-adding process of homoclinic orbits occurs.



6. References

- [1] D. Linaro, A. Champneys, M. Desroches, and M. Storace. Codimension-two homoclinic bifurcations underlying spike adding in the Hindmarsh-Rose burster. *SIAM J. Appl. Dyn. Syst.*, 11(3):939–962, 2012.
- [2] R. Barrio, S. Ibáñez, and L. Pérez. Hindmarsh-Rose model: close and far to the singular limit. *Phys. Lett. A*, 381(6):597–603, 2017.
- [3] R. Barrio, S. Ibáñez, and L. Pérez. Homoclinic organization in fold/hom bursters: the Hindmarsh-Rose model. *Preprint*.
- [4] R. Barrio, S. Ibáñez, L. Pérez, and S. Serrano. Spike-adding structure in fold/hom bursters. *Preprint*.

4.7 Publications' report

- R. Barrio, S. Ibáñez and L. Pérez, “Hindmarsh-Rose model: Close and far to the singular limit”, *Physics Letters A* 2017; 381(6), 597-603.
Indexed in JCR. Impact factor (2017): 1'863. Position 35/78 (Q2) in Multidisciplinary Physics.
- R. Barrio, S. Ibáñez and L. Pérez, “Homoclinic organization in the Hindmarsh–Rose model: A three parameter study”, *Chaos* 2020; 30(5): 053132.
Featured article. Indexed in JCR. Impact factor (2019): 2.832. Position 16/261 (Q1) in Applied Mathematics.
- R. Barrio, S. Ibáñez, L. Pérez and S. Serrano, “Spike-adding structure in fold/hom bursters”, *Communications in Nonlinear Science and Numerical Simulation* 2020; 83: 105100.
Indexed in JCR. Impact factor (2019): 4'115. Position 3/261 (Q1) in Applied Mathematics.
- R. Barrio, M.A. Martínez, L. Pérez and E. Pueyo, “Bifurcations and Slow-fast Analysis in a Cardiac Cell Model for Investigation of Early Afterdepolarizations”, *Mathematics* 2020; 8(6):880.
Indexed in JCR. Impact factor (2019): 1.747. Position 28/325 (Q1) in Mathematics.
- R. Barrio, S. Ibáñez, L. Pérez and S. Serrano, “Classification of fold/hom and fold/Hopf spike-adding phenomena”. Submitted.

Chapter 5

Conclusions and future research

The present thesis delves into the dynamics of the Hindmarsh-Rose model. We have adopted two different perspectives. The first one consists in studying the structure of the bifurcation diagram in the (b, I, ε) parameter space, being ε the small parameter responsible of the fast-slow dynamics. Thus, we study what happens with the bifurcation diagram, specially with the homoclinic structure, when the system goes far from the singular limit ($\varepsilon = 0$) and the dynamics is not longer of fast-slow type. We have found relevant phenomena, as the disappearance of codimension-two homoclinic bifurcation points due to different processes and the correlation between the existence of bursting of n spikes for fixed values of ε and the existence of the corresponding homoclinic surface for that value of ε . The results are developed in Paper I and Paper II.

The second perspective consists of deepening into the relationship between the homoclinic bifurcation structure and the spike-adding processes for biophysically plausible (small) values of ε . We propose a global scheme that connects the different views of the spike-adding mechanisms and explains the role of the homoclinic bifurcations. A preliminary study of the Sherman model of pancreatic β -cells is provided, suggesting that our theoretical scheme may be general for fold/hom bursting models. We obtain a map in the (b, I) parameter plane in which the different spike-adding processes are located. All these mechanisms are illustrated in detail and explanations about the transitions states are also provided. Papers III and IV deal with all these results.

Lastly, we have studied the dynamics of a three-dimensional reduction of the Luo-Rudy model of cardiac cells. The Luo-Rudy model exhibits healthy beats as well as pathological beats (EADs) for appropriate values of the parameters. Neurological and cardiac phenomena are obviously different, but their dynamics have some common elements. So, techniques as the spike-counting method can also be employed in the analysis of cardiac models. Besides, every ODE system depending on parameters can be studied using bifurcation theory. We show how a 1 fast, 2 slow variable decomposition can be used to analyse the dynamics of the model. The spike-counting method is used to construct

maps in different parametric planes in which healthy cardiac beats and pathological cardiac beats are located. We choose a one-dimensional parametric cut and show how the pathological regions are organised by isolas of periodic orbits. Our results are presented in Paper V.

The results obtained throughout this thesis and collected in the contribution papers raise challenging questions whose investigation attracts our greatest interest. Our analysis reveals that one of the mechanisms of disappearance of codimension-two points in the Hindmarsh-Rose model as ε grows is a folding process. This is the case of the inclination flip curve lying in the homoclinic surface $hom(1, 2)$. There appear connections between bifurcation curves arising from such codimension-two bifurcation points as these organizing centers collapse. If fixed values of ε are considered, we have that in the corresponding (b, I) diagrams different pairs of period-doubling bifurcation curves joint each other forming single curves. This is a relevant change in the bifurcation diagram of the model. We aim to investigate the dynamics in systems exhibiting similar phenomena, that is, foldings of codimension n bifurcation curves. There are authors which use to say codimension $n+1$ to refer to this foldings in the bifurcation diagram

Another natural question is whether the structure we have found in the Hindmarsh-Rose equations appears in other models showing fold/hom or similar bursting mechanisms.. In Paper III we performed a preliminary study of the Sherman model that shows that the dynamics display elements similar to those that appear in the Hindmarsh-Rose model. One of our future goals is to broaden the collection of models in order to show that the theoretical scheme not only works for a particular system, but it has a universal character. To support this claim, we need to consider fast-slow systems coming from different fields, not only neuron models.

We are also interested in analysing the coupling of Hindmarsh-Rose systems, a first step towards real world applications. This would allow to study the phenomenon of synchronization, which is believed to have a relevant role in neural processing. The initial motivation of this PhD candidate was to study neuron dynamics to discover the role that mathematics can play in addressing illnesses such as Parkinson disease, which has been related to excess of synchronization in certain areas of the brain. Thus, the study of coupled neurons or networks of neurons is a challenge of great interest for the candidate.

Bibliography

- [1] A. Abad, R. Barrio, F. Blesa, and M. Rodríguez. Tides. <http://gme.unizar.es/software/tides>, 1993.
- [2] A. Abad, R. Barrio, F. Blesa, and M. Rodríguez. TIDES: a Taylor Integrator for Differential EquationS. *ACM Transactions on Mathematical Software*, 39:5:1–5:28, 2012.
- [3] R. Barrio, S. Ibáñez, Pérez, and S. Serrano. Spike-adding structure in fold/hom bursters. *Communications in Nonlinear Science and Numerical Simulations*, 83:105100, 2020.
- [4] R. Barrio, S. Ibáñez, and L. Pérez. Hindmarsh-Rose model: close and far to the singular limit. *Phys. Lett. A*, 381(6):597–603, 2017.
- [5] R. Barrio, S. Ibáñez, and L. Pérez. Homoclinic organization in the hindmarsh-Rose model: A three parameter study. *Chaos*, 30(5):053132, 2020.
- [6] R. Barrio, M. A. Martínez, S. Serrano, and A. Shilnikov. Macro- and micro-chaotic structures in the Hindmarsh–Rose model of bursting neurons. *Chaos*, 24(2):023128, 2014.
- [7] R. Barrio, M.A. Martínez, Pérez, and E. Pueyo. Bifurcations and slow-fast analysis in a cardiac cell model for investigation of early afterdepolarizations. *Mathematics*, 8(6):880, 2020.
- [8] R. Barrio and A. Shilnikov. Parameter-sweeping techniques for temporal dynamics of neuronal systems: case study of Hindmarsh-Rose model. *Journal of Mathematical Neuroscience*, 1:6:1–6:22, 2011.
- [9] E. Benoît, J. F. Callot, F. Diener, and M. Diener. Chasse au canard. *Collectanea Mathematica*, 32:37–76, 1981.
- [10] H. A. Braun, M. T. Huber, M. Dewald, K. Schäfer, and K. Voigt. Computer simulations of neuronal signal transduction: The role of nonlinear dynamics and noise. *International Journal of Bifurcation and Chaos*, 8(5):881—889, 1998.

- [11] TR. Chay and J. Keizer. Minimal model for membrane oscillations in the pancreatic β -cell. *Biophys J.*, 42(2):181–190, 1983.
- [12] Mathieu Desroches, John Guckenheimer, Bernd Krauskopf, Christian Kuehn, Hinke M. Osinga, and Martin Wechselberger. Mixed-mode oscillations with multiple time scales. *SIAM Rev.*, 54(2):211–288, 2012.
- [13] F. Drubi, S. Ibáñez, and P. Pilarczyk. Nilpotent singularities and chaos: Tritrophic food chains. *Chaos, Solitons and Fractals*, 142(6):110406, 2020.
- [14] F. Drubi, S. Ibáñez, and J.A. Rodríguez. Coupling leads to chaos. *J. Differ.Equ.*, 239(2):371–385, 2007.
- [15] N. Fenichel. Geometric singular perturbation theory for ordinary differential equations. *J. Differential Equations*, 31(1):53–98, 1979.
- [16] C. Finke, J.A. Freund, E. J. Rosa, H.A. Braun, and U. Feudel. Computer simulations of neuronal signal transduction: The role of nonlinear dynamics and noise. *Chaos*, 20(4):045107, 2010.
- [17] R. FitzHugh. Impulses and physiological states in theoretical models of nerve membrane. *Biophysical J.*, 1:445–466, 1961.
- [18] J. M. González-Miranda. Block structured dynamics and neuronal coding. *Phys. Rev. E*, 72:051922, 2005.
- [19] J. M. Gonzalez-Miranda. Complex bifurcation structures in the Hindmarsh-Rose neuron model. *Int. J. Bifurcation Chaos*, 17:3071, 2007.
- [20] B. Hille. *Ion Channels of Excitable Membranes*. MIT Press, Sunderland, Mass, Sinauer, 2007.
- [21] J. L. Hindmarsh and R. M. Rose. A model of the nerve impulse using two first-order differential equations. *Nature.*, 296:162–164, 1982.
- [22] J. L. Hindmarsh and R. M. Rose. A model of the nerve impulse using three coupled first-order differential equations. *Proc. Roy. Soc. Lond.*, B221:87–102, 1984.
- [23] A. L. Hodgkin and A. F. Huxley. A quantitative description of membrane current and its application to conduction and excitation in nerve. *J. Physiol.*, 117:500–544, 1952.
- [24] A. J. Homburg and B. Krauskopf. Resonant homoclinic flip bifurcations. *J. Dynam. Differential Equations*, 12(4):807–850, 2000.

- [25] A. J. Homburg and B. Sandstede. Homoclinic and heteroclinic bifurcations in vector fields. *Handbook of Dynamical Systems*, 3:379–524, 2010.
- [26] Giacomo Innocenti, Alice Morelli, Roberto Genesio, and Alessandro Torcini. Dynamical phases of the Hindmarsh-Rose neuronal model: Studies of the transition from bursting to spiking chaos. *Chaos: An Interdisciplinary Journal of Nonlinear Science*, 17(4):043128, 2007.
- [27] E.M. Izhikevich. *Dynamical systems in neuroscience. The geometry of excitability and bursting*. MIT Press, Cambridge, Mass, 2007.
- [28] Eugene M Izhikevich. Neural excitability, spiking and bursting. *International Journal of Bifurcation and Chaos*, 10(6):1171–1266, 2000.
- [29] Aarushi Khanna. Teach me physiology: Action potential. <https://teachmephysiology.com/nervous-system/synapses/action-potential/>.
- [30] T.A. Kinard, G. de Vries, A. Sherman, and L.S. Satin. Modulation of the bursting properties of single mouse pancreatic b-cells by artificial conductances. *Biophysical Journal*, 76(3):1423–1435, 1999.
- [31] Y.A. Kuznetsov. *Elements of applied bifurcation theory*, volume 112 of *Applied Mathematical Sciences*. Springer-Verlag, New York, third edition, 2004.
- [32] Yu. A. Kuznetsov, O. De Feo, and S. Rinaldi. Belyakov homoclinic bifurcations in a tritrophic food chain model. *SIAM J. Appl. Math.*, 62(2):462–487, 2001.
- [33] D. Linaro, A. Champneys, M. Desroches, and M. Storace. Codimension-two homoclinic bifurcations underlying spike adding in the Hindmarsh-Rose burster. *SIAM J. Appl. Dyn. Syst.*, 11(3):939–962, 2012.
- [34] L. Mora and M. Viana. Abundance of strange attractors. *ActaMath.*, 171:1–71, 1993.
- [35] J. P. Domínguez Morales. *Neuromorphic audio processing through real-time embedded spiking neural networks*. PhD thesis, Universidad de Sevilla, July 2018.
- [36] Erik Mosekilde, Brian Lading, Sergiy Yanchuk, and Yuri Maistrenko. Bifurcation structure of a model of bursting pancreatic cells. *Biosystems*, 63(1):3–13, 2001.
- [37] B.E. Oldeman, B. Krauskopf, and A.R. Champneys. Death of period-doublings: locating the homoclinic-doubling cascade. *Physica D: Nonlinear Phenomena*, 146(1-4):100–120, 2000.
- [38] Nagumo J. Arimoto S. and Yoshizawa S. An active pulse transmission line simulating nerve axon. *Proceeding IRE*, 50:2061–2070, 1962.

- [39] A. Sherman and J. Rinzel. Model for synchronization of pancreatic β -cells by gap junction coupling. *Biophysical Journal*, 59(3):547 – 559, 1991.
- [40] A. Sherman, J. Rinzel, and J. Keizer. Emergence of organized bursting in clusters of pancreatic β -cells by channel sharing. *Biophysical Journal*, 54:411–425, September 1988.
- [41] A. Shilnikov and M. Kolomiets. Methods of the qualitative theory for the Hindmarsh-Rose model: A case study. a tutorial. *International Journal of Bifurcation and Chaos*, 18(8):2141–2168, 2008.
- [42] L. P. Shilnikov, A. L. Shilnikov, D. Turaev, and L. O. Chua. *Methods of qualitative theory in nonlinear dynamics. Part II*. World Scientific Publishing Co. Inc., 2001.
- [43] M. Storace, D. Linaro, and E. de Lange. The Hindmarsh-Rose neuron model: Bifurcation analysis and piecewise-linear approximations. *Chaos*, 18:033128, 2008.
- [44] D. Terman. Chaotic spikes arising from a model of bursting in excitable membranes. *SIAM J. Appl. Math.*, 51(5):1418–1450, 1991.
- [45] C. Tresser. About some theorems by L. P. Shilnikov. *Ann. Inst. H. Poincaré Phys. Théor.*, 40(4):441–461, 1984.
- [46] T. Vo and M. Wechselberger. Canards of folded saddle-node type i. *SIAM J. Math. Anal.*, 47:3235–3283, 2015.

